UNIVERSITY OF CALIFORNIA
SANTA CRUZ

THEORY AND PHENOMENOLOGY OF CP-CONSERVING TWO-HIGGS-DOUBLET MODELS WITH FLAVOR-ALIGNED AND FOUR-TEXTURE YUKAWA COUPLINGS

A dissertation submitted in partial satisfaction of the
requirements for the degree of

DOCTOR OF PHILOSOPHY

in

PHYSICS

by

Joseph M. Connell

June 2024

The Dissertation of Joseph M. Connell
is approved:

Professor Howard E. Haber, Chair

Professor Stefania Gori

Professor Michael Hance

Peter F. Biehl
Vice Provost and Dean of Graduate Studies

Table of Contents

List of Figures

List of Tables

Abstract

Theory and Phenomenology of

CP-conserving Two-Higgs-doublet Models with Flavor-Aligned and

Four-Texture Yukawa Couplings

by

Joseph M. Connell

As our ability to probe the nature of the fundamental particles and their interactions improves with increasing particle collider data, we have more compelling reasons to explore models beyond the Standard Model (SM). Searches for new Higgs bosons of an extended Higgs sector beyond the SM (BSM) at the Large Hadron Collider (LHC) can be interpreted in the framework of the two-Higgs-doublet model. Two-Higgs-doublet Models (2HDMs) are among the simplest extensions extensions of the SM that yield interesting phenomenology. Understanding the pattern in which Higgs bosons couple to fermions is important for searches for Higgs bosons beyond the SM and flavor physics. In this dissertation, we study two specific patterns of Yukawa couplings which are designed to provide a more general Yukawa framework than the common $\mathbb{Z}_2$-symmetric models, providing access to more 2HDM parameter space, while still controlling the potentially dangerous flavor changing neutral currents (FCNCs).

The first project presented demonstrates that $\mathbb{Z}_2$-symmetric models are too restrictive and experimentalists should not limit themselves to these specialized models. Instead, we should allow experiments to determine the nature of Yukawa couplings. In this work, we assume the Yukawa coupling matrices are flavor-diagonal

and so proportional to the mass matrices. This model is known as the flavor-aligned 2HDM (A2HDM), of which $\mathbb{Z}_2$-symmetric models are a subset. To demonstrate this paradigm shift, we devised two scenarios in which we simultaneously fit two excesses for BSM scalars in LHC data within the A2HDM via parameter scans. We then present a few benchmark parameter points of interest to demonstrate what channels may reveal more information in future BSM Higgs boson searches.

In the second project, we work under the assumption that the 2HDM Yukawa matrices are of the four-texture form, with zeros in particular entries, and the parameters therein have a hierarchy in accordance with the fermion masses. This structure is motivated by the Cheng-Sher-like physical Yukawa couplings that it can produce, which enables small flavor-violating processes occur but systematically avoids current limits on FCNCs. We show that these models are phenomenologically viable and recast the calculation of the physical Yukawa couplings in a basis-independent formulation by rotating into the Higgs basis before assuming a particular structure for the Yukawa coupling matrices. Finally, we discuss the landscape of flavor-violating observables' predictions in this model, the landscape of their measurements, and the prospect of these channels to be measured at future high-energy particle colliders.

I dedicate this dissertation to Papa Joe,

whose few words, many lessons, and innumerable plants

continue to grow.

Acknowledgments

One big MAHALO to my web of supporters who walked, biked, and paddled alongside me through this surging journey:

- From the beginning, Mother Ocean encouraged me in academia, surfing, and washing my hands. And Grandmom Daphne, who loved being naughty as much as I do.
- Christeeno, whose example and rivalry kept the candle burning and the ripe papayas hidden.
- Erin O'Connor, beacon of light and laughter, family and friend, you are a warrior for science's true, youthful, wise wishes for humans.
- Mike and Sarah Bigheardt, who always raise my spirits, get me out of bed, and make one mean foofy coffee.
- Chris Owens, Jensen Hassett, and Avery Stuver who opened my eyes and heart to what is possible in the ocean and in friendship.
- Howard E. Haber, whose patience and long drives will be missed.

The text of this dissertation includes reprint of the following previously published material: Accommodating hints of new heavy scalars in the framework of the flavor-aligned two-Higgs-doublet model. Connell, Joseph M. and Ferreira, P. M. and Haber, Howard E., Phys. Rev. D 108, 055031, published 28 September 2023. Pedro M. Ferreira provided valuable feedback and checks of those results. Howard E. Haber directed and supervised the research which forms the basis for the dissertation.

Part I

Introduction to

Two-Higgs-Doublet Models

Chapter 1

Introduction

After ten years of Higgs boson studies, the LHC data show no significant deviations from the predictions of the Standard Model (SM). The phenomenological profile of the Higgs boson resembles that of the SM with precisions approaching 10% in some channels [1,2]. One may be left wondering whether we have reached the end of our exploration of the theory of elementary particles and their interactions.

However, the Standard Model is known to be incomplete (e.g., it cannot accommodate dark matter, baryogenesis, and neutrino masses, while providing no explanation for the origin of the electroweak energy scale). Whether departures will first be revealed at the TeV scale, perhaps in future LHC experiments, or whether physics beyond the SM enters at a much higher energy scale remains to be seen. Nevertheless, independently of whether the more profound questions associated with the incompleteness of the SM can be directly addressed at the LHC, one can pose the following pedestrian query. Given the nonminimal nature of the matter and gauge multiplets that comprise the SM, should one also expect a nonminimal scalar sector as well? If yes, is it possible (and perhaps even likely) that additional particles beyond the SM not yet discovered will eventually emerge from future LHC data?

Examples of such additional states could be new gauge bosons [implying that the gauge group relevant for TeV scale physics is larger than $SU(3)\times SU(2)\times U(1)$], new fermionic states (such as vectorlike quarks and leptons), new scalar states (e.g., an extended Higgs sector), supersymmetric partners of SM particles, or even more exotic objects such as leptoquarks.

In this work, we focus on the possibility that the scalar sector includes additional color singlet neutral and charged scalars beyond the SM Higgs boson. It is certainly an important experimental question to ask whether such states exist in a mass range accessible to the LHC. Indeed, the ATLAS and CMS Collaborations have performed numerous searches for such new scalar states using the Run 1 and Run 2 data sets, and such searches will continue and will be expanded during Run 3 and beyond.

So far, no definitive signals of new scalar states have been announced. From time to time, small excesses of events emerge in some search channels, as one would expect based on fluctuations of data from the size of the data samples. Nevertheless, if new scalar states do exist in Nature in a range that can be probed by the LHC, then the initial signal of these states will often resemble the excesses due to expected fluctuations in the data. Of course, increasing the size of the data samples as more data is collected will reveal which of these two possibilities is the correct interpretation.

In searching for evidence for new scalar states, one often is required to make model assumptions in developing the search strategies and in interpreting the results. The more specific the model assumptions are, the less flexible the data analysis. On the other hand, the more generic the model, the more difficult it is to focus on specific experimental signatures. In proposing searches for extended Higgs sector

phenomena, we find it convenient to focus on the two Higgs doublet extension of the Standard Model (2HDM) [3]. This model possesses the main ingredients for new phenomena that one expects in most extended Higgs sectors. These include charged scalars, CP-odd scalars (if the neutral scalar sector is CP-conserving) or neutral scalars of indefinite CP (if the scalar sector is CP-violating), and the possibility of Higgs-mediated flavor changing neutral currents (FCNCs), which if present must be small enough to avoid conflict with present experimental data.

The most general 2HDM adds a significant number of new parameters to the Standard Model. Recall that the Standard Model (where neutrino masses are zero and are not counted as separate parameters) is governed by 19 parameters, which include three gauge couplings, $\Theta_{\rm QCD}$, nine quark and lepton masses, three Cabibbo-Kobayashi-Maskawa (CKM) angles, one CKM phase, and two parameters of the Higgs sector that can be taken to be the Higgs vacuum expectation value, $v \simeq 246$ GeV and the Higgs mass (e.g., see Ref. [**?**]). In the most general 2HDM, the two Higgs sector parameters of the SM are expanded to eleven, and new Higgs-fermion Yukawa matrix couplings arise that are in principle independent of the quark and lepton masses. In light of Eq. (2.36), these new Yukawa matrix couplings correspond to the six 3×3 hermitian matrices ρ_R^F and ρ_I^F (where $F = U, D, E$ refers to the couplings to up-type quarks, down-type quarks and charged leptons, respectively) and yield 54 new parameters. Thus, the most general two-Higgs-doublet extension of the SM is governed by 82 parameters!

It is not practical to devise search strategies that scan over all 82 parameters of the general 2HDM. Moreover, a generic point in this 82-dimensional space would be immediately ruled out due to scalar-mediated FCNCs that can already be experimentally ruled out. In the literature, the standard practice is to eliminate tree-

level Higgs-mediated FCNCs by imposing an appropriate discrete symmetry [4, 5]. By considering all possible symmetries of this type, one finds four classes of 2HDM Yukawa couplings, which are called Types I, II, X and Y in the literature [6–8]. From a purely phenomenological point of view, this assumption is too strong as it reduces the size of the 2HDM parameter space more strictly than necessary. Indeed, it is sufficient to simply require that the hermitian matrices ρ_R^F and ρ_I^F are diagonal, as in the case of the flavor-aligned model, or roughly diagonal, as in the case of the four-texture Yukawa coupling matrices. These are the two approaches to simplifying the 2HDM that we will study in this dissertation.

One can reduce the number of 2HDM parameters even further by assuming that ρ_R^F and ρ_I^F are each proportional to the 3×3 identity matrix (with coefficients, called flavor-alignment parameters, that depend on F), which yields the flavor-aligned 2HDM (A2HDM) [9]. Flavor-aligned extended Higgs sectors can naturally arise from symmetries of ultraviolet completions of low-energy effective theories of flavor as shown in Refs. [10–13]. In such models, departures from exact flavor alignment due to renormalization group running down to the electroweak scale are typically small enough [14, 52] to be consistent with all known experimental FCNC bounds.

The other mechanism which can sufficiently suppress FCNCs in 2HDMs that are more generic than the $\mathbb{Z}_2$-symmetric models is the Cheng-Sher Ansatz. This is a pattern of physical Yukawa couplings in which the matrices depend on the fermion masses like $\rho^F \sim \frac{\sqrt{m_1 m_2}}{v}$. Because of the hierarchy of fermion masses $m_3 > m_2 > m_1$ for up- and down-type quarks and charged leptons, the off-diagonal flavor-violating elements are sufficiently suppressed.

Although there are theoretical arguments for favoring the stricter Types I,

II, X and Y structures (which are renormalization group stable [16] and hence can be realized without an artificial fine-tuning of parameters in the 82-dimensional 2HDM parameter space), ultimately it will be experiment that will determine the structure of the Yukawa interactions. Indeed, if potential signals of an extended Higgs sector arise, we believe that it is prudent to employ the less restrictive A2HDM framework in order to test the validity of the 2HDM interpretation of the data.

Likewise, one must decide whether to include new sources of CP-violation in the 2HDM when confronting potential signals of extended Higgs sector phenomenology. Experimental constraints exist due to the absence of evidence for an electric dipole moment of the electron [17, 18]. In this work, we choose to assume a CP-conserving scalar sector for simplicity to reduce the number of parameters of the model and simplify the subsequent analysis. This is accomplished by taking the flavor-alignment parameters to be real and demanding the existence of a Higgs basis in which all the scalar potential parameters are real. It is quite likely that any initial discovery of new scalars at the LHC will be insensitive to assumptions regarding possible CP-violating parameters associated with the extended Higgs sector. However, it is certainly worth considering the phenomenological implications of scalar sector CP violation, which we will leave for a future work.

In Chapter 2 we review the theoretical structure of the 2HDM. We explicitly specify the parameters that govern the A2HDM or Cheng-Sher models' parameter space, specializing to the case where no CP-violating parameters (beyond the CKM phase) are present. In particular, the model parameters are defined such that they are manifestly basis-independent quantities and hence directly related to physical observables. In Chapter 3 we discuss the most relevant constraints on 2HDMs that will be used in Parts 2 and 3 of this dissertation.

Chapter 2

Theoretical Background

In this chapter we introduce the mathematical framework of the Two-Higgs-Doublet Model (2HDM). The 2HDM consists of two identical, complex, hypercharge-one, SU(2) doublet scalar fields

$$\Phi_i(x) \equiv \begin{pmatrix} \Phi_i^+(x) \\ \Phi_i^0(x) \end{pmatrix} \tag{2.1}$$

which are labeled by the Higgs flavor index $i \in \{1, 2\}$. In a generic basis, which has no physical significance, and is called the Φ-basis, the most general renormalizable $\mathrm{SU(2)_L} \times \mathrm{U(1)_Y}$ invariant scalar potential takes the form

$$\begin{aligned} \mathcal{V} = {} & m_{11}^2 \Phi_1^\dagger \Phi_1 + m_{22}^2 \Phi_2^\dagger \Phi_2 - [m_{12}^2 \Phi_1^\dagger \Phi_2 + \text{h.c.}] \\ & + \tfrac{1}{2}\lambda_1 (\Phi_1^\dagger \Phi_1)^2 + \tfrac{1}{2}\lambda_2 (\Phi_2^\dagger \Phi_2)^2 + \lambda_3 (\Phi_1^\dagger \Phi_1)(\Phi_2^\dagger \Phi_2) + \lambda_4 (\Phi_1^\dagger \Phi_2)(\Phi_2^\dagger \Phi_1) \\ & + \left\{ \tfrac{1}{2}\lambda_5 (\Phi_1^\dagger \Phi_2)^2 + \left[\lambda_6 (\Phi_1^\dagger \Phi_1) + \lambda_7 (\Phi_2^\dagger \Phi_2)\right] \Phi_1^\dagger \Phi_2 + \text{h.c.} \right\}, \end{aligned} \tag{2.2}$$

where the parameters m_{11}^2, m_{22}^2, and $\lambda_{1,2,3,4}$ are real and m_{12}^2 and $\lambda_{5,6,7}$ are potentially complex. We assume that the parameters of the scalar potential are chosen such that the minimum of the scalar potential respects the $\mathrm{U(1)_{EM}}$ gauge symmetry.

Then the scalar field vacuum expectation values (vevs) of these fields are of the form

$$\langle \Phi_i \rangle = \frac{v}{\sqrt{2}} \begin{pmatrix} 0 \\ \widehat{v}_i \end{pmatrix} , \tag{2.3}$$

where $v = 246$ GeV and $\widehat{v}$ is a complex vector of unit norm, parametrized by the angles β and ξ,

$$\widehat{v} = (\widehat{v}_1, \widehat{v}_2) = (c_\beta, s_\beta e^{i\xi}) . \tag{2.4}$$

Without loss of generality, $\widehat{v}_1$ is chosen to be nonnegative, $0 \leq \beta \leq \frac{1}{2}\pi$, $0 \leq \xi \leq 2\pi$, and we employ the convenient notation $c_\beta \equiv \cos(\beta)$ and $s_\beta \equiv \sin(\beta)$ throughout this work. Note that Eq. (2.4) defines the angle β which is an important quantity in the study of 2HDMs, which will appear as

$$\tan\beta = \frac{|\widehat{v}_2|}{|\widehat{v}_1|} \tag{2.5}$$

in the study of CP-conserving $\mathbb{Z}_2$-symmetric 2HDMs. The constant v is determined by the Fermi constant,

$$v \equiv \frac{2m_W}{g} = (\sqrt{2}G_F)^{-1/2} = 246 \text{ GeV} . \tag{2.6}$$

2.1 The Higgs Basis

The interaction Φ-basis presented above is arbitrary and has no physical significance. We are always free to redefine the scalar doublet fields via a unitary transformation,

$$\Phi_i \to U_{ij}\Phi_j . \tag{2.7}$$

Utilizing this freedom, we create linear combinations of the Φ_i to create the so-called Higgs basis fields $\mathcal{H}_{1,2}$ for which the vevs are real $\langle \mathcal{H}_1 \rangle = (0, v/2)$ and vanishing

$\langle \mathcal{H}_2 \rangle = (0,0)$, respectively. In terms of the Φ-basis doublet fields, the Higgs basis fields $\mathcal{H}_i$ are then,

$$\begin{aligned} \mathcal{H}_1 &= (\mathcal{H}_1^+ \,,\, \mathcal{H}_1^0) \equiv \widehat{v}_i^* \Phi_i \\ \mathcal{H}_2 &= (\mathcal{H}_2^+ \,,\, \mathcal{H}_2^0) \equiv e^{i\eta} \widehat{w}_i^* \Phi_i \equiv e^{i\eta} \epsilon_{ij} \widehat{v}_i \Phi_j \,, \end{aligned} \tag{2.8}$$

where $\epsilon_{12} = -\epsilon_{21} = 1$ and $\epsilon_{11} = \epsilon_{22} = 0$, and there is an implicit sum over repeated indices. The phase factor $e^{i\eta}$ is present because one can rephase $\mathcal{H}_2^0$ while $\langle \mathcal{H}_2^0 \rangle$ remains zero, so the Higgs basis is not fully unique.

The scalar potential rewritten in terms of the Higgs basis fields defined in Eq. (2.8) takes the same form as in the Φ-basis but with new coefficients $Y_{1,2,3}$ and Z_{1-7},

$$\begin{aligned} \mathcal{V} =& Y_1 \mathcal{H}_1^\dagger \mathcal{H}_1 + Y_2 \mathcal{H}_2^\dagger \mathcal{H}_2 + [Y_3 e^{-i\eta} \mathcal{H}_1^\dagger \mathcal{H}_2 + \text{h.c.}] \\ &+ \tfrac{1}{2} Z_1 (\mathcal{H}_1^\dagger \mathcal{H}_1)^2 + \tfrac{1}{2} Z_2 (\mathcal{H}_2^\dagger \mathcal{H}_2)^2 + Z_3 (\mathcal{H}_1^\dagger \mathcal{H}_1)(\mathcal{H}_2^\dagger \mathcal{H}_2) + Z_4 (\mathcal{H}_1^\dagger \mathcal{H}_2)(\mathcal{H}_2^\dagger \mathcal{H}_1) \\ &+ \left\{ \tfrac{1}{2} Z_5 e^{-2i\eta} (\mathcal{H}_1^\dagger \mathcal{H}_2)^2 + \left[Z_6 e^{-i\eta} (\mathcal{H}_1^\dagger \mathcal{H}_1) + Z_7 e^{-i\eta} (\mathcal{H}_2^\dagger \mathcal{H}_2) \right] \mathcal{H}_1^\dagger \mathcal{H}_2 + \text{h.c.} \right\} , \end{aligned} \tag{2.9}$$

where $Y_{1,2}$ and $Z_{1,2,3,4}$ are invariant under the basis transformation $\Phi_i \to U_{ij} \Phi_j$, and the remaining parameters transform as,

$$[Y_3, Z_6, Z_7, e^{i\eta}] \to (\det\ U)^{-1} [Y_3, Z_6, Z_7, e^{i\eta}] \quad \text{and} \quad Z_5 \to (\det\ U)^{-2} Z_5 \,. \tag{2.10}$$

It follows that the Higgs basis fields $\mathcal{H}_i$, the scalar potential in terms of Higgs basis fields $\mathcal{V}$, and the parameters therein, are all invariant under U(2) basis transformations. The relationships,

$$Y_1 = -\tfrac{1}{2} Z_1 v^2 \,, \qquad Y_3 = -\tfrac{1}{2} Z_6 v^2 \,, \tag{2.11}$$

are the minimization conditions of the scalar potential in the Higgs basis.

2.2 Scalar Mass Eigenstates

From the scalar potential in the Higgs basis given in Eq. (2.9) (along with the minimization conditions given in Eq. (2.11)) one can identify the masses of the neutral scalars and the corresponding eigenstates. We construct the 4×4 neutral scalar mass-squared matrix in the $\{\sqrt{2}\,\mathrm{Re}\,\mathcal{H}_1^0 - v, \sqrt{2}\,\mathrm{Im}\,\mathcal{H}_1^0, \sqrt{2}\,\mathrm{Re}\,\mathcal{H}_2^0, \sqrt{2}\,\mathrm{Im}\,\mathcal{H}_2^0\}$ basis, remove the massless Goldstone boson $G^0 = \sqrt{2}\,\mathrm{Im}\,\mathcal{H}_1^0$, and are left with a 3×3 mass-squared matrix that can be diagonalized to find the physical neutral scalar masses,

$$\mathcal{M}^2 = v^2 \begin{pmatrix} Z_1 & \mathrm{Re}(Z_6 e^{-i\eta}) & -\mathrm{Im}(Z_6 e^{-i\eta}) \\ \mathrm{Re}(Z_6 e^{-i\eta}) & \frac{1}{2}\big[Z_{34} + \mathrm{Re}(Z_5 e^{-2i\eta})\big] + \overline{Y_2} & -\frac{1}{2}\,\mathrm{Im}(Z_5 e^{-2i\eta}) \\ -\mathrm{Im}(Z_6 e^{-i\eta}) & -\frac{1}{2}\,\mathrm{Im}(Z_5 e^{-2i\eta}) & \frac{1}{2}\big[Z_{34} - \mathrm{Re}(Z_5 e^{-2i\eta})\big] + \overline{Y_2} \end{pmatrix}, \tag{2.12}$$

where for brevity we defined $Z_{34} \equiv Z_3 + Z_4$ and $\overline{Y_2} = Y_2/v^2$. The eigenvalues of $\mathcal{M}^2$ are the squared masses m_k^2 (where $k = 1, 2, 3$) of the physical scalars. The squared masses m_k^2 do not depend on the phase angle η.

To find the eigenvalues m_k^2 we diagonalize $\mathcal{M}^2$ via a real orthogonal transformation with unit determinant,

$$R\mathcal{M}^2 R^T = \mathcal{M}_D^2 \equiv \mathrm{diag}\,(m_1^2\,,\, m_2^2\,,\, m_3^2)\,, \tag{2.13}$$

where $RR^T = I$. The matrix R can be found by multiplying three rotation matrices R_{12}, R_{13}, R_{23}, corresponding to subrotations parametrized by mixing angles θ_{12}, θ_{13}, and θ_{23},

$$\begin{aligned} R = R_{12}R_{13}R_{23} &= \begin{pmatrix} c_{12} & -s_{12} & 0 \\ s_{12} & c_{12} & 0 \\ 0 & 0 & 1 \end{pmatrix} \begin{pmatrix} c_{13} & 0 & -s_{13} \\ 0 & 1 & 0 \\ s_{13} & 0 & c_{13} \end{pmatrix} \begin{pmatrix} 1 & 0 & 0 \\ 0 & c_{23} & -s_{23} \\ 0 & s_{23} & c_{23} \end{pmatrix} \\ &= \begin{pmatrix} c_{13}c_{12} & -c_{23}s_{12} - c_{12}s_{13}s_{23} & -c_{12}c_{23}s_{13} + s_{12}s_{23} \\ c_{13}s_{12} & c_{12}c_{23} - s_{12}s_{13}s_{23} & -c_{23}s_{12}s_{13} - c_{12}s_{23} \\ s_{13} & c_{13}s_{23} & c_{13}c_{23} \end{pmatrix}, \end{aligned} \tag{2.14}$$

where $c_{ij} \equiv \cos\theta_{ij}$ and $s_{ij} \equiv \sin\theta_{ij}$. If the angles are taken to be $\theta_{12} \geq -\pi$, $\theta_{23} < \pi$, and $|\theta_{13}| \leq \pi/2$, then R encompasses all SO(3) rotations. A rationale of these angle choices can be found in section 4 of Ref. [19]. In light of Eq. (2.10), $\mathcal{M}^2$ is independent of the scalar field basis being used, therefore the mixing angles θ_{ij} are basis-independent parameters.

We can parametrize the Higgs basis fields as,

$$\mathcal{H}_1 = \begin{pmatrix} \mathcal{H}_1^+ \\ \frac{1}{\sqrt{2}}\left(v + \varphi_1^0 + iG^0\right) \end{pmatrix}, \qquad \mathcal{H}_2 = \begin{pmatrix} \mathcal{H}_2^+ \\ \frac{1}{\sqrt{2}}\left(\varphi_2^0 + ia^0\right) \end{pmatrix}, \tag{2.15}$$

where in the general CP-violating 2HDM, the fields $\varphi_{1,2}^0$ and a^0 all mix, producing three CP-indefinite Higgs mass eigenstates. The charged scalar mass-eigenstates are defined by the charged components of the Higgs basis fields,

$$G^\pm = \mathcal{H}_1^\pm\,, \qquad H^\pm \equiv e^{\pm i\theta_{23}}\mathcal{H}_2^\pm\,, \tag{2.16}$$

where the charged Goldstone fields $G^\pm$ are massless, the charged Higgs scalar masses are given by,

$$m_{H^\pm}^2 = Y_2 + \tfrac{1}{2}Z_3 v^2\,, \tag{2.17}$$

and we have rephased the charged Higgs field for later convenience.

The physical neutral Higgs mass-eigenstates are denoted by h_k (where $k = 1, 2, 3$) and can be found by rotating to the mass basis,

$$\begin{pmatrix} h_1 \\ h_2 \\ h_3 \end{pmatrix} = R \begin{pmatrix} \varphi_1^0 \\ \varphi_2^0 \\ a^0 \end{pmatrix}, \tag{2.18}$$

or in terms of Higgs basis fields,

$$\begin{pmatrix} h_1 \\ h_2 \\ h_3 \end{pmatrix} = RW \begin{pmatrix} \sqrt{2}\,\mathrm{Re}\,\mathcal{H}_1^0 - v \\ \mathcal{H}_2^0 \\ \mathcal{H}_2^{0\dagger} \end{pmatrix}, \tag{2.19}$$

k	q_{k1}	q_{k2}
1	$c_{12}c_{13}$	$-s_{12} - ic_{12}s_{13}$
2	$s_{12}c_{13}$	$c_{12} - is_{12}s_{13}$
3	s_{13}	ic_{13}

Table 2.1: The invariant quantities $q_{k\ell}$ are functions of the invariant neutral Higgs mixing angles θ_{12} and θ_{13}, and they are used to define the physical Higgs mass-eigenstate fields in term of the Higgs basis fields.

where we have introduced the unitary matrix,

$$W = \begin{pmatrix} 1 & 0 & 0 \\ 0 & 1/\sqrt{2} & 1/\sqrt{2} \\ 0 & -i/\sqrt{2} & i/\sqrt{2} \end{pmatrix}. \tag{2.20}$$

We choose a convention where $m_1 \leq m_2 \leq m_3$ so that m_1 is the lightest Higgs boson and will have properties that approximate those of the SM Higgs boson in this work. In terms of the Higgs basis fields, the mass-eigenstates h_k are given by,

$$h_k = q_{k1}\big(\sqrt{2}\,\mathrm{Re}\,\mathcal{H}_1^0 - v\big) + \frac{1}{\sqrt{2}}\big(q_{k2}^*\mathcal{H}_2^0 e^{i\theta_{23}} + \mathrm{h.c.}\big)\,, \tag{2.21}$$

where the expressions for the q_{k1} and q_{k2} are shown in Table 2.1.

The Higgs basis fields can be expressed in terms of the mass eigenstate fields by inverting Eq. (2.21),

$$\mathcal{H}_1 = \begin{pmatrix} G^+ \\ \dfrac{1}{\sqrt{2}}\left(v + iG + \displaystyle\sum_{k=1}^{3} q_{k1}h_k\right) \end{pmatrix}, \qquad e^{i\theta_{23}}\mathcal{H}_2 = \begin{pmatrix} H^+ \\ \dfrac{1}{\sqrt{2}}\displaystyle\sum_{k=1}^{3} q_{k2}h_k \end{pmatrix}. \tag{2.22}$$

In Eq. (2.16) we conveniently rephased the charged Higgs field so that the charged and neutral components have the same phase, which then becomes an overall phase on $\mathcal{H}_2$. This phase can be eliminated by rephasing $\mathcal{H}_2 \to e^{-i\theta_{23}}\mathcal{H}_2$. Therefore even though θ_{23} is an invariant parameter, it has no physical significance. Thus, without loss of generality, we henceforth set $\theta_{23} = 0$.

2.3 2HDM Yukawa Couplings

The Yukawa Lagrangian governs how the 2HDM scalar fields interact with fermions. We begin by writing the most general Higgs-quark interaction Lagrangian in terms of Higgs fields in a generic interaction Φ-basis and interaction eigenstate quark fields. We denote left-handed quark doublet fields by $Q_L^0 = (U_L^0, D_L^0)$ and right-handed quark singlet fields by U_R^0 and D_R^0, where the superscript means that fermion field is in the interaction basis, and we will remove the superscript after rotating to the mass basis. The left- and right-handed quark fields are defined via the projection operators $Q_{R,L} \equiv P_{R,L}Q$, where $P_{R,L} \equiv \frac{1}{2}(1 \pm \gamma_5)$.

In order to discuss Higgs-fermion interactions in a basis-independent formalism, we rewrite the Yukawa Lagrangian in the Higgs basis. We then obtain the quark mass matrices by setting the Higgs fields to their vacuum expectation values. The two resulting 3×3 quark mass matrices can be diagonalized via a singular value decomposition, which also enables one to find the left- and right-handed quark mass-eigenstate fields $U_{R,L}$ and $D_{R,L}$, where $D = (d, s, b)$ and $U = (u, c, t)$. Finally, by expressing the Yukawa Lagrangian in terms of Higgs mass-eigenstate fields, we can read off the physical Higgs-fermion-fermion' couplings.

The Higgs-fermion-fermion' interaction Yukawa Lagrangian in terms of interaction eigenstate Higgs doublet fields Φ_i and quark interaction eigenstates is [25]

$$-\mathscr{L}_{\rm Y} = \overline{Q}_L^0 \widetilde{\Phi}_1 \eta_1^{U,0} U_R^0 + \overline{Q}_L^0 \Phi_1 \eta_1^{D,0\dagger} D_R^0 + \overline{Q}_L^0 \widetilde{\Phi}_2 \eta_2^{U,0} U_R^0 + \overline{Q}_L^0 \Phi_2 \eta_1^{D,0\dagger} D_R^0 + \text{h.c.} \quad (2.23)$$

where $\widetilde{\Phi}_a \equiv i\sigma_2 \Phi^*$ and σ_2 is the second Pauli matrix with $\sigma_{2,11} = \sigma_{2,22} = 0$ and $\sigma_{2,21} = -\sigma_{2,12} = i$. By inverting Eq. (2.8), the Higgs interaction eigenstates can be

written in terms of the Higgs basis fields,

$$\Phi_i = \mathcal{H}_1 \widehat{v}_i + \mathcal{H}_2 \widehat{w}_i$$
$$\widetilde{\Phi}_i = \widetilde{\mathcal{H}}_1 \widehat{v}_i^* + \widetilde{\mathcal{H}}_2 \widehat{w}_i^* \,, \tag{2.24}$$

and the Yukawa Lagrangian can be rewritten in terms of the Higgs basis fields as,

$$\begin{aligned} -\mathscr{L}_{\rm Y} \;=\; & \overline{Q}^0_L(\widetilde{\mathcal{H}}_1 \widehat{v}_1^* + \widetilde{\mathcal{H}}_2 \widehat{w}_1^*)\eta_1^{U,0} U^0_R \;+\; \overline{Q}^0_L(\mathcal{H}_1 \widehat{v}_1 + \mathcal{H}_2 \widehat{w}_1)\eta_1^{D,0\dagger} D^0_R \\ & + \overline{Q}^0_L(\widetilde{\mathcal{H}}_1 \widehat{v}_2^* + \widetilde{\mathcal{H}}_2 \widehat{w}_2^*)\eta_2^{U,0} U^0_R \;+\; \overline{Q}^0_L(\mathcal{H}_1 \widehat{v}_2 + \mathcal{H}_2 \widehat{w}_2)\eta_2^{D,0\dagger} D^0_R + \text{h.c.}\,, \end{aligned} \tag{2.25}$$

Next we construct invariant and pseudo-invariant Yukawa coupling matrices:

$$\kappa^{Q,0} \equiv \widehat{v}_i^* \eta_i^{Q,0}, \qquad \rho^{Q,0} \equiv \widehat{w}_i^* \eta_i^{Q,0} \tag{2.26}$$
$$\kappa^{Q,0\dagger} = \widehat{v}_i \eta_i^{Q,0\dagger}, \qquad \rho^{Q,0\dagger} = \widehat{w}_i \eta_i^{Q,0\dagger} \,. \tag{2.27}$$

and rewrite the Yukawa Lagrangian in terms of these invariant coupling matrices,

$$-\mathscr{L}_{\rm Y} \;=\; \overline{Q}^0_L(\widetilde{\mathcal{H}}_1 \kappa^{U,0} + \widetilde{\mathcal{H}}_2 \rho^{U,0}) U^0_R \;+\; \overline{Q}^0_L(\mathcal{H}_1 \kappa^{D,0\dagger} + \mathcal{H}_2 \rho^{D,0\dagger}) D^0_R + \text{h.c.} \tag{2.28}$$

After expanding the products of Higgs doublets and quark doublets (*i.e.* $\overline{Q^0_L}\widetilde{\mathcal{H}}_i$ and $\overline{Q^0_L}\mathcal{H}_i$), we arrive at the following Yukawa Lagrangian in terms of singlet interaction eigenstate quark fields,

$$\begin{aligned} -\mathscr{L}_{\rm Y} \;=\; & \overline{U}^0_L(\mathcal{H}_1^{0\dagger} \kappa^{U,0} + \mathcal{H}_2^{0\dagger} \rho^{U,0}) U^0_R \;-\; \overline{D}^0_L(\mathcal{H}_1^{-} \kappa^{U,0} + \mathcal{H}_2^{-} \rho^{U,0}) U^0_R \\ & + \overline{U}^0_L(\mathcal{H}_1^{+} \kappa^{D,0\dagger} + \mathcal{H}_2^{+} \rho^{D,0\dagger}) D^0_R \;+\; \overline{D}^0_L(\mathcal{H}_1^{0} \kappa^{D,0\dagger} + \mathcal{H}_2^{0} \rho^{D,0\dagger}) D^0_R \;+\; \text{h.c.}\,. \end{aligned} \tag{2.29}$$

Now by inspecting the vacuum with $\langle \mathcal{H}_1^0 \rangle = \frac{v}{\sqrt{2}}$ and $\langle \mathcal{H}_2^0 \rangle = 0$, we see that the $\kappa^{Q,0}$ are proportional to the mass matrices $M_{Q,0}$, as intended in the construction of the $\kappa^{Q,0}$ matrices.

We now diagonalize the quark mass matrices and express the Yukawa Lagrangian in terms of quark mass eigenstates, which also involves transforming the

Yukawa coupling matrices $\rho^{Q,0}$ into the quark mass-eigenstate basis. The diagonalization of the $\kappa^{Q,0}$ matrices, and the corresponding redefinition of the $\rho^{Q,0}$ matrices, are accomplished via a singular value decomposition:

$$\begin{aligned} \kappa^U &= V_L^U \kappa^{U,0} V_R^{U\dagger}\,, & \rho^U &= V_L^U \rho^{U,0} V_R^{U\dagger} \\ \kappa^D &= V_R^D \kappa^{D,0} V_L^{D\dagger}\,, & \rho^D &= V_R^D \rho^{D,0} V_L^{D\dagger}. \end{aligned} \tag{2.30}$$

Notice that L and R are swapped on κ^D and ρ^D compared to κ^U and ρ^U. The diagonalization of the $\kappa^{Q,0}$ matrices does not imply simultaneous diagonalization of the $\rho^{Q,0}$ matrices. The diagonal quark mass matrices $M_{U,D}$ are then,

$$\begin{aligned} M_U &= \frac{v}{\sqrt{2}}\kappa^U = \mathrm{diag}(m_u, m_c, m_t) = V_L^U M_U^0 V_R^{U\dagger} \\ M_D &= \frac{v}{\sqrt{2}}\kappa^{D\dagger} = \mathrm{diag}(m_d, m_s, m_b) = V_L^D M_D^0 V_R^{D\dagger}\,, \end{aligned} \tag{2.31}$$

and the quark interaction eigenstate fields are then transformed to the quark mass eigenstate fields by,

$$\begin{aligned} U_L &= V_L^U U_L^0, & U_R &= V_R^U U_R^0 \\ D_L &= V_L^D D_L^0, & D_R &= V_R^D D_R^0\,. \end{aligned} \tag{2.32}$$

In terms of quark mass eigenstates, diagonalized quark mass matrices, and Higgs-quark-quark' coupling matrices in the quark mass basis, the Yukawa Lagrangian becomes,

$$\begin{aligned} -\mathscr{L}_{\mathrm{Y}} = {} & \overline{U}_L(\mathcal{H}_1^{0\dagger}\kappa^U + \mathcal{H}_2^{0\dagger}\rho^U)U_R - \overline{D}_L K^\dagger(\mathcal{H}_1^-\kappa^U + \mathcal{H}_2^-\rho^U)U_R \\ & + \overline{U}_L K(\mathcal{H}_1^+\kappa^{D\dagger} + \mathcal{H}_2^+\rho^{D\dagger})D_R + \overline{D}_L(\mathcal{H}_1^0\kappa^{D\dagger} + \mathcal{H}_2^0\rho^{D\dagger})D_R + \text{h.c.} \end{aligned} \tag{2.33}$$

where K is the CKM matrix defined by $K = V_L^U V_L^{D\dagger}$. Using Eq. (2.22), we can rewrite the most general form of the Yukawa Lagrangian in terms of Higgs mass-

eigenstate fields,

$$
\begin{aligned}
-\mathscr{L}_Y = & \frac{1}{\sqrt{2}}\overline{D}\Big\{q_{k1}\kappa^{D\dagger} + q_{k2}\,\rho^{D\dagger}P_R + q_{k2}^*\,\rho^D P_L\Big\}Dh_k \\
& + \frac{1}{\sqrt{2}}\overline{U}\Big\{q_{k1}\kappa^{U} + q_{k2}^*\,\rho^{U} P_R + q_{k2}\,\rho^{U\dagger} P_L\Big\}Uh_k \\
& + \Big\{\overline{U}\left[K\rho^{D\dagger}P_R - \rho^{U\dagger}KP_L\right]D\mathcal{H}^+ \\
& + \overline{U}\left[K\kappa^{D\dagger}P_R - \kappa^{U}KP_L\right]DG^+ \,+\, \text{h.c.}\Big\}\,,
\end{aligned}
\tag{2.34}
$$

where there is an implicit sum over $k = 1, 2, 3$. The matrices ρ^U and ρ^D are independent basis-invariant complex 3×3 matrices that define the Higgs-quark Yukawa couplings of the model. It is convenient to rewrite the $\rho^{U,D}$ matrices in terms of the following 3×3 hermitian matrices that are invariant with respect to the rephasing of the Higgs basis field $\mathcal{H}_2$,

$$
\rho_R^Q \equiv \frac{v}{2\sqrt{2}}\,M_Q^{-1/2}(\rho^Q + \rho^{Q\,\dagger})M_Q^{-1/2}\,, \qquad \rho_I^Q \equiv \frac{v}{2\sqrt{2}\,i}M_Q^{-1/2}(\rho^Q - \rho^{Q\,\dagger})M_Q^{-1/2}\,,
\tag{2.35}
$$

In terms of these redefinitions, the Yukawa couplings take the following form

$$
\begin{aligned}
-\mathscr{L}_Y = & \frac{1}{v}\,\overline{U}\sum_{k=1}^{3} M_U^{1/2}\Big\{q_{k1}\mathbb{1} + \text{Re}(q_{k2})\big[\rho_R^U + i\gamma_5\rho_I^U\big] + \text{Im}(q_{k2})\big[\rho_I^U - i\gamma_5\rho_R^U\big]\Big\}M_U^{1/2}Uh_k \\
& + \frac{1}{v}\,\overline{D}\sum_{k=1}^{3} M_D^{1/2}\Big\{q_{k1}\mathbb{1} + \text{Re}(q_{k2})\big[\rho_R^D - i\gamma_5\rho_I^D\big] + \text{Im}(q_{k2})\big[\rho_I^D + i\gamma_5\rho_R^D\big]\Big\}M_D^{1/2}Dh_k \\
& + \frac{\sqrt{2}}{v}\Big\{\overline{U}\big[KM_D^{1/2}(\rho_R^D - i\rho_I^D)M_D^{1/2}P_R - M_U^{1/2}(\rho_R^U - i\rho_I^U)M_U^{1/2}KP_L\big]DH^+ \\
& + \text{h.c.}\Big\},
\end{aligned}
\tag{2.36}
$$

where $\mathbb{1}$ is the 3×3 identity matrix. The Yukawa Lagrangians above, Eq. (2.34) and Eq. (2.36), can be generalized to include leptons simply by replacing $D \to E = (e, \mu, \tau)$ and $U \to N = (\nu_e, \nu_\mu, \nu_\tau)$, and using,

$$
M_E = \frac{v}{\sqrt{2}}\kappa^{E\,\dagger} = \text{diag}(m_e\,,\, m_\nu\,,\, m_\tau)\,, \qquad M_N = 0
\tag{2.37}
$$

since neutrinos are massless in the 2HDM. Therefore, from now on, instead of Q we will include leptons and use the label $F = U, D, E$.

The unconstrained hermitian 3×3 Yukawa matrices $\rho^F_{R,I}$ in Eq. (2.36) imply the existence of potentially dangerous flavor-changing neutral Higgs–quark and Higgs–lepton interactions, known as Higgs-mediated flavor changing neutral currents (FCNCs). If the $\rho^F_{R,I}$ have off-diagonal elements that are not suppressed, they can produce sizable Higgs-mediated FCNCs at tree-level that are not observed in Nature, and hence unviable models. Therefore, we are interested in models with some mechanism in place to control and suppress tree-level Higgs-mediated FCNCs.

2.4 $\mathbb{Z}_2$-symmetric 2HDMs

To accommodate the non-observation of tree-level Higgs-mediated FCNCs, one must suppress off-diagonal terms of the Higgs-fermion coupling matrices in the Yukawa Lagrangian of the 2HDM. This is normally accomplished by imposing a $\mathbb{Z}_2$ symmetry on the dimension-4 terms of the Higgs Lagrangian expressed in the Φ-basis. The $\mathbb{Z}_2$ symmetry entails a discrete transformation $\phi \to \pm\phi$ for each field, with each field taking a $+$ or $-$ charge assignment. Imposing a symmetry of this type forces the off-diagonal elements of the Higgs-fermion Yukawa coupling matrices to be zero, completely prohibiting tree-level Higgs-mediated FCNCs. There are four unique ways to assign the $\mathbb{Z}_2$ symmetry charges that accomplish this goal, as specified in Table 2.2. These charge assignments are known as the common 2HDM Types I, II, X, and Y.

With one of these $\mathbb{Z}_2$ symmetries imposed, it follows that $\lambda_6 = \lambda_7 = 0$. One can show [20] that there exists a scalar field basis where $\lambda_6 = \lambda_7 = 0$ if and

	Φ_1	Φ_2	U_R	D_R	E_R	U_L, D_L, N_L, E_L
Type I	$+$	$-$	$-$	$-$	$-$	$+$
Type II	$+$	$-$	$-$	$+$	$+$	$+$
Type X	$+$	$-$	$-$	$-$	$+$	$+$
Type Y	$+$	$-$	$-$	$+$	$-$	$+$

Table 2.2: The four possible, unique $\mathbb{Z}_2$ symmetry charge assignments for scalar and fermion fields in the 2HDM. The $\mathbb{Z}_2$ symmetry is imposed to constrain the Higgs-fermion Yukawa couplings such that tree-level Higgs-mediated FCNCs are naturally absent.

only if the following two conditions are satisfied:

$$(Z_1 - Z_2)\big[(Z_3 + Z_4)|Z_{67}|^2 - Z_2|Z_6|^2 - Z_1|Z_7|^2 - (Z_1 + Z_2)\,\mathrm{Re}(Z_6^* Z_7) + \mathrm{Re}(Z_5^* Z_{67}^2)\big]$$
$$-2|Z_{67}|^2\big(|Z_6|^2 - |Z_7|^2\big) = 0\,, \tag{2.38}$$

$$(Z_1 - Z_2)\,\mathrm{Im}(Z_6^* Z_7) + \mathrm{Im}\big(Z_5^* Z_{67}^2\big) = 0\,, \tag{2.39}$$

where $Z_{67} \equiv Z_6 + Z_7$.

In models with Type I and II Yukawa couplings, the matrices ρ^U and ρ^D are diagonal and fixed as follows,

$$\text{Type I:}\quad \rho^U = \frac{e^{i(\xi+\eta)}\sqrt{2}M_U\cot\beta}{v}\,, \qquad \rho^D = \frac{e^{i(\xi+\eta)}\sqrt{2}M_D\cot\beta}{v}\,, \tag{2.40}$$

$$\text{Type II:}\quad \rho^U = \frac{e^{i(\xi+\eta)}\sqrt{2}M_U\cot\beta}{v}\,, \qquad \rho^D = -\frac{e^{i(\xi+\eta)}\sqrt{2}M_D\tan\beta}{v}\,, \tag{2.41}$$

where $\tan\beta = |\widehat{v}_2/\widehat{v}_1|$ (cf. Eq. (2.5)). In Type X models, the quarks possess Type-I Yukawa couplings whereas the leptons possess Type-II Yukawa couplings. In Type Y models, the quarks possess Type-II Yukawa couplings whereas the leptons possess Type-I Yukawa couplings.

Note that in the generic 2HDM, $\tan\beta$ is not a physical parameter, since the Φ-basis has no physical significance. However, after imposing a $\mathbb{Z}_2$ symmetry on the dimension-4 terms of the Higgs Lagrangian, the Φ-basis where the $\mathbb{Z}_2$ symmetry

is manifestly realized becomes meaningful, in which case $\tan\beta$ is promoted to a physical parameter of the model [19, 20].

2.5 The CP-conserving 2HDM

Formally, 2HDMs which preserve charge-parity symmetry are understood to have CP-violation only entering the model through complex CKM matrix elements. If the 2HDM is restricted to having a CP-conserving Higgs scalar potential and vacuum, then the scalar mass eigenstate analysis presented in Section 2.2 and the Yukawa coupling expressions in Section 2.3 take much simpler forms. We can fix the Higgs basis by rephasing the Higgs basis field $\mathcal{H}_2$ such that the potentially complex scalar potential parameters Y_3 and $Z_{5,6,7}$ are all simultaneously real, yielding the so-called the real Higgs basis. This basis is uniquely defined up to an ambiguity in the sign of the field $\mathcal{H}_2$. As in Refs. [19,20], we set $s_{13} = 0$, $c_{13} = 1$ and $e^{i\eta} = \pm 1$, however the field $\mathcal{H}_2$ can still be of either sign. If one transforms $\mathcal{H}_2 \to -\mathcal{H}_2$, then $e^{i\eta}$ changes sign and the scalar potential parameters parameters Y_3, Z_6 and Z_7 change sign whereas the remaining parameters remain unchanged. Thus, one can define the parameter ε to keep track of the sign changes upon resigning $\mathcal{H}_2$,

$$\varepsilon \equiv e^{i\eta} = \begin{cases} \operatorname{sgn} Z_6\,, & \text{if } Z_6 \neq 0, \\ \operatorname{sgn} Z_7\,, & \text{if } Z_6 = 0 \text{ and } Z_7 \neq 0. \end{cases} \tag{2.42}$$

In the standard notation for the CP-conserving 2HDM, we identify

$$h = h_1\,, \qquad H = -\varepsilon h_2\,, \qquad A = \varepsilon h_3\,, \qquad H^\pm \to \varepsilon H^\pm\,, \tag{2.43}$$

where we have assumed that the lighter of the two CP-even Higgs bosons is SM-like. The neutral CP-odd Higgs mass eigenstate is related to the Higgs basis fields by $A = \varepsilon\sqrt{2}\,\operatorname{Im}\mathcal{H}_2^0$. Eq. (2.43) means that the signs of the fields H and A (and the

sign of $c_{\beta-\alpha}$, as we will see) all flip under the redefinition of the Higgs basis field $\mathcal{H}_2 \to -\mathcal{H}_2$. In the CP-conserving 2HDM literature, in models in which the choice of the Φ-basis is physically meaningful due to the presence of a discrete $\mathbb{Z}_2$ symmetry of the scalar potential, it is traditional to impose one further restriction that $\tan\beta$ is real and positive, which removes the final sign ambiguity in defining the real Higgs basis.

In a real Φ-basis of scalar fields, the mixing angle that diagonalizes the CP-even Higgs squared-mass matrix is denoted by α. However, in the generic CP-conserving 2HDM, the Φ-basis has no physical meaning, which implies that the angles α and β are not separate physical quantities. It is therefore more convenient to analyze the CP-even Higgs squared-mass matrix in the real Higgs basis, in which the 3×3 mass-squared matrix given in Eq. (2.12) simplifies to an upper 2×2 block,

$$\mathcal{M}^2 = \begin{pmatrix} Z_1 v^2 & \varepsilon Z_6 v^2 \\ \varepsilon Z_6 v^2 & m_A^2 + Z_5 v^2 \end{pmatrix}, \tag{2.44}$$

and the squared mass of the CP-odd scalar A is given by the lower 1×1 block,

$$m_A^2 = Y_2 + \tfrac{1}{2}(Z_3 + Z_4 - Z_5)v^2\,. \tag{2.45}$$

The CP-even Higgs mass eigenstates, h and H (with $m_h \leq m_H$), are then related to the neutral fields of the Higgs basis via,

$$\begin{pmatrix} H \\ h \end{pmatrix} = \begin{pmatrix} c_{\beta-\alpha} & -s_{\beta-\alpha} \\ s_{\beta-\alpha} & c_{\beta-\alpha} \end{pmatrix} \begin{pmatrix} \sqrt{2}\,\mathrm{Re}\,\mathcal{H}_1^0 - v \\ \varepsilon\sqrt{2}\,\mathrm{Re}\,\mathcal{H}_2^0 \end{pmatrix}. \tag{2.46}$$

Although it is possible to tune the parameters of the 2HDM such that $m_h = m_H$, this parameter choice does not yield a phenomenologically viable scenario, and is thus excluded from further consideration.Comparing with Eq. (2.21) after setting $s_{13} = \theta_{23} = 0$, we can then identify,

$$c_{12} = s_{\beta-\alpha}\,, \qquad\qquad s_{12} = -\varepsilon\, c_{\beta-\alpha}\,. \tag{2.47}$$

k	h_k	q_{k1}	q_{k2}
1	h	$s_{\beta-\alpha}$	$\varepsilon c_{\beta-\alpha}$
2	$-\varepsilon H$	$-\varepsilon c_{\beta-\alpha}$	$s_{\beta-\alpha}$
3	εA	0	i

Table 2.3: In the CP-conserving limit, the simplified basis-invariant combinations q_{kj} (originally defined in Table 2.1), corresponding to a real Higgs basis where $\varepsilon = \pm 1$ with the choice of sign defined by Eq. (2.42).

The angle $\beta - \alpha$ is defined modulo π. It is conventional to take $0 \leq \beta - \alpha \leq \pi$, in which case $0 \leq s_{\beta-\alpha} \leq 1$. Note that the signs of $c_{\beta-\alpha}$ and ε are not physical as they change when redefining the Higgs basis field $\mathcal{H}_2 \to -\mathcal{H}_2$. However, the product $\varepsilon\, c_{\beta-\alpha}$ is invariant with respect to this sign change and hence is a physical quantity. Moreover, if $s_{\beta-\alpha}c_{\beta-\alpha} \neq 0$ then Eq. (2.52) implies that $Z_6 \neq 0$ and $\varepsilon c_{\beta-\alpha} < 0$ in the convention for $\beta - \alpha$ adopted above. In this case, Eq. (2.42) yields $\varepsilon = \operatorname{sgn} Z_6$, and it follows that,

$$\varepsilon\, c_{\beta-\alpha} = -|c_{\beta-\alpha}|\,. \tag{2.48}$$

In the CP-conserving 2HDM, the q_{kj} given in Table 2.1 simplify to the results given in Table 2.3, where they are written in terms of ε, $\cos(\beta - \alpha)$, and $\sin(\beta - \alpha)$.

Given the values of $\beta - \alpha$ and the masses of h, H, A and $H^{\pm}$, four of the seven real Higgs basis parameters Z_i are determined:

$$Z_1 v^2 \;=\; m_h^2 s_{\beta-\alpha}^2 + m_H^2 c_{\beta-\alpha}^2\,, \tag{2.49}$$

$$Z_4 v^2 \;=\; m_h^2 c_{\beta-\alpha}^2 + m_H^2 s_{\beta-\alpha}^2 + m_A^2 - 2m_{H^\pm}^2\,, \tag{2.50}$$

$$Z_5 v^2 \;=\; m_h^2 c_{\beta-\alpha}^2 + m_H^2 s_{\beta-\alpha}^2 - m_A^2\,, \tag{2.51}$$

$$Z_6 v^2 \;=\; -(m_H^2 - m_h^2) s_{\beta-\alpha} c_{\beta-\alpha}\,, \tag{2.52}$$

and the remaining three parameters $Z_{2,3,7}$ are free. Eq. (2.52) is consistent with the condition $\varepsilon c_{\beta-\alpha} < 0$ in the convention for $\beta - \alpha$ adopted above where $0 \leq s_{\beta-\alpha} \leq 1$.

Chapter 3

Constraints on 2HDMs

In this chapter, we describe the most important constraints that pertain to both of our research projects to follow in Parts 2 and 3. First, the models we construct must obey theoretical principles which enable them to be physically possible. There are indeed 2HDM parameter regimes which are capable of producing a universe which resembles our own, with some caveats. Our models must also contain all of the particles we observe experimentally, and they must not predict particles that would have already been discovered, but have not been.

We must also always check that our models are compatible with previous searches for neutral scalars. In particular, the ATLAS and CMS collaborations at the LHC have performed numerous dedicated searches for new elementary scalar particles, and they frequently present exclusion plots designed to aid theorists in their quest for valid models. Our models must not predict violations the exclusion limits obtained from LHC data, and we also must be able to produce a so-called SM-like Higgs boson with properties approximately like the scalar observed at the LHC with $m_h = 125$ GeV.

The SM makes an astounding number of predictions that are extremely

consistent with experimental data. The 2HDM is a simple extension of the SM which predicts more scalar states that can modify many SM processes. We must scrutinize our models for consistency with bounds placed on a variety of observables that can be affected by new Higgs bosons.

In many cases, one observable has limits that provide more excluding power than other similar observables, so we do not need to consider all the relevant constraints on the 2HDM parameter space. Instead, we are only interested in the most stringent constraints and how they carve out the allowed parameter space. That being said, we also strategically impose some preemptive constraints before performing parameter scans to shorten computation times. In the next few sections, we describe the most severe constraints that are relevant for both projects in this dissertation.

3.1 Stability, Unitarity, and Perturbativity

Stability: The stability conditions ensure that the vacuum of the 2HDM does not develop unphysical vevs. This constraint implies that the scalar potential must be positive at arbitrarily large Higgs field values, or that it is bounded from below. This condition can be realized as a list of inequalities between the quartic scalar potential parameters λ_i in a generic Φ-basis, or equivalently between the Z_i in the Higgs basis. The stability inequalities are derived in Refs. [21,22], and presented here:

$$\lambda_1 > 0 \qquad \lambda_2 > 0 \qquad \lambda_3 + \sqrt{\lambda_1 \lambda_2} > 0 \qquad \lambda_3 + \lambda_4 - |\lambda_5| + \sqrt{\lambda_1 \lambda_2} > 0\,, \tag{3.1}$$

Unitarity: To ensure that high energy scattering processes between Higgs bosons and gauge bosons or fermions respect the principle of probability conservation, we must enforce that the scattering amplitude matrix is unitary. The unitarity

conditions in the 2HDM impose constraints on the Higgs masses and couplings. This requirement translates to conditions on the scalar potential parameters, as given in Ref. [23], which can be imposed by requiring $|Z_i| < 16\pi$.

Perturbativity: Since we utilize perturbation theory to compute scattering processes, we must require that the expansion parameters are small enough for perturbative calculculations to be valid. To ensure that the couplings of the Higgs bosons to gauge bosons and fermions are small enough, we require $|Z_i| < 4\pi$.

3.2 Higgs Signal Strengths

We have a plethora of data collected from the LHC about the SM-like Higgs boson with $m_h = 125$ GeV. The couplings between h and other SM particles are known quite well, however the experimental uncertainties on these measurements are still around 10% in many channels, leaving room for the possibility of new physics that yields small deviations from SM-like Higgs phenomenology. If one is to propose a BSM model, they must require that their model predicts behavior of the h that closely resembles the observed SM-like Higgs boson. The standard measures of this consistency are called Higgs signal strengths, denoted by μ_i^X, where i refers to the h production mechanism and the X the final state particles. The Higgs signal strengths are defined by the ratio of the BSM model's prediction divided by the SM prediction,

$$\mu_i^X = \frac{\sigma(h)_{\text{A2HDM}} \times \text{BR}(h \to XX)_{\text{A2HDM}}}{\sigma(h)_{\text{SM}} \times \text{BR}(h \to XX)_{\text{SM}}} \sim 1\,. \tag{3.2}$$

One must require the Higgs signal strengths to be close to 1 to ensure the h in their model does not have coupling properties significantly different from the observed Higgs boson.

Some Higgs production and decay channels have tight experimental limits placed on the Higgs signal strengths, while others are slightly less definitive. In particular, we enforce that the Higgs signal strengths are within the experimental errors for the $\gamma\gamma$ and ZZ final states, and within two times the experimental errors for W^+W^-, $\tau^+\tau^-$, and $b\bar{b}$. We use the Higgs signal strength limits to place bounds on the magnitudes of the A2HDM coupling modifiers $|f_{\phi,F}|$ [cf. Eqs. (5.11)–(5.13)].

3.3 The Oblique T-parameter

The oblique parameters S, T, and U are observables that quantify the deviation of a model's electroweak radiative corrections from those of the SM. Specifically, the oblique parameters involve the functions $\delta\Pi_{XY}$ (with $X, Y = \gamma, W^{\pm}, Z$) which are the new physics contributions to the radiative corrections of gauge-boson two point correlation functions $\Pi_{XY}(q^2)$, as defined by,

$$\Pi_{XY}(q^2) \,=\, \Pi^{SM}_{XY}(q^2) \,+\, \delta\Pi_{XY}(q^2)\,. \tag{3.3}$$

For 2HDMs, the most stringent constraints come from the T-parameter, which is related to the ρ-parameter of electroweak physics through the relation $\rho - 1 = \alpha T$. In the 2HDM, since new physics appears well above the m_Z scale, there are no new electroweak gauge bosons, and light fermion interactions are suppressed (appearing at two-loop order), then the T-parameter can be approximated by,

$$T \,=\, \left(\frac{1}{\alpha}\right)\left[\frac{\delta\Pi_{WW}(0)}{m_W^2} - \frac{\delta\Pi_{ZZ}(0)}{m_Z^2}\right]. \tag{3.4}$$

In the CP-conserving 2HDM, the T parameter is given by [19]:

$$\alpha T = \frac{3g'^2\cos^2(\beta-\alpha)}{64\pi^2(m_Z^2-m_W^2)}\left\{\mathcal{F}(m_Z^2,m_H^2)-\mathcal{F}(m_W^2,m_H^2)-\mathcal{F}(m_Z^2,m_h^2)+\mathcal{F}(m_W^2,m_{m_h})\right\}$$
$$+\frac{g^2}{64\pi m_W^2}\Bigg\{\mathcal{F}(m_{H^\pm}^2,m_A^2)+\sin^2(\beta-\alpha)\left[\mathcal{F}(m_{H^\pm}^2,m_H^2)-\mathcal{F}(m_A^2,m_H^2)\right]$$
$$+\cos^2(\beta-\alpha)\left[\mathcal{F}(m_{H^\pm}^2,m_h^2)-\mathcal{F}(m_A^2,m_h^2)\right]\Bigg\}, \quad (3.5)$$

where $\alpha \simeq 1/137$ is the fine structure constant and the function $\mathcal{F}$ is defined by,

$$\mathcal{F}(m_1^2,m_2^2) \equiv \tfrac{1}{2}(m_1^2+m_2^2) - \frac{m_1^2m_2^2}{m_1^2-m_2^2}\ln\left(\frac{m_1^2}{m_2^2}\right). \quad (3.6)$$

Notice that,

$$\mathcal{F}(m_1^2,m_2^2) = \mathcal{F}(m_2^2,m_1^2), \qquad \mathcal{F}(m^2,m^2) = 0. \quad (3.7)$$

For a custodial symmetric scalar potential, the term proportional to g^2 in Eq. (3.5) must vanish, so the following equation must be satisfied,

$$\mathcal{F}(m_{H^\pm}^2,m_A^2)+\sin^2(\beta-\alpha)\left[\mathcal{F}(m_{H^\pm}^2,m_H^2)-\mathcal{F}(m_A^2,m_H^2)\right]$$
$$+\cos^2(\beta-\alpha)\left[\mathcal{F}(m_{H^\pm}^2,m_h^2)-\mathcal{F}(m_A^2,m_h^2)\right]=0. \quad (3.8)$$

Assuming we are not in the exact alignment limit, i.e. $\sin(\beta-\alpha)\cos(\beta-\alpha)\neq 0$, then there is only one solution to Eq. (3.8), which is $m_{H^\pm}^2 = m_A^2$. This implies that the T parameter will be small and hence consistent with the current experimental limits if the charged Higgs mass is roughly mass degenerate with the A mass.

There is a second way to achieve consistency with the tight experimental limits on the T parameter. Precision electroweak data tells us that T is close to zero, so we seek solutions that cause the left hand side of Eq. (3.8) to be close to zero. Utilizing precision Higgs data, recall that one the the scalars in our 2HDM, which we assume to be the lightest one, must have properties approximately like the

observed SM-like Higgs boson. This implies that we are near the alignment limit, so $|\cos(\beta-\alpha)|$ is small. Thus, a second way to achieve a very small value for the left hand side of Eq. (3.8) is to demand that,

$$|\mathcal{F}(m_{H^\pm}^2, m_A^2) + \mathcal{F}(m_{H^\pm}^2, m_H^2) - \mathcal{F}(m_A^2, m_H^2)| = \mathcal{O}\big((\cos^2(\beta-\alpha)\big) \ll 1\,. \tag{3.9}$$

Eq. (3.9) is approximately satisfied if either $m_{H^\pm}^2 \simeq m_A^2$ or $m_{H^\pm}^2 \simeq m_H^2$. These results imply that the T-parameter provides limits on differences between the masses of the charged Higgs boson and the H or A. More specifically, to remain consistent with current experimental limits, the T-parameter forces the mass of the charged Higgs boson to be roughly mass degenerate with m_H or m_A.

Electroweak precision data provide tight bounds on S, T, and U, so they must be very small if our extension of the SM is to be phenomenologically viable. The current experimental limits on the oblique parameters are [24]:

$$S = 0.014 \pm 0.10\,, \tag{3.10}$$

$$T = 0.03 \pm 0.11\,, \tag{3.11}$$

$$U = 0.06 \pm 0.10\,. \tag{3.12}$$

In this work, the models are easily consistent with experimental limits on the S and U parameters, and we only need to ensure the T parameter is small enough.

3.4 Constraints from $b \to s + \gamma$

The SM makes valid predictions for numerous flavor observables. If one is to posit an extension of the SM, they must not introduce contributions to flavor observables that are inconsistent with current experimental limits. Any extension of

the SM must avoid tree-level Higgs-mediated FCNCs, which, in this work, is achieved via the flavor alignment conditions in Eq. (5.1) or the Cheng-Sher ansatz for the Yukawa matrices. In the A2HDM, charged Higgs boson exchange can still generate devastating FCNCs at the one-loop level. Therefore, there are many experimental limits on flavor observables that provide constraints on $m_{H^\pm}$ and the flavor alignment parameters. In Ref. [49], a thorough analysis of the constraints on the A2HDM is presented for a variety of processes, including $B \to \tau\nu, D \to \mu\nu, D_s \to \tau\nu$, $D_s \to \mu\nu, K \to \mu\nu, \pi \to \mu\nu, B_s^0 \to \mu^+\mu^-, B_d^0 \to \mu^+\mu^-, \tau \to K\nu, \tau \to \pi\nu, \bar{B} \to X_s\gamma$, K–$\bar{K}$ mixing, B_d^0–$\bar{B}_d^0$ mixing, and B_s^0–$\bar{B}_s^0$ mixing. Some of these flavor observables have also been considered in Ref. [73].

In almost all of the relevant A2HDM parameter space, the most severe constraints come from measurements of the rate of inclusive radiative decay $b \to s\gamma$. The processes in which these decays occur are $\bar{B} \to X_s\gamma$, where X_s is any hadronic state that contains an s quark. The SM prediction and its uncertainty for this process is consistent with the experimental measurements and their uncertainties. However, new physics could still be allowed as long as it only contributes a small amount to $\bar{B} \to X_s\gamma$, such that the proposed BSM model's prediction falls within one or two times the uncertainty on the measurement.

In practice, one must take the observed photon energy E_γ to be larger than some cutoff, denoted by E_0. The prediction for the branching ratio of $b \to s\gamma$ in the Standard Model obtained in Ref. [59] is,

$$\mathrm{BR}(b \to s\gamma)_{E_\gamma > E_0 = 1.6\ \mathrm{GeV}} = (3.40 \pm 0.17) \times 10^{-4}\,, \tag{3.13}$$

whereas the current world average of the experimentally measured branching ratio

compiled by the HFLAV Collaboration [74] is,

$$\mathrm{BR}(b \to s\gamma)_{E_\gamma > E_0 = 1.6\ \mathrm{GeV}} = (3.49 \pm 0.19) \times 10^{-4}\,. \tag{3.14}$$

The SM prediction exhibited in Eq. (3.13) is modified in the 2HDM due to charged Higgs boson exchange,

$$\mathrm{BR}(b \to s\gamma)_{E_\gamma > E_0} = \mathrm{BR}(b \to s\gamma)^{\mathrm{SM}} + \delta\mathrm{BR}(b \to s\gamma)\,. \tag{3.15}$$

In the 2HDM, the dominant contributions to $\delta\mathrm{BR}(b \to s\gamma)$ arise through the effective operators,

$$\mathcal{O}_7 = \frac{e}{16\pi^2} m_b (\bar{s}_L \sigma^{\mu\nu} b_R) F_{\mu\nu}\,, \qquad \mathcal{O}_8 = \frac{g_s}{16\pi^2} m_b (\bar{s}_L \sigma^{\mu\nu} t^a b_R) G^a_{\mu\nu}\,, \tag{3.16}$$

corresponding to one-loop electroweak and QCD penguin diagrams, respectively, at lowest order (LO). Next-to-leading order (NLO) corrections have also been obtained in Refs. [75–79]. A convenient numerical formula based on Refs. [80–82] has been provided in Ref. [49] in terms of the Wilson coefficients evaluated at the scale $\mu_t = 160$ GeV,

$$\begin{aligned}\delta\mathrm{BR}(b \to s\gamma) = 10^{-4} \times \left(\frac{r_V}{0.9626}\right) \mathrm{Re}\Big[&- 8.100\, \mathcal{C}_7^{\mathrm{LO}} - 2.509\, \mathcal{C}_8^{\mathrm{LO}} + 2.767\, \mathcal{C}_7^{\mathrm{LO}} \mathcal{C}_8^{\mathrm{LO}*} \\ &+ 5.348 \left|\mathcal{C}_7^{\mathrm{LO}}\right|^2 + 0.890 \left|\mathcal{C}_8^{\mathrm{LO}}\right|^2 - 0.085\, \mathcal{C}_7^{\mathrm{NLO}} - 0.025\, \mathcal{C}_8^{\mathrm{NLO}} \\ &+ 0.095\, \mathcal{C}_7^{\mathrm{LO}} \mathcal{C}_7^{\mathrm{NLO}*} + 0.008\, \mathcal{C}_8^{\mathrm{LO}} \mathcal{C}_8^{\mathrm{NLO}*} + 0.028 \left(\mathcal{C}_7^{\mathrm{LO}} \mathcal{C}_8^{\mathrm{NLO}*} + \mathcal{C}_7^{\mathrm{NLO}} \mathcal{C}_8^{\mathrm{LO}*}\right) \Big],\end{aligned} \tag{3.17}$$

where $\mathcal{C}_i^{\mathrm{LO}}$ and $\mathcal{C}_i^{\mathrm{NLO}}$ indicate the charged Higgs contributions from $\mathcal{O}_i$ for $i = 7, 8$ at leading and next-to-leading order, respectively, and r_V is the ratio of the product of CKM matrix elements [24],

$$r_V \equiv \left|\frac{V_{ts}^* V_{tb}}{V_{cb}}\right|^2 \simeq 0.964\,. \tag{3.18}$$

In the A2HDM, the forms of $\mathcal{C}_i^{\rm LO}$ and $\mathcal{C}_i^{\rm NLO}$ for $i = 7, 8$ are given by,

$$\mathcal{C}_i^{\rm LO} = \tfrac{1}{3}(a^U)^2\, G_1^i(y_{H^\pm}^t) - a^U a^D\, G_2^i(y_{H^\pm}^t)\,, \tag{3.19}$$

$$\begin{aligned}\mathcal{C}_i^{\rm NLO} &= (a^U)^2\, C_1^i(y_{H^\pm}^t) - a^U a^D\, C_2^i(y_{H^\pm}^t) \\ &\quad + \Big[(a^U)^2 D_1^i(y_{H^\pm}^t) - a^U a^D D_2^i(y_{H^\pm}^t)\Big] \ln\frac{\mu_t^2}{m_{H^\pm}^2}\,,\end{aligned} \tag{3.20}$$

where $y_{H^\pm}^t \equiv m_t^2/m_{H^\pm}^2$ and the explicit expressions for the loop functions G_a^i, C_a^i, and D_a^i are given in Appendix 5.1 of Ref. [49] and reproduced in the appendix of this work for convenience.

The uncertainties in Eqs. (3.13) and (3.14) imply that contributions from new physics $\delta{\rm BR}(b \to s\gamma)$ will fall within the experimental uncertainties if they are smaller than about 2×10^{-5}. To definitively rule out a model at roughly the 95% confidence level, one should consider the 2σ error bars on the SM prediction and the experimental observation. This requirement corresponds to allowing the new physics contributions to fall within the range,

$$|\delta{\rm BR}(b \to s\gamma)| \leq 4 \times 10^{-5}\,. \tag{3.21}$$

Using Eq. (3.21), one can constrain the $\{a^U, a^D, m_{H^\pm}\}$ parameter space of the CP-conserving A2HDM. To check that the results of our ${\rm BR}(b \to s\gamma)$ constraints are consistent with those found in the literature, we can take the Type I and Type II limits of the A2HDM, which are special cases with $a^U = a^D$ and $a^U = -1/a^D$, respectively, and compare with the Type I and II results in the literature. The most recent $b \to s\gamma$ constraints of the Type-I and II 2HDMs can be found in Refs. [51,59]. More general A2HDM constraints can be found in Refs. [49, 83].

The plots in Fig. 3.1 are a more detailed display of the $b \to s\gamma$ constraints on the CP-conserving A2HDM parameter space. These constraints are applied in the work below on A2HDM scenarios of interest, in Sections 8 and 9.

In Part II, when considering specific scenarios of Higgs masses and Yukawa couplings, we will discuss which regions of parameter space are appropriate to scan through. In this more general analysis of the constraints presented by $\delta\mathrm{BR}(b \to s\gamma)$ on the parameter space, we begin by selecting appropriate, and rather generous, ranges of a^U and a^D, and considering which signs of each yield physically unique consequences. If physical observables are invariant under a resigning of a parameter, or combination of parameters, then scanning over only positive values will probe the space without loss of generality. In this case, if one were to take both signs, they would unnecessarily duplicate the parameter space.

In our initial exploration of the A2HDM parameter space, considering only $\delta\mathrm{BR}(b \to s\gamma)$ constraints, we allow $0 < a^U < 2$ and $|a^D| < 100$. Notice that Eqs. (3.19) and (3.21) are invariant under the simultaneous transformation $a^U \to -a^U$ and $a^D \to -a^D$, which means $\delta\mathrm{BR}(b \to s\gamma)$ in Eq. (**??**) is invariant under this transformation. Changing the sign $a^F \to -a^F$ in the charged Higgs Yukawa couplings given in Eq. (5.4) corresponds to changing the sign of ε [cf. Eq. (2.42)] or equivalently changing the sign of the Higgs basis field $\mathcal{H}_2$, which has no physical consequence. However, the sign of the product $a^U a^D$ is physical. For convenience, we shall henceforth take a^U positive without loss of generality.

In Fig. 3.1, we exhibit the allowed regions of the A2HDM parameter space that satisfy the $b \to s\gamma$ constraint given in Eq. (3.21). The six panels of Fig. 3.1 are combined into one plot in Fig. 3.2. It is reassuring to recover the constraints in the literature on the Type I and II 2HDM from the more general A2HDM constraints shown in Fig. 3.2. We can demonstrate the evolution of the $\delta\mathrm{BR}(b \to s\gamma)$ constraints from Type I to Type II inside the A2HDM parameter space by employing

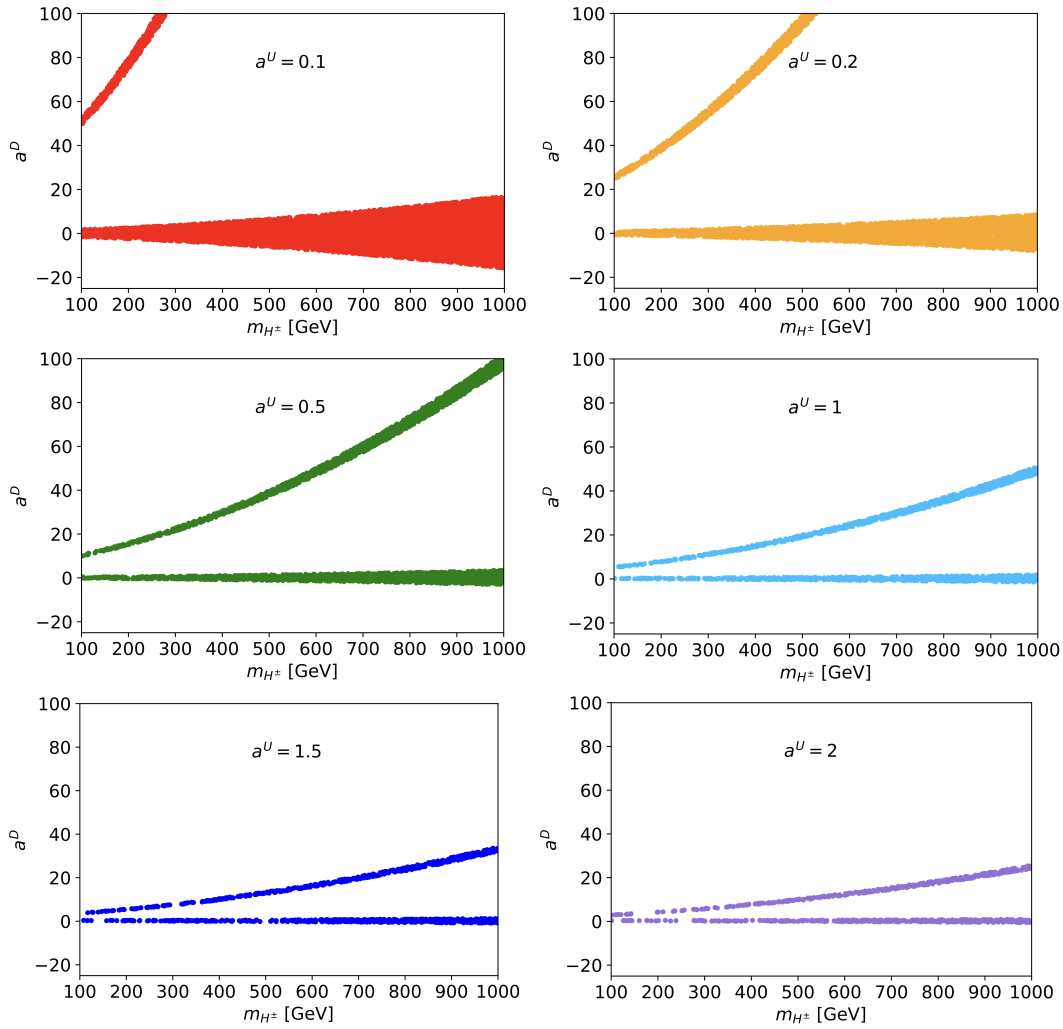

Figure 3.1: Regions of the A2HDM parameter space (indicated by the various colors) that satisfy $|\delta \mathrm{BR}(b \to s\gamma)| \leq 4 \times 10^{-5}$.

the parameterization (in a convention where $a^U > 0$),

$$a^D = (a^U)^p \operatorname{sgn} p\,, \quad -1 \leq p \leq 1\,. \tag{3.22}$$

where $\operatorname{sgn} p = 1$ for $p > 0$ and $\operatorname{sgn} p = -1$ for $p < 0$. This parametrization was created such that $p = 1$ corresponds to Type I Yukawa couplings whereas $p = -1$ corresponds to Type II Yukawa couplings. By varying p, one can determine a^D via Eq. (3.22) [subject to $|a^D| < 100$]. The evolution of the Type-I 2HDM constraints into the Type-II constraints can be seen as p varies from $+1$ to -1 in Fig. 3.3. We show results in the $m_{H^\pm}$ vs. $1/a^U$ plane, since in both the Type-I and Type-II 2HDM

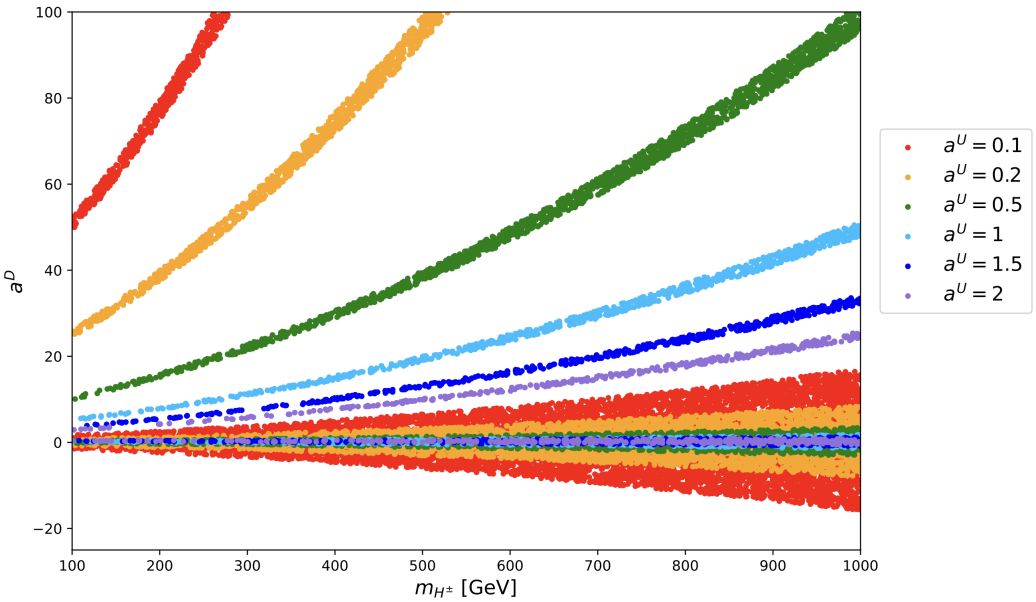

Figure 3.2: The six panels of Fig. 3.1 are combined into one plot shown above.

we can identify $\tan\beta = 1/a^U$. (In light of Eqs. (5.7) and (5.8), in a convention where $0 \leq \beta \leq \pi/2$, one must fix $\varepsilon = 1$ for positive values of a^U.) Indeed, we see that the $a^D = a^U$ panel of Fig. 3.3 is consistent with the excluded parameter regime of the Type-I 2HDM, whereas the $a^D = -1/a^U$ panel of Fig. 3.3 is consistent with the excluded parameter regime of the Type-II 2HDM (cf. Ref. [51]). For values of $|p| \neq 1$, $1/a^U$ does not have the interpretation of $\tan\beta$ (as this parameter is no longer physical). Nevertheless, the sequence of panels exhibited in Fig. 3.3 provides some understanding on how the evolution between Type-I and Type-II occurs. Strictly speaking, the evolution is not continuous, since at $p = 0$, the sign of p is undefined and one switches between positive and negative p as one passes through zero. Indeed, only half of the A2HDM parameter space is accessed in this way, since we do not consider parameter points where the sign of a^D is $-\operatorname{sgn} p$ (in the convention of positive a^U).

In some earlier works, only the leading order (LO) corrections to $b \to s\gamma$ were included. Although the LO results provide a fairly good representation of

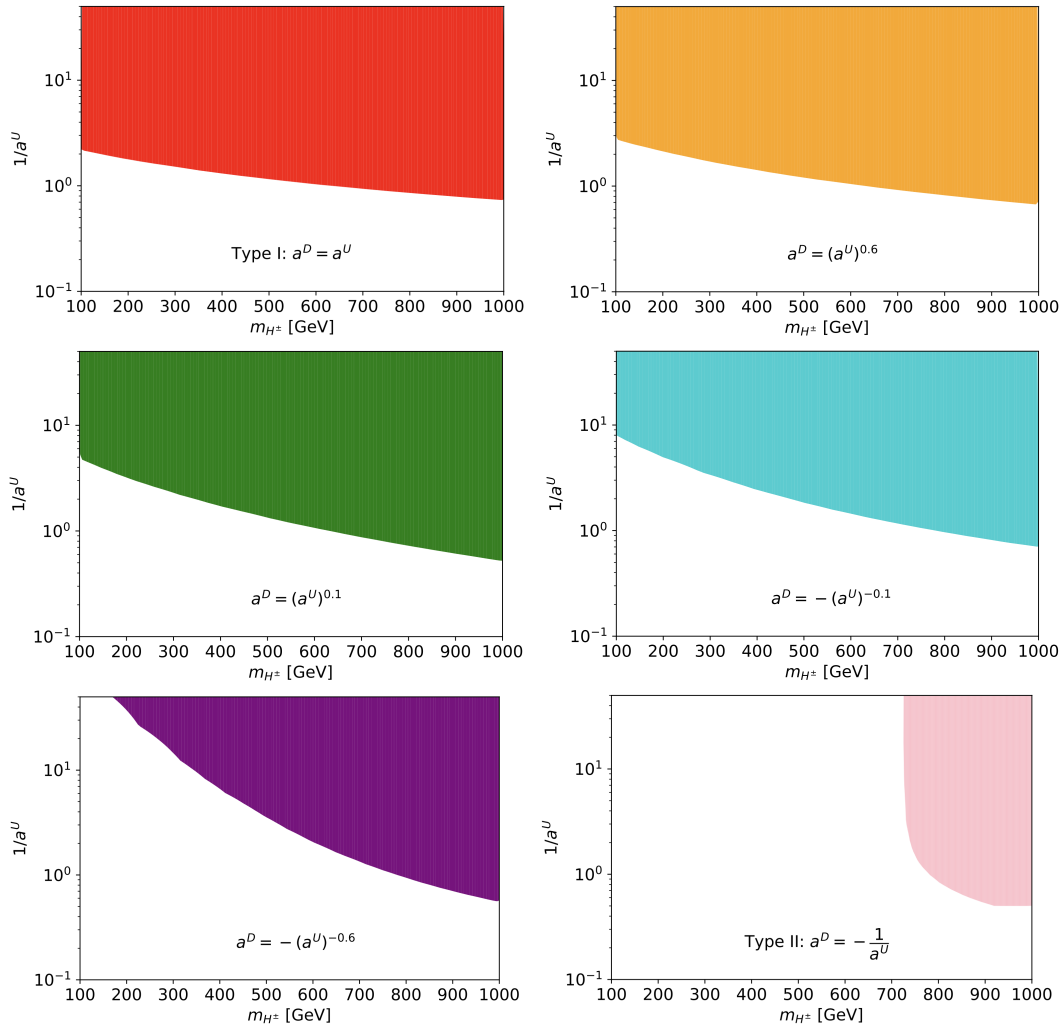

Figure 3.3: Regions of the A2HDM parameter space (indicated by the various colors) in the $m_{H^\pm}$ vs. $1/a^U$ plane that satisfy $|\delta\mathrm{BR}(b \to s\gamma)| \leq 4 \times 10^{-5}$. The uncolored regions are excluded. The value of a^D is fixed by $a^D = (a^U)^p \mathrm{sgn}\, p$. As p varies, we include all parameter points in which $|a^D| < 100$. The sequence of panels correspond to $p = 1, 0.6, 0.1, -0.1, -0.6$, and -1. The case of $p = 1$ ($p = -1$) corresponds to the Type I (Type II) 2HDM; in these two cases, one may identify $\tan\beta = 1/a^U$.

the excluded regions in much of the parameter regime, there are some noticeable differences with the more accurate NLO result. In Fig. 3.5, we exhibit the regions of the a^U vs. a^D parameter space in which $|\delta\mathrm{BR}(b \to s\gamma)| \leq 4 \times 10^{-5}$ based on the LO computation (where $C_i^{\mathrm{NLO}} = 0$ in Eq. (3.18)) and the NLO computation, respectively. A blue point is plotted as long as the branching ratio inequality is satisfied for at least one value of the charged Higgs mass (which is allowed to vary

between 100 and 1000 GeV).

The NLO terms in $\delta\overline{\mathcal{B}}(b \to s\gamma)$ contain dilogarithm functions, so one may ask if the LO terms are a good approximation. In the plots below, we show that one must go beyond LO and compute NLO contributions if they wish to use $\delta\overline{\mathcal{B}}(b \to s\gamma)$ to constrain the A2HDM parameter space. There are situations in which the LO result is greater than the NLO result, and less than the NLO result, and the two terms can be comparable in size. Therefore, placing constraints on a LO calculation would both allow models that are forbidden at NLO and eliminate models that are allowed at NLO.

3.5 ΔM_{B_s} Constraints

While $b \to s\gamma$ considerations provide the most sensitive constraints in most regions of the A2HDM parameter space, there are regions in which B_s–$\overline{B}_s$ oscillations add an additional constraint beyond what is excluded by $b \to s\gamma$. The prediction for B_s–$\overline{B}_s$ oscillation is given by ΔM_{B_s}, which includes SM and new physics terms,

$$\Delta M_{B_s} \equiv 2\left|\left\langle B_s^0\right| H^{\Delta B=2} \overline{B}_s^0\right\rangle| = \left(\Delta M_{B_s}\right)^{\mathrm{SM}} + \delta\Delta M_{B_s}\,. \tag{3.23}$$

The new physics term $\delta\Delta M_{B_s}$ is due to contributions from charged Higgs bosons and arises through the effective operators:

$$\mathcal{O}_{VLL} = \bar{s}^{\alpha}\gamma_{\mu}\left(1-\gamma_5\right) b^{\alpha}\bar{s}^{\beta}\gamma^{\mu}\left(1-\gamma_5\right) b^{\beta}\,, \tag{3.24}$$

$$\mathcal{O}_{SRR} = \bar{s}^{\alpha}\left(1+\gamma_5\right) b^{\alpha}\bar{s}^{\beta}\left(1+\gamma_5\right) b^{\beta}\,, \tag{3.25}$$

$$\mathcal{O}_{TRR} = \bar{s}^{\alpha}\sigma_{\mu\nu}\left(1+\gamma_5\right) b^{\alpha}\bar{s}^{\beta}\sigma^{\mu\nu}\left(1+\gamma_5\right) b^{\beta}\,, \tag{3.26}$$

as shown in the results of Ref. [50]. Ref. [49] shows how $\delta\Delta M_{B_s}$ can be calculated as,

$$\delta\Delta M_{B_s} = \frac{G_F^2\, m_W^2\, m_{B_s}}{24\pi^2}\, |V_{tq}V_{tb}^*|^2\, f_{B_s}^2 \left[\hat{B}_{B_s}\eta_B \mathcal{C}_V + \hat{B}_{B_s}^{ST}\eta_{B_s}^{ST}\mathcal{C}_{ST}\right], \qquad (3.27)$$

where the $\hat{B}_{B_s}$ $[\hat{B}_{B_s}^{ST}]$ parameterize the nonperturbative effects in the hadronic matrix element of $\mathcal{O}_{VLL}$ [$\mathcal{O}_{SRR}$ and $\mathcal{O}_{TRR}$], η_B $[\eta_{B_s}^{ST}]$ account for NLO QCD corrections [84], and the corresponding Wilson coefficients are given by,

$$\begin{aligned} \mathcal{C}_V &= x_t \left[2x_t A_{WH}\left(x_t, x_b\right) + x_t A_{HH}\left(x_t, x_b\right)\right], \\ \mathcal{C}_{ST} &= 4x_b x_t^2 \left[A_{WH}^{ST}\left(x_t\right) + A_{HH}^{ST}\left(x_t\right)\right], \end{aligned} \qquad (3.28)$$

with $x_q \equiv [m_q(m_q)]^2/m_W^2$ equal to the square of the $\overline{\rm MS}$ quark mass normalized to the W boson mass. The explicit expressions for A_{WH}, A_{HH}, A_{WH}^{ST} and A_{HH}^{ST} can be found in Appendix B.2 of Ref. [49]. The Standard Model contribution to $\mathcal{C}_V$ has been omitted from Eq. (3.28). We have evaluated these functions using the Standard Model parameters taken from UT*fit* Collaboration global fit of flavor parameters [50] and the parameters associated with the charged Higgs contributions given in Ref. [49]. Values for G_F and m_W are taken from Ref. [24] and we employ the value of $\eta_B = 0.5510 \pm 0.0022$ quoted in Ref. [84].

In Ref. [50], the observed value of $\Delta M_{B_s} = 17.241(20)$ ps^{-1} obtained from B_s–$\overline{B}_s$ oscillation data is compared with the Standard Model prediction, which is 17.94(69) ps^{-1} based on a global fit of flavor observables. Since the error in the Standard Model prediction is still considerably larger than the precision of the measured value, we chose to identify the 2σ error in the theoretical prediction as the upper limit to the contribution to $|\Delta M_{B_s}|$ of new physics beyond the Standard Model.

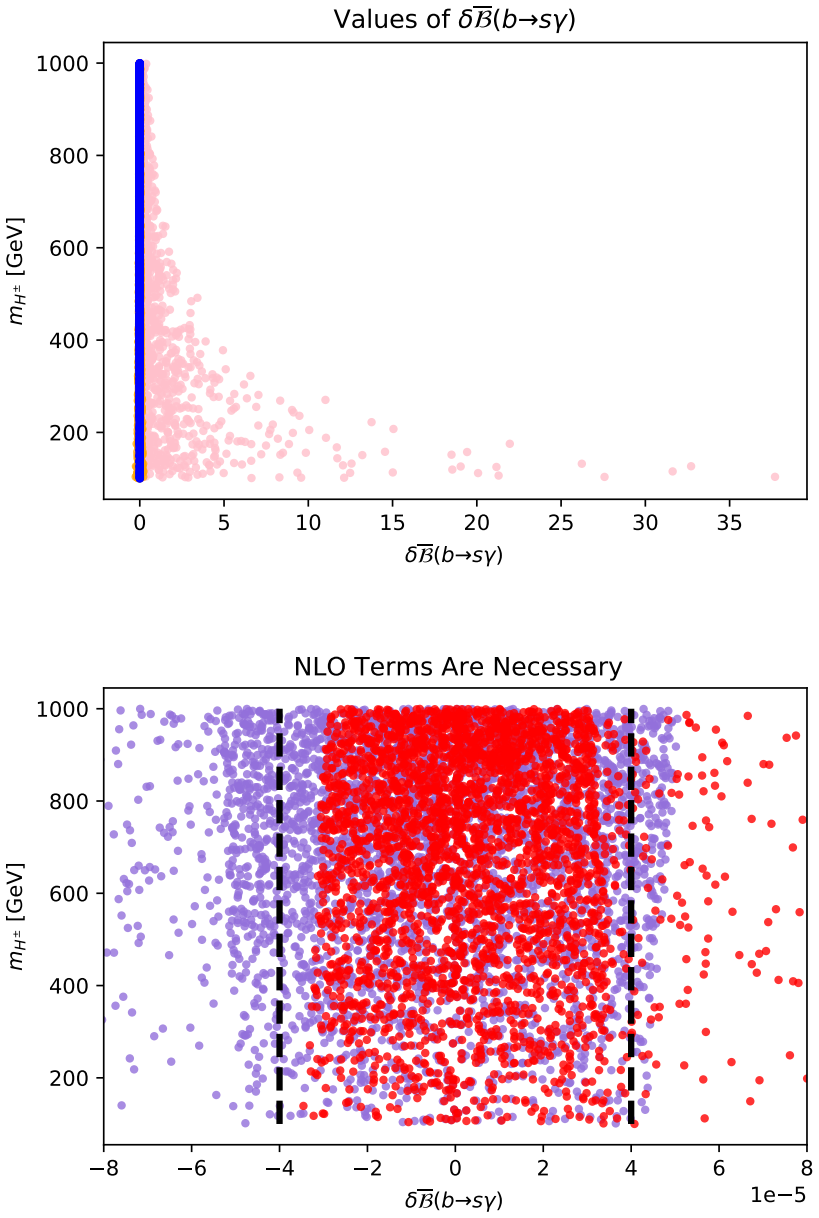

Figure 3.4: In the A2HDM, $\delta\overline{\mathcal{B}}(b \to s\gamma)$ can be much larger than the 2σ uncertainties on the experimental results, invalidating those parameter points. This is especially so at low values of $m_{H^\pm}$. One must compute $\delta\overline{\mathcal{B}}(b \to s\gamma)$ to NLO since the NLO contributions can be as large as the LO with opposite sign, which can either eliminate or enable points judged by the LO results only.

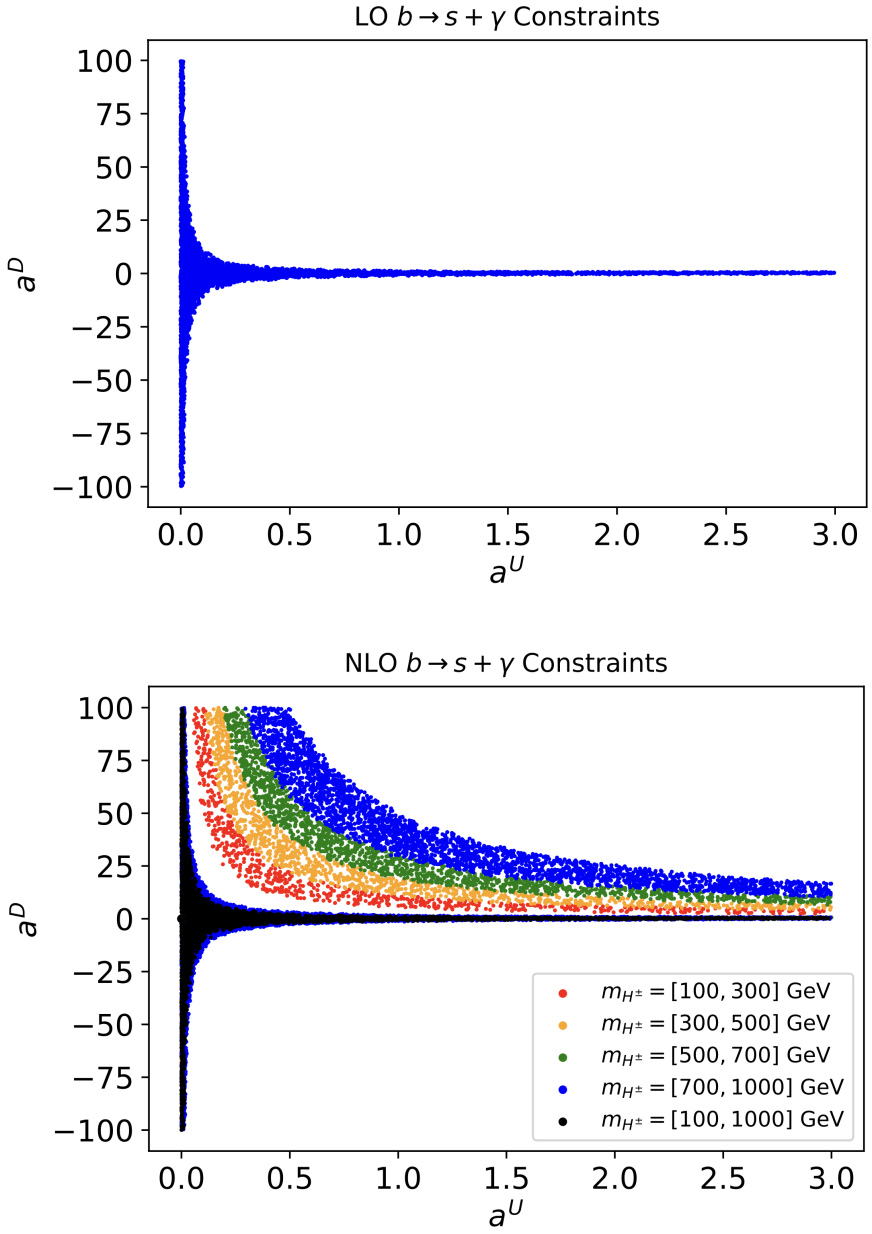

Figure 3.5: LO vs. NLO constraints due to $b \to s\gamma$ in the a^U vs. a^D plane, with charged Higgs masses separated by color. Due to cancelations between LO and NLO terms, a second region of parameter space becomes available when one computes $\delta\overline{\mathcal{B}}(b \to s\gamma)$ at NLO. All points shown above satisfy $|\delta\mathrm{BR}(b \to s\gamma)| \leq 4 \times 10^{-5}$.

Part II

Flavor-aligned 2HDM:

Scenarios and Benchmarks

Chapter 4

Introduction

In particle physics, one wishes to know the complete, or at least effective, spectrum of physical particle states in Nature, their masses, and how they interact. In this part, we describe a body of work that investigates whether the nature of Higgs-fermion interactions are the consequence of a symmetry or not. We employ generic flavor-aligned Yukawa couplings and compare the predictions with experimental data to investigate the possible patterns of Yukawa couplings. We then test if the allowed Yukawa couplings are akin to those of the commonly studied $\mathbb{Z}_2$-symmetric models. The $\mathbb{Z}_2$-symmetric models are a subset of the flavor-aligned 2HDM (A2HDM), which have more general Yukawa coupling matrices. If only A2HDMs with Yukawa couplings like $\mathbb{Z}_2$-symmetric models are found to be consistent with experimental data, then we would conclude that the Yukawa coupling pattern must be due to a $\mathbb{Z}_2$ symmetry. However, we find that $\mathbb{Z}_2$-symmetric models are too restrictive, and more general Yukawa couplings can be consistent with experimental results. We therefore conclude that the Higgs-fermion Yukawa coupling patterns do not need to arise from a $\mathbb{Z}_2$ symmetry. The commonly studied $\mathbb{Z}_2$-symmetric 2HDMs have Yukawa couplings that are drastically, and unnecessarily,

restricted compared to the full parameter space available in the A2HDM.

In the case of 2HDM states, the hypothesized new neutral scalars are particles with quite large masses and are therefore difficult to produce in colliders, yielding insufficient data to draw absolute conclusions at present. In coming years, more particle collider data and improved experiments and analyses will shed more light on the search for new neutral scalars. In the meantime, it implores us to use what hints and limits we have to determine the likelihood of discovering new Higgs bosons, and how they might interact with fermions.

We also use these investigations to aid experimentalists in their searches for new neutral scalars. After our analyses of the available A2HDM parameter space for the two scenarios presented, we provide benchmark points which elucidate the most important branching ratios of the Higgs bosons. Equipped with these benchmark points, experimentalists can look for exemplifying decay signatures as more data is collected.

In Chapter 5 we establish the flavor-aligned 2HDM, which is the model employed in this part of this work, and describe the remaining important constraints on the parameter space that were not already discussed in Part 1. In Chapter 6 we survey the search for non-SM-like Higgs bosons at the LHC and discuss a few intriguing Higgs excesses that have been reported by the ATLAS and CMS Collaborations [27–30]. We interpret these excesses as hints of new BSM scalars described as A2HDM states. We propose to analyze two different A2HDM scenarios that could yield excesses of events that would be compatible with the reported LHC data. In Scenario 1, we take $m_A = 610$ GeV and $m_H = 290$ GeV, motivated by an ATLAS excess of events with a local (global) significance of $3.1(1.3)\sigma$ [27], which is compatible with the interpretation of $gg \to A \to ZH$, where $H \to b\bar{b}$ and $Z \to \ell^+\ell^-$

(where $\ell = e,\ \mu$). Scenario 2 is based on an ATLAS excess of $\tau^+\tau^-$ events with an invariant mass of around 400 GeV, with local significances of 2.2σ in the gg fusion production channel and 2.7σ in the b-associated production channel [28–30]. The CMS Collaboration sees no excess in the $\tau^+\tau^-$ channel [31], but still leaves some room for a possible signal. However, the CMS Collaboration observes an excess of $t\bar{t}$ events with an invariant mass of around 400 GeV, with a local (global) significance of $3.5(1.9)\sigma$, that favors identifying the excess with A production [30]. In Chapter 7 we explain how we scanned through the A2HDM parameter space to find regions which can predict Higgs signals large enough to explain the Higgs excesses in LHC data while upholding consistency with experimental and theoretical constraints. In Chapters 8 and 9 we present two scenarios in which we can simultaneously explain two Higgs excesses within the A2HDM, and perform parameter scans to interpret the allowed Yukawa coupling patterns in each. We demonstrate that the common Types-I, II, X, and Y models cannot accommodate the excesses in our scenarios, but the flavor-aligned model can. In these chapters we also provide telltale benchmark points to establish decay signatures experimentalists can look for in the case that any of the small excesses that have been previously reported by the ATLAS and CMS collaborations should turn out to be something more than a statistical fluctuation.

Chapter 5

Theoretical Background

5.1 The Flavor-aligned 2HDM

The most general 2HDM is not phenomenologically viable, as it generates FCNCs via off diagonal terms in the Yukawa coupling matrices. To suppress potentially dangerous tree-level Higgs-mediated FCNCs, one must establish a mechanism by which the off-diagonal elements of the Yukawa coupling matrices are sufficiently small. There are numerous ways to suppress FCNCs, the most common of which involve imposing a symmetry on the Lagrangian which eliminates off diagonal terms in the Yukawa Lagrangian. Because this approach has a symmetry which protects the zeros in the off-diagonal Yukawa coupling matrix elements, these models are stable under renormalization group evolution. We, however, suppress off-diagonal Yukawa couplings by positing that the Yukawa coupling matrices are flavor diagonal, with off-diagonal elements equal to zero, so FCNCs are brought under control.

In the $\mathbb{Z}_2$ symmetry rationale of flavor-diagonality, the κ^F and ρ^F matrices are not independent and overly restricted. Instead, we take a slightly more general approach and posit that the $\rho^{U,D}$ matrices are proportional to the $\kappa^{U,D}$ matrices,

which are already diagonal since they are proportional to the diagonalized fermion mass matrices $\kappa^F = \sqrt{2}M_F/v$. We define proportionality constants, called *alignment parameters* a^F,

$$\rho^F = a^F \kappa^F \,, \qquad \text{for} \qquad F = U, D, E \,, \tag{5.1}$$

where the potentially complex numbers a^F (which we will take to be real) are invariant under the rephasing of the Higgs basis field $\mathcal{H}_2 \to e^{i\chi}\mathcal{H}_2$. Establishing this relationship between the Yukawa coupling matrices and mass matrices defines the flavor-aligned 2HDM (A2HDM), which is the model employed in Part II of this work. The convenient redefinition of the Yukawa coupling matrices given in Eq. (2.35) yields,

$$\rho_R^F = (\mathrm{Re}\, a^F)\mathbb{1} \,, \qquad \rho_I^F = (\mathrm{Im}\, a^F)\mathbb{1} \,, \tag{5.2}$$

and inserting these results into Eq. (2.36), the Yukawa Lagrangian takes the form,

$$\begin{aligned} -\mathscr{L}_Y \,=\, & \frac{1}{v}\,\overline{U} M_U \sum_{k=1}^{3}\Big\{ q_{k1} + \, q_{k2}^* a^U P_R + q_{k2} a^{U*} P_L \Big\} U h_k \\ & + \frac{1}{v} \sum_{F=D,E} \Big\{ \overline{F} M_F \sum_{k=1}^{3} \big(q_{k1} + \, q_{k2} a^{F*} P_R + q_{k2}^* a^F P_L \big) F h_k \Big\} \\ & + \frac{\sqrt{2}}{v} \Big\{ \overline{U} \big[a^{D*} K M_D P_R - a^{U*} M_U K P_L \big] D H^+ + a^{E*} \overline{N} M_E P_R E H^+ \\ & + \text{h.c.} \Big\} \,. \end{aligned} \tag{5.3}$$

The Yukawa couplings displayed in Eq. (5.3) have no tree-level Higgs-mediated FCNCs, they are much simpler than the general couplings in Eq. (2.36), and they will simplify further if one considers CP-conserving models.

In the CP-conserving case the Yukawa couplings given in Eq. (5.3) then

take the following form,

$$
\begin{aligned}
-\mathscr{L}_Y \,=\, & \frac{1}{v}\sum_{F=U,D,E}\overline{F}M_F\big[s_{\beta-\alpha}-a^F|c_{\beta-\alpha}|\big]Fh \\
& -\frac{1}{v}\sum_{F=U,D,E}\varepsilon\,\overline{F}M_F\big[|c_{\beta-\alpha}|+a^F s_{\beta-\alpha}\big]FH \\
& -\frac{i}{v}\sum_{F=U,D,E}\varepsilon_F\,\varepsilon\,a^F\,\overline{F}M_F\gamma_5 FA \\
& +\frac{\sqrt{2}}{v}\,\varepsilon\Big\{\overline{U}\big[a^D KM_D P_R-a^U M_U K P_L\big]DH^+ + a^E\overline{N}M_E P_R E H^+ \\
& +\ \text{h.c.}\Big\}\,,
\end{aligned}
\tag{5.4}
$$

where ε is defined in Eq. (2.42) and we have introduced the notation,

$$
\varepsilon_F = \begin{cases} +1 & \text{for } F=U\,, \\ -1 & \text{for } F=D,E\,. \end{cases}
\tag{5.5}
$$

Of course, the explicit factors of ε are not physical as previously noted. Indeed, ε can always be absorbed into the definitions of the H, A and $H^\pm$ fields. In this paper, we shall interpret LHC searches for new scalar states in terms of the CP-conserving A2HDM. Thus, we shall employ the Yukawa couplings of Eq. (5.4) in which the real parameters a^U and a^D can take either sign and only the absolute value of $c_{\beta-\alpha}$ is physical, in light of Eq. (2.48).

5.2 $\mathbb{Z}_2$-symmetric A2HDMs

The commonly studied Types I, II, X and Y 2HDMs are indeed special cases of the A2HDM, where we can identify the corresponding complex alignment parameters as follows,

1. Type-I: $a^U = a^D = a^E = e^{i(\xi+\eta)}\cot\beta$.

2. Type-II: $a^U = e^{i(\xi+\eta)}\cot\beta$ and $a^D = a^E = -e^{i(\xi+\eta)}\tan\beta$.

3. Type-Y: $a^U = a^E = e^{i(\xi+\eta)} \cot\beta$ and $a^D = -e^{i(\xi+\eta)} \tan\beta$.

4. Type-X $a^U = a^D = e^{i(\xi+\eta)} \cot\beta$ and $a^E = -e^{i(\xi+\eta)} \tan\beta$.

If the absence of neutral Higgs-mediated FCNCs is enforced naturally via a symmetry (which may be softly broken by dimension-2 squared-mass terms), then one should impose a $\mathbb{Z}_2$ symmetry on the dimension-4 terms of the Higgs Lagrangian in the Φ-basis as specified in Table 2.2, which implies that $\lambda_6 = \lambda_7 = 0$. It is convenient to define the quantity,

$$T_{Z_2} \equiv \big|(Z_1{-}Z_2)[Z_1Z_7{+}Z_2Z_6{-}(Z_3{+}Z_4{+}Z_5)(Z_6{+}Z_7)]{+}2(Z_6{+}Z_7)^2(Z_6{-}Z_7)\big| \,. \quad (5.6)$$

Applying Eq. (2.39) to the real Higgs basis of a CP-conserving 2HDM, it follows that the real Higgs basis parameters satisfy $T_{Z_2} = 0$ if and only if a $\mathbb{Z}_2$ symmetry is present in some scalar field basis.

Moreover, it is conventional to rephase the Φ-basis scalar fields such that $\xi = 0$ (i.e., the vevs are real and nonnegative), in which case one can identify $e^{i(\xi+\eta)} = \varepsilon$ and $\tan\beta \equiv \langle\Phi_2^0\rangle/\langle\Phi_1^0\rangle$ [cf. Eq. (2.4)]. In particular, the CP-conserving Type-I, II, X and Y 2HDMs are special cases of the A2HDM, where we can identify the corresponding real flavor-alignment parameters as follows,

$$\text{Type-I:} \quad a^U = a^D = a^E = \varepsilon \cot\beta. \quad (5.7)$$

$$\text{Type-II:} \quad a^U = \varepsilon \cot\beta \text{ and } a^D = a^E = -\varepsilon \tan\beta. \quad (5.8)$$

$$\text{Type-Y:} \quad a^U = a^E = \varepsilon \cot\beta \text{ and } a^D = -\varepsilon \tan\beta. \quad (5.9)$$

$$\text{Type-X:} \quad a^U = a^D = \varepsilon \cot\beta \text{ and } a^E = -\varepsilon \tan\beta. \quad (5.10)$$

Inserting the CP-conserving Type I or Type II values of the flavor-alignment parameters in Eq. (5.4) and writing the Yukawa couplings of h and H in terms of $c_{\beta-\alpha}$ rather than its absolute value [using Eq. (2.48)], we see that the factors of ε now

cancel exactly, as they must since there is no remaining two-fold ambiguity in defining the real Higgs basis once the ratio of vevs has been chosen to be non-negative. In particular, in the conventions of the Type-I, II, X and Y 2HDMs adopted above (where $\xi = 0$), the sign of $c_{\beta-\alpha}$ is now a physical parameter. Moreover, the sign ε is now fixed as determined by Eq. (2.48). We shall adopt this approach in the Type-I 2HDM benchmark presented in Section 8.2.

In contrast, a less common approach for examining the Type-I, II, X and Y limits of the CP-conserving A2HDM is to allow for both values of $e^{i\xi} = \pm 1$. In this case, one can extend the definition of β such that $-\frac{1}{2}\pi \leq \beta \leq \frac{1}{2}\pi$, in which case the parameter $\tan\beta$ can be of either sign. Eqs. (5.7)–(5.10) remain valid, but now we see that neither $\tan\beta$ nor $c_{\beta-\alpha}$ is physical (since both change sign when redefining the Higgs basis field $\mathcal{H}_2 \to -\mathcal{H}_2$), although the product $c_{\beta-\alpha}\tan\beta$ is physical. In this case, one could adopt a convention where $c_{\beta-\alpha}$ is always negative while allowing for both signs of $\tan\beta$, which is equivalent to employing Eq. (5.4) with $\varepsilon = +1$ [in light of Eq. (2.48)].

5.3 Coupling Modifiers in the CP-conserving A2HDM

Formally, the CP-conserving 2HDM is defined such that the only source of CP violation enters via the nontrivial phase of the CKM matrix K that appears in the respective interactions of the $W^\pm$ and the $H^\pm$ with fermion pairs. In particular, in the CP-conserving 2HDM, the flavor-alignment parameters are real.

In the CP-conserving A2HDM, the couplings of the h, H, and A to fermions are very similar to those of the SM, but augmented by simple functions of the alignment parameters a^F, $\cos(\beta-\alpha)$, and $\sin(\beta-\alpha)$. We call these functions, which

are obtained from Eq. (5.4), the A2HDM *coupling modifiers*, and denote them by $f_{\phi,F}$ (for $F = U, D, E$),

$$f_{h,F} = s_{\beta-\alpha} - |c_{\beta-\alpha}| a^F, \tag{5.11}$$

$$f_{H,F} = -|c_{\beta-\alpha}| + s_{\beta-\alpha} a^F, \tag{5.12}$$

$$f_{A,F} = -\epsilon_F \, a^F, \tag{5.13}$$

after absorbing the factors of ε into the definitions of the corresponding scalar fields. Cross sections and branching ratios can be computed in the A2HDM by taking an otherwise SM-like calculation, replacing $m_h = 125$ GeV with the mass of the scalar under study, and using the coupling modifiers appropriately. In the case of the pseudoscalar A, one must also insert a factor of $i\gamma_5$ into the SM-like calculation.

We utilize the public code `SusHi` [53] to compute gluon-gluon fusion and b-associated Higgs boson production cross sections. We use the `SusHi` SM setting with $m_\phi = m_h, m_H,$ or m_A (and the pseudoscalar setting for the A). For the gluon-gluon fusion production mode, we neglect the first and second generations of quarks due to their insignificant couplings to the Higgs bosons. We then toggle the top and bottom quark couplings on and off to obtain the the total cross section $\sigma(gg\phi)_{\rm tot}$, the contribution from top loops only $\sigma(gg\phi)_t$, and the contribution from bottom loops only $\sigma(gg\phi)_b$. Equipped with these factors, we extract the interference term by subtracting the top loop and bottom loop contributions from the total cross section $\sigma_{\rm tot}$,

$$\sigma(gg\phi)_{\rm int} = \sigma(gg\phi)_{\rm tot} - \sigma(gg\phi)_t - \sigma(gg\phi)_b, \tag{5.14}$$

The gluon-gluon fusion production cross sections for Higgs bosons in the CP-conserving A2HDM are then obtained by inserting the appropriate coupling modifiers to the

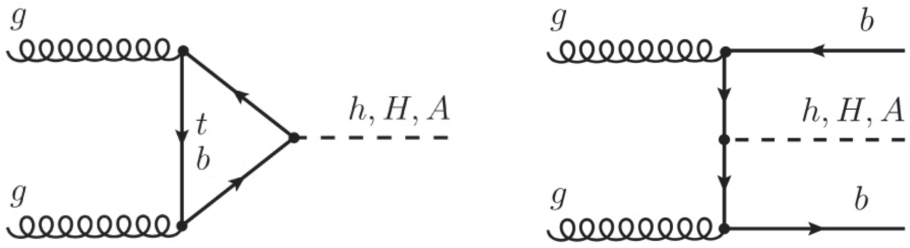

Figure 5.1: Feynman diagrams of the (a) gluon-gluon fusion and (b) b-associated Higgs boson production mechanisms. Cross sections in the A2HDM are calculated by modifying the SM calculation by inserting the appropriate coupling modifier at the vertex on the right, and replacing the mass of the SM Higgs boson with m_ϕ.

top, bottom, and interference terms,

$$\sigma(gg\phi)_{\text{A2HDM}} = \sigma(gg\phi)_t(f_{\phi,U})^2 + \sigma(gg\phi)_b(f_{\phi,D})^2 + \sigma(gg\phi)_{\text{int}}(f_{\phi,U})(f_{\phi,D}). \quad (5.15)$$

as can be deduced by inspecting the Feynman diagram shown in panel (a) of Fig. 5.1. In that diagram, the vertex on the right adopts a coupling modifier $f_{\phi,F}$ in the A2HDM relative to the SM vertex factor. The b-associated production cross sections are also computed using the SM mode of `SusHi` and adjusted to the A2HDM by inserting the coupling modifier,

$$\sigma(gg \to bb\phi)_{\text{A2HDM}} = \sigma(gg \to bb\phi)(f_{\phi,D})^2. \quad (5.16)$$

as can be deduced from panel (b) of Fig. 5.1. `SusHi` implements the five-flavor scheme for the b-associated production mechanism. In this scheme, the top quark is treated as being sufficiently heavy to decouple from the b-associated cross section calculation. This assertion is justified by the fact that top quark contributions only enter the calculation at loop-order, which are suppressed compared to the five lighter quarks. The bottom quark and its associated parton distribution functions are included in the five-flavor scheme.

We then compute partial and total decay widths, and hence branching ratios, using our modified version of the public code `2HDMC` [54], which was designed

to perform calculations in the CP-conserving 2HDM. We extended `2HDMC` to also handle A2HDM Yukawa coupling matrices. Finally, we can multiply our production cross section results by our branching ratio results to obtain predictions for the number of events expected for a given process, for any point in the A2HDM parameter space. Using this computational framework, we can also compute many of the relevant constraints and compare the results with experimental limits to test the validity of all points in the A2HDM parameter space that we probe.

Chapter 6

Hints of Heavy Scalars at the LHC

Particle collider experiments provide a methodology for measuring what physical particles exist and their properties, such as their masses and interactions with one another. To discover a new particle, there must be overwhelming evidence, beyond any reasonable doubt, that a state at a particular invariant mass caused an excess of events over background in a detector. These excesses are called resonances, or peaks, due to their appearance in plots with the invariant mass of the collision on the x-axis and production cross section times a decay branching ratio on the y-axis. A particle discovery can only be claimed when the statistical significance of a peak is 5 standard deviations or more (corresponding to a p-value of less than 0.00006). The excesses we consider in this chapter are far less significant than discoveries, yet they are large enough to require our attention and scrutiny. In the literature, the word anomalies is sometimes used to refer to excesses, but this terminology implies a more convincing signal of higher significance than we investigate, so we avoid this term altogether.

Given that the LHC is searching broadly for new scalars, it is not improbable that a few excesses of a few sigma will appear from upward statistical

fluctuations. These excesses could be interpreted as local hints of signals above expected SM backgrounds, but due to the look elsewhere effect, the global significance is far less. For example, a local excess with a significance of 3σ typically corresponds to a global significance between 1σ and 2σ.

The ATLAS and CMS Collaborations have performed dedicated searches for new elementary scalar bosons, which if discovered would need a theoretical framework to explain their existence. Any experimental indication of new neutral or charged (or both) scalars would motivate models with an extended Higgs sector. The simplest way to extend the Higgs sector and obtain new scalar phenomena is to add a second hypercharge one electroweak Higgs doublet, as in the 2HDM. In this chapter, we present the most suggestive excesses in LHC data that could potentially be hints of BSM neutral scalars, and we interpret them as though they are hints of signals arising from A2HDM states.

While we cannot definitively determine whether a small excess is due to a statistical fluctuation or hints of a new state, we prudently argue that a new scalar would initially appear as a small excess in ATLAS and CMS searches. If the excess is in fact due to a new state, the significance excess will grow as more data is accumulated. If we study one excess at a time, it is likely that it proves to be a statistical fluctuation. However, if we can explain two excess at once within a model framework, then it is more plausible that both excesses arise from new states in that model. We devise two scenarios in which more than one excess can be simultaneously described by the same A2HDM parameter point, making it more plausible that they arise from BSM scalars rather than two independent statistical fluctuations.

If one peruses the literature in search for hints of new scalars, they will find an underwhelming number of reports with significant deviations from the SM.

However, there are a few reports of excesses significant enough that they should be thoroughly investigated before throwing in the towel. These reports display their measurements in the form of exclusion limit plots, which one can use to eliminate any model that predicts a cross section times branching ratio larger than the observed limit at a given invariant mass.

Our procedure for finding hints of new scalars in LHC data goes as follows. First, we find papers that show an excess in an exclusion plot for a certain production and decay channel at a specific invariant mass. The excess is a place where the observed exclusion limit greatly exceeds the expected exclusion limit. This means that the experiment thought it would be sensitive enough to rule out cross sections times branching ratios of a particular value, but an excess in data caused the actual limit to be somewhat higher. In cases in which the expected and observed limits differ significantly, we interpret the deviations as being sourced by new scalar states in the CP-conserving A2HDM. We do not claim to have discovered these particles; instead, we find this approach instructive about 2HDMs and the possible nature of Yukawa couplings.

If one tries to explain the pairs of excesses we studied within the standard $\mathbb{Z}_2$-symmetric 2HDM types, the parameter space is too restrictive to accommodate them in most cases. This is one motivation for extending our Yukawa couplings beyond those of the common $\mathbb{Z}_2$-symmetric 2HDMs, and considering the A2HDM instead. One benefit of this flavor-aligned approach is that it allows experiment to determine whether the models with symmetry based Yukawa coupling restrictions are viable. We show that there are regions of A2HDM parameter space available which can describe multiple Higgs excesses simultaneously. In one case, two excesses can be explained by a $\mathbb{Z}_2$-symmetric 2HDM, however there is a wide region

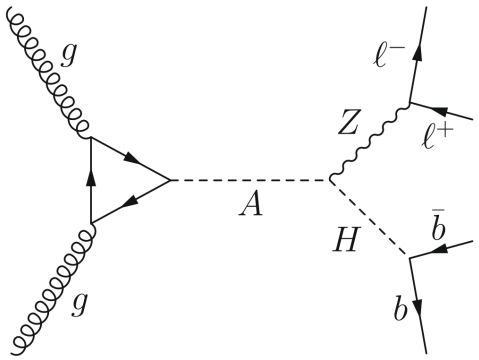

Figure 6.1: Feynman diagram of the process in which the ATLAS Collaboration reported an excess with a local (global) significance of 3.1 (1.3) standard deviations at $(m_A, m_H) = (610, 290)$ GeV in Ref. [27]. The process is a CP-odd scalar A, produced via gluon-gluon fusion, decaying into a Z boson and CP-even H. Subsequently, the Z decays into leptons and the H into a pair of b quarks. We interpret this excess as arising from states in the CP-conserving A2HDM, and denote it as Scenario 1.

of A2HDM parameter space that can also describe that scenario, so there is no preferential reason to settle on $\mathbb{Z}_2$-symmetric models.

6.1 ATLAS $A \to ZH$ Excess

The first excess we introduce was reported by the ATLAS Collaboration, based on 139 fb^{-1} of data. The signal is interpreted as the simultaneous observation of two heavy scalars [27]. The process entails the CP-odd pseudoscalar A being produced via gluon-gluon fusion ($gg \to A$), which then decays to a Z boson and a CP-even H ($A \to ZH$). The Z is detected via leptonic decays (e^+e^- and $\mu^+\mu^-$) and the H decays directly via $H \to b\bar{b}$. The ATLAS Collaboration writes: "The most significant excess for the gluon-gluon fusion production signal assumption is at the $(m_A, m_H) = (610, 290)$ GeV signal point, for which the local (global) significance is 3.1 (1.3) standard deviations."

The ATLAS heat plots provided in Fig. 9 of Ref. [27] yield a 95% CL upper limit of $\sigma \times \mathrm{BR}(A \to ZH) \times \mathrm{BR}(H \to b\bar{b}) \lesssim 0.08$ [0.03] pb observed [expected] for

$(m_A, m_H) = (610, 290)$ GeV. These ATLAS limits were obtained with the using the Mac Digital Color Meter application. We will study this suggestive excess, denoted as Scenario 1. In this scenario, we interpret the ATLAS excess in the $\ell^+\ell^- b\bar{b}$ channel as having arisen from heavy neutral scalar states in the A2HDM where $\sigma \times \text{BR}(A \to ZH) \times \text{BR}(H \to b\bar{b}) \simeq 0.06 \pm 0.02$ pb for $m_A = 610$ GeV and $m_H = 290$ GeV. We pick this range in accordance with the experimental uncertainties and so that we do not violate the exclusion limit, while requiring the A2HDM parameter points to produce an excess. In this scenario, all neutral Higgs boson masses are fixed, whereas the charged Higgs mass will be taken as a free parameter for which we will scan a broad range of values.

The ATLAS Collaboration has also searched for evidence of the $A \to ZH$ process in the $\ell^+\ell^- b\bar{b}$ channel, where the A is produced in association with $b\bar{b}$. In contrast to the gluon fusion channel, only a small excess is seen for $(m_A, m_H) = (610, 290)$ GeV [27] in the b-associated production channel, corresponding to a 95% CL upper limit of $\sigma \times \text{BR}(A \to ZH) \times \text{BR}(H \to b\bar{b}) \lesssim 0.05$ [0.03] pb observed [expected]. We impose this 95% CL upper limit constraint on our A2HDM interpretation of Scenario 1. On the other hand, the ATLAS Collaboration reports that "for b-associated production, the most significant excess is at the $(m_A, m_H) = (440, 220)$ GeV signal point, for which the local (global) significance is 3.1 (1.3) standard deviations." The heat plots provided in Fig. 9 of Ref. [27] yield a 95% CL upper limit of $\sigma \times \text{BR}(A \to ZH) \times \text{BR}(H \to b\bar{b}) \lesssim 0.15$ [0.07] pb observed [expected] for $(m_A, m_H) = (440, 220)$ GeV. However, if one were to interpret this latter excess as an A2HDM signal where $m_A = 440$ GeV and $m_H = 220$ GeV with a cross section of order 0.1 pb, then in the A2HDM parameter regime of interest one would predict a production cross section for gg fusion production of A that is

excluded by Fig. 9(b) of Ref. [27]. Thus, we shall henceforth assume that the ATLAS excess in the b-associated production channel at the $(m_A,\, m_H) = (440,\, 220)$ GeV signal point reported in Ref. [27] is a statistical fluctuation.

Finally, in a recent paper, the ATLAS Collaborations reports on a search for $gg \to A \to ZH$ where $H \to hh$ and both final state Higgs bosons decay to $b\bar{b}$ [39]. No excess is seen in this channel for $(m_A,\, m_H) = (610,\, 290)$ GeV, corresponding to a 95% CL upper limit of $\sigma \times \mathrm{BR}(A \to ZH \to Zhh \to Zb\bar{b}b\bar{b}) \lesssim 10$ [8] fb observed [expected]. These results are obtained from the heat plots provided in Fig. 9 of Ref. [39], under the assumption that the width of A is narrow compared to the experimental mass resolution. Again, we shall assume that the most significant excess observed for a somewhat higher value of m_A in this search channel is a statistical fluctuation.

6.2 A or H at 400 GeV

Other interesting excesses have also been observed in the search for a scalar, with a mass of 400 GeV. For example, the ATLAS Collaboration conducted a search for a heavy scalar that decays into $\tau^+\tau^-$ [28]. Two possible production mechanisms were considered: gluon-gluon fusion (ggF) into a heavy scalar (singly produced) and the production of a heavy scalar in association with a $b\bar{b}$ pair ($bb\phi$). Employing 139 fb^{-1} of data and scanning over possible scalar masses, the ATLAS Collaboration concluded that "for ggF, the lowest local p_0, the probability that the background can produce a fluctuation greater than the excess observed in data, is 0.014 (2.2σ) at $m_\phi = 400$ GeV, while for $bb\phi$ production it is 0.003 (2.7σ) at $m_\phi = 400$ GeV."

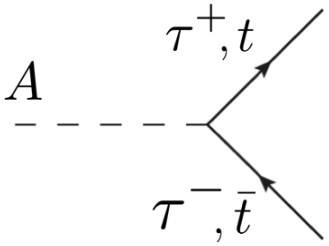

Figure 6.2: Feynman diagram of the processes in which the ATLAS ($gg \to A, b\bar{b}A \to \tau^+\tau^-$) and CMS ($gg \to A \to t\bar{t}$) Collaborations reported excesses. The processes are a CP-odd scalar A, produced via gluon-gluon fusion or b-associated production decaying into two $\tau^\pm$ leptons.

The best fit point at $m_\phi = 400$ GeV corresponds roughly to [29]:

$$\sigma_{\text{ggF}} \times \text{BR}(\phi \to \tau^+\tau^-) \simeq 20^{+37}_{-20}\ \text{fb}\,, \tag{6.1}$$

$$\sigma_{bb\phi} \times \text{BR}(\phi \to \tau^+\tau^-) \simeq 38^{+30}_{-29}\ \text{fb}\,, \tag{6.2}$$

where the error bars correspond to a region of 68% CL. These results are gathered from the ellipses in the two dimensional planes of $\sigma_{ggF} \times \text{BR}(\phi \to \tau^+\tau^-)$ vs. $\sigma_{bb\phi} \times \text{BR}(\phi \to \tau^+\tau^-)$ as shown in Fig. 08 of Ref. [29]. These results were found in ancillary material and did not appear in the actual paper. The ATLAS analysis does not distinguish between a CP-even scalar H and a CP-odd scalar A, so we interpret it as either one.

The CMS Collaboration has also searched for a heavy scalar that decays into $\tau^+\tau^-$ and does not see any excess [31]. Employing 138 fb^{-1} of data, maximum likelihood estimates and 95% CL contours obtained from scans of the signal likelihood are provided in Fig. 11 of Ref. [31] for selected values of the scalar mass. Although the 95% CL contours for $m_\phi = 400$ GeV are not given, we can interpolate between two mass values provided ($m_\phi = 250$ and 500 GeV) by making use of the observed 95% CL upper limits on the product of the cross sections (ggF and $bb\phi$) and branching fraction for $\phi \to \tau^+\tau^-$ as a function of m_ϕ shown in Fig. 10 of Ref. [31]. We then obtain an approximate 95% CL exclusion contour in the plane of

	m_H	m_A	A2HDM interpretation of the excess of events
Scenario 1	290 GeV	610 GeV	$gg \to A \to ZH$, where $H \to b\bar{b}$ and $Z \to \ell^+\ell^-$ [27]
Scenario 2	> 450 GeV	400 GeV	$gg \to A \to \tau^+\tau^-$ [29] $gg \to b\bar{b}A$, where $A \to \tau^+\tau^-$ [29] $gg \to A \to t\bar{t}$ [30]

Table 6.1: Scenario 1 is based on an ATLAS excess of events with a local (global) significance of $3.1(1.3)\sigma$, where the observed lepton is $\ell = e$, μ. Scenario 2 is based on an ATLAS excess of $\tau^+\tau^-$ events with an invariant mass of around 400 GeV, with local significances of 2.7σ in the gg fusion production channel and 2.2σ in the b-associated production channel. The CMS Collaboration sees no excess, but still leaves some room for a possible signal. The ATLAS data does not distinguish between H and A production. However, the CMS excess of $t\bar{t}$ events with an invariant mass of around 400 GeV, with a local (global) significance of $3.5(1.9)\sigma$, favors identifying the excess at 400 GeV with A production.

$\sigma_{\rm ggF}{\rm BR}(\phi\to\tau^+\tau^-)$ vs. $\sigma_{bb\phi}{\rm BR}(\phi\to\tau^+\tau^-)$ for $m_\phi = 400$ GeV, which is exhibited by the dashed contour in Fig. 9.3 (see Section 9). In particular, the 95% CL exclusion contours intersect the x and y axis at the following values:

$$\sigma_{\rm ggF} \times {\rm BR}(\phi \to \tau^+\tau^-) \lesssim 40 \text{ fb} \quad \text{at } 95\% \text{ CL}\,, \tag{6.3}$$

$$\sigma_{bb\phi} \times {\rm BR}(\phi \to \tau^+\tau^-) \lesssim 40 \text{ fb} \quad \text{at } 95\% \text{ CL}\,. \tag{6.4}$$

To obtain Eqs. (6.3) and (6.4) from Fig. 10 of Ref. [31], we have multiplied the latter results by $(5.99/3.84)^{1/2}$ (see Table 40.2 of Ref. [24]), which yields the 95% CL values for the x and y axis intercepts of the two-dimensional contour. These results still leave room for the possibility that the ATLAS excess in the $\tau^+\tau^-$ channel could correspond to a real signal. Meanwhile, the CMS Collaboration has also searched for a heavy CP-even scalar or a heavy CP-odd scalar, or both, decaying into $t\bar{t}$ [30]. Based on 35.9 fb^{-1} of data and scanning over a range of masses, the CMS Collaboration concludes that "a moderate signal-like deviation compatible with an A boson with a mass of 400 GeV is observed" with a local significance of

3.5 ± 0.3 standard deviations. Taking the look-elsewhere effect into consideration, the CMS Collaboration quotes a global significance of 1.9 standard deviations, which corresponds to a p-value of 0.028.

Taken together, the ATLAS and CMS results quoted above suggest a second scenario of interest, which we call Scenario 2. In this scenario, we interpret the ATLAS excess in the $\tau^+\tau^-$ channel and the CMS excess in the $t\bar{t}$ channel as having arisen in the A2HDM where $m_A = 400$ GeV. We take $m_H > 450$ GeV to avoid the possibility of both H and A contributing to the $\tau^+\tau^-$ and $t\bar{t}$ excesses. Smaller values of m_H are excluded based on the ATLAS search for $gg \to A \to ZH$ [27]. The two A2HDM scenarios introduced above are summarized in Table 6.1.

Other extended Higgs model interpretations of the $\tau^+\tau^-$ and $t\bar{t}$ excesses described above have been previously considered in the literature. Both the $\tau^+\tau^-$ and $t\bar{t}$ excesses were suggested as possible evidence for a CP-odd Higgs boson of mass 400 GeV in Refs. [40–42]. In particular, the analysis of Ref. [40] interprets the $\tau^+\tau^-$ and $t\bar{t}$ excesses without specifying the extended Higgs sector model (along with a comment that these excesses cannot be accommodated by the Higgs sector of the MSSM). See also Ref. [43] for a follow-up to the results initially reported in Ref. [40], which invokes an extended Higgs sector with $\mathrm{SU}(2)_L$ triplets [70]. The authors of Ref. [41] employ an enlarged composite Higgs sector where the observed Higgs boson is identified as a pseudo-Goldstone boson state. Finally, the CP-odd scalar of mass 400 GeV is interpreted in the context of an extended Higgs sector consisting of two $\mathrm{SU}(2)_L$ doublets and an $\mathrm{SU}(2)_L$ singlet. More recently, the authors of Ref. [44] assert that it is possible to accommodate the ATLAS $\tau^+\tau^-$ excess in a Type I 2HDM while at the same time explaining the muon $g-2$ anomaly [45].

Chapter 7

Parameter Scans

We performed parameter scans to probe the CP-conserving A2HDM parameter space for regions which predict the excesses of events for Scenarios 1 and 2 (as described in Chapter 6) and are otherwise consistent with other measured observables pertaining to Higgs physics. A generic point in the CP-conserving A2HDM parameter space is uniquely specified by the following set of real parameters,

$$v,\, m_h,\, m_H,\, m_A,\, m_{H^\pm},\, |c_{\beta-\alpha}|,\, Z_2,\, Z_3,\, Z_7,\, a^U,\, a^D,\, a^E. \tag{7.1}$$

As indicated in Eqs. (2.49)–(2.52), the masses of h, H, and A can then be used to obtain Z_1, Z_4, Z_5 and $|Z_6|$. In Scenario 1, after fixing v, m_h, m_H and m_A, we scan over the remaining parameters. In Scenario 2, m_H is not fixed so we must scan over this parameter as well. Phenomenologically, the parameters Z_1 and Z_2 only appear in the Higgs self couplings, so one could set them equal to one another in order to scan over one less parameter; we however let them vary independently.

Given the dimensionality of the parameter space, it would take an extraordinary amount of computing time to probe the entire parameter space. There are large regions of parameter space which are excluded by theoretical or experimental

(or both) constraints, so we can perform a more efficient scan by first imposing a variety of preemptive conditions before calculating observables of interest. The most important constraints in our two scenarios, which were introduced in Chapter 3 of Part 1, are given below:

1. Stability, Unitarity, and Perturbativity – Enforcing tree-level unitarity on interactions between Higgs bosons and gauge bosons places upper bounds on a set of equations involving the Higgs basis scalar potential parameters Z_i. Due to the complexity of these formulae, we impose this constraint numerically after performing parameter scans [23, 46, 47]. To ensure our models are perturbative, we require the quartic couplings in the scalar potential such that $|Z_i| \leq 4\pi$. Applying this restriction before performing a parameter scan can make the scan far more efficient.

2. Higgs Signal Strengths (μ_i^f) – The lightest Higgs scalar h must be SM-like and have properties consistent with the current data, which forces μ_i^f 1, where μ_i^f is the ratio of the h cross section times branching ratio into a particular final state computed in the A2HDM and SM. In particular, we check that the Higgs signal strengths are within the experimental errors for $\gamma\gamma$ and ZZ, and within two times the experimental errors for W^+W^-, $\tau^+\tau^-$, and $b\bar{b}$. We use the Higgs signal strength limits to place bounds on the magnitudes of the A2HDM coupling modifiers $|f_{\phi,F}|$.

3. Oblique T-parameter – Precision electroweak data provides the most stringent constraint on the A2HDM parameters [48] via the experimental measurements of the oblique parameter T. In particular, we impose the requirement that T is within 2σ of its central value as reported in Ref. [24]. Imposing this constraint

restricts the possible values of the charged Higgs mass and forces $m_{H^\pm}$ to be within about ± 60 GeV of either m_A or m_H. this limit causes two bands of allowed charged Higgs masses.

4. $b \to s\gamma$ – In almost all of the parameter space in our scenarios, the most constraining heavy flavor observable is derived from the observed $\bar{B} \to X_s\gamma$ decay. We apply this constraint via calculating the difference between the rates for $b \to s\gamma$ SM and A2HDM.

5. ΔM_{B_s} – Data for B_s–$\overline{B}_s$ mixing provides an additional constraint that limits the value of $|a^U|$ as a function of the charged Higgs mass, but it is only more restrictive than $b \to s\gamma$ constraints in an insignificant number of parameter points in the scanning region of interest. In particular, within the parameter intervals exhibited in Table 7.1, a rough upper bound of $|a^U| \lesssim 1$ was obtained [although this value can be lower for charged Higgs masses below 500 GeV as shown in Fig. 9.2(a)], whereas no constraint on a^D was obtained in the scanning region of interest. As a result, the excluded region of the A2HDM parameter space due to the constraint on ΔM_{B_s} roughly coincides with the corresponding excluded region of the Type-I 2HDM in the $m_{H^\pm}$ vs. $\tan\beta$ plane exhibited in Fig. 8 of Ref. [51] after identifying $\tan\beta = 1/|a^U|$. However, in the A2HDM parameter space, imposing the ΔM_{B_s} constraint can eliminate a small region of parameter space with values of $|a^U| \gtrsim 1$ that otherwise would be allowed by the $b \to s\gamma$ constraints shown in Fig. 3.1. CHECK

6. LHC Searches for BSM Scalars – Numerous other searches for new elementary scalar states at the LHC have been performed by the ATLAS and CMS Collaborations. We have checked that the 95% CL upper limits obtained in

Parameter Intervals Scanned

$\lvert c_{\beta-\alpha}\rvert$	0 , 0.45
Z_2	0 , 4.5
Z_3	-2 , 12
Z_7	-10 , 10
$m_{H^\pm}$	200 , 1000 GeV
a^U	-1.5 , 1.5
a^D	-50 , 50
a^E	-50 , 50

Table 7.1: Parameter intervals scanned in the analysis of Scenarios 1 and 2.

all these searches are satisfied by A2HDM parameter points which predict the excesses in each scenario.

Having imposed all the conditions listed above, we scan values of $|c_{\beta-\alpha}|$ from 0 to 0.45 to keep the Yukawa couplings roughly within 20% of their SM model values (in light of the precision LHC Higgs data). The parameter Z_7 only enters Hhh and HH^+H^- couplings multiplied by $c^2_{\beta-\alpha}$ which is extremely small for most of the valid points in the scan. Hence, our results are quite insensitive to the choice of Z_7. As noted above, the charged Higgs mass must be nearly degenerate in mass with m_A or m_H due to the T parameter constraint. We also require that $m_{H^\pm} > m_t + m_b$ (thereby avoiding the possibility of an on-shell $t \to H^+b$ decay, which is not observed at the LHC). Hence, we initially allow for values of $m_{H^\pm}$ in the range of $[200, 1000]$ GeV. We scan over up-type Yukawa coupling parameters a^U between -1.5 and 1.5 and down- and lepton-type Yukawa coupling parameters a^D and a^E between -50 and 50, which ensures the absence of Landau poles significantly below the Planck scale [52]. A summary of the parameter intervals employed in our scans is presented in Table 7.1.

Chapter 8

Scenario 1: $m_A = 610$ GeV, $m_H = 290$ GeV

In Scenario 1 we consider the CP-conserving 2HDM with a CP-odd scalar mass of $m_A = 610$ GeV and two CP-even scalars with masses $m_H = 290$ GeV and $m_h = 125$ GeV, where h is identified as the Higgs boson observed in LHC data. This scenario is motivated by a slight excess of events over the expected backgrounds in the ATLAS search for gluon-gluon fusion production of a CP-odd scalar A followed by its decay to ZH, with the subsequent decay of $H \to b\bar{b}$ and $Z \to \ell^+\ell^-$ ($\ell = e$, μ). Using the results of Ref. [27] and the 95% CL upper limits reported therein, we propose that the excess of events must lie in the range of,

$$0.04 \leq \sigma(gg \to A)\,\mathrm{BR}(A \to ZH)\,\mathrm{BR}(H \to b\bar{b}) \leq 0.08 \text{ pb}\,. \tag{8.1}$$

In contrast, no significant excess was seen by the ATLAS Collaboration for $(m_A, m_H) = (610, 290)$ GeV in the $Zb\bar{b}b\bar{b}$ final state that can arise either via the b-associated production process $gg \to b\bar{b}A$ where $A \to ZH \to Zb\bar{b}$, or via $gg \to A \to ZH \to Zhh \to Zb\bar{b}b\bar{b}$, as discussed in Section 6.1.

A separate search for the gluon fusion production of a CP-even scalar H

also did not yield any significant excesses. For example, the ATLAS Collaboration reported in Ref. [55] a 95% CL upper limit for $\sigma(gg \to H \to hh) < 0.241$ pb for $m_H \sim 290$ GeV. The corresponding limit obtained by the CMS Collaboration in Ref. [56] is nearly identical to the quoted ATLAS result.

In this chapter, we show our results of probing the A2HDM parameter space that is consistent with the Scenario 1 interpretation of the ATLAS excess specified in Eq. (8.1), subject to the following conditions,

$$\sigma(gg \to Ab\bar{b})\,\mathrm{BR}(A \to ZH)\,\mathrm{BR}(H \to b\bar{b}) \leq 0.05 \text{ pb}\,, \tag{8.2}$$

$$\sigma(gg \to A)\mathrm{BR}(A \to ZH)\mathrm{BR}(H \to hh \to b\bar{b}b\bar{b}) \leq 0.01 \text{ pb}\,, \tag{8.3}$$

$$\sigma(gg \to H)\,\mathrm{BR}(H \to hh) \leq 0.241 \text{ pb}\,, \tag{8.4}$$

obtained from the 95% CL upper limits reported in Refs. [27, 39, 55], respectively.

8.1 A2HDM Interpretation of Scenario 1

In Fig. 8.1 we show points in a plane of signal rates of $gg \to A \to ZH \to Zb\bar{b}$ and $gg \to H \to hh$ obtained by scanning the A2HDM parameter space. All points respect the theoretical and experimental constraints discussed in Section 7. The points in the red box also satisfy the conditions specified in Eqs. (8.1)–(8.4). Fig. 8.1 shows that we can accommodate the $gg \to A \to ZH \to Zb\bar{b}$ signal while remaining consistent with $gg \to H \to hh$ data and all other constraints.

To gain understanding of the expected cross sections involved in Scenario 1, we can approximate the cross section calculations and see how they scale with the alignment parameters a^U and a^D. In the gluon-gluon fusion production mode, we can neglect the term arising from interference of t and b quarks, which contribute less than a 5% of the total. By using the program `SusHi` [53] to accomplish this,

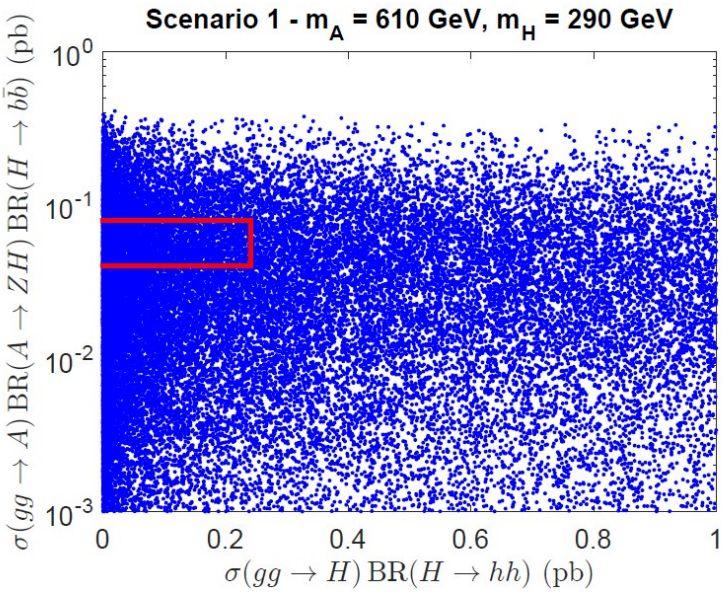

Figure 8.1: Signal rates for the production of A and H in Scenario 1. The A2HDM parameter generation complies with all theoretical and experimental constraints elucidated in Section 7. Events inside the rectangular box with red boundaries are consistent with the conditions specified in Eqs. (8.1)–(8.4), which correspond to a small excess of events reported in Ref. [27] and interpreted as $gg \to A \to ZH \to b\bar{b}\ell^+\ell^-$ (with no significant excess in the corresponding b-associated production of A), and with the nonobservation of $gg \to H \to hh$ derived from the 95% CL upper limits obtained in Refs. [55, 56].

using the procedure described in Section 5.3, we obtain:

$$\sigma(gg \to A) \simeq 2.85\,|a^U|^2 \text{ pb}, \qquad \sigma(gg \to H) \simeq 10.28\,|a^U|^2 \text{ pb}, \tag{8.5}$$

$$\sigma(gg \to b\bar{b}A) \simeq 1.11\,|a^D|^2 \text{ fb}, \qquad \sigma(gg \to b\bar{b}H) \simeq 26.98\,|a^D|^2 \text{ fb}\,. \tag{8.6}$$

In Fig. 8.2(a), we exhibit the three main decay channels of A in Scenario 1. One of the experimental constraints that has been applied derives from the search for $A \to t\bar{t}$ reported by the CMS Collaboration in Ref. [30]. Indeed, the latter constraint rules out any points to the right of the dashed line shown in Fig. 8.2(b). In light of Fig. 8.2(a), $A \to ZH$ is a dominant decay channel for the CP-odd scalar in Scenario 1 if $|a^U| \lesssim 1$.

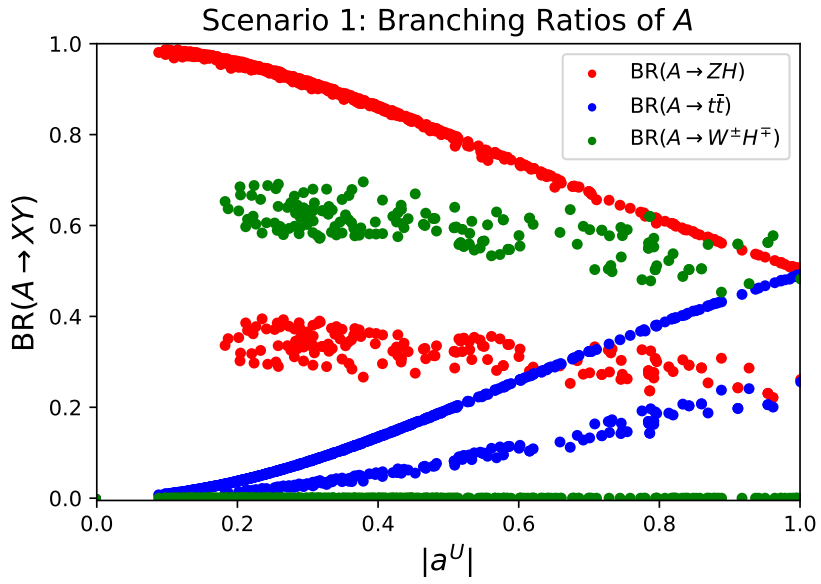

(a)

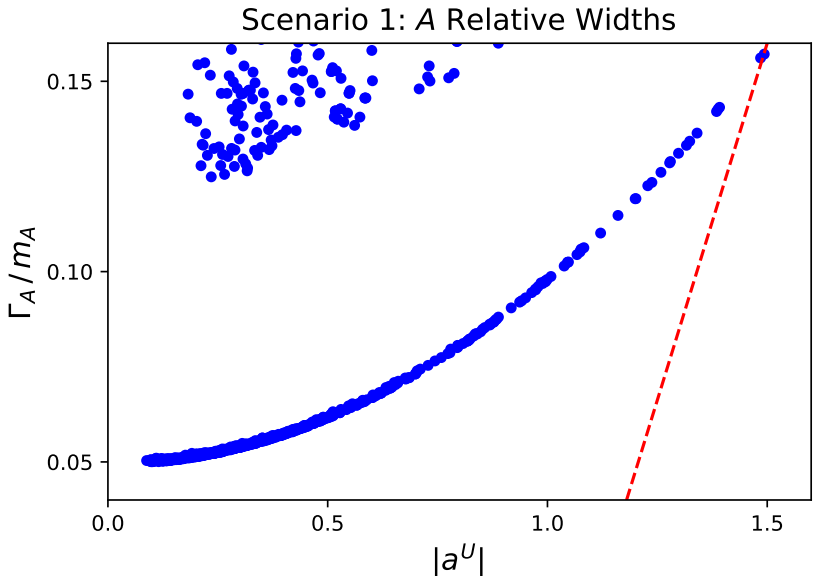

(b)

Figure 8.2: Results of a scan over A2HDM parameter points in Scenario 1 that satisfy the theoretical and experimental constraints elucidated in Section 7 and the constraints of Eqs. (8.1)–(8.4). Panel (a) shows the branching ratios for the decay of A into its dominant final state channels, and panel (b) shows the total A width divided by its mass, as functions of $|a^U|$. Applying the 95% CL upper limit for $\sigma(gg \to A \to t\bar{t})$ reported in Ref. [30] eliminates points to the right of the dashed line shown in panel (b) from further consideration. The two distinct branches of a given color of points correspond to the cases where the decay $A \to W^{\pm}H^{\mp}$ is either kinematically allowed or disallowed.

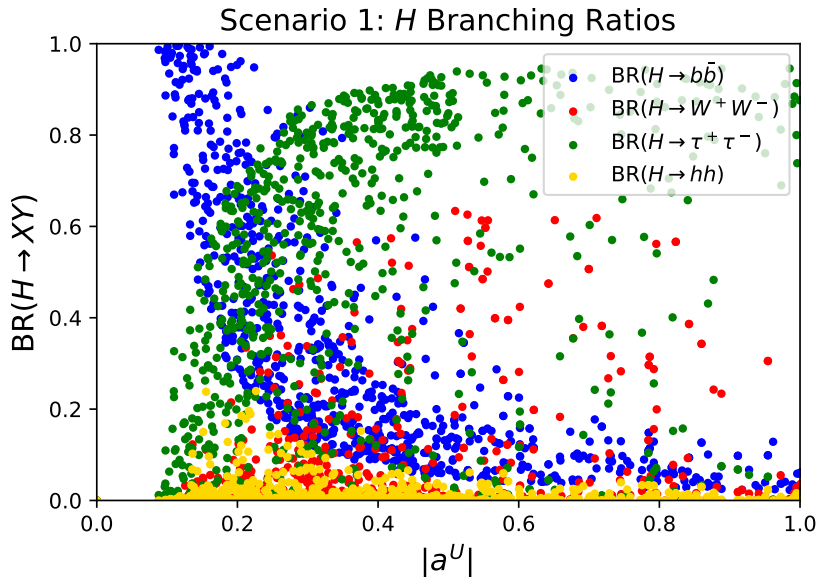

(a)

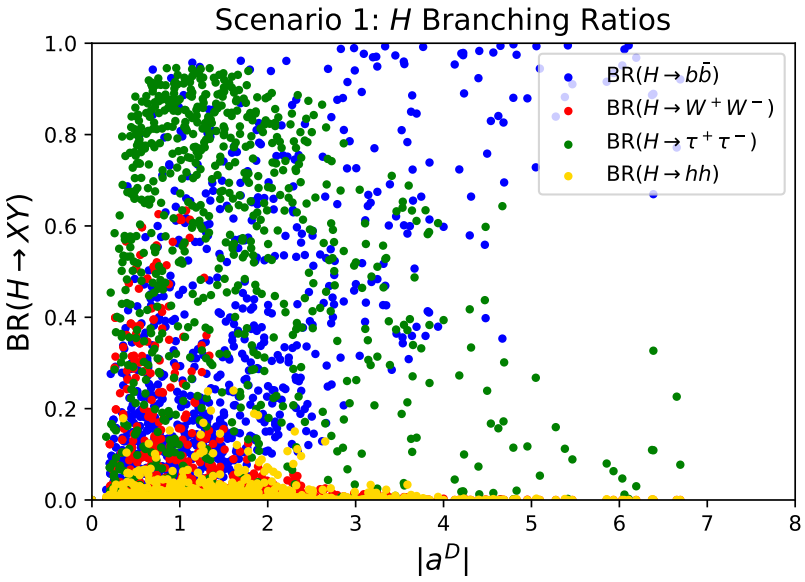

(b)

Figure 8.3: Results of a scan over A2HDM parameter points in Scenario 1 that satisfy the theoretical and experimental constraints elucidated in Section 7 and the constraints of Eqs. (8.1)–(8.4). Panels (a) and (b) exhibit the branching ratios of the four main H decay channels as functions of $|a^U|$ (allowing a^D to vary) and $|a^D|$ (allowing a^U to vary), respectively.

In Fig. 8.3, we exhibit four of the dominant H decay channels: $H \to b\bar{b}$ (blue), $H \to W^+W^-$ (red), $H \to \tau^+\tau^-$ (green), and $H \to hh$ (yellow). The $H \to ZZ$ channel would also have a significant decay fraction, but the $H \to W^+W^-, ZZ$ branching ratios are related via constant phase space factors so that $\mathrm{BR}(H \to WW) \simeq 2.23\,\mathrm{BR}(H \to ZZ)$, so it is sufficient to display results for W^+W^- only.

For example, using Eq. (8.5) it follows that if $|a^U| \sim 1$ then $\mathrm{BR}(H \to hh)$ cannot be larger than about 2% in light of Eq. (8.4), as shown in Fig. 8.3(a). For example, Eq. (8.5) implies that for values of $|a^U| \sim 1$, a signal of about 0.06 pb in the channel $gg \to A \to ZH \to Zb\bar{b}$ can be achieved with $\mathrm{BR}(H \to b\bar{b}) \sim 5\%$.

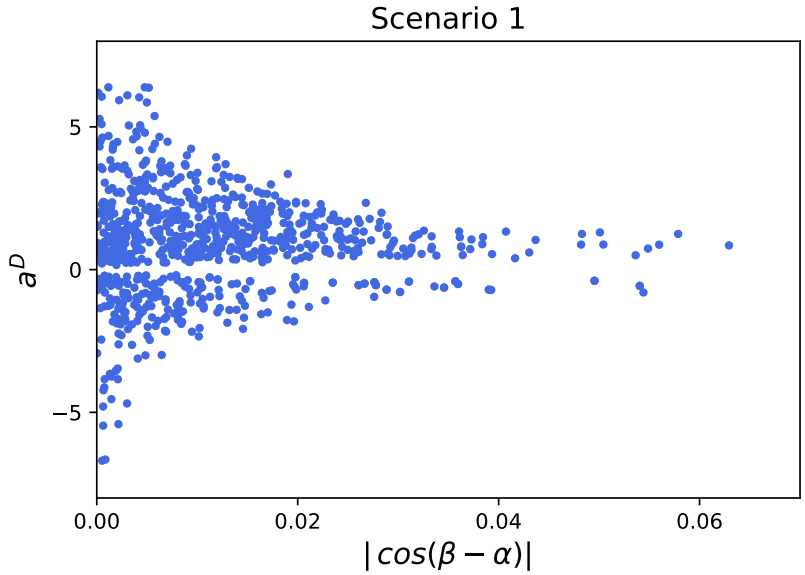

(a)

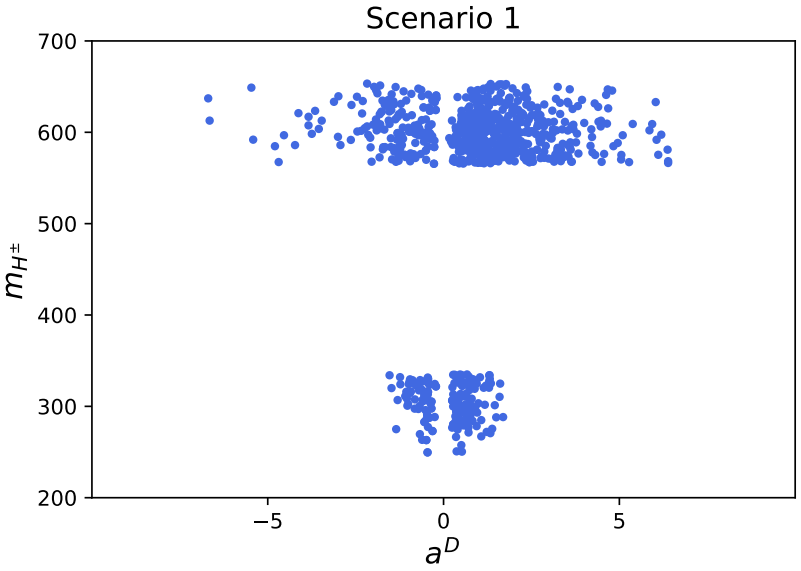

(b)

Figure 8.4: Results of a scan over A2HDM parameter points in Scenario 1 that satisfy the theoretical and experimental constraints elucidated in Section 7 and the constraints of Eqs. (8.1)–(8.4). Panel (a) show the allowed values of the flavor-alignment parameter a^D as a function of $|\cos(\beta-\alpha)|$ and panel (b) shows the charged Higgs mass as a function of a^D.

We now proceed to analyze more closely the A2HDM parameter space that can describe Scenario 1. The scatter plot in Fig. 8.4(a) indicates that $|c_{\beta-\alpha}| \lesssim 0.07$, which is very close to the Higgs alignment limit, as a consequence of the precision Higgs data as discussed in Section 3.2. We see there is no preference in Scenario 1 for a specific sign of the alignment parameter a^D. The range of a^D consistent with the ATLAS excess in $gg \to A$ at $(m_A, m_H) = (610, 290)$ GeV is roughly $0.18 \lesssim |a^D| \lesssim 8.2$. In particular, both very small and very large values of $|a^D|$ are excluded. Both regimes can be understood as follows. From Eq. (5.4), we see that the down-quark coupling modifier for H is

$$f_{H,d} = -\varepsilon(|c_{\beta-\alpha}| + s_{\beta-\alpha} a^D)\,. \tag{8.7}$$

This means that in the approximate Higgs alignment limit of the A2HDM, where $|c_{\beta-\alpha}| \ll 1$, the coupling modifier $f_{H,d}$ will grow with a^D. Consequently, $a^D \sim 0$ is excluded, since the A signal excess depends on a branching ratio of the decay $H \to b\bar{b}$ that is not too small. On the other hand, for very large absolute values of $|a^D|$, both $\mathrm{BR}(H \to b\bar{b})$ and $\sigma(gg \to Ab\bar{b})$ become too large to be consistent with the constraints exhibited in Eqs. (8.1)–(8.4).

The allowed regions of the charged Higgs mass are exhibited Fig. 8.4(b). The charged Higgs mass is constrained to lie either in the interval $575 \lesssim m_{H^\pm} \lesssim 665$ GeV or $220 \lesssim m_{H^\pm} \lesssim 330$ GeV. These ranges could be anticipated following the discussion of precision electroweak constraints in Section 3.3. In particular, since there is a sizable mass splitting between H and A in Scenario 1, in order for the oblique T parameter to be suitably small in the approximate Higgs alignment limit, it is necessary for the charged Higgs mass to be roughly degenerate in mass with either A or H.

The parameter points in Scenario 1 must also be consistent with the non-observation of H and A production and subsequent decay in other search channels examined by the ATLAS collaboration in their analysis of the Run 2 LHC data. In particular, for $(m_A, m_H) = (610, 290)$ GeV, there is no experimental evidence (yet) for H and A production followed by the subsequent decay of the scalar into other final states, such as ZZ, W^+W^-, $\tau^+\tau^-$ and $\gamma\gamma$.

The ditau channel is one of the main search channels for new scalars, and there are stringent constraints from LHC Run 2 data. In particular, we can use the results of the ATLAS Collaboration reported in Fig. 08 of Ref. [29] to determine whether $m_H \sim 290$ GeV and/or $m_A \sim 610$ GeV might not have already been excluded by existing ditau data.

We begin by examining the implications of the ditau data for the production of H. In Fig. 8.5 (a), we show the results of a scan over A2HDM parameter points in Scenario 1 that satisfy the theoretical and experimental constraints elucidated in Section 7 and the constraints of Eqs. (8.1)–(8.4). Although most of these points survive, some of them are excluded by the ATLAS search for $H \to \tau^+\tau^-$. In particular, applying the limits reported by the ATLAS Collaboration in Ref. [29] for $m_H = 300$ GeV, we find that at the 1σ exclusion level,

$$\sigma(gg \to H)\,\mathrm{BR}(H \to \tau^+\tau^-) \leq 120 \text{ fb}\,, \tag{8.8}$$

$$\sigma(gg \to b\bar{b}H)\,\mathrm{BR}(H \to \tau^+\tau^-) \leq 70 \text{ fb}\,. \tag{8.9}$$

The exclusion limits of Eqs. (8.8) and (8.9) correspond to the vertical and the horizontal red lines, respectively, of Fig. 8.5 (a). Thus, all points exhibited in Fig. 8.5 (a) that lie below the horizontal red line and to the left of the vertical red line are consistent with the exclusion limits obtained in Ref. [29]. After excluding the points that lie

above the horizontal red line and/or to the right of the vertical red line in Fig. 8.5(a), we increased the scanning statistics to obtain the plot of $\sigma(gg \to H) \times \mathrm{BR}(H \to ZZ)$ as a function of $\cos(\beta - \alpha)$ shown in Fig. 8.5(b). The horizontal green line shown in Fig. 8.5(b) corresponds to the 95% CL exclusion limit,

$$\sigma(gg \to H)\, \mathrm{BR}(H \to ZZ) \leq 0.1 \text{ pb}\,, \tag{8.10}$$

reported by the ATLAS Collaboration in Ref. [57]. Note that the points that lie below the horizontal green line of Fig. 8.5(b), which take into account the constraint of Eq. (8.10), satisfy $\cos(\beta - \alpha) \sim 0.045$. Imposing similar constraints from the exclusion limit for $\sigma(gg \to H \to W^+W^-)$ obtained in Ref. [58] does not eliminate additional points from the A2HDM scan exhibited in Fig. 8.5.

The ditau exclusion limits of Eqs. (8.8) and (8.9) have implications for the flavor-alignment parameter a^E, as exhibited in Fig. 8.6(a). In particular, after applying all the relevant constraints, $|a^E| \lesssim 5$, where the precise upper bound can be even more restrictive depending on the value of $|a^U|$. Note that the A2HDM parameter space of interest is insensitive to the sign of a^U. This is a consequence of the fact that precision Higgs data is compatible with either sign of a^U. In light of the top quark Yukawa modifier,

$$f_{h,t} \;=\; s_{\beta-\alpha} - |c_{\beta-\alpha}| a^U\,, \tag{8.11}$$

we see that due to the constraint on $c_{\beta-\alpha}$ exhibited in Fig. 8.5(a) and the upper bound of $|a^U| \lesssim 1.0$, it follows that $f_{h,t} \simeq 1$, regardless of the sign of a^U. We scanned over values of a^U such that $|a^U| \lesssim 1.5$ in order to avoid a Landau pole significantly below the Planck scale. As noted in Section 7.1, the constraint of ΔM_{B_s} reduces this upper bound to roughly $|a^U| \lesssim 1$ (with a weak dependence on the charged Higgs mass). A second feature that is evident from Fig. 8.6(a) is the existence of a lower

bound, $|a^U| \gtrsim 0.11$. This arises from the fact that the gluon fusion production cross section of A relies on the $At\bar{t}$ coupling that is proportional to a^U [cf. Eq. (8.5)]. Thus, to be consistent with Eq. (8.1), $|a^U|$ cannot be arbitrarily small.

Next, consider the implications of the ditau data for the production of A. In particular, applying the limits reported by the ATLAS Collaboration in Ref. [29] for $m_A = 600$ GeV, we find that at the 2σ exclusion level,

$$\sigma(gg \to A)\,\mathrm{BR}(A \to \tau^+\tau^-) \leq 12.5 \text{ fb}\,, \tag{8.12}$$

$$\sigma(gg \to b\bar{b}A)\,\mathrm{BR}(A \to \tau^+\tau^-) \leq 4.5 \text{ fb}\,. \tag{8.13}$$

No further reduction of the A2HDM parameter space follows after imposing the $A \to \tau^+\tau^-$ exclusion limits of Eqs. (8.12) and (8.13). In particular, the red parameter points of Fig. 8.6(b) lie considerably below the ATLAS exclusion limits quoted above, which is not surprising given that the $\tau^+\tau^-$ decay mode is subdominant. Indeed, in light of Fig. 8.2(a), if $m_{H^\pm} \sim m_A$ then the dominant A decay channels are $A \to ZH$ and $A \to t\bar{t}$, which account for more than 99% of all A decays. As expected, the branching ratio for $A \to t\bar{t}$ increases with $|a^U|$, since the $At\bar{t}$ coupling is proportional to a^U. Moreover, as illustrated in Fig. 8.2(b), the total width of A also increases with $|a^U|$. In Scenario 1, an experimental upper limit on $|a^U|$ can be deduced based solely on the absence of evidence for $A \to t\bar{t}$ for $m_A = 610$ GeV, as reported in Ref. [30] by the CMS Collaboration, where the region of $|a^U| \gtrsim 1.2$ is excluded. However, after applying the full constraints of the Scenario 1 parameter scan, the results of Fig. 8.6(a) imply a somewhat stronger constraint of $|a^U| \lesssim 0.9$. Nevertheless there is still room for a large enough value of $|a^U|$ to yield a sizable $A \to t\bar{t}$ signal rate, which therefore remains a tantalizing possibility to be probed in the near future at the LHC.

Having successfully accommodated the proposed signal of Scenario 1 [cf. Eq. (8.1)] in the framework of the CP-conserving 2HDM, one can now propose additional Higgs signals that could be discovered in future LHC searches. As an example, we can provide the possible values of the cross section that are consistent with the ATLAS data excess given in Eq. (8.1) for the gluon fusion production and the b-associated production of H, followed by its decay into a pair of Higgs bosons, which are exhibited in the plots shown in Fig. 8.7. In particular, given that $\text{BR}(h \to b\bar{b}) \simeq 58\%$, the b-associated production process would yield spectacular events with six b-quarks in the final state.

Although the proposed signal of $A \to ZH$ specified in Eq. (8.1) can be successfully accommodated in the framework of the A2HDM, one can now ask whether this signal is viable in two Higgs doublet models with natural flavor conservation. In light of Eqs. (5.7)–(5.10), the following four special cases of the A2HDM are of interest:

$$\text{Type-I:} \quad a^U = a^D = a^E, \qquad \text{Type-X:} \quad a^U = a^D = -\frac{1}{a^E}\,, \tag{8.14}$$

$$\text{Type-II:} \quad -\frac{1}{a^U} = a^D = a^E, \qquad \text{Type-Y:} \quad a^U = -\frac{1}{a^D} = a^E. \tag{8.15}$$

In all four cases above, the corresponding conditions are a consequence of a $\mathbb{Z}_2$ symmetry that is preserved by all dimension-4 terms of the Higgs Lagrangian. Consequently, the condition $T_{Z_2} = 0$ must also be satisfied [cf. Eq. (5.6)].

To investigate whether the surviving points of the A2HDM parameter scans presented above are consistent with any of the relations given in Eqs. (8.14) and

(8.15), we introduce the following four quantities,

$$T_I \equiv \left|1 - a^D/a^U\right| + \left|1 - a^E/a^U\right| + T_{Z_2}\,,$$

$$T_X \equiv \left|1 - a^D/a^U\right| + \left|1 + a^E a^U\right| + T_{Z_2}\,, \tag{8.16}$$

$$T_{II} \equiv \left|1 + a^D a^U\right| + \left|1 - a^E/a^U\right| + T_{Z_2}\,,$$

$$T_Y \equiv \left|1 + a^D a^U\right| + \left|1 - a^E/a^U\right| + T_{Z_2}\,. \tag{8.17}$$

By design, $T_I = 0$ only for the Type-I 2HDM, $T_{II} = 0$ only for the Type-II 2HDM, $T_Y = 0$ only for the Type-Y 2HDM, and $T_X = 0$ only for the Type-X 2HDM.

In light of Fig. 8.4(b), $m_{H^\pm} \lesssim 670$ GeV for the A2HDM scan points that satisfy all of the Scenario 1 constraints. However, as shown in Ref. [59], the constraint imposed by the $b \to s\gamma$ measurement yields $m_{H^\pm} \gtrsim 800$ GeV in the Type-II 2HDM, and the same rough upper bound applies to the Type-Y 2HDM [51]. Hence, Scenario 1 is incompatible with the Type-II and Type-Y 2HDM. In contrast, the range of charged Higgs masses shown in Fig. 8.4(b) are not excluded by the $b \to s\gamma$ measurement in the Type I and X 2HDM [51]. Thus, we now explore whether or not Scenario 1 is compatible with some range of parameters within the Type-I or X 2HDM. In Fig. 8.8, we have plotted the values of T_I and T_X for those A2HDM scan points that survive the theoretical and experimental constraints elucidated in Section 7 and the constraints of Eqs. (8.1)–(8.4) and Eqs. (8.8)–(8.10). Given that the scan points of Fig. 8.8 appear to be approaching the horizontal (Type-X) or the vertical (Type I) axes, it seems plausible (with a higher statistics scan) that Scenario 1 could be compatible within the Type-I and/or X 2HDM frameworks. To investigate this possibility in more detail, we have performed dedicated Type-I and Type-X scans for Scenario 1 and confirmed that it is indeed possible to fit all Scenario 1 constraints in the Type-I 2HDM but *not* in the Type-X 2HDM.

	Type-I 2HDM	A2HDM
$\sigma(gg \to H)\,\mathrm{BR}(H \to \tau^+\tau^-)$	$\lesssim 90$ fb	$\lesssim 120$ fb
$\sigma(gg \to b\bar{b}H)\,\mathrm{BR}(H \to \tau^+\tau^-)$	$\lesssim 0.26$ fb	$\lesssim 70$ fb
$\sigma(gg \to A)\,\mathrm{BR}(A \to \tau^+\tau^-)$	$\lesssim 1.6 \times 10^{-3}$ fb	$\lesssim 0.1$ fb
$\sigma(gg \to b\bar{b}A)\,\mathrm{BR}(A \to \tau^+\tau^-)$	$\lesssim 6.1 \times 10^{-7}$ fb	$\lesssim 0.05$ fb

Table 8.1: In the parameter scans subjected to all Scenario 1 constraints, the maximal values of $\sigma \times \mathrm{BR}$ is shown for four different production processes of neutral heavy scalars that decay to $\tau^+\tau^-$. Results in the case of the A2HDM are taken from Figs. 8.5(a) and 8.6(b). Results in the case of the Type-I 2HDM are obtained from a dedicated scan.

The failure to find solutions within the Type-X 2HDM framework can be attributed to the constraints of the $H \to \tau^+\tau^-$ decays. For all points that satisfied the constraints of eqs. (8.1)–(8.4), we obtained values of $\sigma(gg \to H)\,\mathrm{BR}(H \to \tau^+\tau^-)$ between 0.9 and 1.3 pb, in violation of the bound of eq. (8.8). In particular, imposing the bounds of eqs. (8.1)–(8.4) on the Type-X (and Type-I) scans require values of $1/a^U = \tan\beta \gtrsim 2$, which implies that in the Type-X 2HDM we also have $a^E = \tan\beta \gtrsim 2$. That is, the decay rate for $H \to \tau^+\tau^-$ is enhanced by a factor of $\tan^2\beta$, thereby producing values of $\sigma(gg \to H \to \tau^+\tau^-)$ that exceed the observed upper bound given in Eq. (8.8).

Although it is possible to accommodate Scenario 1 in a Type-I 2HDM, more flexibility is achieved by employing the generic A2HDM framework. For example, in Table 8.1, we exhibit the maximal $\sigma \times \mathrm{BR}$ for the production of H and A (either via gluon fusion or via b-associated production) followed by the decay into $\tau^+\tau^-$. If the Scenario 1 data excesses persist, the detection of the $\tau^+\tau^-$ decay mode in multiple channels would be inconsistent with a Type-I interpretation but could be compatible in the more general A2HDM framework. This exercise illustrates the advantage of employing the A2HDM in analyzing evidence for the production of

new scalar states. In particular, the larger parameter space (relative to the special cases of the A2HDM corresponding to Type I, II, X, and Y Yukawa couplings) provides the freedom to independently vary the a^U, a^D and a^E flavor-alignment parameters, thereby providing the A2HDM with greater flexibility in interpreting different signals of heavy scalar production and decay.

If the proposed signal of Eq. (8.1) is confirmed, then one should expect to discover a charged Higgs boson either in the mass range of [220 , 320] GeV or in the range of [570 , 670] GeV, as indicated in Fig. 8.4. There is an extensive set of experimental results on searches for charged scalars in the literature. The most recent results for charged Higgs boson searches at the LHC yield upper bounds on $\sigma(pp \to H^\pm \to tb)$ [60] and $\sigma(pp \to H^\pm \to \tau\nu)$ [61]. We use the notation $H^\pm \to tb$ to mean either $H^+ \to t\bar{b}$ or $H^- \to \bar{t}b$ and $H^\pm \to \tau\nu$ denotes $H^+ \to \tau^+\nu_\tau$ or $H^- \to \tau^-\bar{\nu}_\tau$.) We have computed the branching ratios for the charged scalar in the A2HDM, and we have used the results of the LHC Cross Section Working Group [62] to obtain the LHC production cross section for $H^\pm$ as a function of the A2HDM flavor-alignment parameters. The A2HDM parameter space obtained in our analysis of Scenario 1 abide by constraints derived from the non-observation of the charged Higgs boson decaying to $\tau\nu$. However, scans with higher values of $|a^U|$ can produce values of $\sigma(pp \to H^\pm \to tb)$ that lie above the observed bound obtained by the CMS Collaboration using 35.9 fb^{-1} of data [60]. As a result, we obtain an upper bound on $|a^U|$ that depends on the range of charged Higgs masses: $|a^U| \lesssim 0.5$ for $m_{H^\pm} \in [220\,,\,320]$ GeV and $|a^U| \lesssim 1$ for $m_{H^\pm} \in [570\,,\,670]$ GeV. These bounds on $|a^U|$ will improve when the full Run 2 dataset and future Run 3 data are analyzed, with the real possibility of a discovery of the $H^\pm$ via its tb decay mode.

8.2 A2HDM Benchmarks for Scenario 1

We present two benchmarks for Scenario 1 in Tables 8.2 and 8.5, chosen to illustrate A2HDM parameter sets that would yield other heavy scalar channels that could be probed in future runs at the LHC.

The parameters of the first benchmark (denoted B1a) corresponds to a CP-conserving Type-I 2HDM, which is a special case of the A2HDM where the flavor-alignment parameters are related according to Eq. (5.7) and satisfy $a^U = a^D = a^E = \varepsilon/\tan\beta$, which defines $\tan\beta$ of the Type-I Yukawa sector. Adopting the convention where $\tan\beta$ is positive then fixes ε to be the (common) sign of the flavor-alignment parameters. The parameters of benchmark B1a are displayed in Table 8.2. For the benchmark parameters shown in Table 8.2, the main production cross sections and some of the relevant branching ratios for H, A and $H^\pm$ are exhibited in Tables 8.3 and 8.4.

Benchmark B1a – Type-I 2HDM				
$m_{H^\pm}$ (GeV)	$\cos(\beta-\alpha)$	Z_2	Z_7	$\tan\beta$
650	-0.0013	2.27	0.58	4.0

Table 8.2: Parameters characterizing Benchmark B1a, for which $m_h = 125$, $m_A = 610$ and $m_H = 290$ GeV. The corresponding A2HDM flavor-alignment parameters satisfy $a^U = a^D = a^E = 1/\tan\beta \simeq 0.25$. Note that $\cos(\beta-\alpha) < 0$ in light of Eqs. (2.48) and (5.7). The parameter $Z_3 = 11.89$ is obtained by imposing the condition for a softly-broken $\mathbb{Z}_2$ symmetric scalar potential by setting $T_{Z_2} = 0$ [cf. Eq. (5.6)].

The results of Tables 8.3 and 8.4 suggest a number of additional channels that could yield possible discoveries in future LHC runs. The most promising channel for H would be production either indirectly via $gg \to A \to ZH$ or directly via $gg \to H$, with the subsequent decay of $H \to hh \to b\bar{b}b\bar{b}$. Upper bounds on the former have been reported by the ATLAS Collaboration in Ref. [39], whereas upper

$\sigma(gg \to H)$ (pb)	0.65
$\sigma(gg \to b\bar{b}H)$ (pb)	1.9×10^{-3}
BR($H \to ZZ$)	0.0053
BR($H \to b\bar{b}$)	0.47
BR($H \to \tau^+\tau^-$)	0.053
BR($H \to hh$)	0.023
BR($H \to gg$)	0.41
Γ_H (GeV)	7×10^{-4}

$\sigma(gg \to A)$ (pb)	0.18
$\sigma(gg \to b\bar{b}A)$ (pb)	6.9×10^{-5}
BR($A \to ZH$)	0.94
BR($A \to t\bar{t}$)	0.057
BR($A \to b\bar{b}$)	1.9×10^{-5}
BR($A \to \tau^+\tau^-$)	2.0×10^{-6}
BR($A \to H^\pm W^\mp$)	0
Γ_A (GeV)	31.99

Table 8.3: Production cross sections and relevant decay branching ratios for H and A in benchmark B1a.

$\sigma(gg \to tbH^\pm)$ (pb)	0.0078
BR($H^\pm \to tb$)	0.040
BR($H^\pm \to \tau^\pm\nu$)	2.0×10^{-6}
BR($H^\pm \to HW^\pm$)	0.96
$\Gamma_{H^\pm}$ (GeV)	45.39

Table 8.4: Production cross sections and relevant decay branching ratios for $H^\pm$ in benchmark B1a.

bounds on the latter have been presented by the ATLAS and CMS Collaborations based on their resonant diHiggs searches [31,63–65]. The most promising alternative channels for A would be production via gluon fusion, with the subsequent decay to $ZH \to \ell^+\ell^- b\bar{b}$ or to $t\bar{t}$. Finally, the most promising channel for $H^\pm$ would be via tb associated production, with the subsequent decay to $HW^\pm$. Upper bounds for this process have already been established in Ref. [66].

To emphasize the difference between the Type-I 2HDM and a generic A2HDM, we present a second benchmark in Table 8.5. For the benchmark parameters shown in Table 8.5, the main production cross sections and some of the relevant branching ratios for H, A and $H^\pm$ are exhibited in Tables 8.6 and 8.7.

Benchmark B1b – generic A2HDM							
$m_{H^\pm}$ (GeV)	$\lvert\cos(\beta-\alpha)\rvert$	Z_2	Z_3	Z_7	a^U	a^D	a^E
600	0.013	1.51	9.79	−0.20	0.20	1.75	3.50

Table 8.5: Parameters characterizing Benchmark B1b, for which $m_h = 125$, $m_A = 610$ and $m_H = 290$ GeV.

The results of Tables 8.6 and 8.7 suggest a number of additional channels that could yield possible discoveries in future LHC runs. In addition to $gg \to A \to ZH$ and $gg \to H$, where $H \to hh \to b\bar{b}b\bar{b}$, as previously mentioned, it may be possible to detect $gg \to b\bar{b}H$ followed by $H \to b\bar{b}$, which would also yield a $b\bar{b}b\bar{b}$ final state but with different kinematics. The most promising alternative channel for A would be production via gluon fusion,with the subsequent decay to $t\bar{t}$, since there is no longer kinematic access to $H^\pm W^\mp$. Finally, the most promising channel for $H^\pm$ would again be via tb associated production, with the subsequent decay to $HW^\pm$.

$\sigma(gg \to H)$ (pb)	0.40
$\sigma(gg \to b\bar{b}H)$ (pb)	0.096
BR($H \to ZZ$)	0.015
BR($H \to b\bar{b}$)	0.61
BR($H \to \tau^+\tau^-$)	0.28
BR($H \to hh$)	0.053
Γ_H (GeV)	0.027

$\sigma(gg \to A)$ (pb)	0.11
$\sigma(gg \to b\bar{b}A)$ (pb)	0.0034
BR($A \to ZH$)	0.96
BR($A \to t\bar{t}$)	0.036
BR($A \to b\bar{b}$)	9.47×10^{-4}
BR($A \to \tau^+\tau^-$)	4.95×10^{-4}
Γ_A (GeV)	31.31

Table 8.6: Production cross sections and relevant decay branching ratios for H and A in benchmark B1b.

$\sigma(gg \to tbH^\pm)$ (pb)	0.0069
BR($H^\pm \to tb$)	0.035
BR($H^\pm \to \tau^\pm\nu$)	5.18×10^{-4}
BR($H^\pm \to HW^\pm$)	0.96
$\Gamma_{H^\pm}$ (GeV)	29.38

Table 8.7: Production cross sections and relevant decay branching ratios for $H^\pm$ in benchmark B1b.

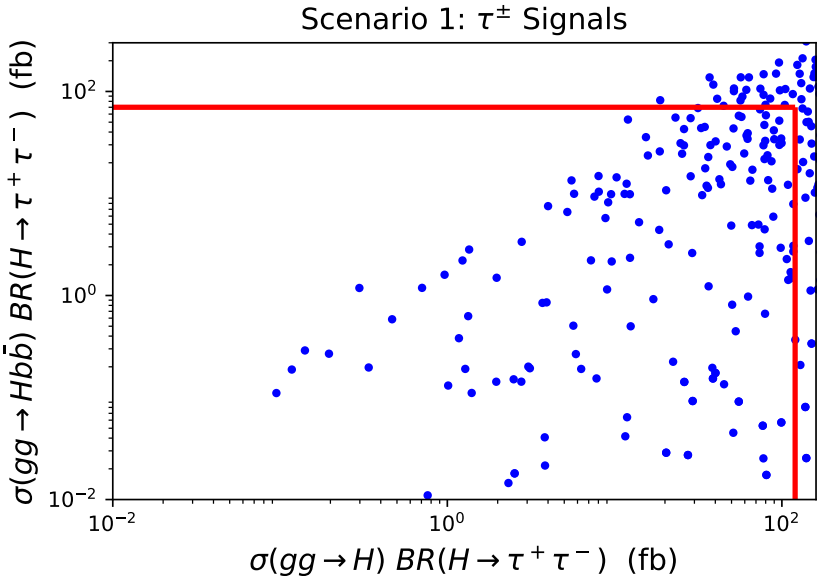

(a)

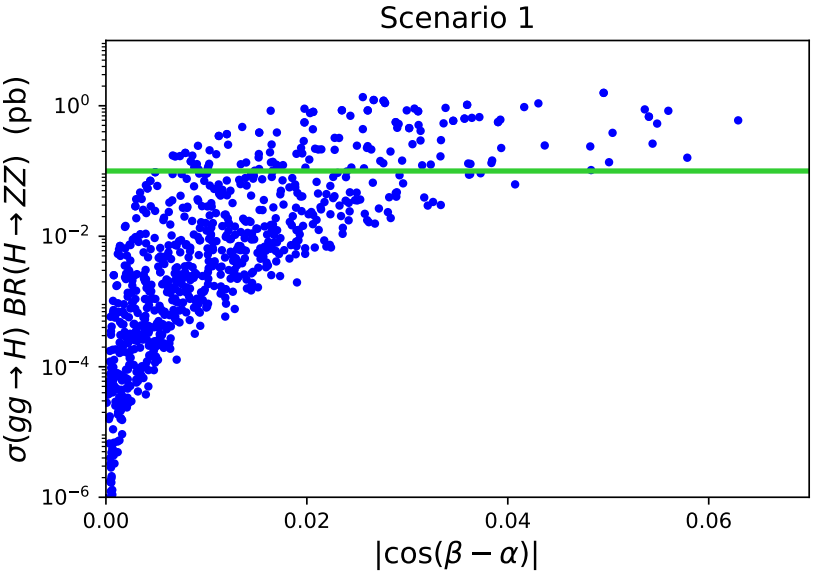

(b)

Figure 8.5: Results of a scan over A2HDM parameter points in Scenario 1 that satisfy the theoretical and experimental constraints elucidated in Section 7 and the constraints of Eqs. (8.1)–(8.4). Panel (a) shows the cross sections for gluon fusion production and b-associated production of H multiplied by BR($H \to \tau^+\tau^-$), and panel (b) shows $\sigma(gg \to H) \times \text{BR}(H \to ZZ)$ as a function of $|\cos(\beta - \alpha)|$. The vertical and horizontal red lines shown in panel (a) correspond to the 1σ exclusion limit (for $m_H = 300$ GeV) exhibited in Eqs. (8.8) and (8.9), respectively [29]. The blue points in panel (b) correspond to the points in panel (a) that lie below the red horizontal line and to the left of the red vertical line, and the horizontal green line shown in panel (b), which corresponds to Eq. (8.10), reflects the 95% CL upper bound reported in Ref. [57].

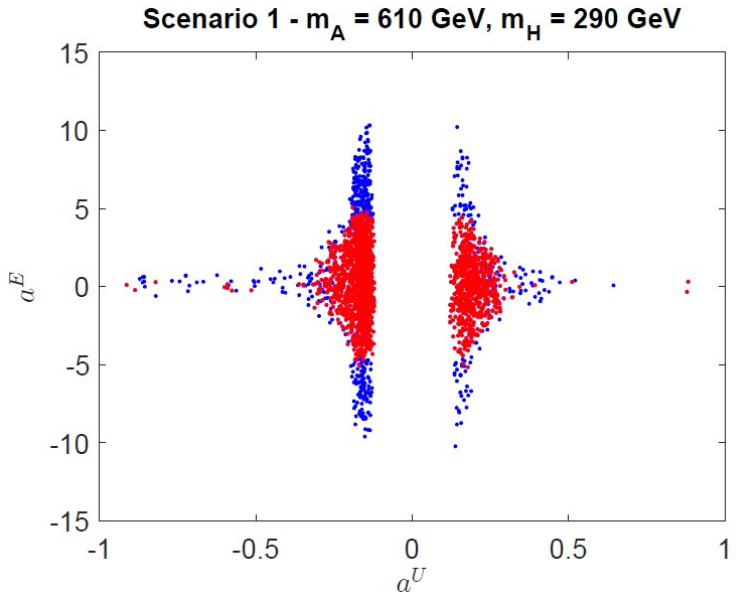

(a)

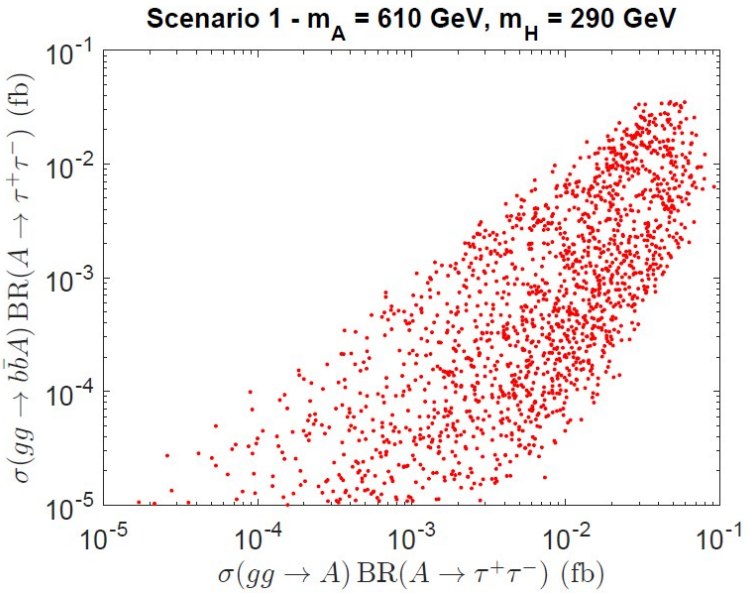

(b)

Figure 8.6: Results of a scan over A2HDM parameter points in Scenario 1 that satisfy the theoretical and experimental constraints elucidated in Section 7 and the constraints of Eqs. (8.1)–(8.4). The values of the flavor-alignment parameters a^E and a^U are then plotted as blue points in panel (a). The red points of panel (a) correspond to those that survive the additional constraints of Eqs. (8.8)–(8.10). The values of the cross sections for gluon fusion production and b-associated production of A multiplied by $\mathrm{BR}(H \to \tau^+\tau^-)$, subject to the same constraints as the red points of panel (a), are plotted as red points in panel (b).

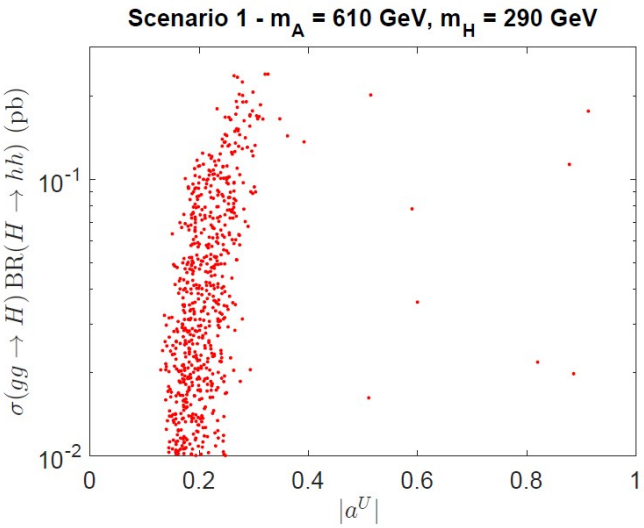

(a)

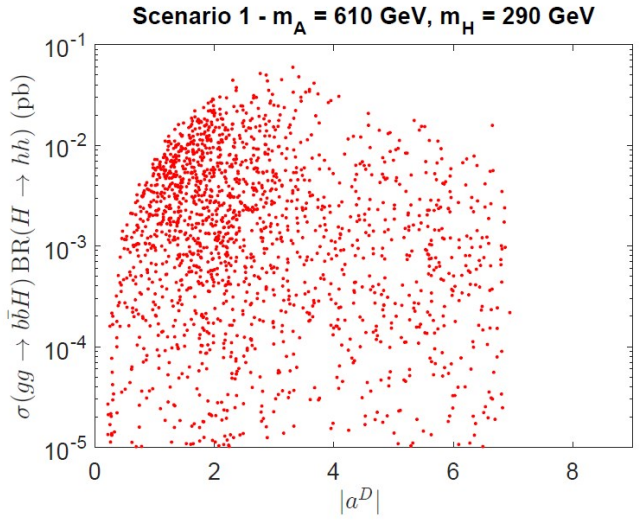

(b)

Figure 8.7: Results of a scan over A2HDM parameter points in Scenario 1 that satisfy the theoretical and experimental constraints elucidated in Section 7 and the constraints of Eqs. (8.1)–(8.4) and Eqs. (8.8)–(8.10). In panel (a) the values of the cross section for gluon fusion production of H multiplied by $\mathrm{BR}(H \to hh)$ are plotted as a function of $|a^U|$. In panel (b), the values of the cross section for b-associated production of H multiplied by $\mathrm{BR}(H \to hh)$ are plotted as a function of $|a^D|$.

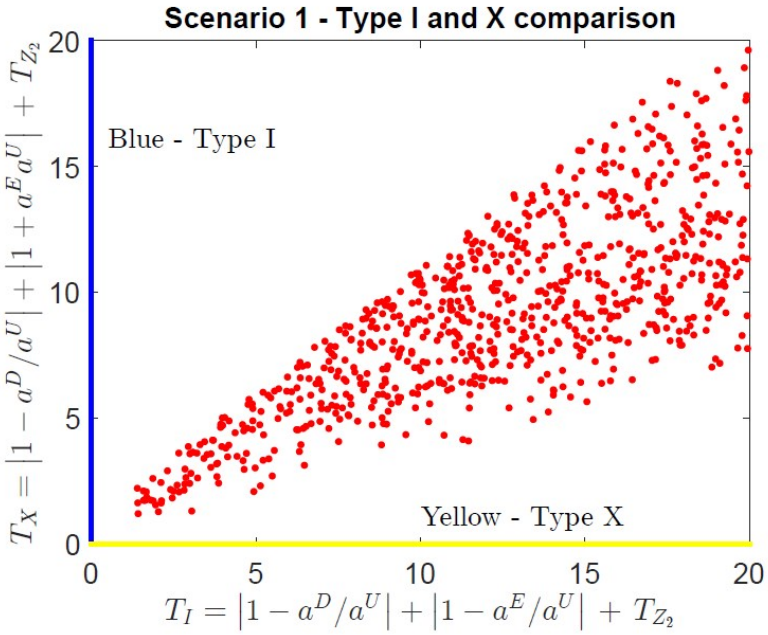

(a)

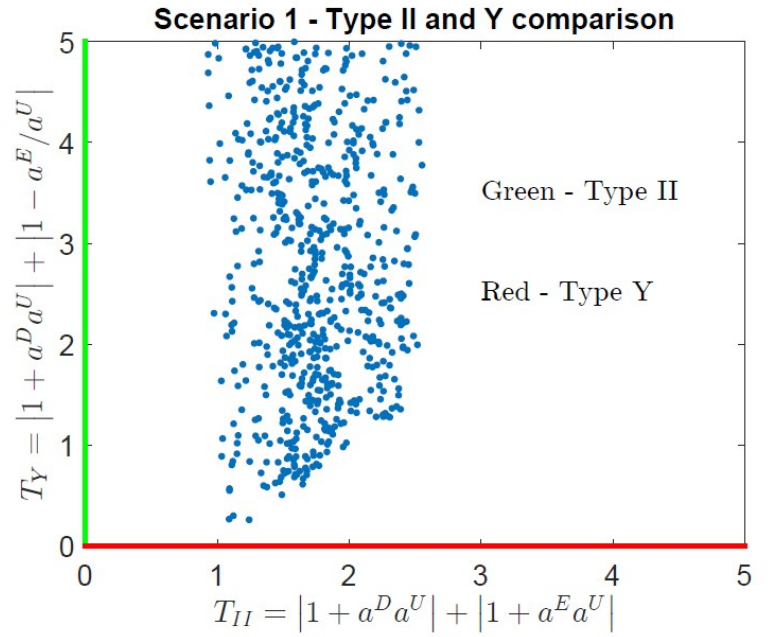

(b)

Figure 8.8: Results of a scan over A2HDM parameter points in Scenario 1 that satisfy the theoretical and experimental constraints elucidated in Section 7 and the constraints of Eqs. (8.1)–(8.4) and Eqs. (8.8)–(8.10). We plot the valuesof T_I vs. T_X ($T_I I$ vs. T_Y) for all surviving scan points. Points that lie along the horizontal yellow (red) axis would be consistent with a Type-X(Y) 2HDM. Points that lie along the vertical blue (green) axis would be consistent with a Type-I(II) 2HDM.

Chapter 9

Scenario 2: $m_A = 400$ GeV

For Scenario 2 we consider the CP-conserving 2HDM with a CP-odd scalar mass of $m_A = 400$ GeV and two CP-even scalars with masses $m_H > 450$ GeV and $m_h = 125$ GeV (where h is identified as the Higgs boson observed in LHC data). This scenario is motivated by a slight excess of events over the expected backgrounds in the ATLAS search for resonant $\tau^+\tau^-$ production and in the CMS search for resonant $t\bar{t}$ production due to the production and the subsequent decay of a heavy neutral scalar. The ATLAS Collaboration observes an excess of events in both gluon fusion and in b-associated production of a heavy scalar (where the CP quantum number is not determined). Although the CMS Collaboration observes no excess in a similar search, there remains some room for the ATLAS excess that is not yet excluded at the 95% CL by the CMS Collaboration, as discussed below Eq. (6.2). Meanwhile, the CMS Collaboration reports an excess of $t\bar{t}$ pairs that are interpreted as the gluon fusion production of $A \to t\bar{t}$ (in which an alternative interpretation of $H \to t\bar{t}$ is excluded). As both data excesses are associated with the production of a scalar of mass 400 GeV, we shall assume that the scalar associated with the ATLAS excess is CP-odd. The CP-even scalar is taken to be heavier, $m_H > 450$ GeV to avoid the

possibility for it to contribute to the ATLAS $\tau^+\tau^-$ excess. Note that this scenario is completely orthogonal to Scenario 1 since the decay $A \to ZH$ is kinematically excluded. The possibility of $m_H < 350$ GeV is less likely to survive the constraints of our model scans, and hence we discard this option in what follows.

9.1 A2HDM Interpretation for Scenario 2

We have performed a scan of the A2HDM parameter space for Scenario 2, while respecting the theoretical and experimental constraints elucidated in Section 7. To determine the range of interest for the flavor-alignment parameter a^U, we exhibit in Fig. 9.1 the width to mass ratio, Γ_A/m_A, as a function of a^U and consider the implications of the excess of $t\bar{t}$ events reported by the CMS Collaboration in Ref. [30], which are interpreted as the production of $A \to t\bar{t}$ via gluon fusion. The blue points of Fig. 9.1 represent the results of our scan prior to imposing the constraints of the $A \to t\bar{t}$ constraints of Ref. [30]. (We can identify the coupling modifier $g_{At\bar{t}}$ of Ref. [30] with a^U.) The CMS Collaboration expected to obtain a 95% CL upper limit on the gluon fusion production of $A \to t\bar{t}$ for $m_A = 400$ GeV, which when translated into a limit on a^U yields the solid black line shown in Fig. 9.1. However, due to an excess of events above background (with a local significance of 3.5σ), the actual 95% CL upper limit on the gluon fusion production of $A \to t\bar{t}$ translated into a limit on a^U yields the dashed cyan line shown in Fig. 9.1. The points in our scan that lie between the black and cyan lines (colored red) will be the parameter points of interest for Scenario 2 going forward.

A more sophisticated approach was undertaken in Ref. [42], in which a chi-squared analysis was performed to determine the best fit value for the A coupling

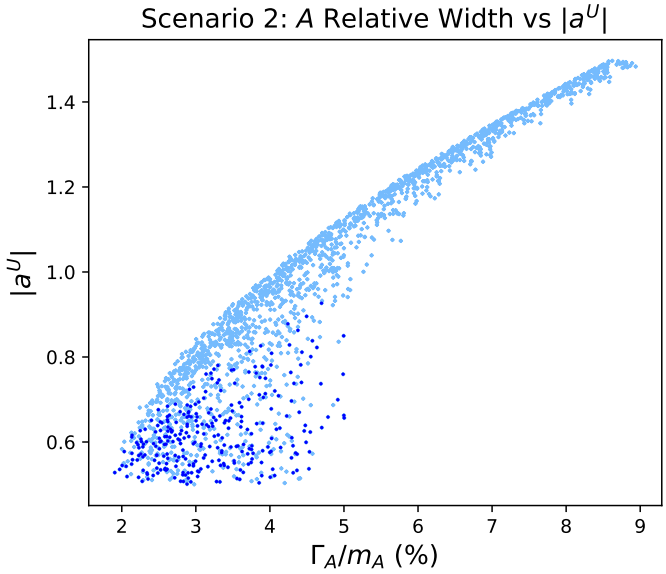

Figure 9.1: The ratio of the A width to its mass (with $m_A = 400$ GeV) as a function of the flavor-alignment parameter a^U in Scenario 2 obtained in a scan over A2HDM parameters, subject to the theoretical and experimental constraints elucidated in Section 7. The dashed cyan (solid black) line shows the observed (expected) 95% CL upper limit on the gluon fusion cross section for $A \to t\bar{t}$ reported by the CMS Collaboration in Ref. [30], translated into an upper limit for a^U as a function of Γ_A/m_A. The points of the scan that lie between the dashed cyan and solid black curve are colored red, which constitute the proposed signal of Scenario 2.

modifier to top quarks for each value of the A width. The chi-squared analysis of Ref. [42] only considered the CMS data excess in the $t\bar{t}$ channel [30], whereas we wish to consider the implications of this data excess together with the ATLAS data excess in the $\tau^+\tau^-$ channel [29]. Nevertheless, we have verified that the red points chosen in our Fig. 9.1 have $\chi^2_{t\bar{t}} \lesssim 5$, for the definition of $\chi^2_{t\bar{t}}$ given in Ref. [42] and the results shown in their Fig. 1. Moreover, a substantial portion of the red points of our Fig. 9.1 have values of $\chi^2_{t\bar{t}}$ well below 1.

Imposing the upper limit of $|\Delta M_{B_s}|$ as discussed in Section 3.5 on the A2HDM parameter space when scanned over the values exhibited in Table 7.1, we have found no constraint on the alignment parameters a^D and a^E (of course, the latter does not appear in Eq. (3.27)). However, we do find an upper bound for $|a^U|$

shown in panel (a) of Fig. 9.2. Note that the excluded region of the A2HDM parameter space due to the constraint on ΔM_{B_s} roughly coincides with the corresponding excluded region of the Type-I 2HDM in the $m_{H^\pm}$ vs. $\tan\beta$ plane exhibited in Fig. 8 of Ref. [51] after identifying $\tan\beta = 1/|a^U|$. This result is not surprising in light of the small numerical contribution from terms that depend on a^D.

In panel (b) of Fig. 9.2, we show the result of Fig. 9.1 prior to imposing the constraint from ΔM_{B_s}. The red, green and blue points are all consistent with the $b \to s\gamma$ constraint. Imposing the experimental constraint based on the 95% CL upper limit on the cross section for $gg \to A \to t\bar{t}$ reported by the CMS Collaboration in Ref. [30], we can eliminate the scan points that lie above the dashed cyan line. Finally, the result of imposing the ΔM_{B_s} constraint is to remove the green points from the scan. The remaining red scan points constitute the proposed signal of Scenario 2 .

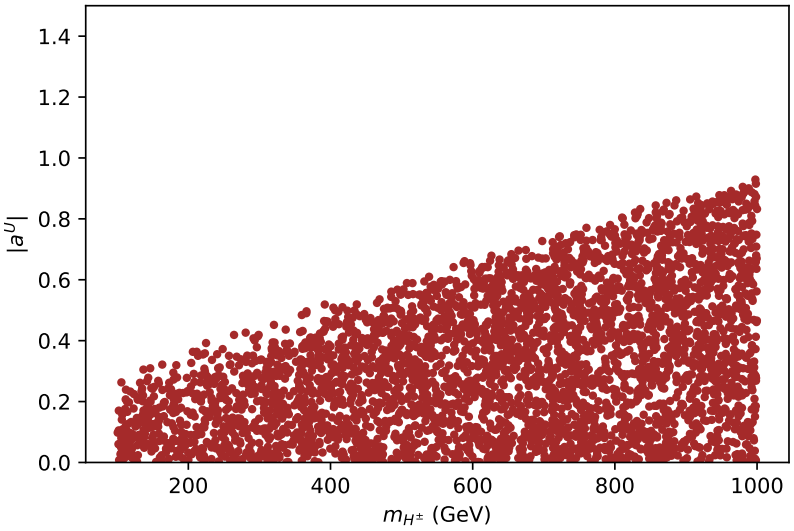

(a)

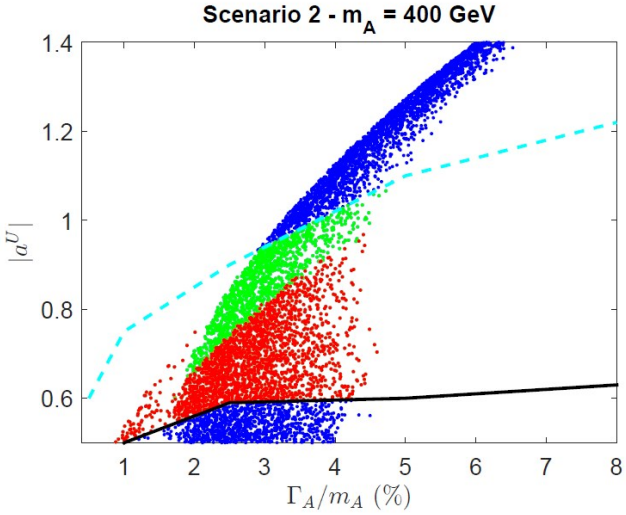

(b)

Figure 9.2: Impact of the ΔM_{B_s} bound on the A2HDM parameter space. In panel (a) all points shown are from a general scan on a^U, a^D and $m_{H^\pm}$ which pass the ΔM_{B_s} bound. In panel (b) we exhibit the ratio of the A width to its mass (with $m_A = 400$ GeV) as a function of the alignment parameter a^U in Scenario 2 obtained in a scan over A2HDM parameters, subject to the theoretical and experimental constraints elucidated in Section 7 prior to imposing the ΔM_{B_s} bound. The dashed cyan (solid black) line correspond to the observed (expected) 95% CL upper limit on the cross section for $gg \to A \to t\bar{t}$ reported by the CMS Collaboration in Ref. [30], translated into an upper limit for a^U as a function of Γ_A/m_A. As for the remaining scan points that lie between the dashed cyan and solid black curve, the green points are eliminated after imposing the ΔM_{B_s} constraint. The surviving red scan points constitute the proposed signal of Scenario 2.

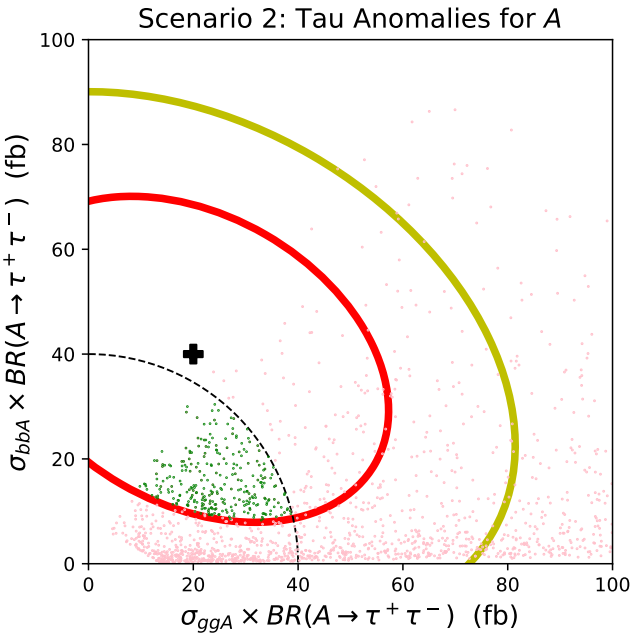

Figure 9.3: Results of a scan over A2HDM parameter points in Scenario 2 that satisfy the theoretical and experimental constraints elucidated in Section 7. The blue points exhibit the values of the cross sections for gluon fusion production and b-associated production of A multiplied by BR($H \to \tau^+\tau^-$). These points are colored red if the corresponding values of a^U and Γ/m_A lie in the red region of Fig. 9.1. The + indicates the best fit point for the ATLAS excess of Ref. [28] interpreted as A production with $m_A = 400$ GeV; the solid yellow and black curves correspond to the corresponding 1σ and 2σ contours. Red points within the 1σ contour are colored green. Finally, all points outside the boundary of the dashed black ellipse are excluded at the 95% CL by the ditau search of the CMS Collaboration [31].

Employing the same A2HDM scan described above, we consider the implications of the ATLAS ditau signal excess interpreted as the production of a CP-odd scalar with $m_A = 400$ GeV. In Fig. 9.3, the best fit point for the ATLAS excess of Ref. [28] is indicated by the + sign; the solid yellow and black curves correspond to the corresponding 1σ and 2σ contours. The nonobservation of the ditau signal by the CMS collaboration [31] excludes (at the 95% CL) values of the A production cross section multiplied by BR($A \to \tau^+\tau^-$) that lie outside the boundary of the dashed black ellipse. The dashed black contour exhibited in Fig. 9.3 was obtained from the results of Ref. [31] by interpolation as explained above Eq. (6.3). The blue points of

our initial scan are constrained to lie within the red region of Fig. 9.1 as discussed above. These points are colored red in Fig. 9.3. In addition, the green points are a subset of the red points that lie within the 1σ contour. Finally, the green points that lie within the dashed black ellipse in the lower left hand corner of Fig. 9.3 constitute the A2HDM parameter regime of interest for Scenario 2. Note that despite of the more restrictive CMS exclusion limits, there are still a significant number of green scan points for Scenario 2 that lie within the 1σ ellipse of the ATLAS ditau data excess. The sharp lower bound $\sigma(gg \to A) \times \text{BR}(A \to \tau^+\tau^-) \gtrsim 19$ fb exhibited by the green points of Fig. 9.3 is noteworthy. This lower bound is a consequence of requiring $|a^U| \gtrsim 0.5$, so as to be above the solid black line in Fig. 9.1 (in order to explain the observed CMS excess of $A \to t\bar{t}$), while also imposing $|a^E| \gtrsim 4.9$ (as illustrated in Fig. 9.5 below) in order that our scan points live within the 1σ ellipse of Fig. 9.3. In particular, the lower bound on $|a^U|$ forces $\sigma(gg \to A)$ to be roughly above 7.1 pb, whereas the lower bound on $|a^E|$ yields a minimum branching ratio of $\text{BR}(A \to \tau^+\tau^-) \gtrsim 1.2 \times 10^{-3}$. Although these considerations omit the implications of scanning over a^D, they do provide a rough understanding of the lower bound on $\sigma(gg \to A \to \tau^+\tau^-)$ observed in Fig. 9.3.

In order to achieve a large enough rate in b-associated production of A that subsequently decays into $\tau^+\tau^-$, a sufficiently large absolute value of the flavor-alignment parameter a^D will be required, which will tend to enhance the $A \to b\bar{b}$ decay rate. The most restrictive bounds on $\sigma(gg \to b\bar{b}A) \times \text{BR}(A \to b\bar{b})$ are provided by the CMS Collaboration [67], with a 95% CL upper limit of roughly 6 pb for $m_A = 400$ GeV. As shown in Fig. 9.4, this latter constraint eliminates a substantial region of the A2HDM parameter space for Scenario 2 and yields an upper bound of $|a_D| \lesssim 40$. In Fig. 9.4 (b) we show the predicted values of $\sigma(gg \to b\bar{b}H) \times \text{BR}(H \to b\bar{b})$ as

a function of m_H, and we compare these values with the 95% CL upper limit from the CMS Collaboration in Ref. [67], obtained with 35.9 fb^{-1} of data and shown as a solid black line in that plot. As we see, a very small set of our points are already excluded. The dashed line shown corresponds to a *naïve* rescaling (by the square root of the corresponding luminosities) of the current CMS bound based on the full Run 2 dataset and an anticipated 300 fb^{-1} of data during Run 3 of the LHC. Indeed, we expect that a substantial portion of the parameter space for Scenario 2, with H masses up to 700 GeV, could be probed in Run 3.

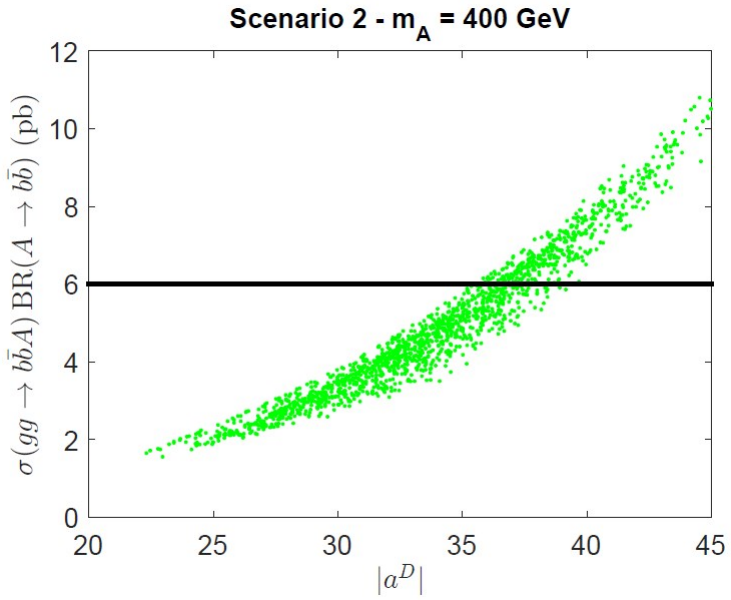

(a)

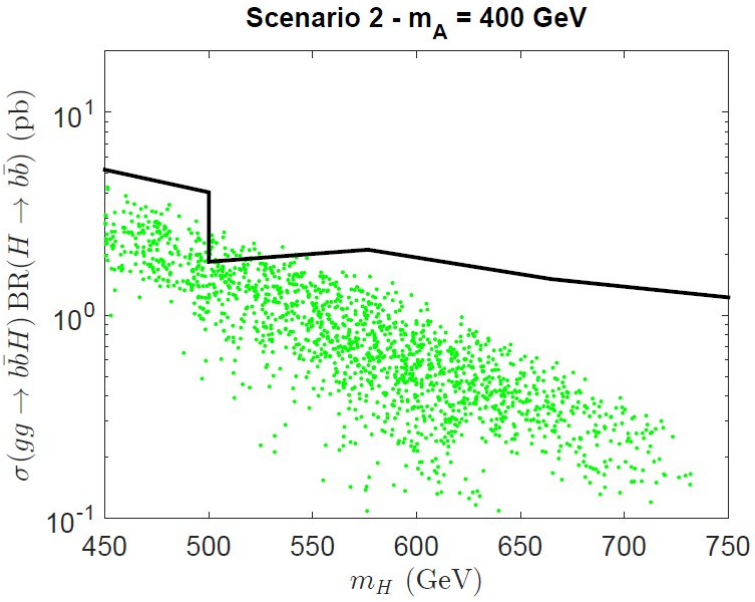

(b)

Figure 9.4: Results of a scan over A2HDM parameter points in Scenario 2 that satisfy the theoretical and experimental constraints elucidated in Section 7. The points shown are the subset of the green points of Fig. 9.3 that are contained within the dashed ellipse shown there. We exhibit (a) the predicted values of $\sigma(gg \to b\bar{b}A) \times \mathrm{BR}(A \to b\bar{b})$ as a function of $|a^D|$, and (b) the predicted values of $\sigma(gg \to b\bar{b}H) \times \mathrm{BR}(H \to b\bar{b})$ as a function of m_H. Points that lie above the solid line are excluded by the 95% CL upper limit obtained by the CMS Collaboration in Ref. [67]. The dashed black line is the expected exclusion at Run 3 of the LHC.

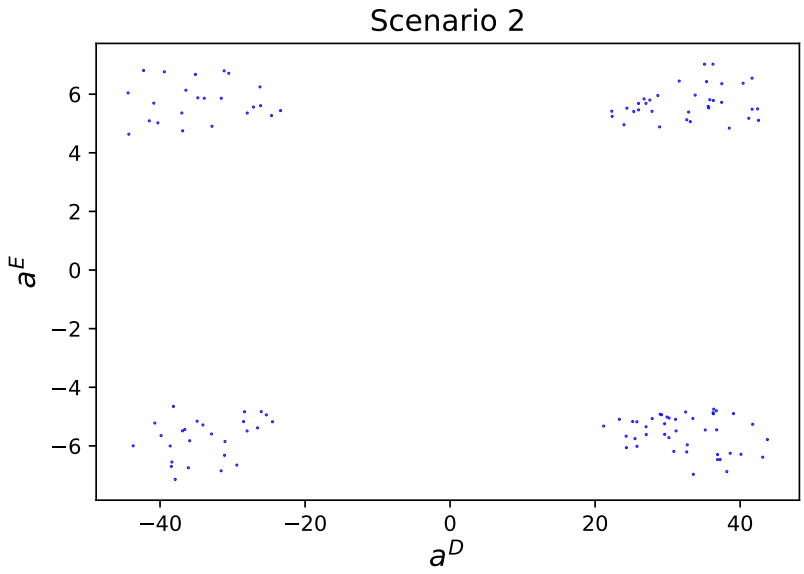

(a)

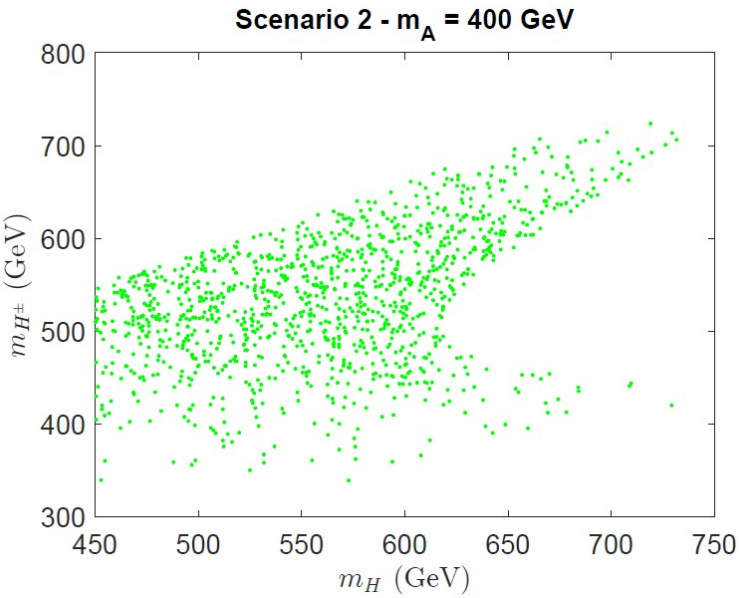

(b)

Figure 9.5: Results of a scan over A2HDM parameter points in Scenario 2 that lie within the region of interest, corresponding to the area of parameter space occupied by the subset of green points that lie inside the rectangular box in Fig. 9.3 and below the dashed line in Fig. 9.4. Panel (a) exhibits the values of the flavor-alignment parameters a^E and a^D and panel (b) exhibits the masses of the heavier CP-even scalar H and the charged Higgs boson $H^\pm$, for each scan point that satisfies all the specified constraints.

We now examine in more detail the properties of the green A2HDM scan points that lie within the dashed black ellipse of Fig. 9.3 and below the solid black lines of Fig. 9.4, which satisfy all known experimental limits while interpreting the ATLAS ditau excess and the CMS $t\bar{t}$ excess as the production of a CP-odd scalar with $m_A \sim 400$ GeV, which from now on we call the "*region of interest*."

In Fig. 9.5, we show in panel (a) the values of the flavor-alignment parameters a^E and a^D and in panel (b) we show the values of m_H and $m_{H^\pm}$ for the A2HDM scan points that satisfy all the specified constraints. Note that the values of $|a^D|$ and $|a^E|$ are restricted to lie within a very narrow range of values, $25 \lesssim |a^D| \lesssim 40$ and $5 \lesssim |a^E| \lesssim 7$. The corresponding lower limiting values are a consequence of the $gg \to b\bar{b}A \to b\bar{b}\tau^+\tau^-$ interpretation of ATLAS excess of Ref. [29]. The upper limit on $|a^D|$ is imposed by the solid black lines of Fig 9.4 and the upper limit on $|a^E|$ is due in part to our $gg \to A \to t\bar{t}$ interpretation of the CMS excess of Ref. [30]. In Fig. 9.5(b), two distinct branches are observed corresponding to $m_H \sim m_A$ and $m_{H^\pm} \sim m_A$, which arise after imposing the T parameter constraint, as discussed in Section 7. Although we scan over h and $H^\pm$ masses up to 1 TeV, we find no scan points above about 750 GeV. This is a consequence of the tree-level unitarity and perturbativity constraints of Section 7 that limit the magnitude of the heavy scalar mass splittings.

Although the proposed Scenario 2 signals are viable in the A2HDM framework, one can again ask whether the same signals can be successfully accommodated in two Higgs doublet models with natural flavor conservation. In Section 8 we introduced four quantities, $T_{I,II,X,Y}$ [cf. Eqs. (8.16) and (8.17)], which if zero would indicate the presence of a (softly-broken) $\mathbb{Z}_2$ symmetry with a Type I, II, X or Y Yukawa coupling pattern. In contrast to Scenario 1, where a Type-I 2HDM pro-

vided a viable framework for the interpretation of the ATLAS excess of Ref. [27], the Scenario 2 signals are incompatible with a Type I, II, X or Y Yukawa coupling pattern, as indicated by the two panels of Fig. 9.6.

If the Scenario 2 interpretation of the ATLAS and CMS excesses of Refs. [29] and [30], respectively, were corroborated by further data, then one could make predictions for the eventual discoveries of H and $H^\pm$. Indeed, some of the scan points of the Scenario 2 region of interest are not too far from the current exclusion limits derived from ATLAS searches for H production (with subsequent decay to $\tau^+\tau^-$) and $H^\pm$ production (with subsequent decay to tb), as exhibited in Fig. 9.7). In panel (a) of Fig. 9.7, we show that the Scenario 2 scan points in the region of interest reside about a factor of 10 below the 95% CL exclusion limits for $\sigma(gg \to H)\mathrm{BR}(H \to \tau^+\tau^-)$ obtained by the ATLAS Collaboration [29]. In panel (b), we show that some of the Scenario 2 scan points in the region of interest lie quite close to the 95% CL exclusion limits for $\sigma(pp \to H^\pm)\mathrm{BR}(H^\pm \to tb)$ obtained by the ATLAS Collaboration in Ref. [68]. We expect that future LHC searches for $H \to \tau^+\tau^-$ and $H^\pm \to tb$ with larger data sets will begin to probe the Scenario 2 region of interest and thus provide the most likely channels for new discoveries.

We have also checked that the ATLAS and CMS exclusion limits on H production with subsequent decays into ZZ, W^+W^-, $\gamma\gamma$, or hh and $H^\pm$ production with subsequent decays into $\tau\nu$ are less constraining and easily satisfied by all the Scenario 2 scan points in the region of interest.

9.2 A2HDM Benchmark for Scenario 2

We present one benchmark for Scenario 2 in Table 9.1, chosen to illustrate an A2HDM parameter set with significant H and A production cross sections, which would provide additional heavy scalar discovery channels that could be probed in future runs at the LHC. In light of the results of Fig. 9.6, there are no viable A2HDM parameter sets that approximate a Type-I, II, X or Y 2HDM. For the benchmark parameters shown in Table 9.1, the main production cross sections and some of the relevant branching ratios for H, A and $H^{\pm}$ are exhibited in Tables 9.2 and 9.3. We do not exhibit the Benchmark B2 values of $\mathrm{BR}(H \to ZZ) \simeq 4 \times 10^{-6}$ and $\mathrm{BR}(H \to hh) \simeq 10^{-7}$, which are too small to be phenomenologically relevant.

Benchmark B2 – generic A2HDM								
m_H	$m_{H^{\pm}}$ (GeV)	$\lvert\cos(\beta-\alpha)\rvert$	Z_2	Z_3	Z_7	a^U	a^D	a^E
492	529	0.0018	2.42	7.58	-1.39	0.60	35.07	6.32

Table 9.1: Parameters characterizing Benchmark B2, for which $m_h = 125$, $m_A = 400$ GeV.

$\sigma(gg \to H)$ (pb)	2.57
$\sigma(gg \to b\bar{b}H)$ (pb)	3.30
$\mathrm{BR}(H \to b\bar{b})$	0.69
$\mathrm{BR}(H \to \tau^+\tau^-)$	0.0028
$\mathrm{BR}(H \to t\bar{t})$	0.31
Γ_H (GeV)	14.54

$\sigma(gg \to A)$ (pb)	10.87
$\sigma(gg \to b\bar{b}A)$ (pb)	8.97
$\mathrm{BR}(A \to t\bar{t})$	0.39
$\mathrm{BR}(A \to b\bar{b})$	0.60
$\mathrm{BR}(A \to \tau^+\tau^-)$	0.0024
Γ_A (GeV)	13.94

Table 9.2: Production cross sections and relevant decay branching ratios for H and A in benchmark B2.

The results of Tables 9.2 and 9.3 suggest a number of additional channels that could yield possible discoveries in future LHC runs. The most promising channels for H would be via gluon fusion production and/or b-associated production

$\sigma(gg \to tbH^{\pm})$ (pb)	0.19
BR($H^{\pm} \to tb$)	0.90
BR($H^{\pm} \to \tau^{\pm}\nu$)	0.0023
BR($H^{\pm} \to AW^{\pm}$)	0.095
$\Gamma_{H^{\pm}}$ (GeV)	19.05

Table 9.3: Production cross sections and relevant decay branching ratios for $H^{\pm}$ in benchmark B2.

followed by $H \to b\bar{b}$ or $t\bar{t}$. Note that although the $\tau^+\tau^-$ branching ratio is quite small, $\sigma(gg \to b\bar{b}H) \times \text{BR}(H \to \tau^+\tau^-) \sim 10$ fb, which will be probed in future runs at the LHC with a sufficiently large data sample (in light of Ref. [29]). In addition to $gg \to A \to \tau^+\tau^-$, $gg \to b\bar{b}A \to b\bar{b}\tau^+\tau^-$, and $gg \to A \to t\bar{t}$ (which constitute the current excesses in data that define Scenario 2), it may be possible to detect $gg \to b\bar{b}A \to b\bar{b}b\bar{b}$ and $gg \to b\bar{b}A \to b\bar{b}t\bar{t}$. Finally, the most promising channel for $H^{\pm}$ would be via tb associated production, with the subsequent decay to either tb or $AW^{\pm}$.

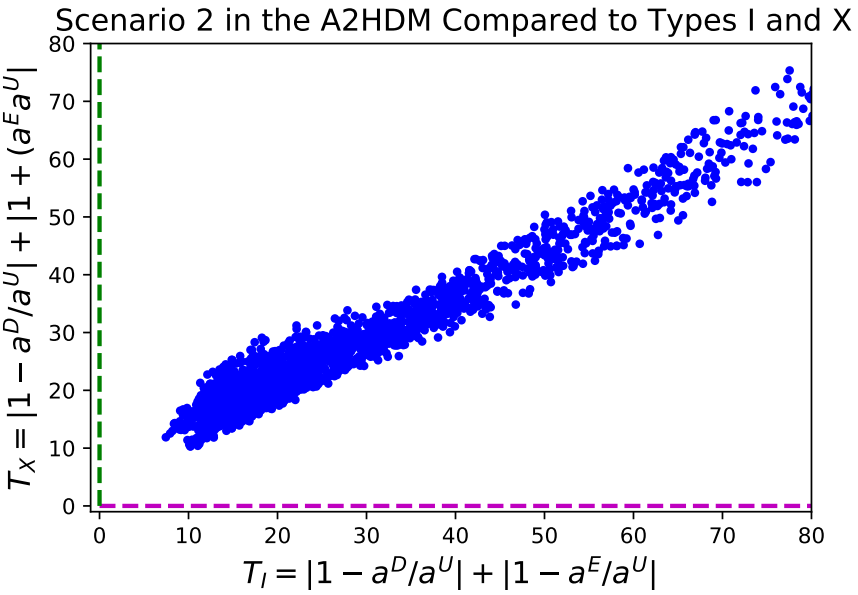

(a)

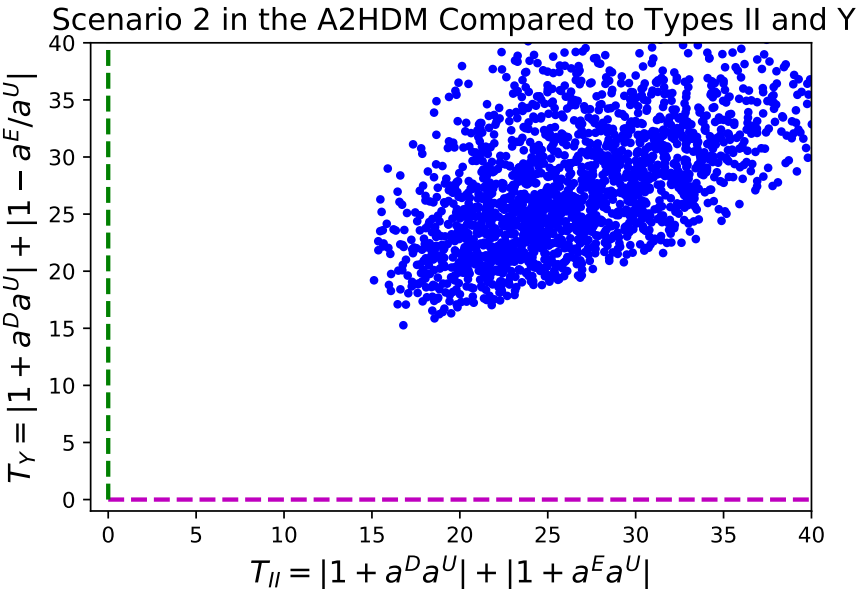

(b)

Figure 9.6: Results of a scan over A2HDM parameter points in Scenario 2 that lie within the region of interest, corresponding to the area of parameter space occupied by the subset of green points that lie inside the circle in Fig. 9.3 and below the solid black lines in Fig. 9.4. Panel (a) exhibits the values of T_I vs. T_X. Points that lie along the horizontal (magenta) axis would be consistent with a Type-X 2HDM. Points that lie along the vertical (green) axis would be consistent with a Type-I 2HDM. Panel (b) exhibits the values of T_{II} vs. T_Y. Points that lie along the horizontal (magenta) axis would be consistent with a Type-Y 2HDM. Points that lie along the vertical (green) axis would be consistent with a Type-II 2HDM.

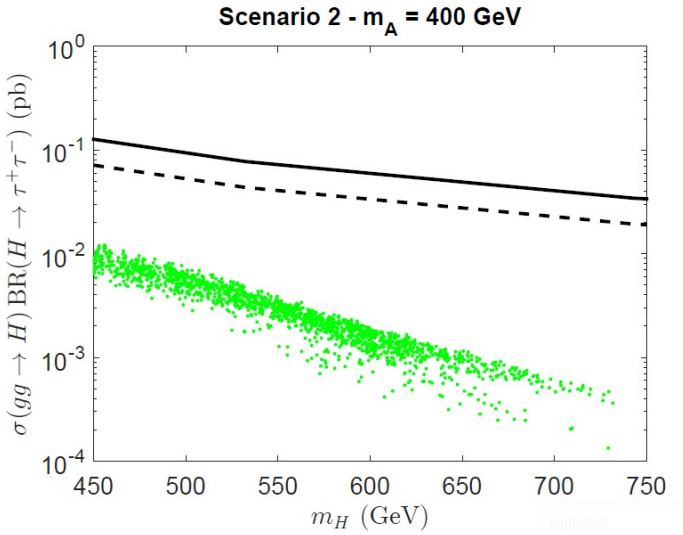

(a)

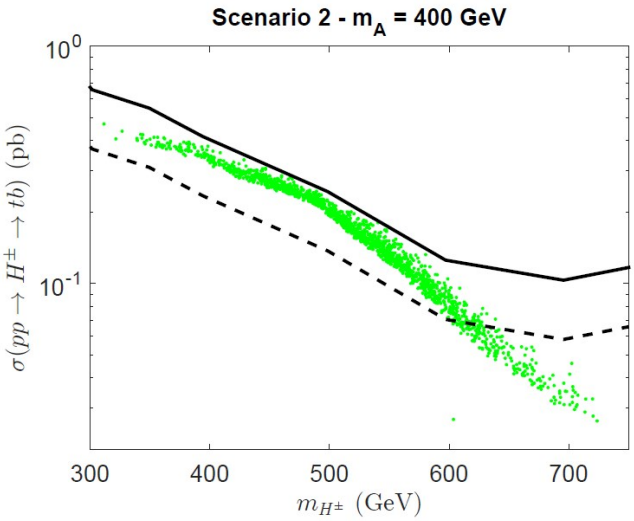

(b)

Figure 9.7: Results of a scan over A2HDM parameter points in Scenario 2 that lie within the region of interest, corresponding to the area of parameter space occupied by the subset of green points that lie inside the rectangular box in Fig. 9.3 and below the solid black lines in Fig. 9.4. In panel (a), we show the predicted value of $\sigma(gg \to H)\mathrm{BR}(H \to \tau^+\tau^-)$ as a function of m_H. The solid black line corresponds to the 95% CL exclusion limit reported by the ATLAS Collaboration in Ref. [29]. In panel (b), we show the predicted value of $\sigma(pp \to tbH^\pm)\mathrm{BR}(H^\pm \to tb)$ as a function of $m_{H^\pm}$ as a function of $m_{H^\pm}$. The solid black line corresponds to the 95% CL exclusion limit reported by the ATLAS Collaboration in Ref. [68]. The solid black lines shown in both plots above are based on 139 fb^{-1} of data. Assuming an additional 300 fb^{-1} of data during Run 3 of the LHC, a *naïve* rescaling of the ATLAS exclusion bounds yields the dashed black lines shown in both plots.

Chapter 10

Conclusions of Part II

If new scalars exist with masses below 1 TeV with cross sections governed by the electroweak scale, then searches now being performed at the LHC would be capable of discovering such states given sufficient data. Indeed, the existence of an extended Higgs sector is primarily a question that must be answered via experimental exploration. If a convincing signal eventually emerges, then it will be important to provide a model interpretation.

Although there is no concrete argument pointing to a specific extended Higgs sector, there are a number of weak assumptions that can be applied to narrow down the appropriate framework in which to interpret the discovery of a new scalar. For example, the observed electroweak rho parameter and the absence of significant flavor changing neutral currents places strong constraints on a viable extended Higgs sector. The former tends to restrict considerations to models of hypercharge-zero singlet and hypercharge-one doublet scalars (e.g., see Ref. [69]), although interesting models with Higgs doublets and triplets arranged to have an (admittedly fine-tuned) custodial symmetric scalar potential would also satisfy the electroweak rho parameter constraint [70, 71]. If a charged scalar were discovered, this would indicate the

presence of additional doublet scalars.

For simplicity, we focus on extended Higgs sectors with additional doublets. Simply adding one doublet already yields a set of new phenomena (charged scalars, new CP-even and CP-odd neutral scalars or new neutral scalars of mixed CP symmetry). Thus employing the framework of the 2HDM may be sufficient to provide an initial interpretation of evidence that points to the discovery of an extended Higgs sector. Employing the most general 2HDM is not appropriate given that a significant portion of its parameter space would yield scalar-mediated FCNCs that are too large to be accommodated by the present data and/or an electric dipole moment (edm) for the electron that is inconsistent with the current experimental bounds. In light of the bounds on edms, one is tempted to restrict the parameters of the 2HDM such that no (significant) new sources of CP violation due to scalar self-interactions or the Higgs-fermion Yukawa couplings are present. This leads to the framework of the CP-conserving 2HDM. This is not to say that the LHC experiments should refrain from searching for CP-violating observables. However, any initial discovery of a new scalar is not likely to be particularly sensitive to the presence of a new scalar-mediated source of CP violation.

This leaves open the question of how to suppress scalar-mediated FCNCs. Theorists tend to demand that their models should yield suppressed scalar-mediated FCNCs naturally, which is theoretically implemented by a symmetry that is either exact or softly-broken. Such an assumption restricts the structure of the Higgs-fermion Yukawa couplings to one of four types (called Types I, II, X and Y), which defines a fundamental parameter of the model, called $\tan\beta$. Experimentalists analyzing their data should ignore such considerations. After all, determining the structure of the Higgs-fermion Yukawa couplings is an experimental endeavor. Ide-

ally, the experimental discovery of new scalars will inform theorists on how Nature has chosen to implement the suppression of FCNCs. With this in mind, we have advocated in this paper that evidence for new scalars at the LHC should be experimentally analyzed within the context of the flavor-aligned 2HDM (or A2HDM), which phenomenologically implements the absence of tree-level scalar-mediated FCNCs by proposing that two initially independent Yukawa coupling matrices are in fact proportional, with the proportionality constant (called the flavor-alignment parameter) an observable to be determined by experiment. Given that there are three pairs of Yukawa matrices (corresponding to up-type quarks, down-type quarks and charged leptons), there are three flavor-alignment parameters of interest, called a^U, a^D and a^E. The Higgs-fermion Yukawa couplings of Types I, II, X and Y are special cases of the A2HDM, so an experimental determination of the flavor-alignment parameters will inform whether one of the Yukawa coupling Types is compatible with the data.

After the completion of Run 2 of the LHC, both ATLAS and CMS have searched a variety of channels for evidence of new scalars. No statistically significant signal has yet to emerge. Nevertheless, we believe that it is a useful exercise to exhibit how one could implement the extended Higgs framework described above to probe the properties of any newly discovered scalar(s). With this in mind, we have reviewed the ATLAS and CMS searches for new scalars and focused on a number of small excesses observed (corresponding typically to local 3σ excesses whose significance reduces to 2σ or below when the look elsewhere effect is taken into account). We selected two different scenarios: Scenario 1 ($m_A = 610$ GeV and $m_H = 290$ GeV observed in $gg \to A \to ZH$, where $H \to b\bar{b}$ and $Z \to \ell^+\ell^-$) and Scenario 2 ($m_A = 400$ GeV, with $A \to t\bar{t}$ and $A \to \tau^+\tau^-$ decays observed). Treating

the small excesses observed as a potential signal of new scalars, we examined whether such excesses could be produced for some reasonable set of A2HDM parameters, and if so whether it would be possible to deduce whether the underlying fermion-Higgs Yukawa couplings were consistent with the symmetry-based Types I, II, X or Y 2HDMs.

Our analysis of both scenarios resulted in the following conclusions. Scenario 1 can be realized in a Type I 2HDM, but this solution is viable only for a rather restricted region of the model parameters. More generally, there is a larger region of the parameter space that is consistent with the A2HDM framework, but inconsistent with all of the symmetry-based Types I, II, X or Y models. In contrast, the Scenario 2 excesses observed at LHC, while again consistent with the A2HDM framework, exhibits no allowed parameter points consistent with the symmetry-based Types I, II, X or Y models. This result highlights one of the main points of our study. If the Scenario 2 excesses had been real (rather than the more likely statistical fluctuation of Standard Model backgrounds), an analysis of these data with a prejudice for the consistency with the symmetry-based Types I, II, X or Y Higgs-fermion Yukawa interactions would have concluded that these data are incompatible with the 2HDM. Of course, such a conclusion is inappropriate, in light of the compatibility of Scenario 2 with the more general A2HDM framework. Indeed, there is more flexibility in fitting a given scenario by employing the A2HDM as compared to each of the symmetry-based Higgs-fermion Yukawa interactions of the 2HDM due to the existence of three independent flavor-alignment parameters, a^U, a^D and a^E, which allows one to independently fit the constraints on flavor and leptonic observables of the model. In contrast, in the symmetry-based Higgs-fermion Yukawa interactions of the 2HDM, the coupling modifiers of the non-SM scalars to fermions (in the ap-

proximate Higgs alignment limit) are governed by a single parameter, $\tan\beta$, which results in strong correlations among the up-quark, down-quark and charged lepton Yukawa couplings.

If the excesses observed by the ATLAS and CMS Collaborations that are the basis for either of the two scenarios analyzed in this paper were confirmed in Run 3 of the LHC, then our analysis also provides predictions for new non-SM Higgs signals that could provide support for the A2HDM framework. In Scenario 1, the allowed A2HDM parameter space yields a signal for $gg \to H \to hh$ that is close to the current experimental bound, in light of Fig. 8.7. Moreover, the cross section for b-associated production of H followed by $H \to hh$ can be as large as 0.07 pb. Thus, resonant production of hh in subsequent runs at the LHC will provide a critical check of the A2HDM interpretation of Scenario 1. In addition, the A2HDM parameter space consistent with Scenario 1 yields cross sections for gg fusion and b-associated production of H followed by $H \to \tau^+\tau^-$ that can be as large as 120 fb and 70 fb, respectively, which could be detected with the future higher luminosity runs of the LHC. In contrast, gg fusion and b-associated production of A followed by $A \to \tau^+\tau^-$ yields smaller cross sections (roughly 0.1 fb and 0.05 fb, respectively), although still significantly larger than one would obtain in a Type-I 2HDM. Finally, Scenario 1 predicts a rather restricted range of masses for $H^\pm$: either $220 \lesssim m_{H^\pm} \lesssim 320$ GeV (i.e., $m_{H^\pm} \sim m_H$) or $570 \lesssim m_{H^\pm} \lesssim 670$ GeV (i.e., $m_{H^\pm} \sim m_A$). The predicted signal rates for $pp \to H^\pm \to tb$ are close to the current experimental bounds, and would provide another important consistency check of the A2HDM interpretation of Scenario 1 if observed. In Scenario 2, the allowed A2HDM parameter space exhibited in Fig. 9.7 implies potentially significant signal rates for $\sigma(gg \to H)\mathrm{BR}(H \to \tau^+\tau^-)$ and $\sigma(pp \to H^\pm)\mathrm{BR}(H^\pm \to tb)$: 10 times below the

current experimental sensitivity for the former, and close to the current exclusion bounds for the latter, for $400 \lesssim m_{H^\pm} \lesssim 600$ GeV. Both of these signals, if present at their expected rates, could be probed at Run 3 of the LHC. We would also expect a potentially observable signal rate for gg fusion and b-associated production of H followed by $H \to t\bar{t}$. Finally, in light of Fig. 9.4, there is a strong possibility of observable signal rates in b-associated production of A and H, followed by their decays to $b\bar{b}$. Observations of any of these non-SM Higgs production and decay processes would provide important consistency checks of the A2HDM interpretation of Scenario 2.

Ultimately, one would like to reduce further the specific extended Higgs sector model assumptions employed in analyzing a potential LHC discovery of a new scalar. Ideally, one should use experimental results to determine how many new doublets make up the extended Standard Model, and whether any singlets are present. It would be interesting to conceive of a scenario in which a general 2HDM is incompatible with an observed signal but a different extended Higgs structure can successfully explain the observed data. An obvious example would be the discovery of a doubly charged Higgs boson, which of course is absent in the 2HDM but present in models that contain hypercharge-two Higgs triplets [72]. However, if the discovery of a new scalar at the LHC indicates the observation of a new colorless neutral or singly-charged scalar, it is not so clear what type of scenario is needed that would require new physics beyond the 2HDM.

Meanwhile, we look forward to new data being taken at Run 3 of the LHC to see whether any of the data excesses that appeared in Run 2 persist or whether any evidence for the production of new scalars emerges. The discovery of a new scalar would have profound implications for physics at the electroweak scale and

perhaps provide a first glimpse of the physics beyond the Standard Model that is necessary to address some of the most pressing problems associated with our current theory of fundamental particles and their interactions.

Part III

Four-texture Yukawas

Chapter 11

Introduction

We have many measurements from particle colliders that require tree-level, Higgs-mediated FCNC's to be highly suppressed, and sufficiently suppressed at loop level. However, that does not mean that they are zero. From time to time, there are small flavor-violating signals observed in LHC data, although they usually go away when more data is collected and as analyses improve. It could be that we will eventually see flavor-violating processes at the LHC, and then we will need a model beyond the SM to explain it. As evident in Part II of this thesis, we do not wish to restrict ourselves to the simplest of 2HDMs. We also wish to explore the possibility that flavor-violating Higgs-fermion interactions could exist, as long as they are small enough to evade current bounds.

The SM has a few shortcomings, such as providing no reason for the Higgs sector to be minimal whereas the up- and down-type quark and lepton sectors have three generations each. The SM also does not explain where the masses of the fermions come from. It tells us how they are generated, but not what their values are, or why they exhibit a large hierarchy. To understand the nature of Higgs-fermion Yukawa couplings gives insight into this story and implores us to investigate

coupling mechanisms beyond the SM.

We still need a mechanism to suppress FCNC's to evade current measurement bounds. It has been shown [94], [85] that four-texture mass and Yukawa coupling matrices can produce physical couplings like the Cheng Sher ansatz, which states that FCNC's bounds can be avoided if Higgs-fermion couplings are proportional to $\sqrt{m_i m_j}/v$. In this pattern, the hierarchy of fermion masses causes off-diagonal, flavor-violating couplings to be small enough in some regions of parameter space.

One can find the Cheng Sher-like coupling pattern emerge in certain approximation schemes, however we elect to use the exact formulae for the physical Yukawa couplings. We also revisit the theoretical formalism and rotate into the Higgs basis before diagonalizing the quark mass matrices. Thus, our four-textures are manifest in the Higgs basis, and our physical results only depend on the angle $\beta - \alpha$, but not α or β separately, so they are basis-independent.

To verify that this is a valid model and explore potentially detectable phenomenological implications, we perform a parameter scan and study the allowed regions of parameter space. The most strict bounds on our models come from searches for scalars at the LHC and precision Higgs boson measurements. We utilize the program HiggsTools [91] to analyze the parameter space of our four-texture model. HiggsTools is comprised of three subprograms. HiggsPredictions can take coupling modifier expressions as inputs and modify SM-like calculations to obtain cross sections and branching ratios in your model. It then can pass those predictions to HiggsBounds which determines if each parameter point is in conflict with any search for new scalars at a variety of particle colliders. The third subprogram is HiggsSignals, which compares the h predictions with properties of the observed h_{SM} (131

observables) and returns a statistical χ^2 value. We define $\Delta\chi^2 = \chi^2 - N_{\text{observables}}$ and require $\Delta\chi^2 < 6$.

Once we have a set of points that satisfy these conditions, we study their flavor-violating predictions and determine which may appear in collider data in the near future, should they exist.

Chapter 12

Theoretical Background

The theoretical foundations of 2HDMs were introduced in detail in Part I. This section will focus on introducing the Type-III Yukawa couplings utilized in Part III of this dissertation (the second project). Specifically we discuss four-texture Yukawa coupling matrices and how they can produce the Cheng Sher Ansatz. In the literature, when authors write out the Yukawa couplings of Type-III 2HDMs, they usually define the Yukawa coupling matrices in a generic Φ-basis of Higgs fields. This yields physical couplings that depend on the parameters α and β separately, and so they depend on which Φ-basis the Yukawa matrices were defined in. We find it more sensible adopt a basis-independent approach, by first rotating into the Higgs basis and then defining a particular structure for the Yukawa coupling matrices. However, to make contact with the couplings displayed in most references in the literature and understand how those physical couplings are computed, we will first reproduce their results by working in a generic Φ-basis, and then revisit the computation starting in the Higgs basis.

12.1 Type-III 2HDM Yukawas in a Generic Φ-basis

We begin with the Yukawa Lagrangian describing Higgs-quark interactions in a generic basis of Higgs fields and the quark interaction-eigenstate basis,

$$-\mathcal{L}_{\rm Y} = \overline{Q}_L^0 \widetilde{\Phi}_1 \eta_1^{U,0} U_R^0 + \overline{Q}_L^0 \Phi_1 \eta_1^{D,0} D_R^0 + \overline{Q}_L^0 \widetilde{\Phi}_2 \eta_2^{U,0} U_R^0 + \overline{Q}_L^0 \Phi_2 \eta_2^{D,0} D_R^0 + \text{h.c.}\,, \quad (12.1)$$

where $\Phi_{1,2}$ are the two Higgs doublets, $\widetilde{\Phi}_i \equiv i\sigma_2 \Phi_i^*$, Q_L^0 are weak isospin quark doublets, and U_R^0, D_R^0 are weak isospin quark singlets. The right and left-handed fermion fields are defined as usual: $\psi_{R,L} \equiv P_{R,L}\psi$, where $P_{R,L} \equiv \frac{1}{2}(1 \pm \gamma_5)$. Here, the superscripts on Q_L^0, U_R^0, and D_R^0 denote the interaction basis eigenstates, which are vectors in quark flavor space, and $\eta_1^{U,0}, \eta_2^{U,0}, \eta_1^{D,0}$, and $\eta_2^{D,0}$ are matrices in quark flavor space. When we rotate into the quark mass basis, we will remove the superscripts. We can see that the four $\eta_i^{Q,0}$ matrices are Higgs basis dependent quantities and will mix when rotating the Higgs basis. For simplicity we have omitted the charged lepton terms in Eq. (12.1), but they follow the exact same pattern as we will show for the down-type quark couplings. We are working under the assumption of massless neutrinos, as in the SM. We will also focus on neutral Higgs-quark interactions, so ignoring charged Higgs terms, the Yukawa Lagrangian becomes,

$$-\mathcal{L}_{\rm Y} = \overline{U}_L^0 \Phi_1^{0*} \eta_1^{U,0} U_R^0 + \overline{D}_L^0 \Phi_1^0 \eta_1^{D,0} D_R^0 + \overline{U}_L^0 \Phi_2^{0*} \eta_2^{U,0} U_R^0 + \overline{D}_L^0 \Phi_2 \eta_2^{D,0} D_R^0 + \text{h.c.}. \quad (12.2)$$

The quark mass matrices are obtained by setting the Higgs fields to their vacuum expectation values (vevs), denoted by $\langle \Phi_i \rangle = \frac{1}{\sqrt{2}}(0, v_i) = \frac{v}{\sqrt{2}}(0, \widehat{v}_i)$, where

$$\widehat{v}_i = \begin{pmatrix} \cos\beta \\ \sin\beta \end{pmatrix}, \qquad \widehat{w}_i = \begin{pmatrix} -\sin\beta \\ \cos\beta \end{pmatrix}, \quad (12.3)$$

as previously shown in Eq. (2.3). By inserting the Higgs vevs into Eq. (12.2) we find

the quark mass matrices M_q^0,

$$M_d^0 = \frac{1}{\sqrt{2}}\Big(v_1\eta_1^{D,0} + v_2\eta_2^{D,0}\Big) \tag{12.4}$$

$$M_u^0 = \frac{1}{\sqrt{2}}\Big(v_1^*\eta_1^{U,0} + v_2^*\eta_2^{U,0}\Big)\,, \tag{12.5}$$

which are not diagonal in the quark interaction basis. If we restrict ourselves to CP-conserving vacuua, then $v_i^* = v_i$ and $w_i^* = w_i$. In the following two sections we reproduce the standard results found in the literature to understand the pattern of Yukawa couplings one finds when starting in a generic Higgs Φ-basis. We will first work out the Yukawa couplings for down-type quarks, then up-type quarks, then restart in the Higgs basis to derive Higgs basis independent results.

12.1.1 Down-type Quark Yukawa Analysis in a Generic Basis

In this section we write out the Yukawa Lagrangian for down-type quarks only, ignoring up-type quarks and charged Higgs interactions, since there are many terms to keep track of. We can rearrange Eq. (12.4) to eliminate $\eta_1^{D,0}$ from the Yukawa Lagrangian, and instead rewrite it in terms of M_d^0 and $\eta_2^{D,0}$,

$$\eta_1^{D,0} \;=\; \frac{1}{v_1}\big(\sqrt{2}M_d^0 - v_2\eta_2^{D,0}\big) = \frac{\sqrt{2}M_d^0}{v\cos\beta} - \tan\beta\,\eta_2^{D,0}\,. \tag{12.6}$$

The Yukawa Lagrangian is then,

$$-\,\mathcal{L}_{\rm Y}^D \;=\; \overline{D}_L^0\Phi_1^0\left[\frac{1}{v_1}\big(\sqrt{2}M_d^0 - v_2\eta_2^{D,0}\big)\right]D_R^0 \;+\; \overline{D}_L^0\Phi_2^0\eta_2^{D,0}D_R^0 \;+\; \text{h.c.}\,. \tag{12.7}$$

The quark mass matrix can be diagonalized by,

$$M_d = O_D^T P_D^\dagger M_d^0 P_D O_D\,, \tag{12.8}$$

where $M_d = \text{diag}(m_d, m_s, m_b)$ and so the quark mass eigenstates are $D = O_D^T P_D^\dagger D^0$. The Yukawa coupling matrices can also be rotated into the quark mass basis by the

same transformation,

$$\eta_i^D = O_D^T P_D^\dagger \eta_i^{D,0} P_D O_D \,. \tag{12.9}$$

The Yukawa Lagrangian then becomes,

$$-\mathcal{L}_{\rm Y}^D \;=\; \overline{D}_L \Phi_1^0 \left[\frac{1}{v_1}\big(\sqrt{2}M_d - v_2\eta_2^D\big)\right] D_R \;+\; \overline{D}_L \Phi_2^0 \eta_2^D D_R \;+\; \text{h.c.}\,. \tag{12.10}$$

In the CP-conserving case, the Higgs fields can be rewritten in terms of mass eigenstates as,

$$\Phi_i^0 = \frac{v_i}{\sqrt{2}} + \frac{1}{\sqrt{2}} \sum_{k=1}^{3} \big(q_{k1}\hat{v}_i + q_{k2}\varepsilon\hat{w}_i\big) h_k \,, \tag{12.11}$$

where the q_{ki} and h_k are given in Table 12.1. We have removed the Goldstone bosons which will be eaten by the $W^\pm$ and Z gauge bosons. Inserting the q_{ki} and Higgs mass eigenstates into the Yukawa Lagrangian we obtain,

$$\begin{aligned} -\mathcal{L}_{\rm Y}^D \;=\; \overline{D}_L \Bigg[\frac{1}{v_1}\big(\sqrt{2}M_d - v_2\eta_2^D\big) \Bigg\{ \frac{v_1}{\sqrt{2}} + \frac{1}{\sqrt{2}} \sum_{k=1}^{3} \big(q_{k1}\hat{v}_1 + q_{k2}\varepsilon\hat{w}_1\big) h_k \Bigg\} \\ + \eta_2^D \Bigg\{ \frac{v_2}{\sqrt{2}} + \frac{1}{\sqrt{2}} \sum_{k=1}^{3} \big(q_{k1}\hat{v}_2 + q_{k2}\varepsilon\hat{w}_2\big) h_k \Bigg\} \Bigg] D_R \;+\; \text{h.c.}\,. \end{aligned} \tag{12.12}$$

Dropping the terms which are not proportional to any of the h_k, we arrive at,

$$\begin{aligned} -\mathcal{L}_{\rm Y}^D \;=\; \overline{D}_L \frac{1}{\sqrt{2}} \Bigg[\frac{1}{v_1}\big(\sqrt{2}M_d - v_2\eta_2^D\big) \Bigg\{ & \big(q_{11}\hat{v}_1 + q_{12}\varepsilon\hat{w}_1\big) h_1 \\ & \big(q_{21}\hat{v}_1 + q_{22}\varepsilon\hat{w}_1\big) h_2 \\ & \big(q_{31}\hat{v}_1 + q_{32}\varepsilon\hat{w}_1\big) h_3 \Bigg\} \\ + \eta_2^D \Bigg\{ & \big(q_{11}\hat{v}_2 + q_{12}\varepsilon\hat{w}_2\big) h_1 \\ & \big(q_{21}\hat{v}_2 + q_{22}\varepsilon\hat{w}_2\big) h_2 \\ & \big(q_{31}\hat{v}_2 + q_{32}\varepsilon\hat{w}_2\big) h_3 \Bigg\} \Bigg] D_R \;+\; \text{h.c.}\,. \end{aligned} \tag{12.13}$$

Inserting the expressions from Table 12.1,

k	h_k	q_{k1}	q_{k2}
1	h	$s_{\beta-\alpha}$	$\varepsilon c_{\beta-\alpha}$
2	$-\varepsilon H$	$-\varepsilon c_{\beta-\alpha}$	$s_{\beta-\alpha}$
3	εA	0	i

Table 12.1: Basis-invariant combinations q_{kj} in the CP-conserving limit, corresponding to a real Higgs basis where $\varepsilon = \pm 1$.

$$
\begin{aligned}
-\mathcal{L}_{\rm Y}^{D} \;=\; \overline{D}_L \frac{1}{\sqrt{2}} \Bigg[\frac{1}{v_1} \big(\sqrt{2} M_d - v_2 \eta_2^D\big) \Bigg\{ & \big(s_{\beta-\alpha}\hat{v}_1 + c_{\beta-\alpha}\hat{w}_1\big) h \\
& - \big((-c_{\beta-\alpha})\hat{v}_1 + s_{\beta-\alpha}\hat{w}_1\big) H \\
& + \big(i\hat{w}_1\big) A \Bigg\} \\
+\; \eta_2^D \Bigg\{ & \big(s_{\beta-\alpha}\hat{v}_2 + c_{\beta-\alpha}\hat{w}_2\big) h \\
& - \big((-c_{\beta-\alpha})\hat{v}_2 + s_{\beta-\alpha}\hat{w}_2\big) H \\
& + \big(i\hat{w}_2\big) A \Bigg\} \Bigg] D_R \;+\; \text{h.c.}\,.
\end{aligned}
\tag{12.14}
$$

Notice that all the factors of ε cancel, as expected. Now if we insert the expressions for $\hat{v}_i$ and simplify, we obtain,

$$
\begin{aligned}
-\mathcal{L}_{\rm Y}^{D} \;=\; \overline{D}_L \frac{1}{\sqrt{2}} \Bigg[\frac{1}{v} \big(\sqrt{2} M_d - v_2 \eta_2^D\big) \Bigg\{ & \big(s_{\beta-\alpha} - c_{\beta-\alpha}\tan\beta\big) h \\
& + \big(c_{\beta-\alpha} + s_{\beta-\alpha}\tan\beta\big) H \\
& - \big(i\tan\beta\big) A \Bigg\} \\
+\; \eta_2^D \Bigg\{ & \big(s_{\beta-\alpha}\sin\beta + c_{\beta-\alpha}\cos\beta\big) h \\
& + \big(c_{\beta-\alpha}\sin\beta - s_{\beta-\alpha}\cos\beta\big) H \\
& + \big(i\cos\beta\big) A \Bigg\} \Bigg] D_R \;+\; \text{h.c.}\,.
\end{aligned}
\tag{12.15}
$$

Making use of the following trigonometric identities:

$$-\frac{\sin\alpha}{\cos\beta} \;=\; s_{\beta-\alpha} - \tan\beta\, c_{\beta-\alpha} \qquad\qquad \frac{\cos\alpha}{\sin\beta} \;=\; s_{\beta-\alpha} + \cot\beta\, c_{\beta-\alpha} \tag{12.16}$$

$$\frac{\cos\alpha}{\cos\beta} \;=\; c_{\beta-\alpha} + \tan\beta\, s_{\beta-\alpha} \qquad\qquad \frac{\sin\alpha}{\sin\beta} \;=\; c_{\beta-\alpha} - \cot\beta s_{\beta-\alpha}\,. \tag{12.17}$$

we arrive at (by multiplying the lower two expressions above by $\cos\beta$),

$$\begin{aligned} -\mathcal{L}_{\rm Y}^{D} \;=\; \overline{D}_L \frac{1}{\sqrt{2}}\Bigg[\frac{1}{v}\big(\sqrt{2}M_d - v_2\eta_2^D\big)\Bigg\{ -\frac{\sin\alpha}{\cos\beta}h + \frac{\cos\alpha}{\cos\beta}H - i\tan\beta A\Bigg\} \\ + \eta_2^D\Bigg\{\cos\alpha h + \sin\alpha H + i\cos\beta A\Bigg\}\Bigg] D_R \;+\; \text{h.c.}\,. \end{aligned} \tag{12.18}$$

Collecting terms proportional to h, H or A, we obtain,

$$\begin{aligned} -\mathcal{L}_{\rm Y}^{D} \;=\; \overline{D}_L \frac{1}{\sqrt{2}}\Bigg[&\Bigg\{-\left(\frac{\sqrt{2}M_d}{v} - \sin\beta\,\eta_2^D\right)\frac{\sin\alpha}{\cos\beta} + \eta_2^D\cos\alpha\Bigg\}h \\ &+\Bigg\{\left(\frac{\sqrt{2}M_d}{v} - \sin\beta\,\eta_2^D\right)\frac{\cos\alpha}{\cos\beta} + \eta_2^D\sin\alpha\Bigg\}H \\ &+i\Bigg\{-\left(\frac{\sqrt{2}M_d}{v} - \sin\beta\,\eta_2^D\right)\tan\beta + \eta_2^D\cos\beta\Bigg\}A\Bigg] D_R \;+\; \text{h.c.}\,. \end{aligned} \tag{12.19}$$

Combining terms proportional to η_2^D, we find,

$$\begin{aligned} -\mathcal{L}_{\rm Y}^{D} \;=\; \overline{D}_L \frac{1}{\sqrt{2}}\Bigg[&\Bigg\{-\frac{\sqrt{2}M_d}{v}\frac{\sin\alpha}{\cos\beta} + \left(\frac{\sin\alpha\sin\beta}{\cos\beta} + \frac{\cos\alpha\cos\beta}{\cos\beta}\right)\eta_2^D\Bigg\}h \\ &+\Bigg\{\frac{\sqrt{2}M_d}{v}\frac{\cos\alpha}{\cos\beta} + \left(-\frac{\cos\alpha\sin\beta}{\cos\beta} + \frac{\sin\alpha\cos\beta}{\cos\beta}\right)\eta_2^D\Bigg\}H \\ &+i\Bigg\{-\frac{\sqrt{2}M_d}{v}\tan\beta + \left(\frac{\sin^2\beta}{\cos\beta} + \frac{\cos^2\beta}{\cos\beta}\right)\eta_2^D\Bigg\}A\Bigg] D_R \;+\; \text{h.c.}\,. \end{aligned} \tag{12.20}$$

Finally using sum angle formulas, and adding the hermitian conjugated terms, which yields the factor of γ_5 in the pseudoscalar couplings, we reproduce the Yukawa Lagrangian shown in Eq. [4] of Ref. [85],

$$\begin{aligned} -\mathcal{L}_{\rm Y}^{D} \;=\; \overline{D}_L \frac{1}{\sqrt{2}}\Bigg[&\Bigg\{-\frac{\sqrt{2}M_d}{v}\frac{\sin\alpha}{\cos\beta} + \frac{c_{\beta-\alpha}}{\cos\beta}\,\eta_2^D\Bigg\}h \\ &+\Bigg\{\frac{\sqrt{2}M_d}{v}\frac{\cos\alpha}{\cos\beta} + \frac{-s_{\beta-\alpha}}{\cos\beta}\,\eta_2^D\Bigg\}H \\ &+\Bigg\{-\frac{\sqrt{2}M_d}{v}\tan\beta + \frac{1}{\cos\beta}\,\eta_2^D\Bigg\}i\gamma_5 A\Bigg] D_R\,. \end{aligned} \tag{12.21}$$

Notice that $s_{\beta-\alpha} = -s_{\alpha-\beta}$ and $c_{\beta-\alpha} = c_{\alpha-\beta}$ when comparing results with the reference listed above. Also notice that these physical couplings depend on the angles α and β separately which is not a Higgs basis invariant way to write them. Recall that the angle β parametrizes the rotation angle from a generic Φ-basis into the Higgs basis and α is the mixing angle of the Higgs bosons. We verified the Type-II limit ($\eta_1^U = 0$ and $\eta_2^D = 0$) of the results in Eq. (12.21) with the well-known Type-II Yukawa couplings.

When adding the hermitian conjugate terms to the scalar interactions, we have terms proportional to,

$$\begin{aligned}
\overline{D}_L D_R + \text{h.c.} &\equiv \overline{D} P_R D + (\overline{D} P_R D)^\dagger \\
&= \overline{D} P_R D + D^\dagger P_R \gamma^0 D \\
&= \overline{D} P_R D + \overline{D} P_L D \\
&= \overline{D} (P_R + P_L) D \\
&= \overline{D} D \,, \qquad (12.22)
\end{aligned}$$

since $P_R + P_L = \mathbb{1}$. This calculation changes slightly for the pseudoscalar couplings because of an extra factor of i, which yields $P_L - P_R = \gamma_5$ in the pseudoscalar coupling only.

12.1.2 Up-type Quark Yukawa Analysis in a Generic Basis

Next we reproduce the Yukawa couplings of up-type quarks to Higgs bosons (still working in the CP-conserving limit). The computation is similar to that of down-type quarks, but we eliminate η_2 instead of η_1, and there will be a conjugated

$q_{32}^* = -i$ on the pseudoscalar coupling. The relevant terms in the Lagrangian are,

$$\begin{aligned} -\mathcal{L}_{\rm Y}^U &= \overline{Q}_L^0 \widetilde{\Phi}_1 \eta_1^{U,0} U_R^0 + \overline{Q}_L^0 \widetilde{\Phi}_2 \eta_2^{U,0} U_R^0 + \text{h.c.} \\ &= \overline{U}_L^0 \Phi_1^{0*} \eta_1^{U,0} U_R^0 + \overline{U}_L^0 \Phi_2^{0*} \eta_2^{U,0} U_R^0 + \text{h.c.}\,. \end{aligned} \tag{12.23}$$

By inspecting the vacuum we find the up-type quark mass matrix,

$$M_u^0 = \frac{1}{\sqrt{2}} \big(v_1^* \eta_1^{U,0} + v_2^* \eta_2^{U,0} \big)\,. \tag{12.24}$$

In the case of a CP-conserving vacuum we have $v_i^* = v_i$. We can rearrange this formula,

$$\eta_2^{U,0} = \frac{1}{v_2} \big(\sqrt{2} M_u^0 - v_1 \eta_1^{U,0} \big) = \frac{\sqrt{2} M_u^0}{v \sin\beta} - \cot\beta\, \eta_1^{U,0}\,, \tag{12.25}$$

to eliminate $\eta_2^{U,0}$ from Eq. (12.23), which becomes,

$$-\mathcal{L}_{\rm Y}^U = \overline{U}_L^0 \Phi_1^{0*} \eta_1^{U,0} U_R^0 + \overline{U}_L^0 \Phi_2^{0*} \frac{1}{v_2} \big(\sqrt{2} M_u^0 - v_1 \eta_1^{U,0} \big) U_R^0 + \text{h.c.}\,. \tag{12.26}$$

Keeping in mind that $q_{32}^* = -i$, we find,

$$\begin{aligned} -\mathcal{L}_{\rm Y}^U = \overline{U}_L \frac{1}{\sqrt{2}} \Bigg[& \eta_1^U \Big\{ \big(s_{\beta-\alpha} \hat{v}_1 + c_{\beta-\alpha} \hat{w}_1 \big) h \qquad (12.27) \\ & - \big((-c_{\beta-\alpha}) \hat{v}_1 + s_{\beta-\alpha} \hat{w}_1 \big) H \\ & - \big(i \hat{w}_1 \big) A \Big\} \\ + \frac{1}{v_2} \big(\sqrt{2} M_u - v_1 \eta_1^U \big) & \Big\{ \big(s_{\beta-\alpha} \hat{v}_2 + c_{\beta-\alpha} \hat{w}_2 \big) h \qquad (12.28) \\ & - \big((-c_{\beta-\alpha}) \hat{v}_2 + s_{\beta-\alpha} \hat{w}_2 \big) H \\ & - \big(i \hat{w}_2 \big) A \Big\} \Bigg] U_R + \text{h.c.}\,. \end{aligned}$$

Inserting the expressions given in Eq. (2.3) for the $\hat{v}_i$ and $\hat{w}_i$, we obtain,

$$
\begin{aligned}
-\mathcal{L}_{\rm Y}^{U} \;=\; \overline{U}_L \frac{1}{\sqrt{2}} \Bigg[\frac{1}{v} \big(M_u - v_1 \eta_1^U\big) \Big\{ & \big(s_{\beta-\alpha} + c_{\beta-\alpha} \cot\beta\big) h \\
& - \big((-c_{\beta-\alpha}) + s_{\beta-\alpha} \cot\beta\big) H \\
& - \big(i \cot\beta\big) A \Big\} \\
+\, \eta_1^U \Big\{ & \cos\beta \big(s_{\beta-\alpha} - c_{\beta-\alpha} \tan\beta\big) h \\
& - \cos\beta \big((-c_{\beta-\alpha}) - s_{\beta-\alpha} \tan\beta\big) H \\
& + \big(i \sin\beta\big) A \Big\} \Bigg] U_R \;+\; \text{h.c.}\,.
\end{aligned}
\tag{12.29}
$$

Using the trigonometric identities displayed in Eq. (12.16), we have,

$$
\begin{aligned}
-\mathcal{L}_{\rm Y}^{U} \;=\; \overline{U}_L \frac{1}{\sqrt{2}} \Bigg[\frac{1}{v} \big(\sqrt{2} M_u - v_1 \eta_1^U\big) & \Big\{ \frac{\cos\alpha}{\sin\beta}\, h \;+\; \frac{\sin\alpha}{\sin\beta}\, H \;-\; i \cot\beta\, A \Big\} \\
& + \eta_1^U \Big\{ -\sin\alpha\, h \;+\; \cos\alpha\, H \;+\; i \sin\beta\, A \Big\} \Bigg] U_R \;+\; \text{h.c.}\,.
\end{aligned}
\tag{12.30}
$$

Distributing the factor with the mass matrix and simplifying, we obtain,

$$
\begin{aligned}
-\mathcal{L}_{\rm Y}^{U} \;=\; \overline{U}_L \frac{1}{\sqrt{2}} \Bigg[\frac{\sqrt{2} M_u}{v} & \Big\{ \frac{\cos\alpha}{\sin\beta}\, h \;+\; \frac{\sin\alpha}{\sin\beta}\, H \;-\; i \cot\beta\, A \Big\} \\
+ \eta_1^U & \Big\{ -\cos\alpha \cot\beta\, h \;-\; \sin\alpha \cot\beta\, H \;+\; i \cos\beta \cot\beta\, A \Big\} \\
& + \eta_1^U \Big\{ -\sin\alpha\, h \;+\; \cos\alpha\, H \;+\; i \sin\beta\, A \Big\} \Bigg] U_R \;+\; \text{h.c.}\,.
\end{aligned}
\tag{12.31}
$$

Collecting terms proportional to h, H or A, we find,

$$
\begin{aligned}
-\mathcal{L}_{\rm Y}^{U} \;=\; \overline{U}_L \frac{1}{\sqrt{2}} \Bigg[& \left(\frac{\sqrt{2} M_u}{v} \frac{\cos\alpha}{\sin\beta} - (\cos\alpha \cot\beta + \sin\alpha) \eta_1^U \right) h \\
& + \left(\frac{\sqrt{2} M_u}{v} \frac{\sin\alpha}{\sin\beta} \;-\; (\sin\alpha \cot\beta - \cos\alpha) \eta_1^U \right) H \\
& + \left(\frac{\sqrt{2} M_u}{v} (-\cot\beta) \;+ (\cos\beta \cot\beta + \sin\beta) \eta_1^U \right) i\gamma_5 A \Bigg] U_R\,.
\end{aligned}
\tag{12.32}
$$

Simplifying further with trigonometric identities, we arrive at,

$$
\begin{aligned}
-\mathcal{L}_{\rm Y}^{U} \,=\, \overline{U}_L\,\frac{1}{\sqrt{2}}\Bigg[&\left(\frac{\sqrt{2}M_u}{v}\frac{\cos\alpha}{\sin\beta}\,-\,\frac{c_{\beta-\alpha}}{\sin\beta}\,\eta_1^U\right)h \\
&+\left(\frac{\sqrt{2}M_u}{v}\frac{\sin\alpha}{\sin\beta}\,+\,\frac{s_{\beta-\alpha}}{\sin\beta}\,\eta_1^U\right)H \\
&+\left(\frac{\sqrt{2}M_u}{v}(-\cot\beta)\,+\,\frac{1}{\sin\beta}\,\eta_1^U\right)i\gamma_5 A\Bigg]\,U_R\,,
\end{aligned}
\tag{12.33}
$$

which reproduces the interactions of Higgs bosons and up-type quarks given in Eq. 4 of Ref. [86].

Beware that Ref. [85] has a typo in the up-type couplings (Y_2 should be exchanged with Y_1 for up-type couplings only). Again, these physical couplings depend on the angles α and β separately which is not a Higgs basis invariant way to write them. We verified the Type-II limit ($\eta_1^U = 0$ and $\eta_2^D = 0$) of the results in Eq. (12.33) with Type-II Yukawa couplings.

This concludes our study of the Yukawa couplings in the Higgs Φ-basis. From now on we will rotate into the Higgs basis before diagonalizing the quark mass matrices or making any assumptions about the Yukawa coupling matrices so that our results will be basis-independent.

12.2 Type-III 2HDM Yukawas in the Higgs Basis

To obtain physical Yukawa couplings that are basis-independent, we begin with the Higgs-fermion-fermion' Yukawa interaction Lagrangian in the Higgs basis, in terms of singlet interaction eigenstate quark fields, which was previously given in Eq. (2.29) and is reproduced here,

$$
\begin{aligned}
-\mathscr{L}_{\rm Y} \,=\, &\overline{U_L^0}(\mathcal{H}_1^{0\dagger}\kappa^{U,0}+\mathcal{H}_2^{0\dagger}\rho^{U,0})U_R^0-\overline{D_L^0}(\mathcal{H}_1^{-}\kappa^{U,0}+\mathcal{H}_2^{-}\rho^{U,0})U_R^0 \\
&+\overline{U_L^0}(\mathcal{H}_1^{+}\kappa^{D,0\dagger}+\mathcal{H}_2^{+}\rho^{D,0\dagger})D_R^0+\overline{D_L^0}(\mathcal{H}_1^{0}\kappa^{D,0\dagger}+\mathcal{H}_2^{0}\rho^{D,0\dagger})D_R^0\,+\,\text{h.c.}\,.
\end{aligned}
\tag{12.34}
$$

Inspecting the vacuum, since $\langle \mathcal{H}_1 \rangle = (0, v)$ and $\langle \mathcal{H}_2 \rangle = (0, 0)$, we find that the $\kappa^{Q,0}$ matrices are proportional to the quark mass matrices, as we intentionally constructed them,

$$M_u^0 = \frac{v}{\sqrt{2}} \kappa^{U,0}, \qquad\qquad M_d^0 = \frac{v}{\sqrt{2}} \kappa^{D,0\dagger} \,. \tag{12.35}$$

The M_u^0 are the interaction basis quark mass matrices and are not yet diagonalized. To enable ourselves to read off the physical Yukawa couplings, we rewrite the Yukawa Lagrangian in terms of quark mass eigenstates and Higgs mass eigenstates h_k,

$$\mathcal{H}_1^0 \,=\, \frac{1}{\sqrt{2}} \left(v + \sum_{k=1}^{3} q_{k1} h_k \right) \qquad\qquad \mathcal{H}_2^0 \,=\, \frac{1}{\sqrt{2}} \sum_{k=1}^{3} q_{k2} h_k \,, \tag{12.36}$$

where the q_{ki} are given in Table 12.1. Writing out the up-type quark terms only for the moment, in the CP-conserving case, we have,

$$\begin{aligned}
-\mathscr{L}_{\rm Y}^U \,&=\, \overline{U}_L^0 (H_1^{0*} \kappa^{U,0} + H_2^{0*} \rho^{U,0}) U_R^0 \,+\, \text{h.c.} \qquad (12.37) \\
&= \tfrac{1}{\sqrt{2}} \, \overline{U}_L^0 \Big[\sum_{k=1}^{3} q_{k1}^* h_k \, \kappa^{U,0} + \sum_{k=1}^{3} q_{k2}^* h_k \, \rho^{U,0} \Big] U_R^0 \,+\, \text{h.c.} \\
&= \tfrac{1}{\sqrt{2}} \, \overline{U}_L^0 \Big[(q_{11}^* h_1 + q_{21}^* h_2) \kappa^{U,0} + (q_{12}^* h_1 + q_{22}^* h_2 + q_{32}^* h_3) \rho^{U,0} \Big] U_R^0 \,+\, \text{h.c.} \\
&= \tfrac{1}{\sqrt{2}} \, \overline{U}_L^0 \Big[(s_{\beta-\alpha} h + c_{\beta-\alpha} H) \kappa^{U,0} + (c_{\beta-\alpha} h - s_{\beta-\alpha} H - iA) \varepsilon \rho^{U,0} \Big] U_R^0 \,+\, \text{h.c.} \\
&= \tfrac{1}{\sqrt{2}} \, \overline{U}_L \Big[(s_{\beta-\alpha} \kappa^U + c_{\beta-\alpha} \varepsilon \rho^U) h + (c_{\beta-\alpha} \kappa^U - s_{\beta-\alpha} \varepsilon \rho^U) H - i \varepsilon \rho^U \gamma_5 A \Big] U_R \,.
\end{aligned}$$

where in the last line we have rewritten the quark fields and Yukawa coupling matrices in the quark mass basis, which we will describe explicitly in Eq. (12.42) and Eq. (12.51) below. Finally, collecting terms proportional to h, H, and A and adding

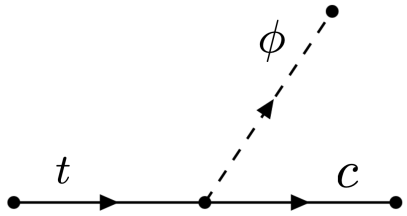

Figure 12.1: Example tree-level Higgs-mediated FCNC interaction that would be generated if flavor non-diagonal ρ^Q matrix elements are not highly suppressed. Interactions such as these are not observed and tight limits exist.

in the down quark terms, we have,

$$\begin{aligned}
-\mathscr{L}_{\rm Y} \;=\; & \frac{1}{v}\,\overline{U}_L\Big[(s_{\beta-\alpha}M_u \,+\, \varepsilon c_{\beta-\alpha}\frac{v}{\sqrt{2}}\rho^U)h \\
& \qquad +(c_{\beta-\alpha}M_u \,-\, \varepsilon s_{\beta-\alpha}\frac{v}{\sqrt{2}}\rho^U)H \\
& \qquad\qquad -i\,\varepsilon\frac{v}{\sqrt{2}}\rho^U\gamma_5 A\Big]U_R \\
& +\frac{1}{v}\,\overline{D}_L\Big[(s_{\beta-\alpha}M_d \,+\, \varepsilon c_{\beta-\alpha}\frac{v}{\sqrt{2}}\rho^{D*})h \\
& \qquad +(c_{\beta-\alpha}M_d \,-\, \varepsilon s_{\beta-\alpha}\frac{v}{\sqrt{2}}\rho^{D*})H \\
& \qquad\qquad +i\,\varepsilon\frac{v}{\sqrt{2}}\rho^{D*}\gamma_5 A\Big]D_R\,. \qquad (12.38)
\end{aligned}$$

We can see exactly how the M_q and ρ^Q matrices appear in the physical Higgs-fermion-fermion' couplings. Also note how only the basis-invariant angle $\beta-\alpha$ appears instead of α or β separately.

12.3 Four-texture Yukawas and the Cheng-Sher Ansatz

In Eq. (12.38) we can see that if the ρ^Q matrices are not flavor-diagonal, then there will be tree-level, Higgs-mediated flavor changing neutral currents (FCNCs), as the one shown in Fig. 12.1, for example. The Cheng-Sher Ansatz [94] is a pattern of physical Yukawa couplings that sufficiently suppresses the flavor off-

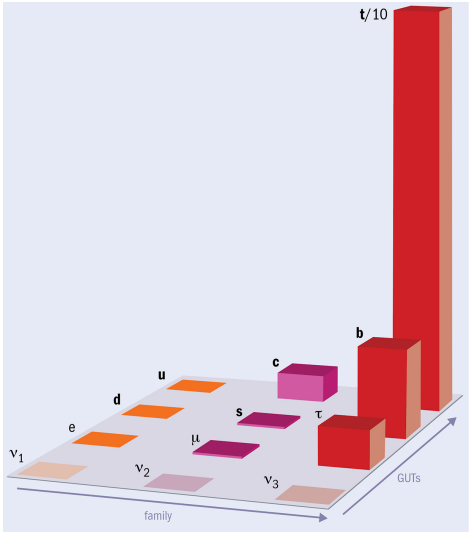

Figure 12.2: The hierarchy of the fermion masses visualized. Notice that top quarks are so heavy that their column has to be divided by 10 to fit. The three hierarchies $m_t > m_c > m_u$, $m_b > m_s > m_d$, and $m_\tau > m_\mu > m_e$ that cause the suppression of the off-diagonal elements of the Yukawa coupling matrices are apparent.

$$\begin{bmatrix} m_u & \sqrt{m_u m_c} & \sqrt{m_u m_t} \\ \sqrt{m_u m_c} & m_c & \sqrt{m_c m_t} \\ \sqrt{m_u m_t} & \sqrt{m_c m_t} & m_t \end{bmatrix}$$

Figure 12.3: The rough hierarchy produced in the Cheng Sher ansatz for the Yukawa coupling matrices ρ^F_{ij}, where $F = U, D, E$, and we have drawn the up-type quark case. The diagram is not drawn to scale, but demonstrates the suppression of off-diagonal elements due to the relative sizes of the observed fermion masses, which are taken as inputs to the model.

diagonal elements of the Yukawa coupling matrices ρ^Q, can correctly generate the CKM quark mixing angles, and accommodates the hierarchy of fermion masses. The ansatz states that the matrix elements are proportional to square roots of products of quark masses as,

$$\rho^Q_{ij} \sim \frac{\sqrt{m_i m_j}}{v}\,, \tag{12.39}$$

where the measured quark masses are usually considered as inputs to the theory.

It has been shown in Refs. [94] and [85], and we shall derive the same results

here, that a particular structure of quark mass and Yukawa coupling matrices, known as four-textures, along with a hierarchy among the parameters therein, can yield the observed hierarchy of fermion masses, and the physical Yukawa coupling patterns of the Cheng Sher ansatz. The four-texture matrices proposed have the form,

$$\kappa^{Q,0} = \frac{\sqrt{2}}{v}\begin{pmatrix} 0 & C_q & 0 \\ C_q^* & \tilde{B}_q & B_q \\ 0 & B_q^* & A_q \end{pmatrix} \qquad \rho^{Q,0} = \frac{\sqrt{2}}{v}\begin{pmatrix} 0 & C_{2,q} & 0 \\ C_{2,q}^* & \tilde{B}_{2,q} & B_{2,q} \\ 0 & B_{2,q}^* & A_{2,q} \end{pmatrix}. \quad (12.40)$$

Without loss of generality, one can assume $A_q > 0$. This structure is called a four-texture because the four elements for quarks $\rho^U_{11}, \rho^U_{13}, \rho^D_{11}$, and ρ^D_{13} are assumed to be zero. We also assume Hermiticity so the couplings do not introduce new sources of CP violation into the model. This implies the ρ^Q_{31} are also zero, $\rho^Q_{21} = \rho^{Q*}_{12}$, and $\rho^Q_{32} = \rho^{Q*}_{23}$, so there are only four unique elements in each matrix (for $Q = U, D, E$). Note that the simpler six-texture form, with $\tilde{B}_q = \tilde{B}_{2,q} = 0$ also has been studied but is found to be disfavored by CKM phenomenology. Four-texture forms on the other hand, can generate the correct CKM matrix angles.

12.4 Rotating into the Quark Mass Basis

We suppose the mass matrices M^0_q, which are proportional to the Yukawa coupling matrices $\kappa^{Q,0}$ have the four-texture form and are Hermitian for simplicity and so the couplings exhibit CP symmetry,

$$M^0_q = \begin{pmatrix} 0 & C_q & 0 \\ C_q^* & \tilde{B}_q & B_q \\ 0 & B_q^* & A_q \end{pmatrix} \qquad \text{with} \qquad |A_q| \gg |\tilde{B}_q|, |B_q|, |C_q|\,, \quad (12.41)$$

where the hierarchy of $A_q, B_q, \tilde{B}_q$, and C_q supports the observed quark mass hierarchy. The parameters A_q and $\tilde{B}_q$ are real due to the hermitian condition, and B_q and

C_q are complex. We will also assume the $\rho^{Q,0}$ matrices have the same four-texture form and hierarchy as the quark mass matrices.

In order to find the Yukawa coupling matrices in the quark mass-eigenstate basis, denoted by ρ^Q, whose elements will appear in the physical Higgs-fermion couplings, we diagonalize the quark mass matrices,

$$M_q = \text{diag}(\pm m_1^q, \mp m_2^q, m_3^q) = O_Q^T P_Q M_q^0 P_Q^\dagger O_Q \,, \tag{12.42}$$

where the matrix P_Q is designed to factor out the phases of B_q and C_q. We denote the phases by Φ_{B_q} and Φ_{C_q}, and they are both taken between $[0, 2\pi]$,

$$P_Q \;=\; \begin{pmatrix} 1 & 0 & 0 \\ 0 & e^{i\Phi_{B_q}} & 0 \\ 0 & 0 & e^{i(\Phi_{B_q}+\,\Phi_{C_q})} \end{pmatrix} . \tag{12.43}$$

At times we may drop the scripts q (or equivalently Q) which distinguish between the unique parameters for the U or D type quarks (or E in the case of leptons) because the pattern is identical for all SM fermions besides the neutrinos. We use the same unitary matrix $O_Q^T P_Q$ which diagonalizes the mass matrix to rotate the ρ^Q into the quark mass-eigenstate basis. Denoting the eigenvalues $\lambda^q_{1,2,3}$ of the diagonalized quark mass matrices M_q and using the trace and determinant properties of similar matrices and the characteristic equation, we can express $\tilde{B}_q, B_q$, and C_q in terms of A_q and the quark mass eigenvalues, denoted as $\lambda^q_{1,2,3}$:

$$\tilde{B}_q \;=\; \lambda_1^q + \lambda_2^q + \lambda_3^q - A_q \,, \tag{12.44}$$

$$|B_q| = \sqrt{\frac{(A_q - \lambda_1^q)(A_q - \lambda_2^q)(\lambda_3^q - A_q)}{A_q}} \,, \tag{12.45}$$

$$|C_q| = \sqrt{\frac{-\lambda_1^q \lambda_2^q \lambda_3^q}{A_q}} \,. \tag{12.46}$$

We will take the fermion masses as inputs to the model, along with the three parameters A_q, for which we take $A_u = A_d = A_e = A = 0.81444$ which comes from the

best fit of the CKM matrix in Ref. [97].

Under the assumption that $A_q \gg |B_q|, |\tilde{B}_q|, |C_q|$, and working in the convention in which $\lambda_3^q > |\lambda_2^q| > |\lambda_1^q|$, one can use second-order perturbation theory to derive,

$$\lambda_{1,2}^q \simeq \frac{1}{2}\left[\widetilde{B}_q - \frac{|B_q|^2}{A_q} \pm \sqrt{\left(\widetilde{B}_q - \frac{|B_q|^2}{A_q}\right)^2 + 4|C_q|^2}\right], \tag{12.47}$$

$$\lambda_3^q \simeq A_q + \frac{|B_q|^2}{A_q}, \tag{12.48}$$

where terms of $\mathcal{O}(1/A_q^2)$ have been dropped. The determinant Eq. (12.46) then forces either $\lambda_1^q < 0$ and $\lambda_2^q > 0$, or $\lambda_1^q > 0$ and $\lambda_2^q < 0$. In order to keep track of both cases at simultaneously, we define the parameter $\eta_q = \lambda_2^q/m_2^q = \pm 1$. We will work in the convention with $\eta_q = 1$, or $\lambda_2^q > 0$ and $\lambda_1^q < 0$, but both $\eta = \pm 1$ will be probed in parameter scans as follow-up work to this dissertation. Note that a six-texture ansatz with $\tilde{B}_q = 0$ would force us into the other convention with $\eta_q = -1$. The $\lambda_{1,2,3}^q$ are related to the quark masses via $\lambda_1^{u,d} = \mp m_{u,d}$, $\lambda_2^{u,d} = \pm m_{s,c}$, and $\lambda_3^{u,d} = m_{t,b}$ for the quarks and similarly for the charged leptons. The masses $m_{1,2,3}^q$ are positive and, without loss of generality, we are working in the sign convention in which $\lambda_3^q > 0$.

The matrix which diagonalizes M_q^0 (after the phases are removed) can be analytically computed in terms of the λ_i^q and A_q,

$$O_q = \begin{pmatrix} \sqrt{\frac{\lambda_2\lambda_3(A-\lambda_1)}{A(\lambda_2-\lambda_1)(\lambda_3-\lambda_1)}} & \eta\sqrt{\frac{\lambda_1\lambda_3(\lambda_2-A)}{A(\lambda_2-\lambda_1)(\lambda_3-\lambda_2)}} & \sqrt{\frac{\lambda_1\lambda_2(A-\lambda_3)}{A(\lambda_3-\lambda_1)(\lambda_3-\lambda_2)}} \\ -\eta\sqrt{\frac{\lambda_1(\lambda_1-A)}{(\lambda_2-\lambda_1)(\lambda_3-\lambda_1)}} & \sqrt{\frac{\lambda_2(A-\lambda_2)}{(\lambda_2-\lambda_1)(\lambda_3-\lambda_2)}} & \sqrt{\frac{\lambda_3(\lambda_3-A)}{(\lambda_3-\lambda_1)(\lambda_3-\lambda_2)}} \\ \eta\sqrt{\frac{\lambda_1(A-\lambda_2)(A-\lambda_3)}{A(\lambda_2-\lambda_1)(\lambda_3-\lambda_1)}} & -\sqrt{\frac{\lambda_2(A-\lambda_1)(\lambda_3-A)}{A(\lambda_2-\lambda_1)(\lambda_3-\lambda_2)}} & \sqrt{\frac{\lambda_3(A-\lambda_1)(A-\lambda_2)}{A(\lambda_3-\lambda_1)(\lambda_3-\lambda_2)}} \end{pmatrix}, \tag{12.49}$$

where we have suppressed the quark flavor indices q for clarity. The coupling matrices become very complicated when they are rotated into the quark mass-eigenstate basis. We will assume that the elements of $\rho^{Q,0}$ have the same hierarchy as the mass matrix

by assuming that its elements are those of the mass matrix A_q, B_q, C_q, and $\tilde{B}_q$, multiplied by order one constants, a_q, b_q, c_q, and $\tilde{b}_q$,

$$\rho^{Q,0} = \frac{\sqrt{2}}{v} \begin{pmatrix} 0 & c_q C_q & 0 \\ c_q C_q^* & \tilde{b}_q \tilde{B}_q & b_q B_q \\ 0 & b_q B_q^* & a_q A_q \end{pmatrix} . \tag{12.50}$$

In principle, these order one parameters can be complex, however, for simplicity in this work shall will restrict ourselves to the CP-conserving case in which they are all real. The coupling matrices in the quark mass-eigenstate basis are,

$$\rho^{\,Q} = O_Q^T P_Q \, \rho^{Q,0} \, P_Q^\dagger O_Q = \begin{pmatrix} \rho_{11}^Q & \rho_{12}^Q & \rho_{13}^Q \\ \rho_{21}^Q & \rho_{22}^Q & \rho_{23}^Q \\ \rho_{31}^Q & \rho_{32}^Q & \rho_{33}^Q \end{pmatrix} , \tag{12.51}$$

where each element is very complicated, in light of Eq. (12.49) and Eq. (12.46). We will use the exact matrix elements, taking the masses and A_q as inputs, so $\cos(\beta-\alpha)$, the order one parameters, and some Higgs potential parameters are the only free parameters in the theory.

However, to see if the Cheng Sher-like coupling pattern is roughly emergent, we take a detour to study an approximation in which $A_q, m_3^q, m_2^q \gg m_1^q$. Defining the relation,

$$A_q \;=\; m_3(1-\beta_q z), \tag{12.52}$$

with $z = m_2/m_3 \ll 1$ and $0 \leq \beta \leq 1$, we can expand in powers of z to approximate the matrix elements ρ_{ij}^Q. Then we define the complex matrices $\tilde{\chi}_{ij}^q = \chi_{ij}^q e^{i\sigma_{ij}^q}$ which include all factors besides the mass dependence and v at leading order in z,

$$\rho_{ij}^Q \;=\; \frac{\sqrt{m_i m_j}}{v} \tilde{\chi}_{ij}^q \, . \tag{12.53}$$

This is similar to the Cheng-Sher ansatz but complex phases can appear now (although we work in the CP-conserving limit). One then finds that $A_q \simeq m_{q_3}$,

$B_q \simeq \sqrt{m_{q_2} m_{q_3}}$, and $C_q \simeq \sqrt{m_{q_1} m_{q_2}}$ [85] The leading order prefactors of the χ_{ij} matrix elements are:

$$\begin{aligned}
\tilde{\chi}^q_{11} &= [\tilde{b}^q_2 - (c^{q*}_2 e^{i\Phi_{C_q}} + c^q_2 e^{-i\Phi_{C_q}})]\eta_q + [a^q_2 + \tilde{b}^q_2 - (b^{q*}_2 e^{i\Phi_{B_q}} + b^q_2 e^{-i\Phi_{B_q}})]\beta_q \\
\tilde{\chi}^q_{12} &= (c^q_2 e^{-i\Phi_{C_q}} - \tilde{b}^q_2) - \eta_q[a^q_2 + \tilde{b}^q_2 - (b^{q*}_2 e^{i\Phi_{B_q}} + b^q_2 e^{-i\Phi_{B_q}})]\beta_q \\
\tilde{\chi}^q_{13} &= (a^q_2 - b^q_2 e^{-i\Phi_{B_q}})\eta_q \sqrt{\beta_q} \\
\tilde{\chi}^q_{22} &= \tilde{b}^q_2 \eta_q + [a^q_2 + \tilde{b}^q_2 - (b^{q*}_2 e^{i\Phi_{B_q}} + b^q_2 e^{-i\Phi_{B_q}})]\beta_q \\
\tilde{\chi}^q_{23} &= (b^q_2 e^{-i\Phi_{B_q}} - a^q_2)\sqrt{\beta_q} \\
\tilde{\chi}^q_{33} &= a^q_2 \,. \qquad (12.54)
\end{aligned}$$

The diagonal elements $\tilde{\chi}^q_{ii}$ are real, while the off-diagonal elements have phases, although we will work in the CP-conserving limit with no phases. Inserting Eq. (12.53) and Eq. (12.54) into Eq. (12.38), the physical Yukawa Lagrangian becomes,

$$\begin{aligned}
-\mathscr{L}_{\rm Y} = \frac{1}{v}\,\overline{u}_i \Big[&(s_{\beta-\alpha} m_{u_i}\delta_{ij} + \varepsilon c_{\beta-\alpha}\frac{\sqrt{m_{u_i} m_{u_j}}}{\sqrt{2}}\tilde{\chi}^u_{ij})h \\
&+ (c_{\beta-\alpha} m_{u_i}\delta_{ij} - \varepsilon s_{\beta-\alpha}\frac{\sqrt{m_{u_i} m_{u_j}}}{\sqrt{2}}\tilde{\chi}^u_{ij})H \\
&- i\,\varepsilon\frac{\sqrt{m_{u_i} m_{u_j}}}{\sqrt{2}}\tilde{\chi}^u_{ij}\gamma_5 A\Big] u_j \\
+ \frac{1}{v}\,\overline{d}_i \Big[&(s_{\beta-\alpha} m_{d_i}\delta_{ij} + \varepsilon c_{\beta-\alpha}\frac{\sqrt{m_{d_i} m_{d_j}}}{\sqrt{2}}\tilde{\chi}^{d*}_{ij})h \\
&+ (c_{\beta-\alpha} m_{d_i}\delta_{ij} - \varepsilon s_{\beta-\alpha}\frac{\sqrt{m_{d_i} m_{d_j}}}{\sqrt{2}}\tilde{\chi}^{d*}_{ij})H \\
&+ i\,\varepsilon\frac{\sqrt{m_{d_i} m_{d_j}}}{\sqrt{2}}\tilde{\chi}^{d*}_{ij}\gamma_5 A\Big] d_j. \qquad (12.55)
\end{aligned}$$

This approximation shows the rough Cheng Sher-like couplings but we employ the exact expressions as in Eq. (12.38). While this expression contains the parameter ε, which keeps track of the sign definition of the field H_2, it is invariant under changing the sign of H_2 since $\varepsilon, \cos(\beta-\alpha), H$, and A all change sign. Note that $\varepsilon\cos(\beta-\alpha) = -|\cos(\beta-\alpha)|$. The expressions below show the translation between the

physical Yukawa couplings for up- and down-type quarks whether the four-texture ansatz is assumed for the coupling matrices in the Higgs basis or a generic Φ-basis, for $\phi = h, H, A$,

$$\underline{\phi u_i u_j}: \qquad \cot\beta \, \frac{\sqrt{2}\, m_{u_i}\delta_{ij}}{v} - \frac{\sqrt{m_{u_i} m_{u_j}}}{v \sin\beta}\tilde{\chi}^{u,G}_{ij} = \varepsilon\, \rho^{U}_{ij}\,, \tag{12.56}$$

$$\underline{\phi d_i d_j}: \; -\tan\beta \, \frac{\sqrt{2}\, m_{d_i}\delta_{ij}}{v} + \frac{\sqrt{m_{d_i} m_{d_j}}}{v \cos\beta}\tilde{\chi}^{d,G*}_{ij} = \varepsilon\, \rho^{D*}_{ij}\,. \tag{12.57}$$

where we have used the trig identities in Eq. (12.16) and the G script denotes quantities defined in a generic Φ-basis.

12.5 Four-texture Ansatz Manifest in a Generic Basis and Expressed in the Higgs Basis

As an aside, we will also show that one obtains the Yukawa coupling results in the literature, as calculated in Eq. (12.21) and Eq. (12.33), if we assume the four-texture forms are manifest in a generic Φ-basis and then express them in the Higgs basis. By establishing an ansatz for M_q^0, which is defined in an arbitrary Φ-basis, the authors of [85] have promoted this generic Φ-basis, and hence the angles α and β, to be physically significant. Here β represents the angle one must rotate in Higgs flavor space to transform from the Φ-basis in which the ansatz is realized to the Higgs basis. These matrices are related to the coupling matrices in the Higgs basis via,

$$\eta_2^{Q,0} = \tfrac{\sqrt{2}}{v}\sin\beta\, M_q^0 + \cos\beta\, \rho^{Q,0}\,. \tag{12.58}$$

To simplify the analysis, and obtain an approximation that looks like the Cheng Sher ansatz, we will assume the Yukawa coupling matrices $\eta_2^{Q,0}$ (which

Ref. [85] calls Y_2^q) have the same four-texture form as the mass matrices,

$$\eta_2^{Q,0} = \begin{pmatrix} 0 & c_q C_q & 0 \\ c_q C_q^* & \tilde{b}_q \tilde{B}_q & b_q B_q \\ 0 & b_q B_q^* & a_q A_q \end{pmatrix}, \tag{12.59}$$

where a_q, b_q, $\tilde{b}_q$, and c_q are real, order-one constants. Then, rearranging Eq. (12.58), the ansatz for M_q^0 and $\eta_2^{Q,0}$ gives the basis-invariant coupling matrix,

$$\rho^{Q,0} \;=\; \frac{1}{\cos\beta}\Big(\eta_2^{Q,0} - \tfrac{\sqrt{2}}{v}\sin\beta\, M_q^0\Big)\,, \tag{12.60}$$

or written out in matrix form, we find,

$$\rho^{Q,0} \;=\; \frac{1}{\cos\beta}\begin{pmatrix} 0 & (c_q - \frac{\sqrt{2}}{v}\sin\beta)C_q & 0 \\ (c_q - \frac{\sqrt{2}}{v}\sin\beta)C_q^* & 0 & (b_q - \frac{\sqrt{2}}{v}\sin\beta)B_q \\ 0 & (b_q - \frac{\sqrt{2}}{v}\sin\beta)B_q^* & (a_q - \frac{\sqrt{2}}{v}\sin\beta)A_q \end{pmatrix}. \tag{12.61}$$

Then the neutral Yukawa Lagrangian in the Higgs basis and quark interaction basis,

$$-\mathscr{L}_{\rm Y} = \overline{U}_L^0(H_1^{0*}\kappa^{U,0} + H_2^{0*}\rho^{U,0})U_R^0 + \overline{D}_L^0(H_1^0\kappa^{D,0\,\dagger} + H_2^0\rho^{D,0\,\dagger})D_R^0 + \text{h.c.}\,, \tag{12.62}$$

with Eq. (12.35) and Eq. (12.60) and writing the Higgs basis field in terms of mass eigenstates,

$$H_1^0 = \frac{1}{\sqrt{2}}\left(v + \sum_{k=1}^{3} q_{k1}h_k\right) \qquad H_2^0 = \frac{1}{\sqrt{2}}\sum_{k=1}^{3} q_{k2}h_k\,, \tag{12.63}$$

reproduces the results in Eq. (12.21) and Eq. (12.33), which are also shown in Ref. [85].

k	q_{k1}	q_{k2}
1	$c_{12}c_{13}$	$-s_{12} - ic_{12}s_{13}$
2	$s_{12}c_{13}$	$c_{12} - is_{12}s_{13}$
3	s_{13}	ic_{13}

Table 12.2: Basis-invariant combinations q_{kj} are functions of the neutral Higgs mixing angles θ_{12} and θ_{13}, where $c_{ij} \equiv \cos(\theta_{ij})$ and $s_{ij} \equiv \sin(\theta_{ij})$. The angles θ_{12} and θ_{13} are defined modulo π. By convention, we take $0 \leq c_{12},\, c_{13} \leq 1$.

12.6 The CP-violating Case

In the CP-violating case, the simple q_{ki} in Table 2.3 above become those in Table 12.2. With these replacements, the Yukawa Lagrangian becomes,

$$
\begin{aligned}
-\mathscr{L}_{\rm Y}^{U} &= \overline{U}_L^0 (H_1^{0*}\kappa^{U,0} + H_2^{0*}\rho^{U,0}) U_R^0 \,+\, \text{h.c.} \\
&= \tfrac{1}{\sqrt{2}}\, \overline{U}_L^0 \Big[\sum_{k=1}^{3} q_{k1}^* h_k\, \kappa^{U,0} + \sum_{k=1}^{3} q_{k2}^* h_k\, \rho^{U,0} \Big] U_R^0 \,+\, \text{h.c.} \\
&= \tfrac{1}{\sqrt{2}}\, \overline{U}_L^0 \Big[(q_{11}h_1 + q_{21}h_2 + q_{31}h_3)\kappa^{U,0} + (q_{12}^* h_1 + q_{22}^* h_2 + q_{32}^* h_3)\rho^{U,0} \Big] U_R^0 \,+\, \text{h.c.} \\
&= \tfrac{1}{\sqrt{2}}\, \overline{U}_L \Big[(q_{11}\kappa^U + q_{12}^*\rho^U) h_1 + (q_{21}\kappa^U + q_{22}^*\rho^U) h_2 + (q_{31}\kappa^U + q_{32}^*\rho^U) h_3 \Big] U_R + \text{h.c.} \\
&\approx \frac{1}{v}\, \overline{U}_L \Big[(q_{11} m_u \delta_{uu'} \,+\, q_{12}^* \frac{\sqrt{m_u m_{u'}}}{\sqrt{2}} \tilde{\chi}_{uu'}) h_1 \\
&\qquad + (q_{21} m_u \delta_{uu'} \,+\, q_{22}^* \frac{\sqrt{m_u m_{u'}}}{\sqrt{2}} \tilde{\chi}_{uu'}) h_2 \\
&\qquad + (q_{31} m_u \delta_{uu'} \,+\, q_{32}^* \frac{\sqrt{m_u m_{u'}}}{\sqrt{2}} \tilde{\chi}_{uu'}) h_3 \Big] U_R \,+\, \text{h.c.}\,. \qquad (12.64)
\end{aligned}
$$

12.7 Approximate Analysis of the Yukawa Matrices

As an aside, if one wishes to only approximate the four-texture matrices and their diagonalization, as shown in [90], one can simplify their analysis greatly. Taking $\tilde{B}_q = 0$ (six-texture) for the moment, and working in the $\lambda_1 = m_1$ and $\lambda_2 = -m_2$ sign case, we can express the parameters in M_q^0 in terms of the quark

masses,

$$A_q \;=\; m_1 - m_2 + m_3 \tag{12.65}$$

$$|B_q| = \sqrt{m_1 m_2 + m_2 m_3 - m_1 m_3 - |C_q|^2} \tag{12.66}$$

$$|C_q| = \sqrt{\frac{m_1 m_2 m_3}{A_q}}\,. \tag{12.67}$$

If we consider m_1 to also be much lighter than m_2, and so extend the mass hierarchy to $m_3 \gg m_2 \gg m_1$, as is roughly evident in the quark mass hierarchy, the expressions above reduce to:

$$A_q \approx m_3\,, \qquad |B_q| \approx \sqrt{m_2 m_3}\,, \qquad |C_q| \approx \sqrt{m_1 m_2}\,. \tag{12.68}$$

The mass matrices are then diagonalized,

$$M_q = O_Q^T P_Q^\dagger M_q^0 P_Q O_Q\,, \tag{12.69}$$

where in this approximation the diagonalization matrix $P_Q O_Q$ is given by,

$$P_Q O_Q \;=\; \begin{pmatrix} 1 & 0 & 0 \\ 0 & e^{i\Phi_{B_q}} & 0 \\ 0 & 0 & e^{i(\Phi_{B_q}+\Phi_{C_q})} \end{pmatrix} \begin{pmatrix} 1 & -\sqrt{m_1/m_2} & 0 \\ \sqrt{m_1/m_2} & 1 & \sqrt{m_2/m_3} \\ -\sqrt{m_1/m_3} & \sqrt{m_2/m_3} & 1 \end{pmatrix}. \tag{12.70}$$

Comparing this with Eq. (12.49), we see that this rotation matrix is much simpler and is easier to understand in terms of a pattern of ratios of quark masses.

Chapter 13

Phenomenology

We return to our main line of reasoning, having assumed the four-texture ansatz is manifest in the Higgs basis and working with the physical couplings that arise after rotating into the quark, lepton, and Higgs mass bases. We employ the program HiggsTools to find the regions of parameter space that are not in conflict with any experimental result for searches for new scalars or precision h_{125} Higgs boson measurements. For parameter points in those regions, we then compute many flavor-violating observables. We compare these results with the latest experimental bounds to determine the range of validity of this model. Finally, we summarize the implications of having suppressed yet nonzero off-diagonal Yukawa couplings on future searches for flavor-violating processes at particle colliders. In particular, we present which flavor-violating channels we expect to appear in collider data first, pertinent to the framework of the four-texture model.

13.1 Parameter Scans

To probe all possible regions of parameter space, we perform a scan over $\cos(\beta - \alpha)$ and the order one parameters a_q, b_q, c_q, and $\tilde{b}_q$. The scan reveals that

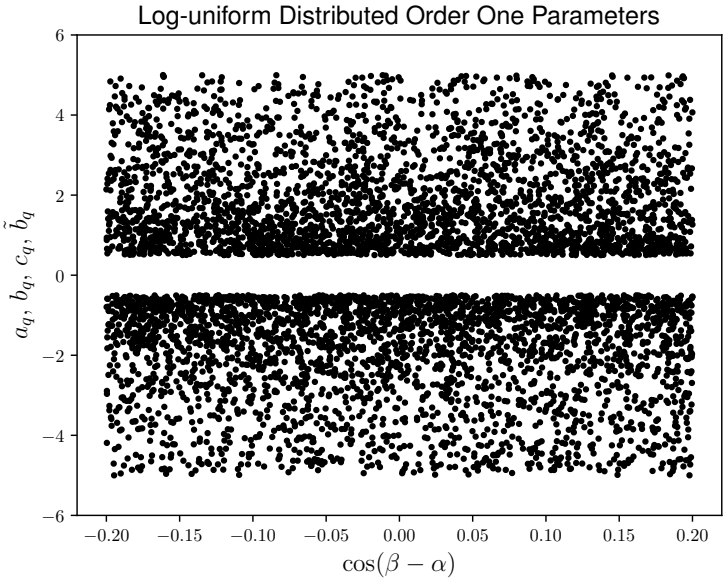

Figure 13.1: When we say we scan over order one parameters, we mean numbers that lie in the range $[0.5, 5]$, have either sign, and are log-uniform distributed, as shown. This way they do not skew the average values higher than 1. Viewed on a logarithmic plot, the distribution would appear flat. One can also see that $\cos(\beta-\alpha)$ has a flat distribution and is restricted to $[-0.2, 0.2]$.

$\cos(\beta-\alpha) \lesssim 0.2$ and we implement log-uniform distributed order one parameters, so that their distribution is flat when viewed on a logarithmic plot. This compresses most points to be near the lower end of the range, and fewer appear up near the upper end of the range. We take all order one parameters to be log-uniformly distributed in the range $(a_q, b_q, c_q, \tilde{b}_q) \in [-5, -0.5] \cup [0.5, 5]$, which is accomplished via,

$$(-1)^p \left[\log_{10}(0.5) \, + \, r(10^{\log_{10}(t)} - \log_{10}(0.5)) \right], \tag{13.1}$$

where p is +1 or -1 chosen randomly to get parameters of either sign, b is the lower limit 0.5, r is a random number between $[0, 1]$ with a flat distribution, and t is the upper limit 5. We first check that the resulting model parameter points produce a scalar, identified as the lightest Higgs boson h in our model, that has production and decay properties that closely resemble the observed SM-like scalar h_{125} with a mass of 125 GeV.

To determine whether a parameter point produces a satisfactory h, we calculate the hff' couplings it predicts and pass this information to the public code HiggsTools [91]. In particular, we define HiggsPredictions objects, run HiggsSignals on them, and only keep points with $\Delta\chi^2 < 6$, where $\Delta\chi^2 = \chi^2 - 123$. These points are colored green in Fig. 13.2. HiggsTools incorporates 131 precision Higgs observables in total but only 123 observables are used in the most precise mode, SMHiggsEW (see the "Reference Model" section of the HiggsTools documentation [91]), which includes higher order electroweak corrections than the SMHiggs reference model.

For the time being, we decouple the other Higgs bosons by setting their masses at $m_{H,A,H^\pm} = 800$ GeV. This causes their contributions to cross sections and branching ratios to be suppressed and become insignificant so we can focus on studying models with a valid h boson. In future work, we will decrease the masses of the other scalars to investigate in which channels they might first appear in new particle collider data, and how they may modify the branching ratios of the channels we discuss below. Recall that the electroweak T parameter forces either m_H or m_A to be within about 60 GeV of $m_{H^\pm}$.

We also pass all parameter points through HiggsBounds, which tests our predictions against particle collider searches for scalars. In Fig. 13.2, red points fail this test, and most of these points have large $\Delta\chi^2$ anyway, while blue points are determined by HiggsBounds to not be in conflict with any bounds coming from collider searches for scalars. Green points also have $\Delta\chi^2 < 6$, so these are the points we use in our phenomenological study.

Due to the formulae for the elements of the matrices χ^q_{ij}, as shown in Eq. (12.54), and the parameters therein being order one, our scans can only produce

points with maximum values for each $|\chi^q_{ij}|$. Also, larger $|\chi^q_{ij}|$ are more likely to violate either HiggsBounds or HiggsSignals because they would produce large deviations from the SM couplings and insufficiently suppressed FCNCs. In Figs. 13.3 and 13.4, we show the allowed values of the most critical coupling matrix elements ρ^Q_{ij}, which are calculated exactly but roughly follow the Cheng Sher-like pattern shown in Eq. (12.53).

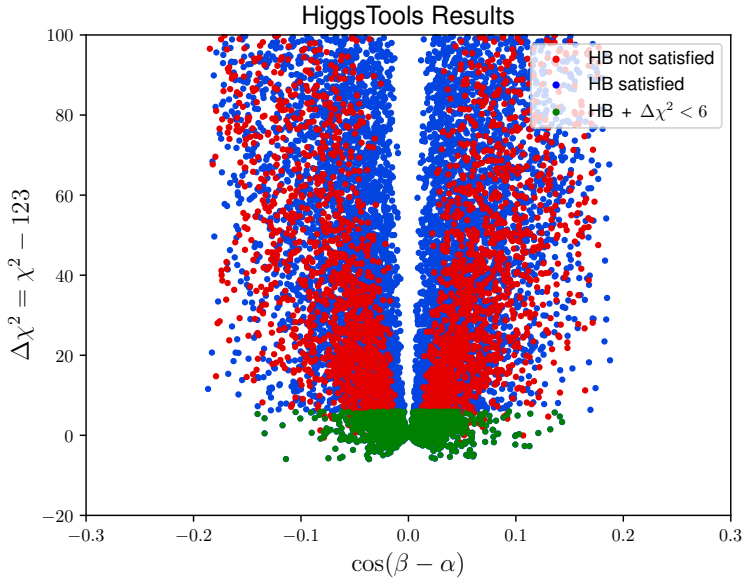

(a)

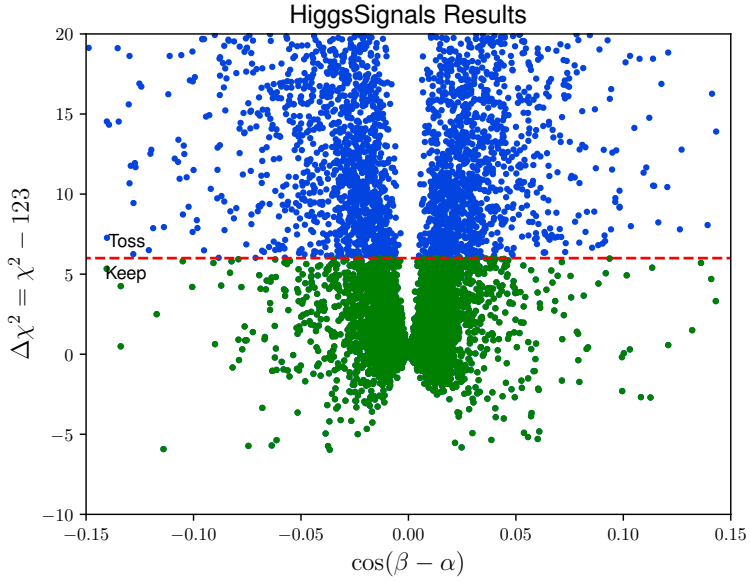

(b)

Figure 13.2: HiggsTools results of a scan over $\cos(\beta-\alpha)$ and the order one parameters $a_q, b_q, c_q, \tilde{b}_q$. Panel (a) shows how most points generated have a $\Delta\chi^2 \lesssim 600$ and the scan also generates many points which horribly violate h_{125} data, and hence have massive $\Delta\chi^2 > 600$. Red points fail the HiggsBounds test which compares our predictions with particle collider searches for scalars. In panel b, we zoom in on the many points which do have small $\Delta\chi^2$ values. From this point forward, we only keep green points with $\Delta\chi^2 < 6$.

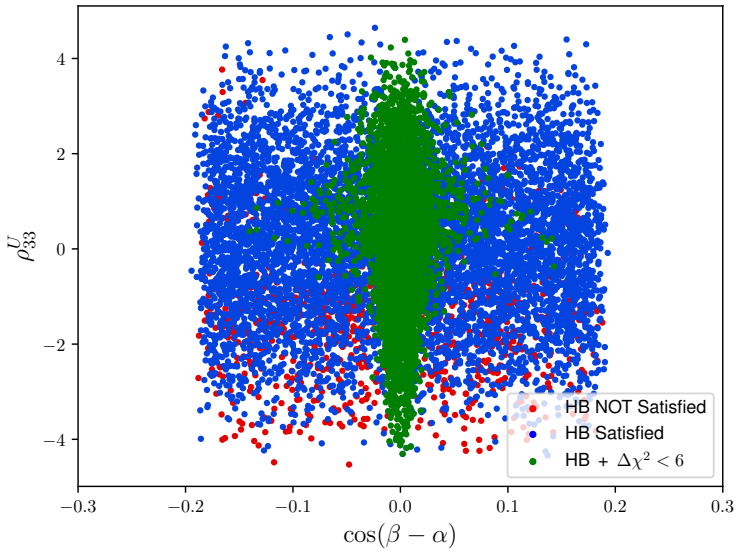

(a)

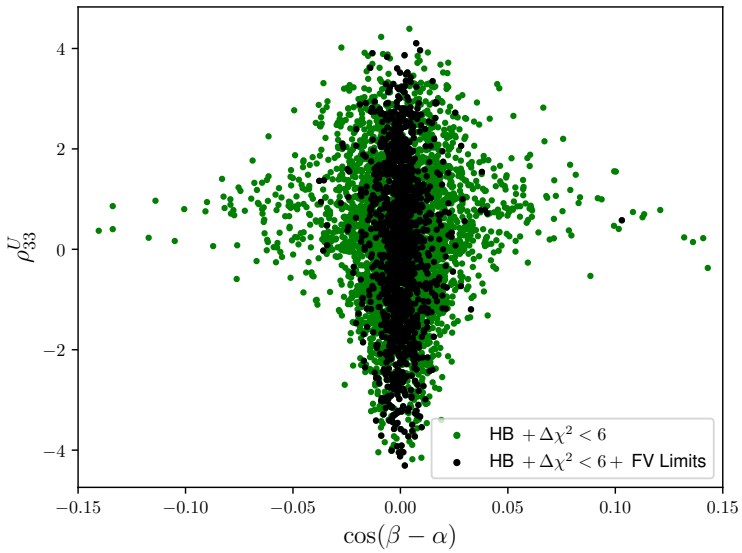

(b)

Figure 13.3: Panel (a) shows where all parameter points land in $\cos(\beta - \alpha)$ vs ρ^U_{33} space. We see that either $\rho^U_{33} = \rho_{tt}$ or $\cos(\beta - \alpha)$ has to be small so the cross section $\sigma(gg \to h)$ is not too far from $\sigma_{\rm SM}(gg \to h)$, since gluon-gluon fusion Higgs boson production is dominated by t quark loops. In Panel (b) we show only points that satisfy HiggsBounds and have $\Delta\chi^2 < 6$, which are the points we keep for our phenomenological studies. Values of ρ_{tt} larger than 4 are inaccessible if $a_u, b_u, c_u, \tilde{b}_u$ are order one parameters. Yellow points also satisfy all flavor-violating limits that we calculated, as discussed in the next section.

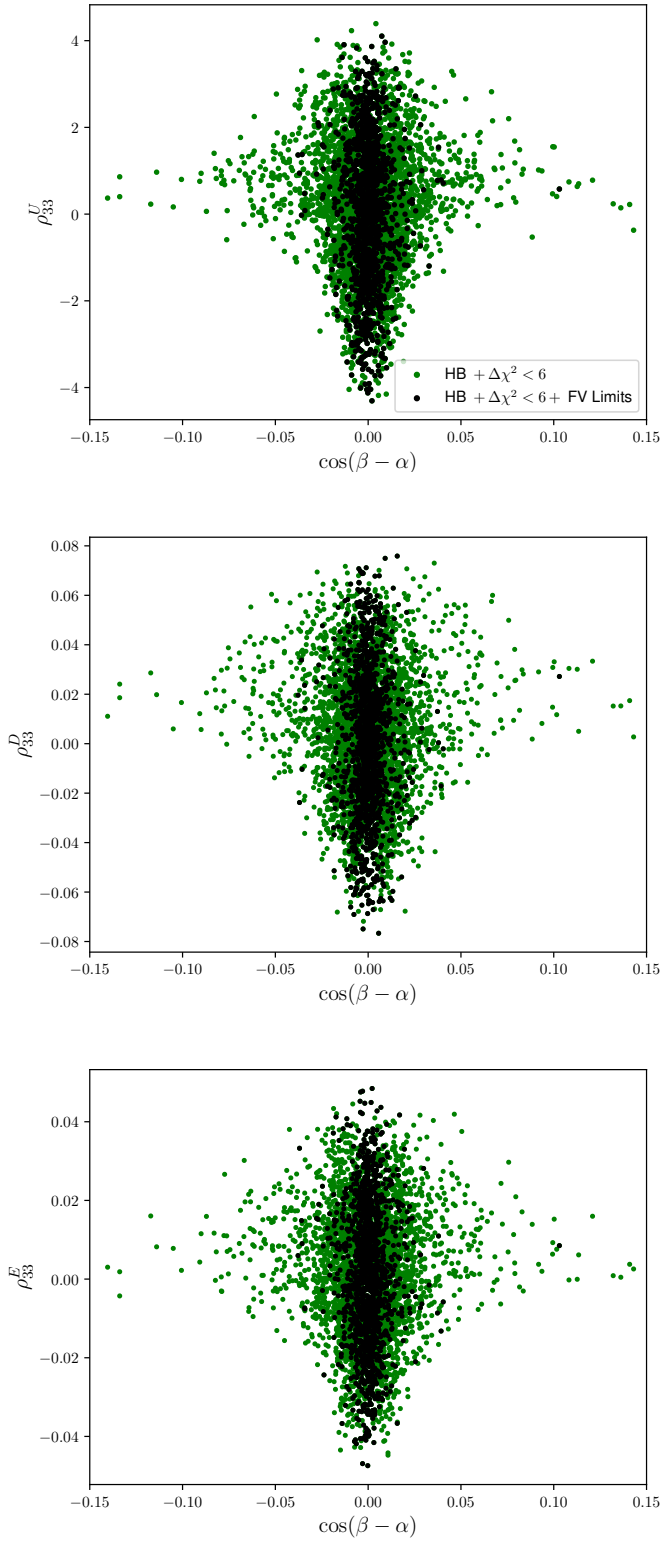

Figure 13.4: The largest elements in $\rho^{U,D,E}$ are the $i = j = 3$ elements on the diagonal, corresponding to Higgs' interactions with t quarks in the top panel, b quarks in the middle panel, and $\tau^{\pm}$ leptons in the bottom panel. We see that small $\cos(\beta - \alpha)$ is favored in all cases, yet values as large as ~ 0.2 can be reached for all ρ^Q_{ij}.

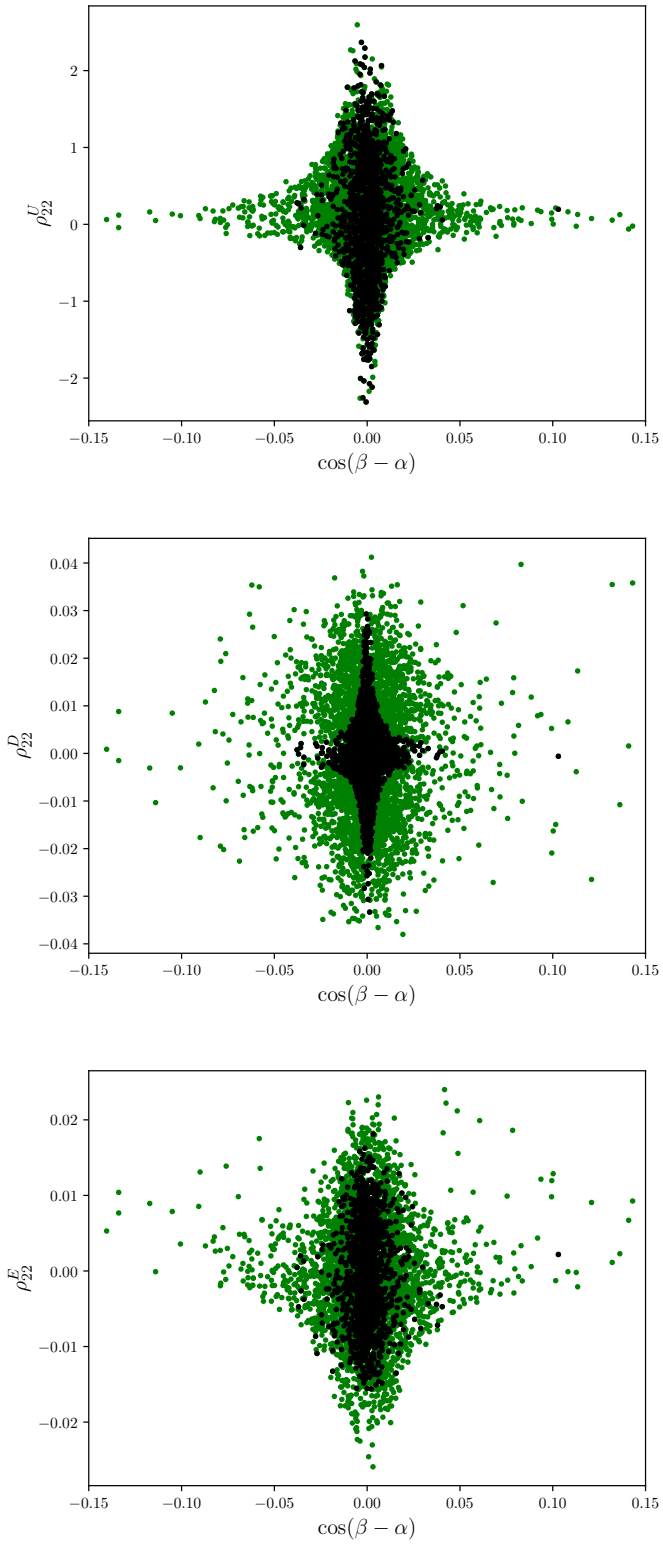

Figure 13.5: The ρ_{22}^F elements on the diagonal are expected to be much smaller than the ρ_{33}^F elements in Fig. 13.4. These correspond to Higgs bosons' interactions with c quarks, s quarks, and muons.

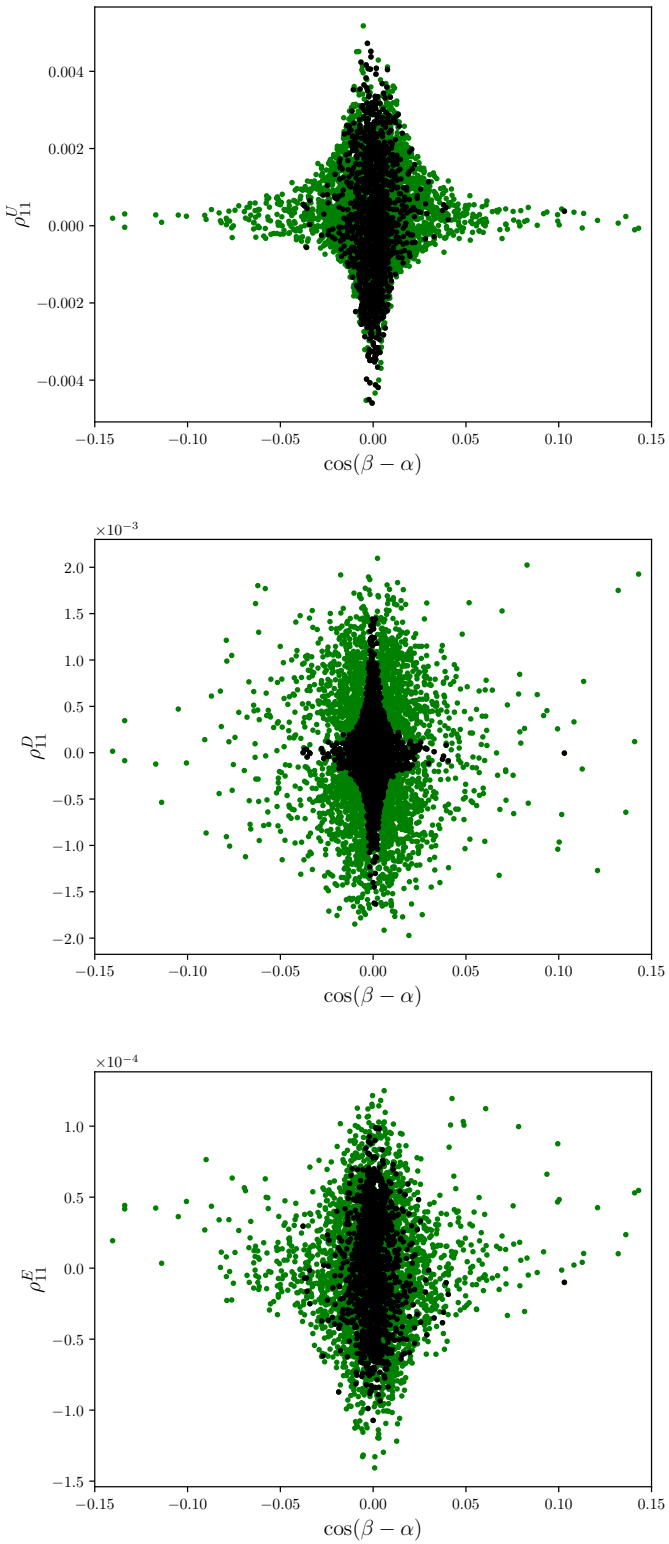

Figure 13.6: The ρ_{11}^F values are expected to be the smallest of the diagonal elements. These correspond to Higgs bosons' interactions with u and d quarks and electrons.

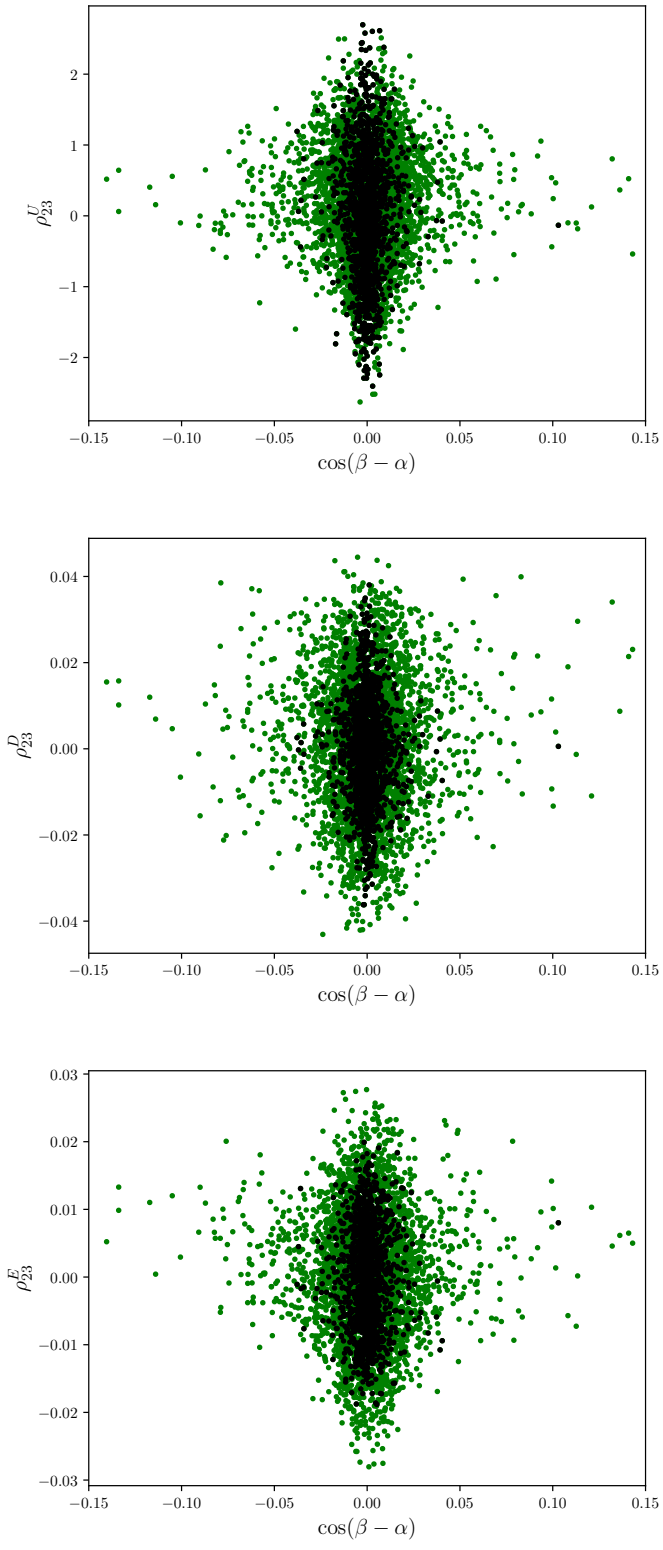

Figure 13.7: The ρ_{23}^F elements should be suppressed compared to the ρ_{33}^F elements. These couplings introduce flavor-violating Higgs-fermion interactions between t and c quarks, b and s quarks, and taus and muons.

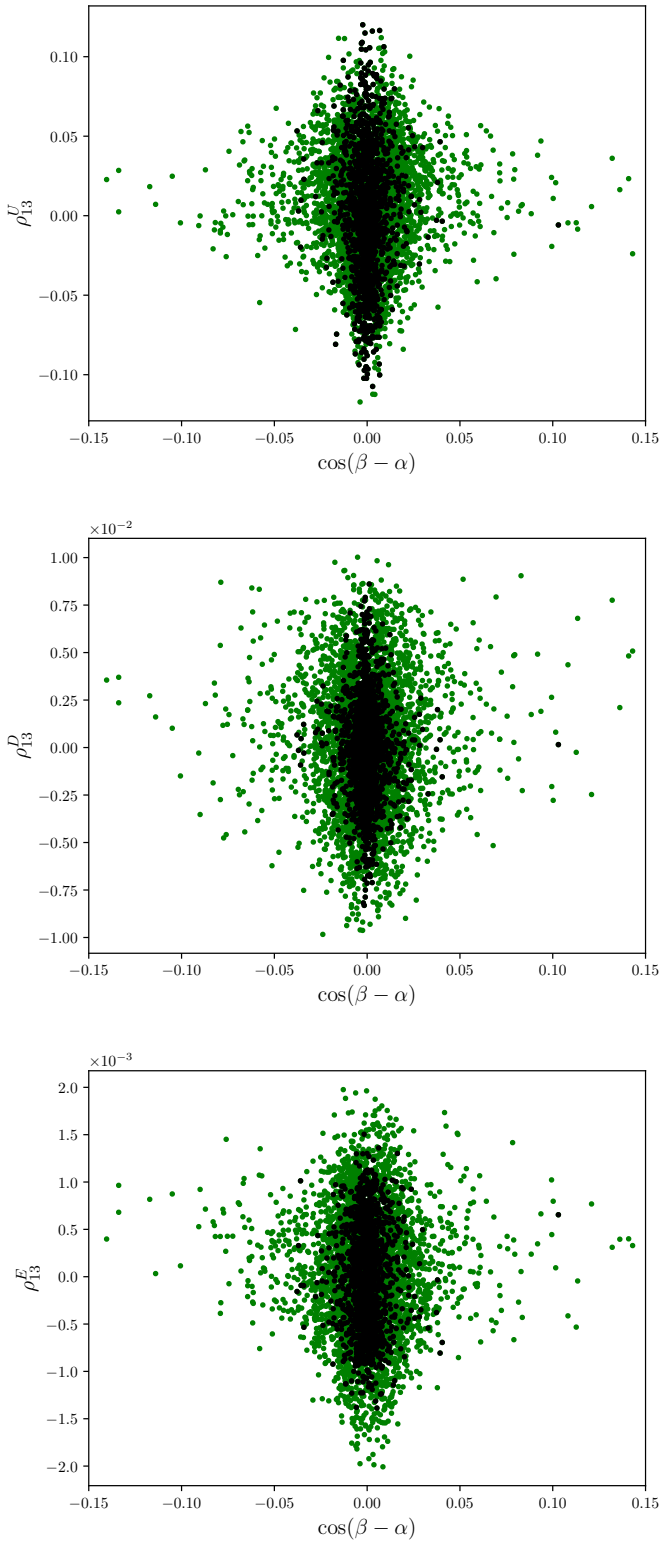

Figure 13.8: The ρ_{13}^F elements should be very suppressed compared to the ρ_{33}^F elements. These couplings introduce flavor-violating Higgs-fermion interactions between t and u quarks, b and d quarks, and taus and electrons.

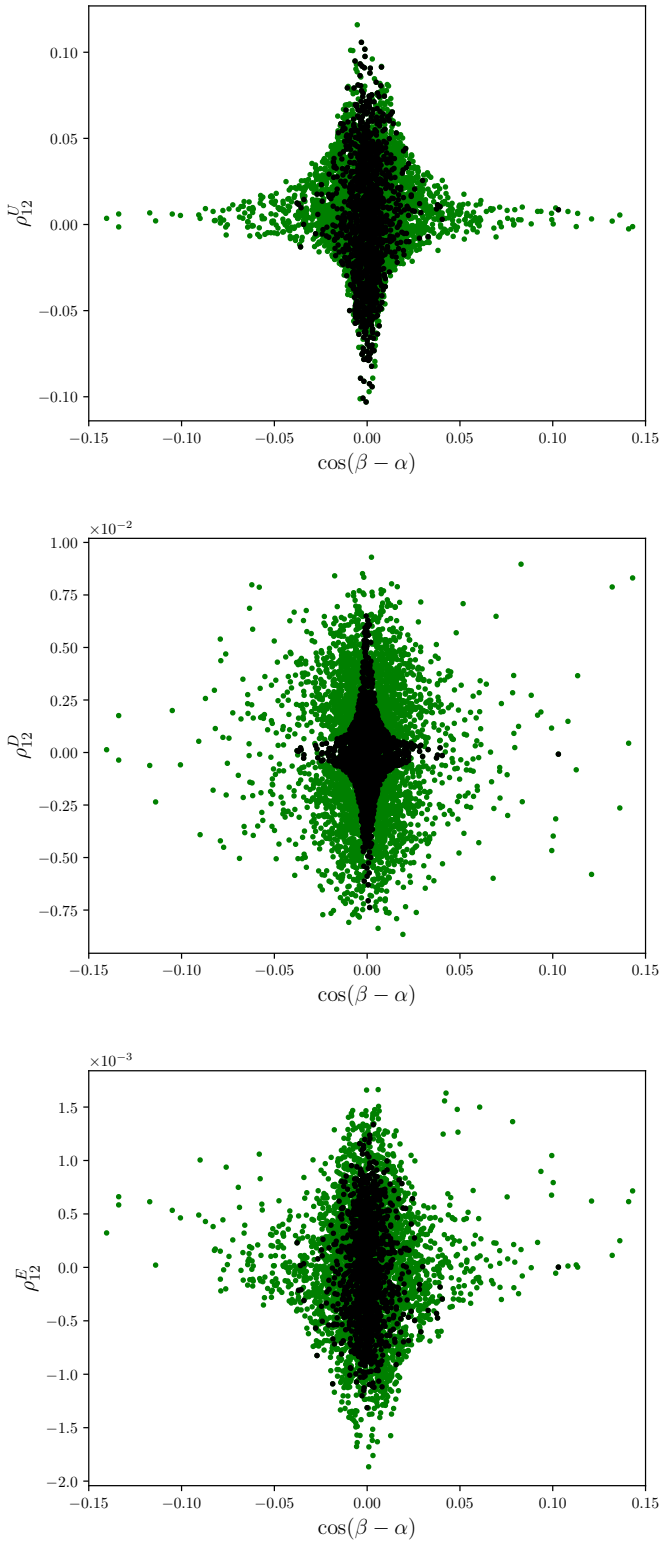

Figure 13.9: The ρ_{12}^F elements should be suppressed compared to the ρ_{22}^F elements. These couplings introduce flavor-violating Higgs-fermion interactions between c and u quarks, s and d quarks, and muons and electrons.

13.2 Bounds on Flavor-violating Observables

With a heap of viable parameter points in hand, we can turn our attention to flavor-violating processes. We ask what kinds of branching ratios our model points predict, and are they near, above, or below current limits. This analysis will eliminate some regions of parameter space. Keep in mind that we can always produce points with arbitrarily small couplings in our scans, so we can always have viable parameter space, yet those kinds of points are not particularly interesting because they do not predict anything observable. The most critical flavor-violating observables in our model are the following processes:

1. $h \to \ell_1^\pm \ell_2^\mp$
2. $\ell_1^\pm \to \ell_2^\pm + \gamma$
3. $\ell^\pm \to \ell_1^\pm \ell_2^\mp \ell_3^\pm$
4. $t \to c + h$
5. Neutral meson mixing: $P^0 - \overline{P}^0$, where $P = K, B_{s,d}, D$
6. $B_{s,d}^0 \to \ell^\pm \ell^\mp$ for $\ell = \mu, \tau$
7. $b \to s + \ell^\pm \ell^\mp$

When we use the $\pm$ symbol on the right side of a process $A \to B^\pm$ only, we mean the sum of the two possible final states, which are equal because we are working in the CP-conserving limit. This doubles the value of the branching ratio. When $\pm$ also appears on the left side of the equation $A^\pm \to B^\pm$, we are mean either one sign or the other, which are equal in the CP-conserving limit. Below, we discuss each process and the formulae used in their calculation, and we plot the resulting predictions and compare with experimental bounds.

FV Channel	4-texture Max. BRs	Exp. Bound on BRs	
$h \to \tau^{\pm} + \mu^{\mp}$	10^{-3}	1.5×10^{-3}	95%
$h \to \tau^{\pm} + e^{\mp}$	10^{-5}	2.2×10^{-3}	95%
$h \to \mu^{\pm} + e^{\mp}$	10^{-5}	6.1×10^{-5}	95%
$\tau^{\pm} \to \mu^{\pm} + \gamma$	10^{-10}	4.2×10^{-8}	90%
$\tau^{\pm} \to e^{\pm} + \gamma$	10^{-11}	3.3×10^{-8}	90%
$\mu^{\pm} \to e^{\pm} + \gamma$	10^{-8} (!)	4.2×10^{-13}	90%
$t \to h + c$	10^{-3}	7.3×10^{-4}	95%
$\mu^{-} \to e^{-}e^{+}e^{-}$	10^{-12}	1.0×10^{-12}	90%
$\tau^{-} \to e^{-}e^{+}e^{-}$	10^{-13}	2.7×10^{-8}	90%
$\tau^{-} \to \mu^{-}e^{+}e^{-}$	10^{-11}	2.7×10^{-8}	90%
$\tau^{-} \to \mu^{+}e^{-}e^{-}$	10^{-11}	1.7×10^{-8}	90%
$\tau^{-} \to e^{-}\mu^{+}\mu^{-}$	10^{-9}	1.8×10^{-8}	90%
$\tau^{-} \to e^{+}\mu^{-}\mu^{-}$	10^{-9}	1.5×10^{-8}	90%
$\tau^{-} \to \mu^{-}\mu^{+}\mu^{-}$	10^{-7}	2.1×10^{-8}	90%
$B_s^0 \to \mu^{+}\mu^{-}$	–	$(3.01 \pm 0.35) \times 10^{-9}$	
$B_s^0 \to \tau^{+}\tau^{-}$	–	6.8×10^{-3}	95%
$B_d^0 \to \mu^{+}\mu^{-}$	–	$7^{+13}_{-11} \times 10^{-11}$	
$B_d^0 \to \tau^{+}\tau^{-}$	–	2.1×10^{-3}	95%
$b \to s + \mu^{+}\mu^{-}$	–	–	
Meson Mixing	4-tex. Max. $\lvert C_4^P \rvert$ GeV^{-2}	Exp. Bound on $\lvert C_4^P \rvert$ GeV^{-2}	
$K^0 - \overline{K}^0$	10^{-11}	3.6×10^{-15}	95%
$B_s^0 - \overline{B}_s^0$	10^{-10}	1.6×10^{-11}	95%
$B_d^0 - \overline{B}_d^0$	10^{-11}	2.1×10^{-13}	95%
$D^0 - \overline{D}^0$	10^{-11} (!)	4.8×10^{-14}	95%

Table 13.1: The column on the left shows all flavor-violating channels' branching ratios that we computed and expected to provide the strongest cuts on our model's parameters. The largest possible BR's predicted by our scans are shown in the second column, and the experimental upper limits [24] for each are shown in the column on the right. Note that we can always produce models with smaller BR's in a given channel to evade the experimental limit, but being able to produce a signal that could eventually be measured is far more interesting The dashes represent channels in which our calculations are still in progress. The neutral meson mixing section at the bottom are included to list all considered flavor-violating processes and the bounds on Wilson coefficients are shown in Table 13.2 below.

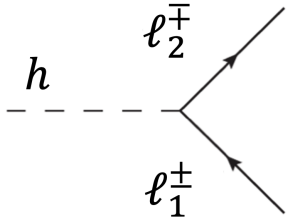

Figure 13.10: Higgs boson decay into two different flavors of leptons due to the flavor non-conserving interactions in this model.

13.2.1 $h \to \ell_1^{\pm}\ell_2^{\mp}$

The processes $h \to \tau^{\pm}\mu^{\mp}$ and $h \to \tau^{\pm}e^{\mp}$ are found to be non-zero in LHC Run 2 data [95]. The most stringent constraint on our model comes from $\mathrm{BR}(h \to \tau^{\pm}\mu^{\mp})$, while limits on $\mathrm{BR}(h \to \tau^{\pm}e^{\mp})$ and $\mathrm{BR}(h \to \mu^{\pm}e^{\mp})$ are likely to be weaker in all regions of parameter space. The $\mathrm{BR}(h \to \tau^{\pm}\ell^{\mp})$ is [88],

$$\begin{aligned}\mathrm{BR}(h \to \tau^{\pm}\ell^{\mp}) &= \frac{\Gamma(h \to \tau^{+}\ell^{-}) + \Gamma(h \to \tau^{-}\ell^{+})}{\Gamma_h} \\ &= \frac{c_{\beta\alpha}^2 m_h}{16\pi^2\,\Gamma_h}\left(|\rho^E_{\tau\ell}|^2 + |\rho^E_{\ell\tau}|^2\right), \end{aligned} \tag{13.2}$$

where $\ell = \mu, e$. Since we are working in the CP-conserving limit, in which the ρ^E matrices are Hermitian, the phases vanish and Eq. (13.2) simplifies to,

$$\mathrm{BR}(h \to \tau^{\pm}\ell^{\mp}) = (4.95 \times 10^2)\, c_{\beta\alpha}^2\, \rho^2_{\tau\ell}\,, \tag{13.3}$$

where we have used the measured value of the Higgs decay width $\Gamma_h = 3.2$ MeV [24]. ATLAS and CMS have both reported excesses in $h \to \tau^{\pm} + \mu^{\mp}$, and they find best fit values consistent with one another [87],

$$\mathrm{BR}_{\mathrm{ATLAS}}(h \to \tau^{\pm}\mu^{\mp}) = (0.77 \pm 0.62)\%\,, \tag{13.4}$$

$$\mathrm{BR}_{\mathrm{CMS}}(h \to \tau^{\pm}\mu^{\mp}) = (0.84^{+0.39}_{-0.37})\%\,. \tag{13.5}$$

The SM cannot generate these values, so this is an indication of BSM physics. We see in Figs. 13.11—13.13 the predictions of our model and the experimental limits.

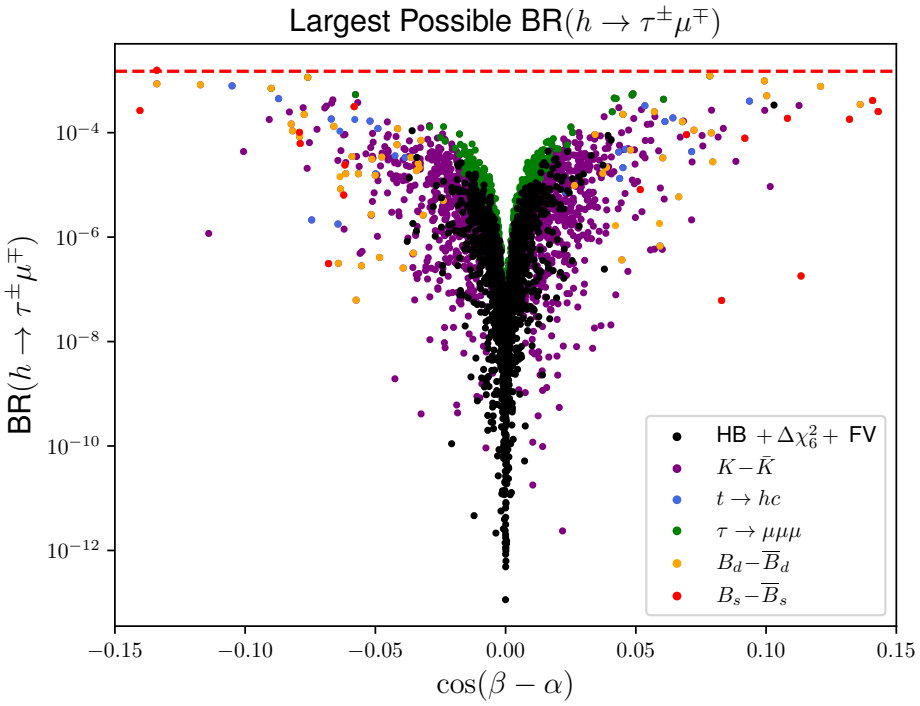

Figure 13.11: Branching ratio vs. $\cos(\beta - \alpha)$ for the process $h \to \tau + \mu$.

Black points pass HiggsBounds, have $\Delta\chi^2 < 6$, and do not make predictions in any FV channel that we calculated (besides $\mu \to e\gamma$ and $D-\bar{D}$) that is in violation with current bounds. The colors represent in which channel a point violated the limit. The purple points are plotted first, then blue, green, yellow, red, and finally black, on top of one another in that order.

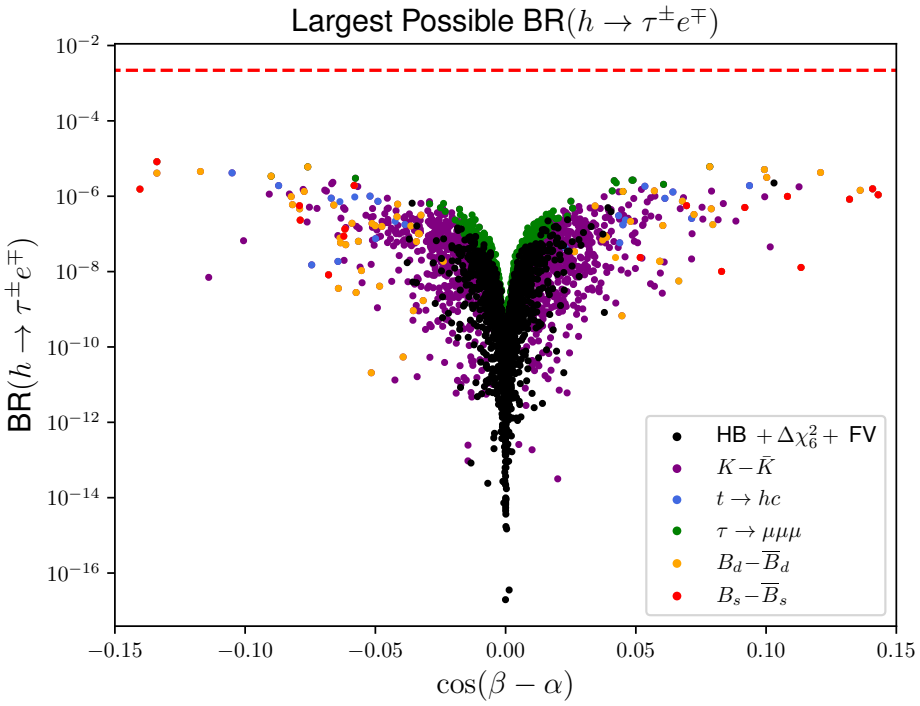

Figure 13.12: Branching ratio vs. $\cos(\beta - \alpha)$ for the process $h \to \tau + e$.

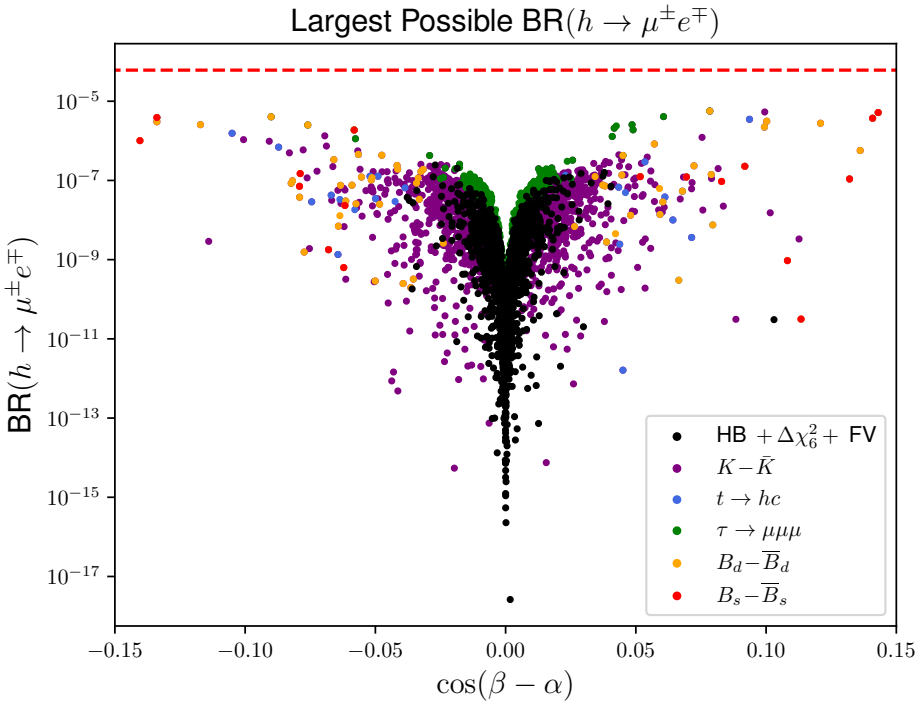

Figure 13.13: Branching ratio vs. $\cos(\beta - \alpha)$ for the process $h \to \mu + e$.

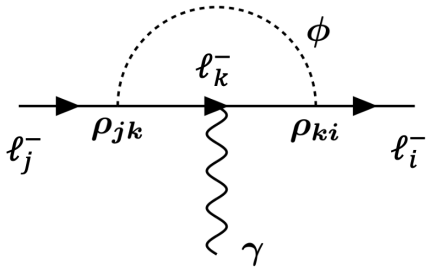

Figure 13.14: One-loop Barr-Zee type Feynman diagrams used in the calculation of $\mathrm{BR}(\ell_1^\pm \to \ell_2^\pm + \gamma)$, where $\phi = h, H, A,$. The diagram with the heaviest lepton $\tau^\pm$ in the loop dominates. These diagrams correspond to the first sum in Eq. (13.8) and are suppressed compared to the two-loop diagrams [92].

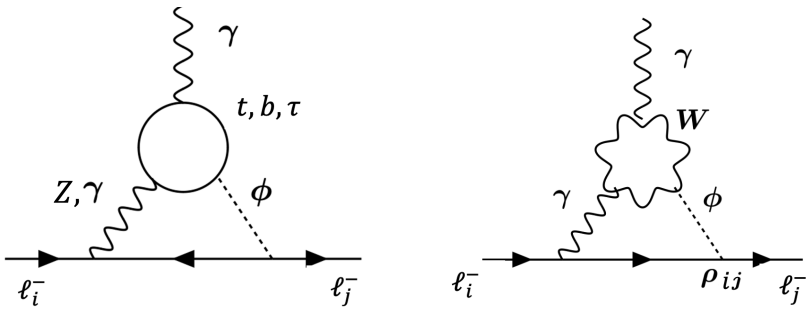

(a) (b)

Figure 13.15: Dominant two-loop Barr-Zee type Feynman diagrams used in the calculation of $\mathrm{BR}(\ell_1^\pm \to \ell_2^\pm + \gamma)$, where $\phi = h, H, A$, and the heaviest fermions $t, b, \tau^\pm$ and $W^\pm$ bosons dominate the loop factors. These diagrams correspond to the second and third sums in Eq. (13.8) from Ref. [92].

13.2.2 $\ell_1^\pm \to \ell_2^\pm + \gamma$.

In these channels, Barr-Zee type contributions at two-loop level are dominant in most cases [87], so we must compute the branching ratios to two-loop level. We know $\mu^\pm \to e^\pm + \gamma$ is measured most precisely but there is a mass factor suppression, so the strongest bounds are likely to come from $\tau^\pm \to \mu^\pm + \gamma$. For the $\tau \to \mu + \gamma$ process, we have [92],

$$\frac{\Gamma(\tau \to \mu\gamma)}{\Gamma(\tau \to \mu\nu\bar{\nu})} = \frac{48\pi^3\alpha}{G_F^2}\left(|A_L|^2 + |A_R|^2\right) < \frac{4.2 \times 10^{-8}}{0.17}, \tag{13.6}$$

where the current bound $\mathrm{BR}(\tau \to \mu\gamma) < 4.2 \times 10^{-8}$ was used [24] to obtain an estimate of the limit on the amplitudes A_L and A_R, which are equal in the CP-

conserving case, so we denote them with A,

$$A \sim 10^{-4} G_F \,. \tag{13.7}$$

Following Ref. [92] (also see [87]), we can estimate $\mathrm{BR}(\tau \to \mu\gamma)$ by neglecting the lepton masses in the kinematics and including the one-loop diagram in Panel (a) of Fig. 13.15, which corresponds to the first sum below, and a subset of two-loop diagrams, as shown in Panel (b) and one with the $W^\pm$ loop replaced with a t or b quark, which correspond to the second and third sums below. The amplitude for $\tau \to \mu + \gamma$, for example, is given by,

$$\begin{aligned} A \simeq \frac{1}{16\pi^2}\Bigg(& \sqrt{2}\sum_\phi \frac{g_{\phi\mu\tau} g_{\phi\tau\tau}}{m_\phi^2}\left(\ln\frac{m_\phi^2}{m_\tau^2} - \frac{3}{2}\right) \\ & + 2\sum_{\phi,f} g_{\phi\mu\tau} g_{\phi ff} \frac{N_c Q_f^2 \alpha}{\pi} \frac{1}{m_\tau m_f} f_\phi\!\left(\frac{m_f^2}{m_\phi^2}\right) \\ & - \sum_{\phi=h,H} g_{\phi\mu\tau} C_{\phi WW} \frac{g\alpha}{2\pi m_\tau m_W} \times \\ & \left[3 f_\phi\!\left(\frac{m_W^2}{m_\phi^2}\right) + \frac{23}{4} g\!\left(\frac{m_W^2}{m_\phi^2}\right) + \frac{3}{4} h\!\left(\frac{m_W^2}{m_\phi^2}\right) + m_\phi^2 \frac{f_\phi\left(\frac{m_W^2}{m_\phi^2}\right) - g\left(\frac{m_W^2}{m_\phi^2}\right)}{2m_W^2} \right] \Bigg) \end{aligned} \tag{13.8}$$

where $\phi = h, H, A$ and $f = t, b$, and the coupling $g_{\phi ff'}$ of the internal loop fermion to the scalar ϕ are,

$$g_{h,ff'} = \frac{m_f}{v} s_{\beta-\alpha} \delta_{ff'} - |c_{\beta-\alpha}| \frac{\rho_{ff'}}{\sqrt{2}} \,, \tag{13.9}$$

$$g_{H,ff'} = \frac{m_f}{v} c_{\beta-\alpha} \delta_{ff'} - s_{\beta-\alpha} \frac{\rho_{ff'}}{\sqrt{2}} \,, \tag{13.10}$$

$$g_{A,ff'} = i\frac{\rho_{ff'}}{\sqrt{2}} \,, \tag{13.11}$$

where $g_{Aff'}$ appears in the Feynman rule with a γ_5, and the coupling $g_{\phi WW}$ is,

$$g_{\phi WW} = i\, g\, m_W\, C_{\phi WW}\, g^{\mu\nu} \,, \tag{13.12}$$

$$C_{hWW} = s_{\beta-\alpha} \,, \quad C_{HWW} = c_{\beta-\alpha} \,, \quad C_{AWW} = 0 \,. \tag{13.13}$$

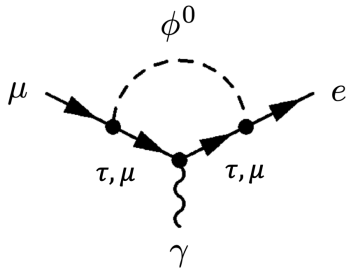

Figure 13.16: The one-loop Barr-Zee type Feynman diagrams in the calculation of $\mathrm{BR}(\mu^\pm \to e^\pm + \gamma)$ where diagrams with virtual τ and μ are included but virtual e are neglected [87]. The two-loop diagrams still dominate since these one-loop diagrams will be suppressed by small off-diagonal couplings [93].

In all these processes, the heaviest fermions in the loops dominate.

Note that for the process $\mu \to e + \gamma$ there are one-loop diagrams with a τ or μ in the loop [87] as shown in Fig. 13.16, and the τ loops dominate the one-loop diagrams. We neglect virtual electrons due to their small mass. At two-loop level we also include Z bosons in the loop for the $\mu \to e + gamma$ case.

The functions $f(z)$, $g(z)$, and $h(z)$ in Eq. (13.8) above are [92]:

$$f_{h,H}(z) = \frac{z}{2}\int_0^1 dx\, \frac{(1-2x(1-x))}{x(1-x)-z} \ln\frac{x(1-x)}{z} \qquad \text{(scalars)}, \tag{13.14}$$

$$g(z) \equiv f_A(z) = \frac{z}{2}\int_0^1 dx \frac{1}{x(1-x)-z} \ln\frac{x(1-x)}{z} \qquad \text{(pseudoscalar)}, \tag{13.15}$$

$$h(z) = -\frac{z}{2}\int_0^1 \frac{dx}{x(1-x)-z}\left[1 - \frac{z}{x(1-x)-z}\ln\frac{x(1-x)}{z}\right]. \tag{13.16}$$

A crude approximation of these functions for arguments z of order 1 are,

$$f(z) \sim g(z) \sim h(z) \sim z\,, \qquad \text{for } z \sim 1\,. \tag{13.17}$$

When $z \ll 1$, they are approximately,

$$f_\phi(z) \simeq \frac{z}{2}(\ln z)^2\,, \qquad h(z) \simeq z\ln(z)\,, \qquad \text{for } z \ll 1\,, \tag{13.18}$$

where $\phi = h, H, A$. Since we are taking $m_{H,A,H^\pm} > m_h = 125$ GeV, we could use the approximations for $z_\phi^{t,b,W}$ being order one or small:

$$\frac{m_t}{m_\phi} \sim 1\,, \qquad \frac{m_b}{m_\phi} \ll 1\,, \qquad \frac{m_W}{m_\phi} \sim 1\,, \tag{13.19}$$

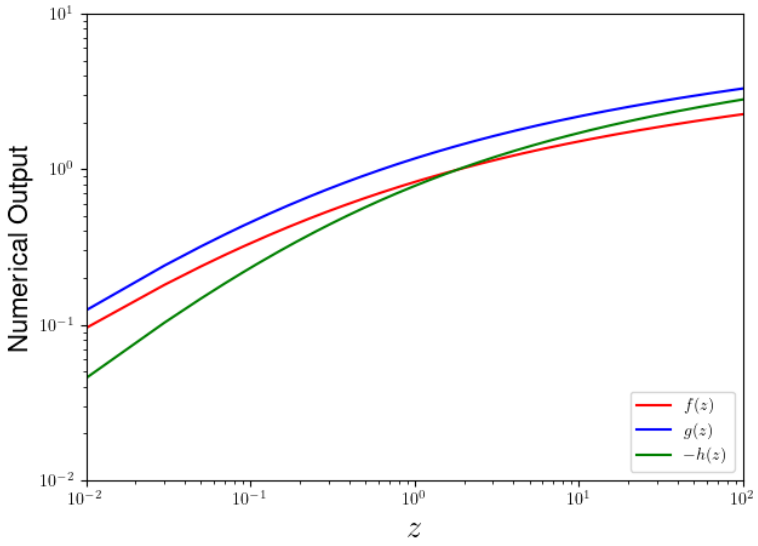

Figure 13.17: Functions used in Eqs. (13.22)–(13.23) for the evaluation of Barr-Zee type diagrams at two-loop level for the processes $\ell_1^\pm \to \ell_2^\pm + \gamma$. They depend on dilogarithmic and Clausen functions.

which implies that for t quarks and W bosons in this approximation,

$$f\left(\frac{m_{t,W}}{m_\phi}\right) \sim \frac{m_{t,W}}{m_\phi}\,, \qquad g\left(\frac{m_{t,W}}{m_\phi}\right) \sim \frac{m_{t,W}}{m_\phi}\,, \qquad h\left(\frac{m_{t,W}}{m_\phi}\right) \sim \frac{m_{t,W}}{m_\phi}\,, \tag{13.20}$$

and for b quarks in this approximation,

$$f\left(\frac{m_b}{m_\phi}\right) \sim \frac{m_b}{2m_\phi} \ln\left(\frac{m_b}{m_\phi}\right)^2, \qquad g\left(\frac{m_b}{m_\phi}\right) \sim \frac{m_b}{2m_\phi} \ln\left(\frac{m_b}{m_\phi}\right)^2,$$
$$h\left(\frac{m_b}{m_\phi}\right) \sim \frac{m_b}{2m_\phi} \ln\left(\frac{m_b}{m_\phi}\right)^2. \tag{13.21}$$

However, we compute the integrals analytically and find results that depend on dilogarithm and Clausen functions,

$$f(z) \;=\; z(2+\ln z) \;+\; (1-2z)g(z)\,, \tag{13.22}$$

$$h(z) \;=\; \frac{z[2g(z)+\ln z]}{1-4z}\,, \tag{13.23}$$

and an explicit expresson for $g(z)$ is,

$$g(z) = \begin{cases} \dfrac{z}{\sqrt{1-4z}} \left\{ \mathrm{Li}_2(x_+) + \mathrm{Li}_2(x_-) - \frac{1}{2} \ln z \ln\left(\dfrac{x_+}{x_-}\right) \right\}, & \text{for } 0 < z \leq \frac{1}{4}, \\ \dfrac{2z}{\sqrt{4z-1}} \mathrm{Cl}_2\left(2 \sin^{-1} \dfrac{1}{2\sqrt{z}}\right), & \text{for } z > \frac{1}{4}, \end{cases} \tag{13.24}$$

where $x_\pm \equiv \frac{1}{2}\left[1 \pm \sqrt{1-4z}\,\right]$ and $0 \leq \sin^{-1}\left[1/(2\sqrt{z})\right] \leq \frac{1}{2}\pi$ for $z < \frac{1}{4}$. The function $g(z)$ is continuous at $z = \frac{1}{2}$ with a value given by $g\left(\frac{1}{2}\right) = \ln(2)$.

Equipped with formulae for these integrals, we can evaluate the two-loop Barr-Zee contributions and plot the resulting $\mathrm{BR}(\ell^\pm \to \ell^\pm + \gamma)$, as shown in Figs. 13.18—13.20.

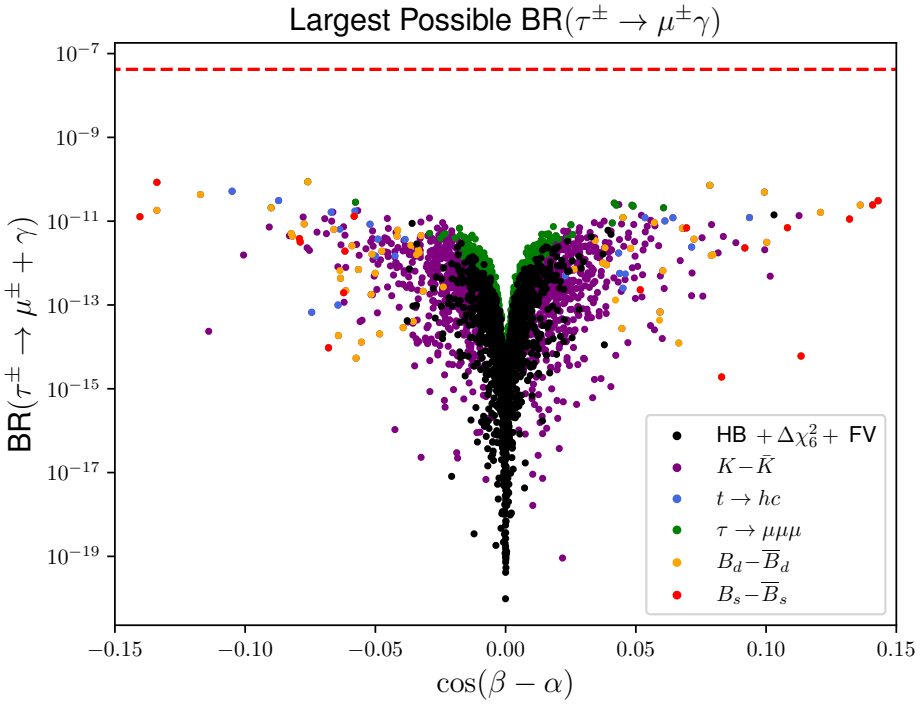

Figure 13.18: Branching ratio vs. $\cos(\beta - \alpha)$ for the process $\tau \to \mu + \gamma$.

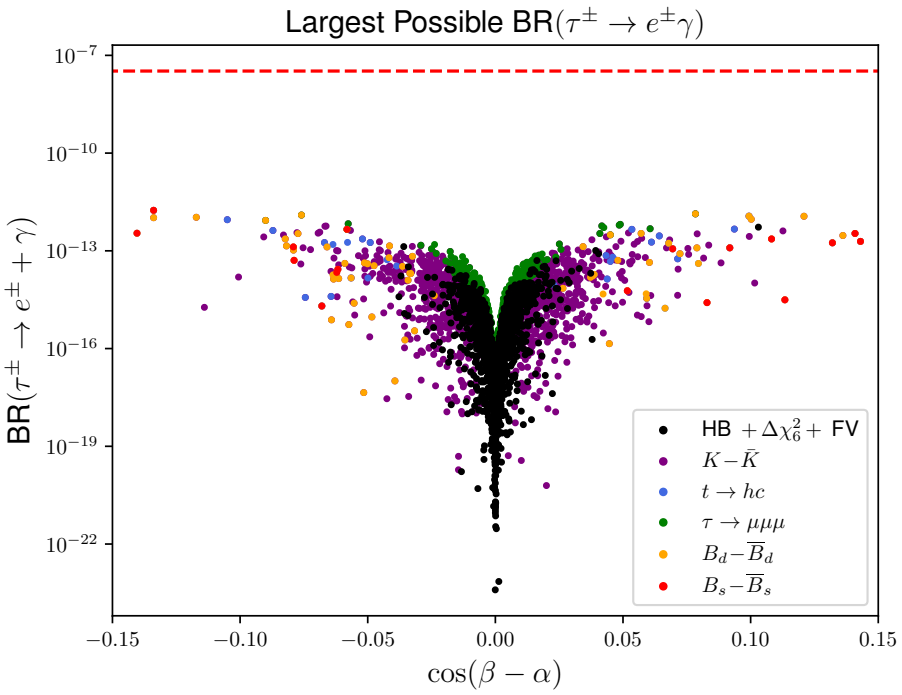

Figure 13.19: Branching ratio vs. $\cos(\beta - \alpha)$ for the process $\tau \to e + \gamma$.

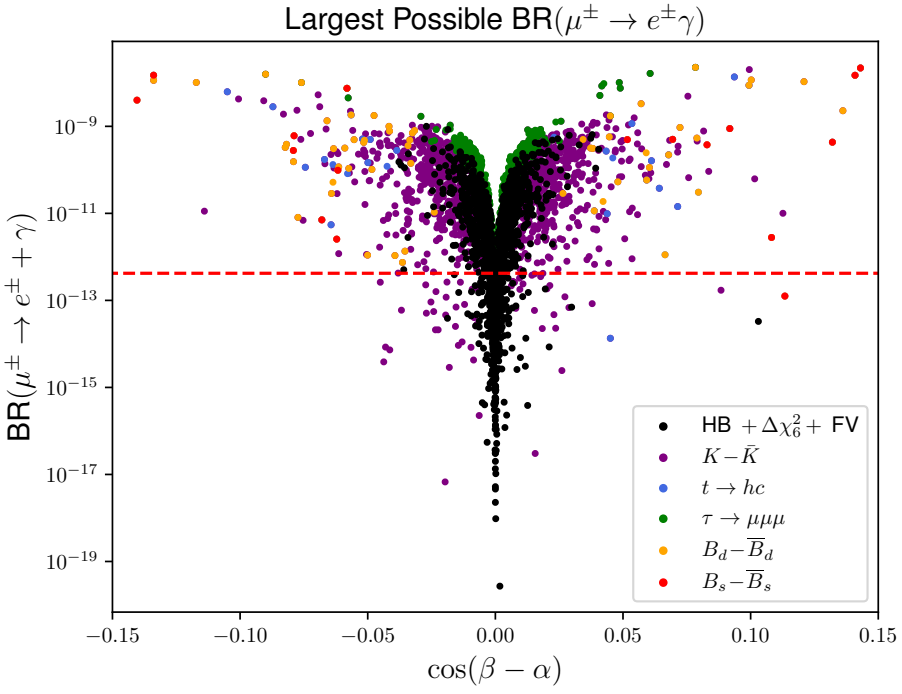

Figure 13.20: Branching ratio vs. $\cos(\beta - \alpha)$ for the process $\mu \to e + \gamma$. We did not expect these predictions to be so large and we continue to study how ρ^E_{12} is larger in our model than when one makes approximations which lead to the explicit Cheng Sher ansatz.

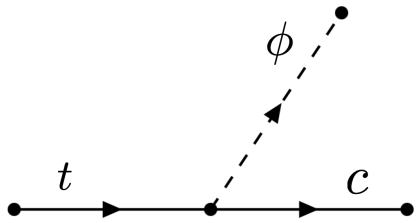

Figure 13.21: Process by which a top quark radiates a Higgs boson and transforms into a charm quark because of flavor non-conserving Yukawa couplings in this model.

13.2.3 $t \to c + h$

For the channel in which a top quark radiates a Higgs boson and becomes a charm quark $t \to c + h$, we have [88],

$$\begin{aligned} \mathrm{BR}(t \to h + c) &= \frac{m_t c_{\beta\alpha}^2 (|\rho_u^{tc}|^2 + |\rho_u^{ct}|^2)}{64\pi\Gamma_t} \left(1 - \frac{m_h^2}{m_t^2}\right)^2 \\ &= 0.28\, c_{\beta\alpha}^2\, \rho_{tc}^2\,, \end{aligned} \tag{13.25}$$

since $\rho_u^{ct} = \rho_u^{tc}$ in the CP-conserving model, and we have used $\Gamma_t = 1.42$ GeV for the top quark width [24]. We can also compute the rates for radiating an H or A by replacing m_h and $c_{\beta\alpha}$ with $s_{\beta\alpha}$ and $m_{H,A}$, respectively. The current ATLAS upper limit is $\mathrm{BR}(t \to hc) \leq 4.0 \times 10^{-4}$ at 95% CL. This is weaker than the expected limit of 2.4×10^{-4} at 95% CL., so a non-zero rate is preferred. Similarly, CMS finds $\mathrm{BR}(t \to hc) \leq 3.7 \times 10^{-4}$ at 95% CL., compared to an expected sensitivity of 3.5×10^{-4}. The high-luminosity LHC can probe $\mathrm{BR}(t \to hc) \leq 1.1 \times 10^{-4}$ [88].

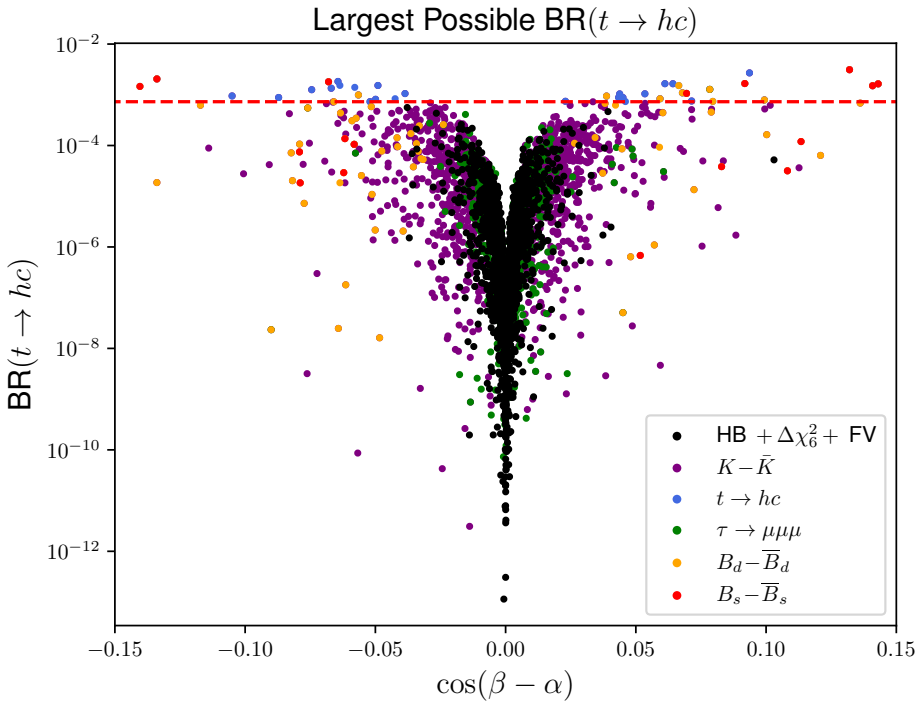

Figure 13.22: Branching ratio vs. $\cos(\beta - \alpha)$ for the process $t \to h + c$.

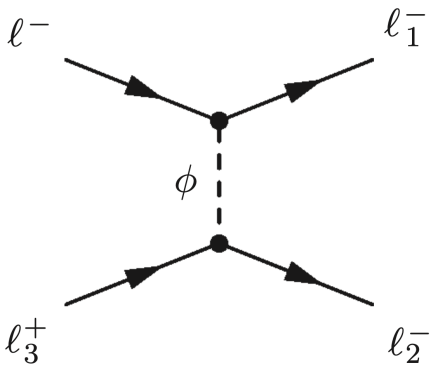

Figure 13.23: Feynman diagram for one lepton decaying into three other leptons, potentially with different flavors $\ell^\pm \to \ell_1^\pm \ell_2^\mp \ell_3^\pm$.

13.2.4 Three-lepton Final States

For the process of one lepton decaying into three others $\ell^\pm \to \ell_1^\pm \ell_2^\mp \ell_3^\pm$, we have the following formulae [96]:

$$\mathrm{BR}(\mu^- \to e^- e^+ e^-) = \frac{5}{3} \cdot \frac{\tau_\mu}{2^{11}\pi^3} \frac{m_\mu^5}{m_\phi^4} (\rho_{e\mu}\rho_{ee})^2, \tag{13.26}$$

$$\mathrm{BR}(\tau^- \to e^- e^+ e^-) = \frac{5}{3} \cdot \frac{\tau_\tau}{2^{11}\pi^3} \frac{m_\tau^5}{m_\phi^4} (\rho_{e\tau}\rho_{ee})^2, \tag{13.27}$$

$$\mathrm{BR}(\tau^- \to \mu^- e^+ e^-) = \frac{1}{3} \cdot \frac{\tau_\tau}{2^{10}\pi^3} \frac{m_\tau^5}{m_\phi^4} \left[(\rho_{\mu\tau}\rho_{ee})^2 + (\rho_{e\tau}\rho_{e\mu})^2 + \frac{1}{2}\rho_{\mu\tau}\rho_{ee}\rho_{e\tau}\rho_{e\mu} \right], \tag{13.28}$$

$$\mathrm{BR}(\tau^- \to \mu^+ e^- e^-) = \frac{5}{3} \cdot \frac{\tau_\tau}{2^{12}\pi^3} \frac{m_\tau^5}{m_\phi^4} (\rho_{e\tau}\rho_{e\mu})^2, \tag{13.29}$$

$$\mathrm{BR}(\tau^- \to e^- \mu^+ \mu^-) = \frac{1}{3} \cdot \frac{\tau_\tau}{2^{10}\pi^3} \frac{m_\tau^5}{m_\phi^4} \left[(\rho_{e\tau}Y_{\mu\mu})^2 + (\rho_{\mu\tau}\rho_{e\mu})^2 + \frac{1}{2}\rho_{e\tau}\rho_{\mu\mu}\rho_{\mu\tau}\rho_{e\mu} \right], \tag{13.30}$$

$$\mathrm{BR}(\tau^- \to e^+ \mu^- \mu^-) = \frac{5}{3} \cdot \frac{\tau_\tau}{2^{12}\pi^3} \frac{m_\tau^5}{m_\phi^4} (\rho_{\mu\tau}\rho_{e\mu})^2, \tag{13.31}$$

$$\mathrm{BR}(\tau^- \to \mu^- \mu^+ \mu^-) = \frac{5}{3} \cdot \frac{\tau_\tau}{2^{11}\pi^3} \frac{m_\tau^5}{m_\phi^4} (\rho_{\mu\tau}\rho_{\mu\mu})^2, \tag{13.32}$$

where τ_μ and τ_τ are the lifetimes of muons and tau leptons in units of GeV. The conversion is 1 GeV $= 6.582119569 \times 10^{-25}\, s^{-1}$. The current limits on the $\ell \to 3\ell$

processes are [24],

$$\mathrm{BR}(\tau \to 3\mu) \;<\; 2.1 \times 10^{-8}\,, \tag{13.33}$$

$$\mathrm{BR}(\tau \to \mu^+ e^- e^+) \;<\; 1.7 \times 10^{-8}\,, \tag{13.34}$$

$$\mathrm{BR}(\mu \to 3e) \;<\; 1.0 \times 10^{-12}\,. \tag{13.35}$$

In Figs. Figs. 13.24—13.30 we show the model's predicted BR's and current limits [24] for these processes.

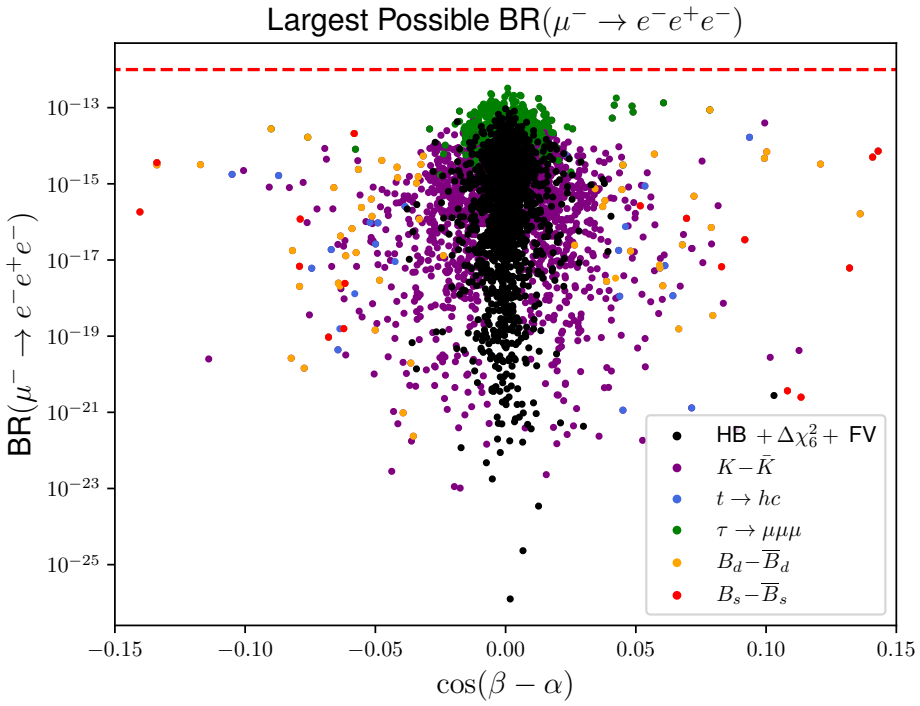

Figure 13.24: Branching ratio vs. $\cos(\beta - \alpha)$ for the process $\mu^- \to e^- e^+ e^-$.

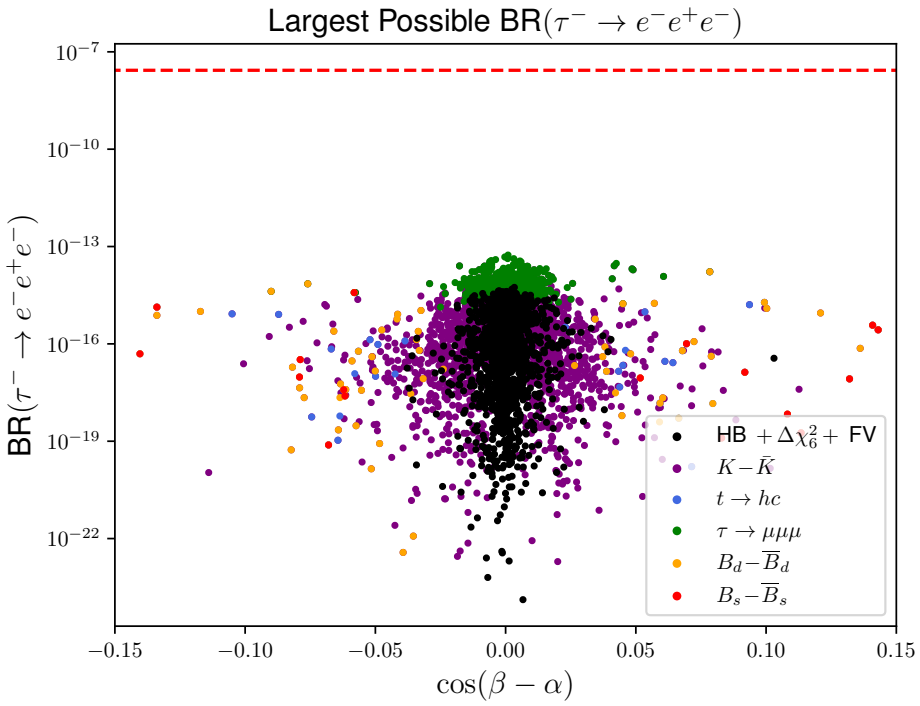

Figure 13.25: Branching ratio vs. $\cos(\beta - \alpha)$ for the process $\tau^- \to e^- e^+ e^-$.

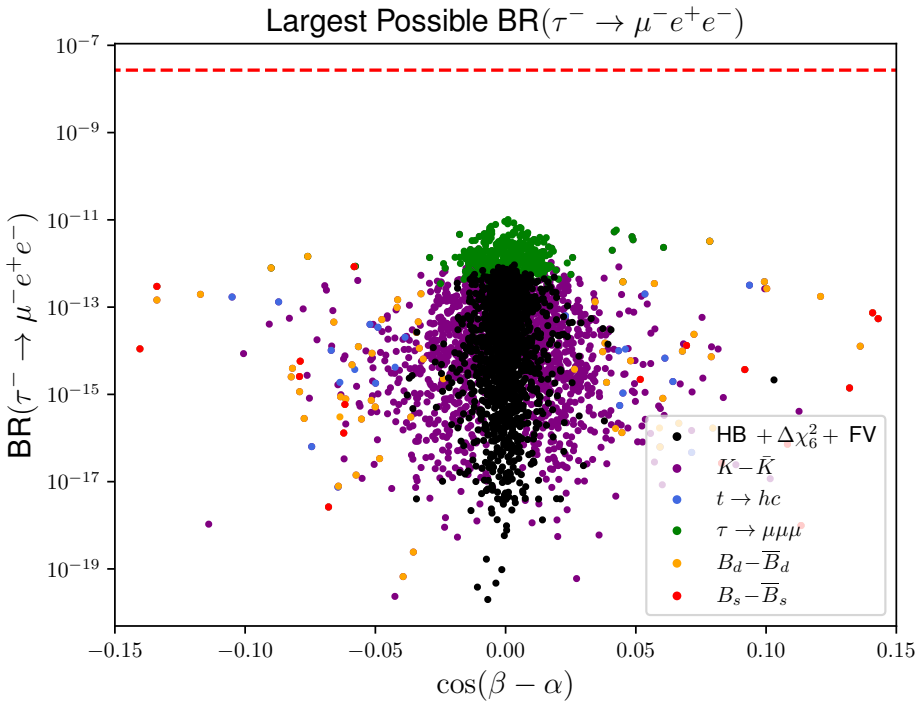

Figure 13.26: Branching ratio vs. $\cos(\beta - \alpha)$ for the process $\tau^- \to \mu^- e^+ e^-$.

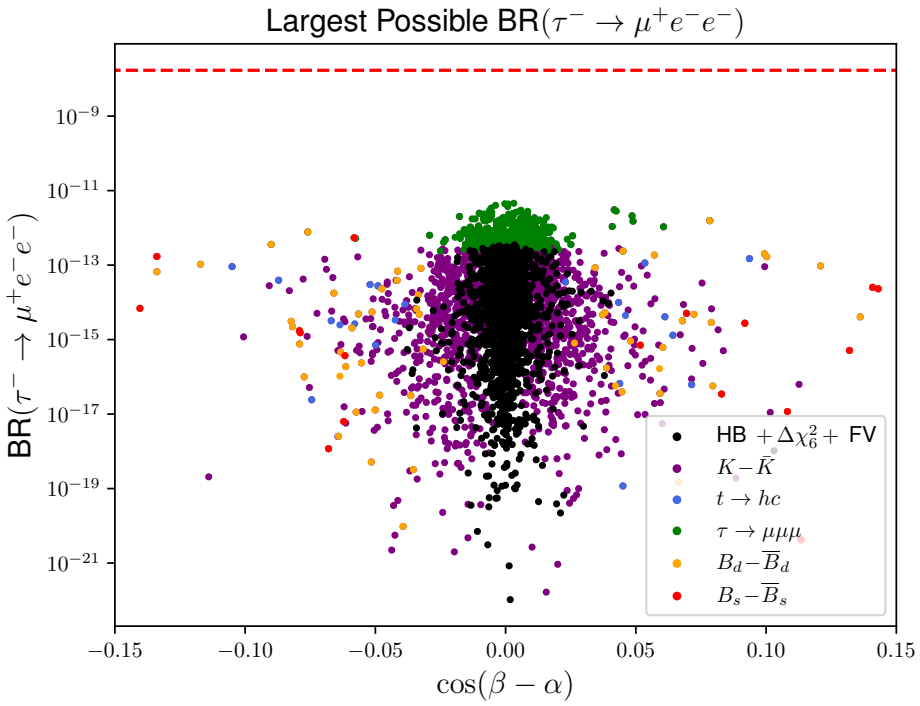

Figure 13.27: Branching ratio vs. $\cos(\beta - \alpha)$ for the process $\tau^- \to \mu^+ e^- e^-$.

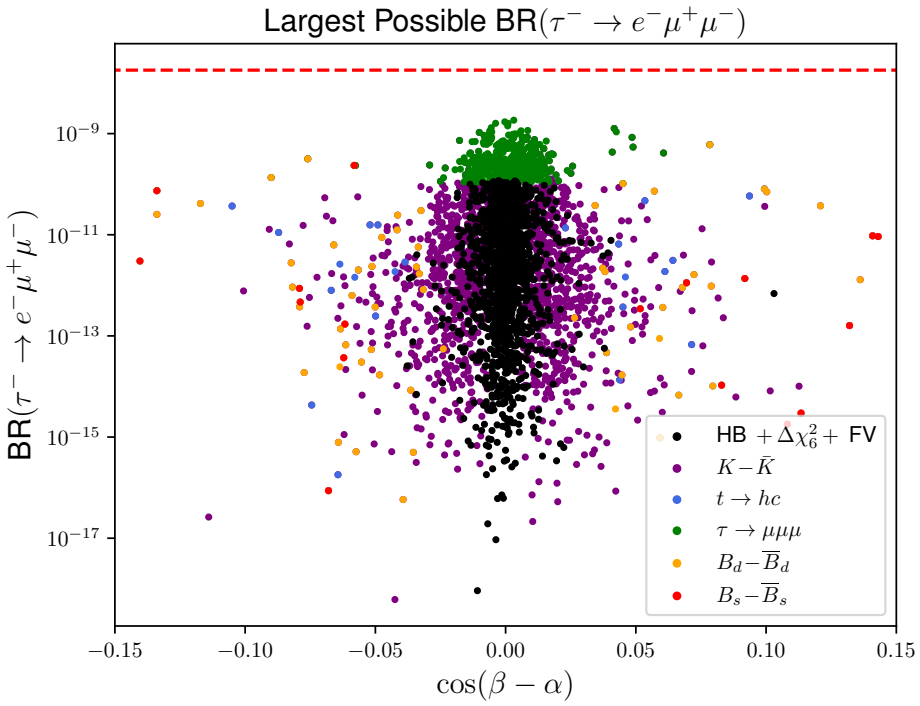

Figure 13.28: Branching ratio vs. $\cos(\beta - \alpha)$ for the process $\tau^- \to e^- \mu^+ \mu^-$.

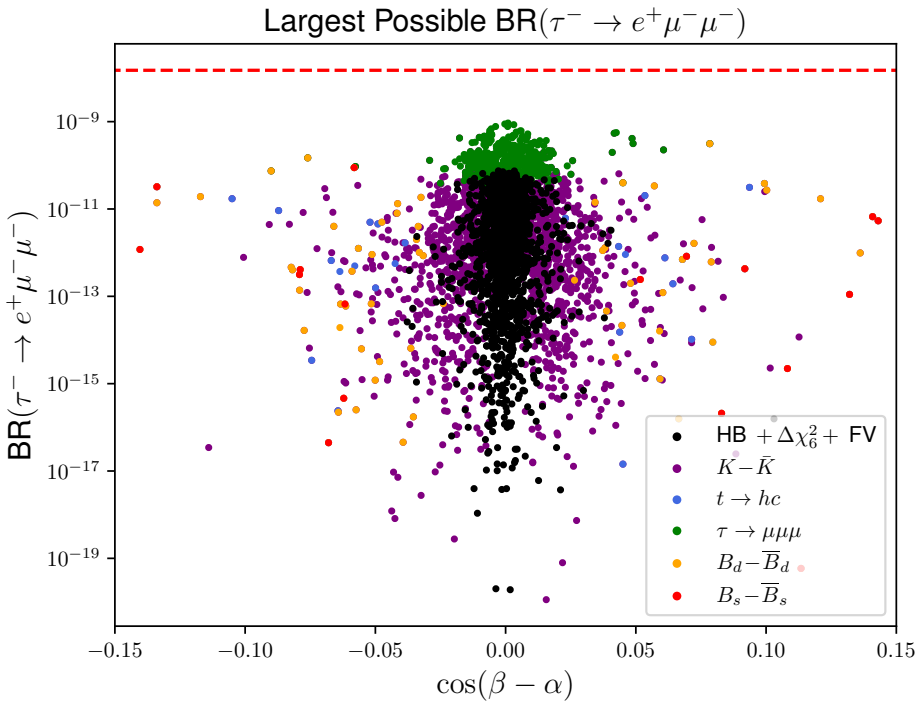

Figure 13.29: Branching ratio vs. $\cos(\beta - \alpha)$ for the process $\tau^- \to e^+\mu^-\mu^-$.

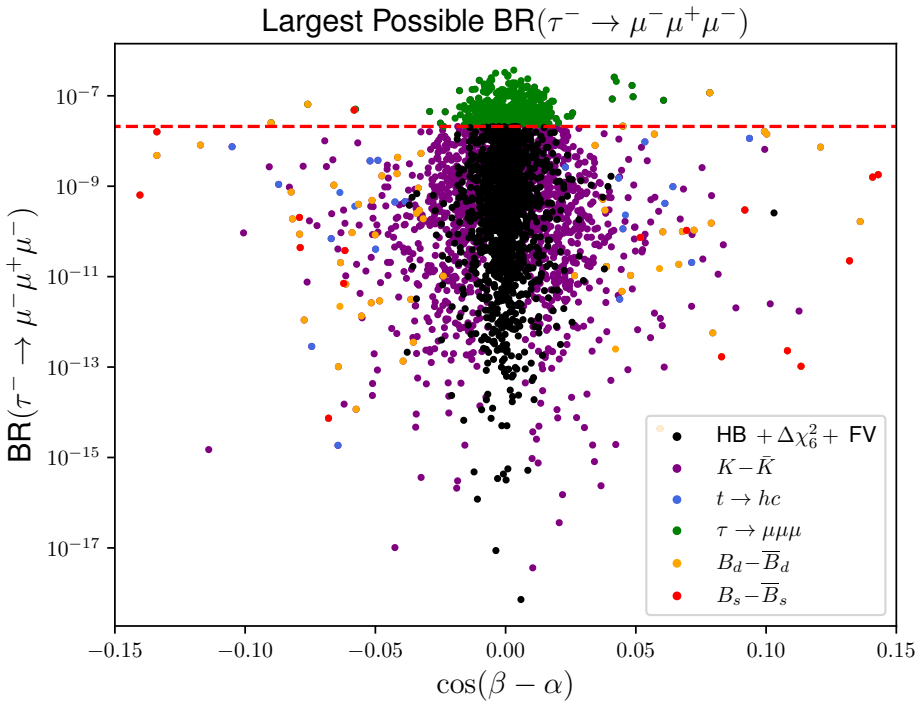

Figure 13.30: Branching ratio vs. $\cos(\beta - \alpha)$ for the process $\tau^- \to \mu^-\mu^+\mu^-$.

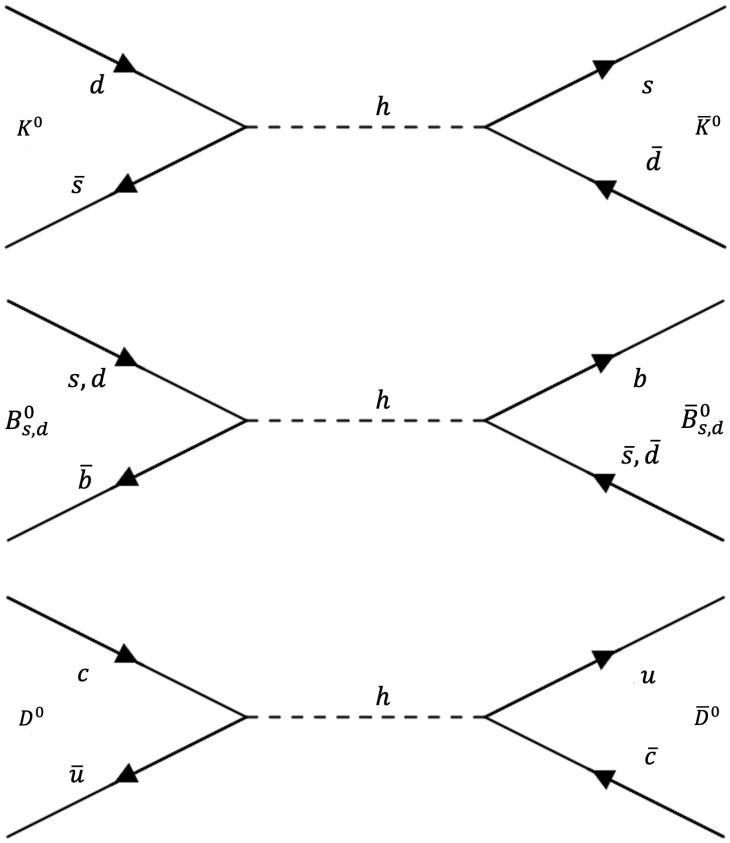

Figure 13.31: Four new tree-level neutral meson mixing diagrams that arise with flavor-violating Yukawa couplings. There are tight bounds on these processes, which only appear at loop-level with $W^{\pm}$ exchange in the SM.

13.2.5 Neutral Meson Mixing

In this flavor-non-conserving model, the mixing of neutral mesons gains tree-level processes mediated by the exchange of a neutral scalar. The process for tree-level $P^0 - \overline{P}^0$ mixing, where $P = K, B_{s,d}, D$, is shown in Fig. 13.31. There are also new box diagrams at loop-level, although they are suppressed compared to the new tree-level diagram. Fig. 13.32 shows a new diagram in the 2HDM which arises because of the presence of charged Higgs bosons, which take the place of $W^{\pm}$ bosons in the SM process. In Fig. 13.33 we see another new process, due to flavor non-conserving neutral Higgs exchange. These loop-level processes will be suppressed compared to the new tree-level diagrams.

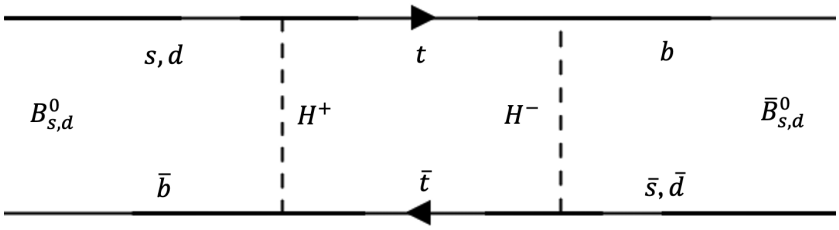

Figure 13.32: A new neutral B meson mixing diagram that arises in the 2HDM with, in which charged Higgs bosons take the place of $W^{\pm}$ exchange. Since we decouple the other states by giving them masses 800 GeV, this diagram does not significantly contribute to the calculation of neutral B meson mixing. There are analogous diagrams for K^0 and D^0 mixing.

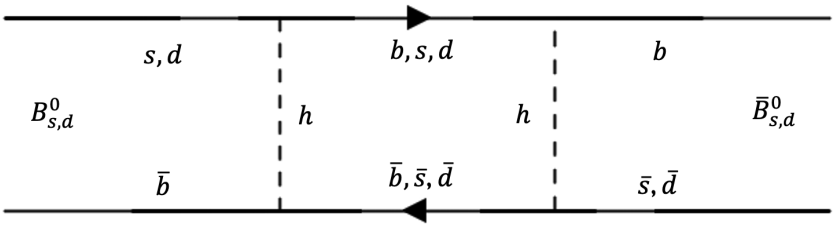

Figure 13.33: New box diagrams that arise due to flavor-violating neutral Higgs interactions, although they are suppressed compared to then new tree-level diagrams. There are analogous diagrams for K^0 and D^0 mixing.

Of the neutral meson mixing processes, kaon mixing $K - \overline{K}$ is measured the most precisely and is expected to place the tightest constraints coming from neutral meson mixing processes on the four-texture model. The processes that we are next to most sensitive to are $B_{s,d} - \overline{B}_{s,d}$ mixing. Finally, we will also check $D - \overline{D}$ mixing because the formulae are so similar, although we do not expect a limit on any ρ^Q_{ij} to arise from considering this process.

For these processes we have bounds on Wilson coefficients, and a crude way of computing them in this model. After integrating out the three neutral Higgs bosons, the dimension six effective Lagrangian describing $B_s - \overline{B}^0_s$ meson mixing is [52],

$$\mathscr{L}_{\text{eff}} = C_2(\bar{b}_R s_L)^2 + \tilde{C}_2(\bar{b}_L s_R)^2 + C_4(\bar{b}_R s_L)(\bar{b}_L s_R) + \text{h.c.}\,, \tag{13.36}$$

Wilson Coeff.	Max. Allowed 95% [GeV^{-2}]
$\lvert\mathrm{Re}\, C_2^K\rvert$	1.9×10^{-14}
$\lvert\mathrm{Re}\, C_4^K\rvert$	3.6×10^{-15}
$\lvert C_2^{B_s}\rvert$	5.6×10^{-11}
$\lvert C_4^{B_s}\rvert$	1.6×10^{-11}
$\lvert C_2^{B_d}\rvert$	7.2×10^{-13}
$\lvert C_4^{B_d}\rvert$	2.1×10^{-13}
$\lvert C_2^{D}\rvert$	1.6×10^{-13}
$\lvert C_4^{D}\rvert$	4.8×10^{-14}

Table 13.2: Wilson coefficients for neutral meson mixing $P^0 - \overline{P}^0$, where $P = K, B_{s,d}, D$. The limits are taken from Ref. [99].

in the CP-conserving limit, with Wilson coefficients given by,

$$C_2 = \frac{(\rho_{32}^D)^2}{4}\left(\frac{\sin^2(\beta-\alpha)}{m_H^2} + \frac{\cos^2(\beta-\alpha)}{m_h^2} - \frac{1}{m_A^2}\right), \tag{13.37}$$

$$\tilde{C}_2 = \frac{(\rho_{23}^{D*})^2}{4}\left(\frac{\sin^2(\beta-\alpha)}{m_H^2} + \frac{\cos^2(\beta-\alpha)}{m_h^2} - \frac{1}{m_A^2}\right), \tag{13.38}$$

$$C_4 = \frac{(\rho_{32}^D)(\rho_{23}^{D*})}{2}\left(\frac{\sin^2(\beta-\alpha)}{m_H^2} + \frac{\cos^2(\beta-\alpha)}{m_h^2} + \frac{1}{m_A^2}\right), \tag{13.39}$$

where $\rho_{23}^{D*} = \rho_{32}^D$ in the CP-conserving case, so $\tilde{C}_2 = C_2$. We also decouple the heavy Higgs bosons for now. There are analogous Wilson coefficients for B_d, K, and D mixing. The limits on these parameters are given in Table 13.2 which were obtained from [99]. Figs. 13.34—13.37 below show the various $C_{2,4}^P$ and their limits.

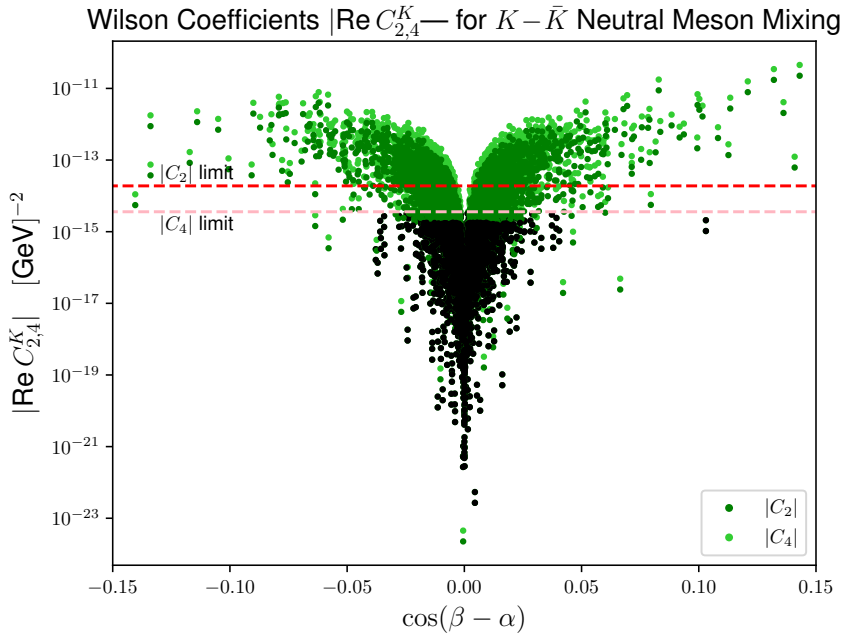

Figure 13.34: Wilson coefficients C_2 and C_4 for neutral kaon mixing $K-\bar{K}$ and their limits shown as dashed red and pink lines, respectively.

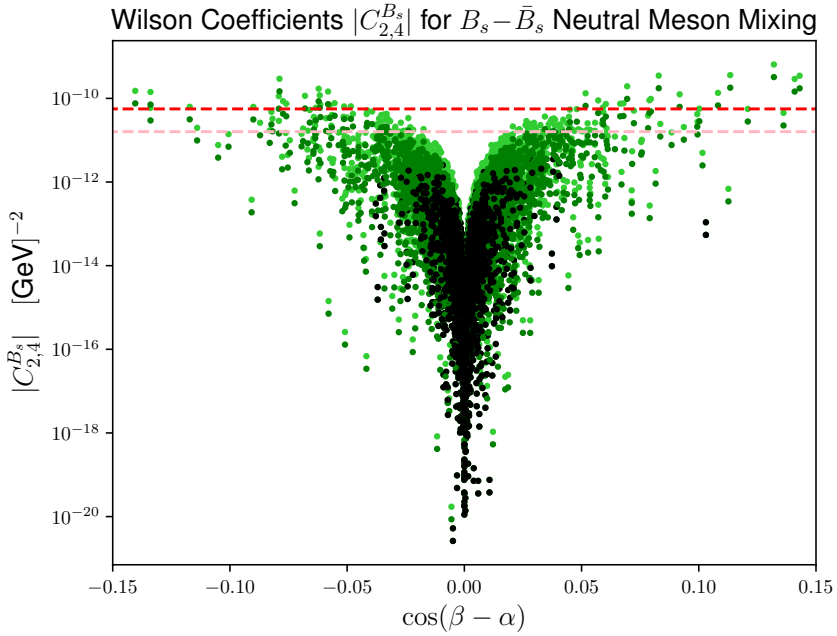

Figure 13.35: Wilson coefficients C_2 and C_4 for neutral strange meson mixing B_s–$\bar{B}_s$ and their limits shown as dashed red and pink lines, respectively.

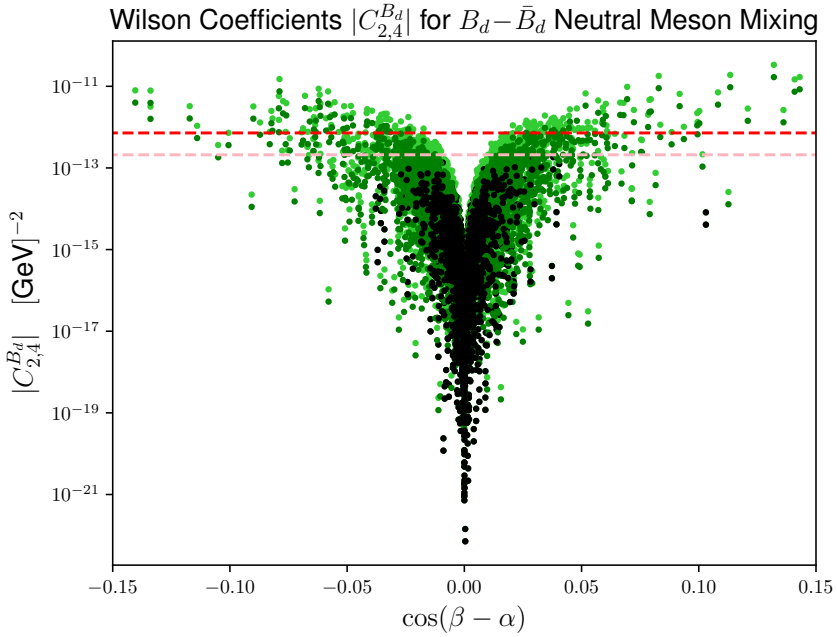

Figure 13.36: Wilson coefficients C_2 and C_4 for neutral kaon mixing $B_d - \bar{B}_d$ and their limits shown as dashed red and pink lines, respectively.

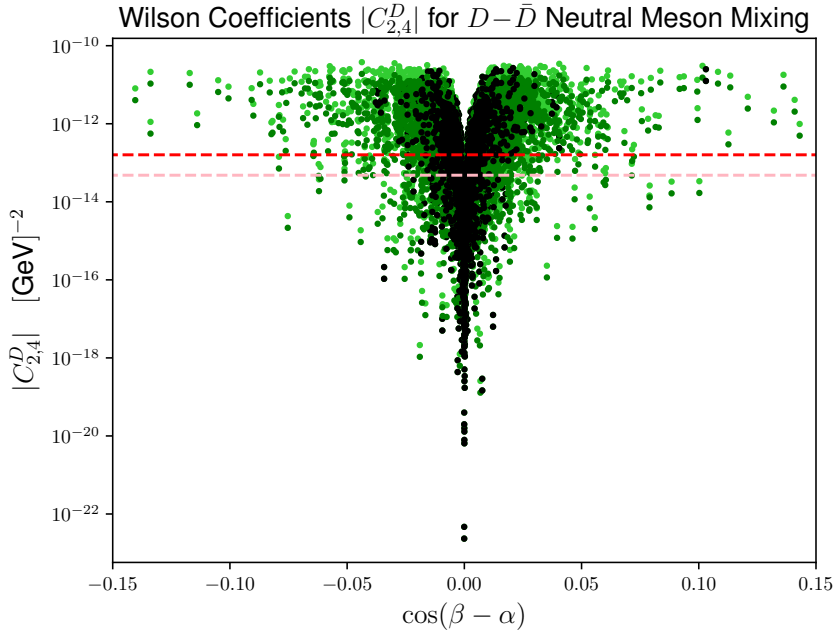

Figure 13.37: Wilson coefficients C_2 and C_4 for neutral kaon mixing $D - \bar{D}$ and their limits shown as dashed red and pink lines, respectively. We did not expect these predictions to be so large and will continue to study the effects of not taking the Cheng Sher approximation but using the full, exact expressions for the ρ_{ij}^F matrix elements.

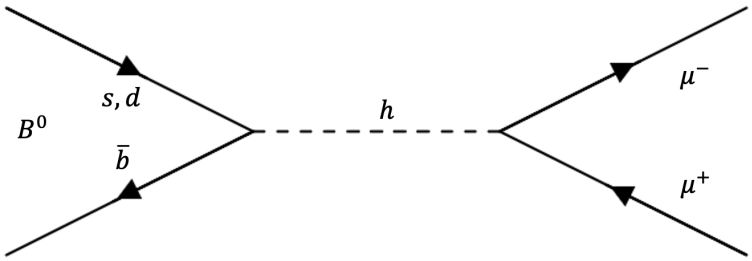

Figure 13.38: A new diagram that arises due to flavor-violating Yukawa couplings. There are analogous diagrams for K^0 and D^0 mesons.

13.2.6 $B^0_{s,d} \to \mu^+\mu^-$

Another process which arises at tree-level in the flavor-non-conserving 4-texture model is $B^0_{s,d} \to \mu^+\mu^-$. Because this channel is prohibited at tree-level in the SM and now present at tree-level, we may obtain limits on ρ_{bs} and ρ_{bd} from applying experimental limits to our analysis. Computing predictions this channel is left for future work.

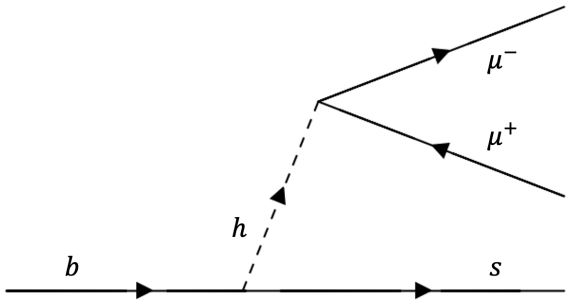

Figure 13.39: Feynman diagram for the process $b \to s + \ell^+\ell^-$ mediated by a neutral Higgs boson with flavor non-conserving couplings to quarks.

13.2.7 $b \to s + \ell^+\ell^-$

The couplings $g_{\phi qq'}$ would allow this process to occur at tree-level in this model. In the 2HDM, loop diagrams with charged Higgs boson mediators also arise, but the tree level diagram shown in Fig. 13.39 dominates. The tree-level process is a b quark decaying into an s quark and a light h, and the h subsequently decays into a lepton pair. The decay of a b quark to muons $b \to s + \mu^+\mu^-$ is of particular concern because of measurements in this channel. However, they are expected to have little impact on the viable parameter space, and computing predictions in this channel is left for future work.

Chapter 14

Conclusions

Experiments have seen signals in some of these channels (such as $h \to \tau\mu$), but new measurements are always changing the landscape. If we do see more hints of flavor-violating processes appear at the LHC, they could likely be explained within the four-texture Yukawa coupling matrix model.

Our results suggest that if one sees an excess in one or more of the flavor-violating Higgs decays $h \to \ell_1^{\pm}\ell_2^{\mp}$, then it can be described by the four-texture model. This is possible because we demonstrated that we can produce branching ratios up to or larger than the current experimental bounds on these processes. Of course, this also means our model's parameters, $\rho_{\tau\mu}$, $\rho_{\tau e}$, and $\rho_{\mu e}$ in particular, can be bounded by these measurements. We can always tune our parameters to remain consistent with current experimental bounds, but it would be more interesting if we see a sizable excess in a flavor-violating process and describe it within the context of the four-texture model.

The same goes for the processes of a lepton changing flavor and emitting a photon $\ell_1 \to \ell_2\gamma$. We can produce branching ratios above the current limits, so our model parameter space is bounded by these non-observations, but if a signal does

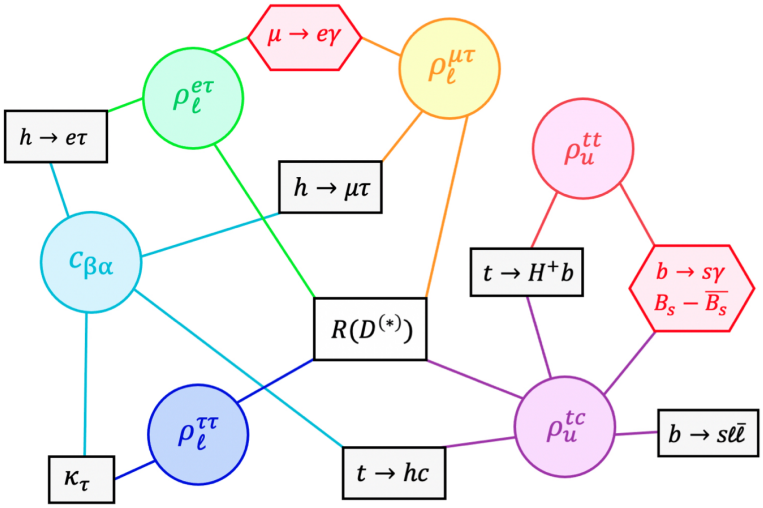

Figure 14.1: Map of relationships between new physics observables, constraints, and their relating coupling parameters, from Ref. [88]. The quantities in circles are free parameters, those in red hexagons provide strong constraints, and the black rectangles are observables that have had, do have, or may have signals of BSM physics.

arise, we will be able to explain it with the four-texture model. Upper limits can be placed on ρ_{12}^E, ρ_{23}^E, and ρ_{13}^E from measurements in these channels. The process $\mu \to e + gamma$ is of particular interest because the ρ_{12}^E element in our model could be substantially larger than in the Cheng Sher ansatz.

The story is different for the three lepton final state processes $\ell \to 3\ell$. In all of these channels, our model cannot produce branching ratios as large as the experimental bounds. This implies that all regions of our model's parameter space predicts that these bounds will continue to get tighter as we collect more collider data, and no real significant excesses are expected to be seen.

The four-texture model can generate sizable $t \to h + c$ larger than the experimental limit, so we could explain an excess in this channel if it arises, and we get an upper bound on ρ_{tc}.

In the neutral meson mixing considerations, kaon mixing measurements are the most restrictive on our model. The D meson results are also, but we continue to

study this process since the ρ_{12}^U elements in our model could be substantially larger than in the Cheng Sher ansatz. B_d and B_s mixing measurements are beginning to probe our model's parameter space.

There are many directions for future work on this project. The manuscript to be submitted for publication is in progress with some of the following considerations. We will incorporate the other heavier scalars in the lower energy regime of the model by reducing their masses from 800 GeV to something in the range $[125, 700]$ GeV so that they can play a role in the coupling dynamics of the model. We also can reinstate the phases on the parameters in the Yukawa coupling matrices and remove the Hermiticity condition on the coupling matrices to study models with CP-violation. We could also introduce CP-violation through the scalar vevs and scalar potential parameters if we desired to do so. Other combinations of signs of the parameters $\eta_q = \lambda_2^q/m_q$ may affect the results, so we will investigate this possibility.

Bibliography

[1] The ATLAS Collaboration, Nature **607**, 52 (2022) [arXiv:2207.00092 [hep-ex]].

[2] The CMS Collaboration, Nature **607**, 60 (2022) [arXiv:2207.00043 [hep-ex]].

[3] G.C. Branco, P.M. Ferreira, L. Lavoura, M.N. Rebelo, M. Sher and J.P. Silva, Phys. Rept. **516**, 1 (2012) [arXiv:1106.0034 [hep-ph]].

[4] S.L. Glashow and S. Weinberg, Phys. Rev. D **15**, 1958 (1977).

[5] E.A. Paschos, Phys. Rev. D **15**, 1966 (1977).

[6] L.J. Hall and M.B. Wise, Nucl. Phys. B **187**, 397 (1981).

[7] V.D. Barger, J.L. Hewett and R.J.N. Phillips, Phys. Rev. D **41**, 3421-3441 (1990)

[8] M. Aoki, S. Kanemura, K. Tsumura and K. Yagyu, Phys. Rev. D **80**, 015017 (2009) [arXiv:0902.4665 [hep-ph]].

[9] A. Pich and P. Tuzon, Phys. Rev. D **80**, 091702 (2009) [arXiv:0908.1554 [hep-ph]].

[10] H. Serodio, Phys. Lett. B **700**, 133 (2011) [arXiv:1104.2545 [hep-ph]].

[11] S. Knapen and D.J. Robinson, Phys. Rev. Lett. **115**, 161803 (2015) [arXiv:1507.00009 [hep-ph]].

[12] D. Egana-Ugrinovic, S. Homiller and P. Meade, Phys. Rev. Lett. **123**, 031802 (2019) [arXiv:1811.00017 [hep-ph]].

[13] D. Egana-Ugrinovic, S. Homiller and P. Meade, Phys. Rev. D **100**, 115041 (2019) [arXiv:1908.11376 [hep-ph]].

[14] C.B. Braeuninger, A. Ibarra and C. Simonetto, Phys. Lett. B **692**, 189 (2010) [arXiv:1005.5706 [hep-ph]].

[15] S. Gori, H.E. Haber and E. Santos, JHEP **06**, 110 (2017) [arXiv:1703.05873 [hep-ph]].

[16] P.M. Ferreira, L. Lavoura and J. P. Silva, Phys. Lett. B **688**, 341 (2010) [arXiv:1001.2561 [hep-ph]].

[17] T.S. Roussy et al., Science **381**, 46 (2023) [arXiv:2212.11841 [physics.atom-ph]].

[18] W. Altmannshofer, S. Gori, N. Hamer and H.H. Patel, Phys. Rev. D **102**, 115042 (2020) [arXiv:2009.01258 [hep-ph]].

[19] H.E. Haber and D. O'Neil, Phys. Rev. D **74**, 015018 (2006) [erratum: Phys. Rev. D **74**, 059905 (2006)] [arXiv:hep-ph/0602242 [hep-ph]].

[20] R. Boto, T.V. Fernandes, H.E. Haber, J.C. Romão and J.P. Silva, Phys. Rev. D **101**, 055023 (2020) [arXiv:2001.01430 [hep-ph]].

[21] I.P. Ivanov, Phys. Rev. D **75**, 035001 (2007) [erratum: Phys. Rev. D **76**, 039902 (2007)] [arXiv:hep-ph/0609018 [hep-ph]].

[22] I.P. Ivanov, Phys. Rev. D **77**, 015017 (2008) [arXiv:0710.3490 [hep-ph]].

[23] I. F. Ginzburg and I. P. Ivanov, Phys. Rev. D **72**, 115010 (2005) [arXiv:hep-ph/0508020 [hep-ph]].

[24] R.L. Workman et al. [Particle Data Group], *Review of Particle Physics*, PTEP **2022**, 083C01 (2022).

[25] Haber, Howard E. and O'Neil, Deva Phys. Rev. D **74**, 015018 (2006)

[26] V. Andreev *et al.* [ACME Collaboration], Nature **562**, no.7727, 355 (2018).

[27] G. Aad et al. [ATLAS Collaboration], Eur. Phys. J. C **81**, 396 (2021) [arXiv:2011.05639 [hep-ex]].

[28] G. Aad et al. [ATLAS Collaboration], Phys. Rev. Lett. **125**, 051801 (2020) [arXiv:2002.12223 [hep-ex]].

[29] See Fig. 08 in `https://atlas.web.cern.ch/Atlas/GROUPS/PHYSICS/PAPERS/HDBS-2018-46/`, which appeared in auxiliary material that was not included in Ref. [28].

[30] A.M. Sirunyan et al. [CMS Collaboration], JHEP **04**, 171 (2020) [arXiv:1908.01115 [hep-ex]].

[31] The CMS Collaboration, arXiv:2208.02717 [hep-ex], to be published in JHEP.

[32] H. Georgi and D.V. Nanopoulos, Phys. Lett. B **82**, 95 (1979)

[33] L. Lavoura, Phys. Rev. D **50**, 7089 (1994) [arXiv:hep-ph/9405307].

[34] L. Lavoura and J.P. Silva, Phys. Rev. D **50**, 4619 (1994) [arXiv:hep-ph/9404276].

[35] F.J. Botella and J. P. Silva, Phys. Rev. D **51**, 3870 (1995) [arXiv:hep-ph/9411288].

[36] G.C. Branco, L. Lavoura and J. P. Silva, *CP Violation* (Oxford University Press, Oxford, UK, 1999).

[37] S. Davidson and H.E. Haber, Phys. Rev. D **72**, 035004 (2005) [erratum: Phys. Rev. D **72**, 099902 (2005)] [arXiv:hep-ph/0504050 [hep-ph]].

[38] E. Gross and O. Vitells, Eur. Phys. J. C **70**, 525 (2010) [arXiv:1005.1891 [physics.data-an]].

[39] ATLAS Collaboration, arXiv:2210.05415 [hep-ex].

[40] F. Richard, arXiv:2003.07112 [hep-ph].

[41] E. Arganda, L. Da Rold, D.A. Díaz and A.D. Medina, JHEP **11**, 119 (2021) [arXiv:2108.03058 [hep-ph]].

[42] T. Biekötter, A. Grohsjean, S. Heinemeyer, C. Schwanenberger and G. Weiglein, Eur. Phys. J. C **82**, 178 (2022) [arXiv:2109.01128 [hep-ph]].

[43] A. Kundu, A. Le Yaouanc, P. Mondal and F. Richard, arXiv:2211.11723 [hep-ph].

[44] F.J. Botella, F. Cornet-Gomez, C. Miró and M. Nebot, arXiv:2302.05471 [hep-ph].

[45] B. Abi et al. [Muon $g-2$ Collaboration], Phys. Rev. Lett. **126**, no.14, 141801 (2021) [arXiv:2104.03281 [hep-ex]].

[46] S. Kanemura and K. Yagyu, Phys. Lett. B **751**, 289-296 (2015) [arXiv:1509.06060 [hep-ph]].

[47] H. Bahl, M. Carena, N.M. Coyle, A. Ireland and C.E.M. Wagner, arXiv:2210.00024 [hep-ph].

[48] H.E. Haber and D. O'Neil, Phys. Rev. D **83**, 055017 (2011) [arXiv:1011.6188 [hep-ph]].

[49] T. Enomoto and R. Watanabe, JHEP **05**, 002 (2016) [arXiv:1511.05066 [hep-ph]].

[50] M. Bona et al. [UT*fit* Collaboration], arXiv:2212.03894 [hep-ph].

[51] A. Arbey, F. Mahmoudi, O. Stal and T. Stefaniak, Eur. Phys. J. C **78**, 182 (2018) [arXiv:1706.07414 [hep-ph]].

[52] S. Gori, H.E. Haber and E. Santos, JHEP **06**, 110 (2017) [arXiv:1703.05873 [hep-ph]].

[53] R.V. Harlander, S. Liebler and H. Mantler, Comput. Phys. Commun. **184**, 1605-1617 (2013) [arXiv:1212.3249 [hep-ph]].

[54] D. Eriksson, J. Rathsman and O. Stal, Comput. Phys. Commun. **181**, 189-205 (2010) [arXiv:0902.0851 [hep-ph]].

[55] The ATLAS Collaboration, ATLAS-CONF-2021-052 (October 21, 2021).

[56] The CMS Collaboration, CMS PAS HIG-21-011 (August 8, 2022).

[57] G. Aad et al. [ATLAS Collaboration], Eur. Phys. J. C **81**, 332 (2021) [arXiv:2009.14791 [hep-ex]].

[58] M. Aaboud et al. [ATLAS Collaboration], Eur. Phys. J. C **78**, 24 (2018) [arXiv:1710.01123 [hep-ex]].

[59] M. Misiak, A. Rehman and M. Steinhauser, JHEP **06**, 175 (2020) [arXiv:2002.01548 [hep-ph]].

[60] A.M. Sirunyan et al. [CMS Collaboration], JHEP **07**, 126 (2020) [arXiv:2001.07763 [hep-ex]].

[61] A.M. Sirunyan et al. [CMS Collaboration], JHEP **07**, 142 (2019) [arXiv:1903.04560 [hep-ex]].

[62] Namely, the figures for $H^{\pm}$ production with $\tan\beta$ equal to 1, 8 and 30 from https://twiki.cern.ch/twiki/bin/view/LHCPhysics/LHCHWGCrossSectionsFigures.

[63] G. Aad *et al.* [ATLAS Collaboration], Phys. Rev. D **106** (2022), 052001 [arXiv:2112.11876 [hep-ex]].

[64] ATLAS Collaboration, ATLAS-CONF-2021-052.

[65] CMS Collaboration, [arXiv:2206.10268 [hep-ex]], to be published in JHEP..

[66] CMS Collaboration, arXiv:2207.01046 [hep-ex].

[67] A.M. Sirunyan et al. [CMS Collaboration], JHEP **08**, 113 (2018) [arXiv:1805.12191 [hep-ex]].

[68] G. Aad et al. [ATLAS Collaboration], JHEP **06**, 145 (2021) [arXiv:2102.10076 [hep-ex]].

[69] J.F. Gunion, H.E. Haber, G.L. Kane and S. Dawson, *The Higgs Hunter's Guide* (Westview Press, Boulder, CO, 2000).

[70] H. Georgi and M. Machacek, Nucl. Phys. B **262**, 463 (1985).

[71] M.S. Chanowitz and M. Golden, Phys. Lett. B **165**, 105 (1985).

[72] J.F. Gunion, R. Vega and J. Wudka, Phys. Rev. D **42**, 1673 (1990).

[73] A. Peñuelas and A. Pich, JHEP **12**, 084 (2017) [arXiv:1710.02040 [hep-ph]].

[74] Y. Amhis et al. [Heavy Flavor Averaging Group (HFLAV)], arXiv:2206.07501 [hep-ex].

[75] M. Ciuchini, G. Degrassi, P. Gambino and G.F. Giudice, Nucl. Phys. B **527**, 21 (1998) [arXiv:hep-ph/9710335 [hep-ph]].

[76] P. Ciafaloni, A. Romanino and A. Strumia, Nucl. Phys. B **524**, 361 (1998) [arXiv:hep-ph/9710312 [hep-ph]].

[77] F. Borzumati and C. Greub, Phys. Rev. D **58**, 074004 (1998) [arXiv:hep-ph/9802391 [hep-ph]].

[78] F. Borzumati and C. Greub, Phys. Rev. D **59**, 057501 (1999) [arXiv:hep-ph/9809438 [hep-ph]].

[79] C. Bobeth, M. Misiak and J. Urban, Nucl. Phys. B **567**, 153 (2000) [arXiv:hep-ph/9904413 [hep-ph]].

[80] A.L. Kagan and M. Neubert, Eur. Phys. J. C **7**, 5 (1999) [arXiv:hep-ph/9805303 [hep-ph]].

[81] T. Hurth, E. Lunghi and W. Porod, Nucl. Phys. B **704**, 56 (2005) [arXiv:hep-ph/0312260 [hep-ph]].

[82] E. Lunghi and J. Matias, JHEP **04**, 058 (2007) [arXiv:hep-ph/0612166 [hep-ph]].

[83] O. Eberhardt, A.P. Martínez and A. Pich, JHEP **05**, 005 (2021) [arXiv:2012.09200 [hep-ph]].

[84] A.J. Buras, *Gauge Theory of Weak Decays* (Cambridge University Press, Cambridge, UK, 2020).

[85] J. L. Diaz-Cruz, R. Noriega-Papaqui and A. Rosado, Phys. Rev. D **71**, 015014 (2005) [arXiv:hep-ph/0410391 [hep-ph]].

[86] M. Gómez-Bock, W. Gonzalez-Olivares, M. Hentschinski, A. Rosado and S. Rosado-Navarro, [arXiv:2303.08890 [hep-ph]].

[87] Y. Omura, E. Senaha and K. Tobe, Phys. Rev. D **94**, no.5, 055019 (2016) [arXiv:1511.08880 [hep-ph]].

[88] A. Crivellin and S. Iguro, [arXiv:2311.03430 [hep-ph]].

[89] A. Crivellin, D. Müller and C. Wiegand, JHEP **06**, 119 (2019) [arXiv:1903.10440 [hep-ph]].

[90] A. E. Carcamo Hernandez, R. Martinez and J. A. Rodriguez, Eur. Phys. J. C **50**, 935-948 (2007) [arXiv:hep-ph/0606190 [hep-ph]].

[91] H. Bahl, T. Biekötter, S. Heinemeyer, C. Li, S. Paasch, G. Weiglein and J. Wittbrodt, Comput. Phys. Commun. **291**, 108803 (2023) [arXiv:2210.09332 [hep-ph]].

[92] S. Davidson and G. J. Grenier, Phys. Rev. D **81**, 095016 (2010) [arXiv:1001.0434 [hep-ph]].

[93] D. Chang, W. S. Hou and W. Y. Keung, Phys. Rev. D **48**, 217-224 (1993) [arXiv:hep-ph/9302267 [hep-ph]].

[94] T. P. Cheng and M. Sher, Phys. Rev. D **35**, 3484 (1987)

[95] S. Baek and J. Tandean, Eur. Phys. J. C **76**, no.12, 673 (2016) [arXiv:1604.08935 [hep-ph]].

[96] Y. F. Zhou, J. Phys. G **30**, 783-792 (2004) [arXiv:hep-ph/0307240 [hep-ph]].

[97] H. Fritzsch, Z. z. Xing and D. Zhang, Nucl. Phys. B **974**, 115634 (2022) [arXiv:2111.06727 [hep-ph]].

[98] B. Aubert *et al.* [BaBar], Phys. Rev. Lett. **104**, 021802 (2010) [arXiv:0908.2381 [hep-ex]].

[99] M. Bona *et al.* [UTfit], JHEP **03**, 049 (2008) [arXiv:0707.0636 [hep-ph]].

Appendix A

Appendices

The loop functions G_a^i, C_a^i, and D_a^i used in Eq. (3.19) and Eq. (3.21) in the $b \to s + \gamma$ constraint calculation are presented in Ref. [49] and reproduced here for convenience:

$$G_1^7(y) = \frac{y(7-5y-8y^2)}{24(y-1)^3} + \frac{y^2(3y-2)}{4(y-1)^4}\ln y\,, \quad G_2^7(y) = \frac{y(3-5y)}{12(y-1)^2} + \frac{y(3y-2)}{6(y-1)^3}\ln y\,, \tag{A.1}$$

$$G_1^8(y) = \frac{y(2+5y-y^2)}{8(y-1)^3} - \frac{3y^2}{4(y-1)^4}\ln y\,, \quad G_2^8(y) = \frac{y(3-y)}{4(y-1)^2} - \frac{y}{2(y-1)^3}\ln y\,, \tag{A.2}$$

$$\begin{aligned} C_1^7(y) = \frac{2}{9}y\Bigg[&\frac{y(18-37y+8y^2)}{(y-1)^4}\mathrm{Li}_2\left(1-\frac{1}{y}\right) + \frac{y(-14+23y+3y^2)}{(y-1)^5}\ln^2 y \\ &+ \frac{-50+251y-174y^2-192y^3+21y^4}{9(y-1)^5}\ln y - \frac{3y-2}{3(y-1)^4}\ln y \\ &+ \frac{797-5436y+7569y^2-1202y^3}{108(y-1)^4} - \frac{16-29y+7y^2}{18(y-1)^3}\Bigg]\,, \end{aligned} \tag{A.3}$$

$$\begin{aligned} C_2^7(y) = -\frac{4}{3}y\Bigg[&\frac{4(-3+7y-2y^2)}{3(y-1)^3}\mathrm{Li}_2\left(1-\frac{1}{y}\right) + \frac{8-14y-3y^2}{3(y-1)^4}\ln^2 y \\ &+ \frac{2(-3-y+12y^2-2y^3)}{3(y-1)^4}\ln y + \frac{7-13y+2y^2}{(y-1)^3}\Bigg]\,, \end{aligned} \tag{A.4}$$

$$C_1^8(y) = \frac{1}{6}y\left[\frac{y(30-17y+13y^2)}{(y-1)^4}\mathrm{Li}_2\left(1-\frac{1}{y}\right) - \frac{y(31+17y)}{(y-1)^5}\ln^2 y\right.$$
$$- \frac{226-817y-1353y^2-318y^3-42y^4}{36(y-1)^5}\ln y - \frac{3y-2}{6(y-1)^4}\ln y$$
$$\left.+\frac{1130-18153y+7650y^2-4451y^3}{216(y-1)^4} - \frac{16-29y+7y^2}{36(y-1)^3}\right], \qquad \text{(A.5)}$$

$$C_2^8(y) = -\frac{1}{3}y\left[\frac{-36+25y-17y^2}{2(y-1)^3}\mathrm{Li}_2\left(1-\frac{1}{y}\right) + \frac{19+17y}{(y-1)^4}\ln^2 y\right.$$
$$\left.+\frac{-3-187y+12y^2-14y^3}{4(y-1)^4}\ln y + \frac{3(143-44y+29y^2)}{8(y-1)^3}\right], \qquad \text{(A.6)}$$

$$D_1^7(y) = \frac{2}{9}y\left[\frac{-31-18y+135y^2-14y^3}{6(y-1)^4} + \frac{y(14-23y-3y^2)}{(y-1)^5}\ln y\right], \qquad \text{(A.7)}$$

$$D_2^7(y) = -\frac{2}{9}y\left[\frac{21-47y+8y^2}{(y-1)^3} + \frac{2(-8+14y+3y^2)}{(y-1)^4}\ln y\right], \qquad \text{(A.8)}$$

$$D_1^8(y) = \frac{1}{6}y\left[\frac{-38-261y+18y^2-7y^3}{6(y-1)^4} + \frac{y(31+17y)}{(y-1)^5}\ln y\right], \qquad \text{(A.9)}$$

$$D_2^8(y) = -\frac{1}{3}y\left[\frac{81-16y+7y^2}{2(y-1)^3} - \frac{19+17y}{(y-1)^4}\ln y\right]. \qquad \text{(A.10)}$$